Characterization Of Gaseous And Scintillator Detectors For High Energy Physics And Cosmic Ray Experiments

Thesis Submitted For The Degree Of

DOCTOR OF PHILOSOPHY (SCIENCE)

in

Physics (Experimental)

by

Shreya Roy

DEPARTMENT OF PHYSICS
UNIVERSITY OF CALCUTTA
KOLKATA, INDIA
2022

Abstract of the Thesis

The thesis is based on the characterization of gaseous detectors for high energy physics experiments and the development of scintillators for cosmic ray experiments.

Gaseous detectors are the most widely used ones in almost all the leading collider experiments such as ALICE, ATLAS, CMS at the LHC and STAR at the RHIC since they are cheap, simple to fabricate, easy to operate and maintain. The upcoming Compressed Baryonic Matter (CBM) experiment at the Facility for Anti-proton and Ion Research (FAIR) will also use gaseous detectors. The CBM experiment is designed to explore the QCD phase diagram in the region of moderate baryon densities. It will have a Muon Chamber (MuCh) subsystem, especially designed to study di-muon physics, which is one of the chief goals of this experiment. The 1^{st} and 2^{nd} station of the CBM-MuCh will have Gas Electron Multiplier (GEM) detector. For the 3^{rd} and 4^{th} station, the classic and widely used straw tube detector is a possible candidate. The main challenge to be faced by the MuCh detectors is the high particle rate that will be reached at CBM. This thesis aims at testing the feasibility of using straw tubes in CBM-MuCh. Another important factor of concern for the HEP experiments is aging in gaseous detectors under long-term operation. This work also reports the basic characterization, rate handling capability, timing properties and aging studies for the straw tube detector.

Cosmic rays of energy more than 10^{14} eV can only be studied through the detection of secondary particles forming extensive air showers (EAS) for which various experimental programs around the world have built large size arrays of detectors. The primary objective of this work was to characterize and set up a detector array using Plastic Scintillation Detectors (PSD) at the mountains of Darjeeling (27°N, 88°E, at an altitude of 2200m above sea level) mainly for the study of cosmic rays at high altitude. In this work, the air shower rate at high altitude was measured and the results were compared with GRAPES-3 (at similar altitude).

The cosmic ray flux is known to be dependent on atmospheric parameters. Astrophysical phenomena like solar eclipses produce disturbance in the atmosphere thereby effecting the cosmic ray intensity. There are earlier reports on decrement in secondary cosmic gamma ray (SCGR) flux during solar eclipses, but there is no concrete physical explanation for this observation. The motivation in this part of the thesis was to perform a systematic measurement of SCGR using an inorganic scintillation detector in laboratory at India, during the total solar eclipse on 2017 over America. This work includes the characterization of NaI(Tl) scintillator and measures the cosmic ray gamma flux during the week surrounding the solar eclipse day. A correlation between the 'solar eclipse induced atmospheric disturbances' and the cosmic ray gamma flux was also drawn.

Dedicated to

My Uncle, Late Mr. Probhat Singh
and
my Mother, Mrs. Sachi Roy

Declaration

I, Shreya Roy, declare that this thesis titled, "Characterization Of Gaseous And Scintillator Detectors For High Energy Physics And Cosmic Ray Experiments" and the work presented in it are my own contributions under the guidance of my supervisor Prof. Supriya Das. I confirm that the work is original and has not been submitted earlier as a whole or in part for a degree/diploma at this or any other Institution/University.

Signed:

Date :

ACKNOWLEDGMENTS

I am very much thankful to my supervisor Prof. Supriya Das, for the patient guidance, encouragement and advice he has provided throughout my time as his student. I have been extremely lucky to have a supervisor who cared so much about my work, and who responded to my questions and queries so promptly.

I acknowledge the constant and invaluable academic and personal support received from Dr. Saikat Biswas. I am really thankful and indebted to him for having been the advisor everyone would like to have, for helping me to learn things in a simpler way and without whose dedicated supervision it would have been never possible to complete this work. I have really enjoyed by working with him. His continuous support, encouragement, and guidance have helped me reach many professional milestones.

I would like to thank Dr. Debapriyo Syam, for his interesting discussion and valuable suggestions during the whole Ph.D. course. He has been the substantial sources of inspirations and profound insight during these years.

I have no words to thank Prof. Somsubhro Bandopadhay, Prof. Rajarsi Ray and Dr. Sidharth K. Prasad of Bose Institute for their clear and enthusiastic discussion and valuable suggestions. They have constantly motivated me throughout my study. Without their support it was very difficult to pursue this work.

I would like to express my gratitude to Prof. Sanjay K. Ghosh and Prof. Sibaji Raha, who supported me and offered deep insight into the study.

I would like to thank Prof. Prabir Roy and Prof. Manasi Roy for inspiring me and for their invaluable suggestions regarding my career.

I would also like to show my deep appreciation to my seniors Dr. Ramaprasad Adak for helping me in all possible ways to analyze the results of my experiments.

Thanks to Dr. Rathijit Biswas for being the most supportive senior colleague of me and for giving me good advices not only on my research but also prespectives of living in general. Even in those very dreaded days, he made my work life easier.

I am very much thankful to Mr. Dipanjan Nag for helping me to understand the basic electronics and basic C++.

I am very much indebted to some scientists at Bose Institute especially, Prof. Swapan K. Saha, Dr. Sandhya Dey and Dr. Atanu Maulik for their encouragement, support, collaboration and for constantly motivating me in my project work.

I am very thankful to Dr. Susnata Seth, for guiding me to use the GEANT4 and CORSIKA7.69 software and for some valuable discussions on simulation works.

I have no words to thank my friend Pratik Ghosal, for being the best person in supporting role, for constantly listening to me, and for his all time friendly behaviour. I

want to thank him for giving me nice suggestions, for debating on interesting topics, and for discussing physics problems with me. He has given me a lot of moral support throughout these years.
Thanks to Arkaprabha Ghosal, for being the ideal senior that one would wish to have. I would like to thank him for his general advices on anything and everything. He has always been very kind and helpful to me.
I wish to acknowledge the help provided by the Bose Institute workshop for all the mechanical work to build the light guide, coupler. I am also thankful to GSI detector laboratory, Germany for providing the optical glue, grease etc. used to build the detector.
I would like to thank Dr. Subikash Choudhuri, Mr. Aritra Mondal and Mr. Debdeep Ghosal, Ms. Sumana Bhattacharyya, Ms. Pracheta Singha, Dr. Atreya, and Dr. Deeptak Biswas for their valuable comments and suggestions during the high energy physics group weekly meetings.
I am also very thankful to my juniors Nilanjana, Shibnath, Sayak, Sayan, Souradeep, Shubham, Abhishek, Debonita, Krishna, Ayushi, Arindam, Rituparna and Rudrapriya who worked with me in the detector laboratory and raised many questions during the experiment that helped me to learn the subject more clearly.
Special thanks to my friends Omveer Singh, Abhishek Seal, Dr. Ajit Kumar, and Apar Agarwal for helping me with C++ and CBMROOT programming techniques.
I am very grateful to Prof. Roger Barlow, University of Huddersfield for giving me a clear understanding of the statiscal methods in experimental physics.
I am pleased by the polite attitude of Dr. David Emschermann, Dr. Volker Friese and Dr. Christian Sturm of GSI, and for their invaluable suggestions that was very useful in my Ph.D. completion. To be honest, I've never met anyone who is more kind-hearted, caring, and supportive than David.
I am most grateful to the colleagues of the Indian Institute of Geomagnetism, Navi Mumbai, especially its Director, Dr. D. S. Ramesh, and Dr. S. Tulasi Ram and his team, for providing us the ionospheric data from their stations in Eastern India.
I would like to thank Late Prof. Vladimir Peshekhonov of JINR, Dubna for providing the straw tube prototype and Dr. Subhasis Chattopadhyay, Mr. J. Saini of VECC, Kolkata, Dr. Christian J. Schmidt and Mr. Jörg Hehner of GSI Detector Laboratory for valuable discussions in the course of the study.
I would like to acknowledge the support of DST-SERB Ramanujan Fellowship (D.O. No. SR/S2/RJN-02/2012) of Dr. S. Biswas. This work is also partially supported by the research grant of CBM-MUCH project from BI-IFCC, Department of Science and Technology, Govt. of India and the research grant SR/MF/PS-01/2014-BI from Department of Science and Technology, Govt. of India.

In my Ph.D. life, I have received the opportunity to visit many schools and conferences that created a great impact on my research career. I would like to thank all the organizers of the PISA conference (Italy 2018), AEPSHEP school (Vietnam 2018), HUGS school (Virginia 2019), FAIR school (Italy 2019), and GetInvolved internship at FAIR (Germany 2021-22) for selecting me and giving me full funding to attend the programmes abroad, and for letting me experience the research life in these countries. Last but not the least I would like to thank my mother, Mrs. Sachi Roy, my uncle Late Mr. Probhat Singh, my sister Mrs. Sharmistha Roy Nag, My brother in law Dr. Sabyasachi Nag, my longterm friend Dr. Avirup Ghosh, my cousin Jaya Bhattacharyya and her two lovely kids Jeet and Joy, and also all my relatives for believing in me, for their patience and for their constant support.

Shreya Roy
Kolkata, India

Thesis is partially based on the following publications

Journals

1. **S. Roy** , S. Jaiswal, S. Chatterjee, A. Sen, S. Das, S. K. Ghosh, S. Raha, V. M. Lysan, G. D. Kekelidze, V. V. Myalkovsky, and S. Biswas, "Stability study and time resolution measurement of Straw Tube detectors", *Pramana - J Phys 95, 50* (2021)

2. **S. Roy**, S. Biswas, S. Das, S. K. Ghosh, S. Raha, "A study of the secondary cosmic γ-ray flux in India during the Great American solar eclipse on 21st August 2017", *Astrophys Space Sci 365, 172* (2020)

3. **S. Roy**, S. Chakraborty, S. Chatterjee, S. Biswas, S. Das, S. K. Ghosh, A. Maulik, S. Raha, "Plastic scintillator detector array for detection of cosmic ray air shower", *Nucl. Instrm. Meth. A, Vol 936* (2019)

4. **S. Roy**, N. Nandi, R. P. Adak, S. Biswas, S. Das, S. K. Ghosh, S. K. Prasad, S. Raha, "Study of performances of a straw tube detector with high rate", *Nucl. Instrm. Meth. A, Vol 936* (2019)

National Conference Proceedings

1. **S. Roy**, S. Chakraborty, S. Chatterjee, S. Biswas, S. Das, S. K. Ghosh, A. Maulik, S. Raha, "Development of an Extended Air Shower array at Darjeeling : an update", *Springer Proceedings in Phys. Volume 261 (2021) 813-817*

2. **S. Roy**, S. K. Prasad, S. Biswas, S. Das, S. K. Ghosh, S. Raha, "A feasibility study to track cosmic ray muons with solid state detectors using GEANT4", *Springer Proceedings in Phys. Volume 261* (2021) 1187-1190

3. **S. Roy**, S. Jaiswal, S. Chatterjee, A. Sen, S. Biswas, S. Das, S. K. Ghosh, S. Raha, V. M. Lysan, G. D. Kekelidze, and V. V. Myalkovsky, "R&D of Straw Tube detector for High Energy Physics experiments", *Proceedings of the DAE Symp. on Nucl. Phys. Volume 64* (2019)

4. **S. Roy**, N. Nandi, R. P. Adak, S. Biswas, S. Das, S. K. Ghosh, S. K. Prasad, and S. Raha, "Variation of gain and energy resolution with temperature and pressure of straw tube detector", *Proceedings of the DAE Symp. on Nucl. Phys. Volume 63* (2018)

5. **S. Roy**, R. P. Adak, R. Biswas, S. Biswas, S. Das, S. Das, D. Nag, D. Paul, S. Rudra, "Measurement of angular variation of cosmic ray flux with plastic scintillator", *Springer Proc. Phys. 201 (2018) 199-204 doi.org*/10.1007/978 − 981 − 10 − 7665 − 720

6. S. Shaw, N. Nandi, S. Chatterjee, P. Chawla, **S. Roy**, R. P. Adak, S. Biswas, S.

Das, S. K. Ghosh, S. Raha, "Study of cosmic ray with plastic scintillator detector", *Proceedings of the DAE Symp. on Nucl. Phys. Volume 62* (2017) 1030-1031
7. N. Nandi, **S. Roy**, R. P. Adak, S. Biswas, S. Das, S. K. Ghosh, S. K. Prasad, S. Raha, "Characterization of Straw tube detector", *Proceedings of the DAE Symp. on Nucl. Phys. Volume 62* (2017)
8. R. P. Adak, S. Biswas, S. Chattopadhyay, S. Das, D. Ghosal, P. Ghosal, A. Mondal, D. Nag, **S. Roy**, and J. Saini, "R&D on Straw Tube detector for CBM Muon Chamber", *Proceedings of the DAE-BRNS Symposium on Nuclear Physics. Volume 61* (2016), 996-997.

Internal notes

1. **S. Roy**, S. Chatterjee, S. Chakraborty, A. Sen, S. Biswas, S. Das, S. K. Ghosh, S. K. Prasad, S. Raha, V. D. Peshekhonov, V. M. Lysan, G. D. Kekelidze, and V. V. Myalkovsky, "Aging studies of Straw tube detector", *CBM Progress Report 2018*, ISBN 978-3-9815227-6-1, DOI:10.15120/GSI-2019-01018
2. **S. Roy**, N. Nandi, R. P. Adak, S. Biswas, S. Das, S.K. Ghosh, S.K. Prasad, and S. Raha, "Study of the rate handling capacity of a straw tube detector", *CBM Progress Report 2017*, ISBN 978-3-9815227-5-4, DOI: 10.15120/GSI-2018-00485

Other publications

1. **Shreya Roy**, Sayak Chatterjee, Sayan Chakraborty, Saikat Biswas, Supriya Das, Sanjay K. Ghosh, Sunil K. Gupta, Atul Jain, Indranil Mazumdar, Pranaba K. Nayak, and Sibaji Raha, "Interplay between eclipses and soft cosmic rays", PoS(ICRC2021)131
2. R. Bhattacharyya, A. Maulik, R.P. Adak, **S. Roy**, T.S. Bhattacharya, S. Biswas, S. Das, S. Dey, S.K. Ghosh, K. Palodhi, S. Raha, A. Singha and D. Syam, "Attenuation of electromagnetic radiation in Nuclear Track Detectors", *2021 JINST 16* T06001
3. A. Sen, S. Chatterjee, **S. Roy**, R. Biswas, S. Das, S. K. Ghosh, S. Biswas, "Cosmic ray flux and lockdown due to COVID19 in Kolkata – any correlation?", *Pramana - J Phys, Vol 95* arXiv:2010.06648 (2021)
4. S. Chatterjee, A. Sen, S. Roy, K. Nivedita G, A. Paul, S. Das and S. Biswas, "Study of charging up effect in a triple GEM detector", *2020 JINST 15* T09011
5. S. Chatterjee, S. Roy, A. Sen, S. Chakraborty, S. Biswas, S. Das, S.K. Ghosh, S.K. Prasad, S. Raha, "Long term stability study of triple GEM detector using different Argon based gas mixtures: an update", *Journal of Physics: Conference Series 1498* (2020) 012037
6. A. Sen, S. Chatterjee, **S. Roy**, S. Biswas and S. Das, "Characterisation of an RPC prototype with moderate resistivity plates using tetrafluoroethane (C2H2F4)", *2020*

JINST 15 C06055

7. **S. Roy**, S. Rudra, S. Shaw, S. Chatterjee, S. Chakraborty, R. P. Adak, S. Biswas, S. Das, S. K. Ghosh, S. K. Prasad, S. Raha. "Stability study of gain and energy resolution for GEM detector", *Nucl. Instrm. Meth. A, Vol 936* (2019)

8. S. Chakraborty, S. Chatterjee, **S. Roy**, A. Roy, S. Biswas, S. Das, S. K. Ghosh, S. K. Prasad, S. Raha, "A new type of RPC with very low resistive plates",*Nucl. Instrm. Meth. A, Vol 936 (2019)*

9. S. Chatterjee, S. Chakraborty, **S. Roy**, S. Biswas, S. Das, S. K. Ghosh, S. K. Prasad, S. Raha, "Study of uniformity of characteristics over the surface for triple GEM detector",*Nucl. Instrm. Meth. A, Vol 936* (2019)

10. Krishana Nivedita G, Ayushi Paul, Sayak Chatterjee, **Shreya Roy**, Arindam Sen, Saikat Biswas, Supriya Das, "Study of charging up effect in GEM detector", *Proceedings of the DAE- BRNS Symposium on Nuclear Physics. Volume 64* (2019), 976-977

11. **S. Roy**, V. Singhal and F. Uhlig, "Event rate calculation after event building with mCBM data", *CBM Progress Report* 2020, ISBN 978-3-9815227-9-2, DOI:10.15120/GSI-2021-00421

12. **S. Roy** and V. Singhal, "Automatized noise separation technique for mMUCH data", *CBM Progress Report* 2019, ISBN 978-3-9815227-8-5, DOI: 10.15120/GSI-2020-00904

13. D. Nag, S. Biswas, S. Das, S. K. Ghosh, D. Paul, S. K Prasad, S. Raha, **S. Roy**, "Some aspects of characterization of GEM detector", *Accepted for Proceedings of ADNHEAP, Springer Book Series doi.org*/10.1007/978 − 981 − 10 − 7665 − 721

Contents

List of Figures

List of Tables

Chapter 1

Introduction

Every nuclear or cosmic ray experiment needs a well-designed detector system which in turn serves as the black box storing all the physics information of interest. The depth of physics that can be studied in such experiments, totally relies on how precisely the detector system can measure the particles and their energy. Thus, detector development and designing stands as a very important branch in this field of study. With the advancement in the field of experimental particle physics, the demand for sophisticated detection methods raised, thereby making the detection system more and more complex in structure. Usually such designs are performed first in simulation before they are practically implemented. An important step is to perform laboratory tests with the detector to check whether it fulfills the experiment requirements or not. The experimental requirements varies from one experiment to the other. Therefore one has to carefully choose the type of detector. Although wire chamber detectors were very commonly used in high energy physics experiments with great success, but it has some drawbacks like rate limitations. Feasibility tests such as testing the rate handling capability and aging of wire chambers like the Straw tube detector that are proposed to be used in high collision rate experiments is a very important study and is one of the aim of this research. With high collision rates, comes the demand for fast data processing electronics. However, this is not a problem for the case of cosmic ray experiments, where event rate is relatively lower than that in collider experiments. In cosmic ray experiments it is rather crucial to maintain a stable operation of the detector and collect data for long time over large surfaces to catch rare events that can shed light to the origin and composition of cosmic rays. Such a cosmic ray air shower detector array can be found in southern part of India, being the only shower array of the country. It is an excellent idea to build another air shower array in India at similar altitude but at different geographical location, such that cosmic ray air showers could be compared. The research aim is to develop such a cosmic ray air shower array using scintillators. Another aim is to study cosmic ray gamma and muons during astrophys-

ical phenomena like solar eclipse. The connection between solar eclipse and cosmic rays is a very old unsolved research problem because the astrophysical events are rare and it is also difficult to monitor all the parameters that influence the cosmic rays.

This chapter provides an introduction to the background and the context of the problems that the thesis try to address, followed by the questions it aims to answer and their significance. In this chapter, application of detectors in High Energy Physics Experiments (HEPex) and Cosmic-ray experiments (Section 1.1) are discussed. Section 1.1.1 discusses the classification of detectors in terms of interaction with matter. Section 1.2 and Section 1.3 will focus particularly on introducing the gaseous and scintillator detectors for high energy physics and cosmic ray experiments respectively along with a general introduction of the experiment themselves. These sections also give an overview of the background, the current focus and open challenges in the research on the particle detectors. Section 1.4 explains the objective of the thesis and how this thesis is organised.

1.1 Detectors in particle and astroparticle physics

Detectors in the world of particle physics are as indispensable as 'eyes' are to a living being. Beginning with the remarkable discoveries such as X-rays in 1895 with Crookes tube or cosmic rays in 1912 using electroscopes and electrometers, and with the advancement of technologies that led to the discovery of quarks in 1968 or Higgs boson in 2012, the history of radiation detectors parallels the growth in our knowledge of nuclear, particle and astroparticle physics.

The historical development of particle detectors begins in the year 1896, when the French engineer, named Henri Becquerel discovered radioactivity. He used photographic plates to observe the radiations from a radioactive uranium salt. At the same time, a German physicist, Wilhelm Conrad Roentgen made the discovery of X-rays, which were produced bombarding materials with high-energy electrons. The Zinc Sulphide (ZnS) screens were the primitive devices that were used in many experiments at that time. Rutherford's gold foil experiment using ZnS screen in 1911, where the structure of the atom was correctly picturized, was the greatest discovery at that time. Electroscopes and spinthariscopes were commonly used to many demonstration experiments. The historical evolution of particle and astroparticle detectors is well described in the Refs. [1].

As years passed by, the detection methods were greatly revised. It was soon realized that working with the primitive scintillators was a tediuos and tiresome activity. Moreover, this method can only be used to detect the presence of radiation. To identify their nature, i.e., to know whether the particle is an electron, a proton, or a γ-ray, or

simply its charge and mass, this primitive method fails. Apart from that an accurate energy and momentum measurement is often required. For this purpose the knowledge of the spatial coordinates of particle trajectories is required, so that the particle tracks can be reconstructed. In the old days the reconstruction was done with the help of visual detection (e.g. in spark, streamer, cloud and bubble chambers). In the modern days, it is generally electronic detection (in multiwire proportional or drift chambers, micropattern detectors). By the year 1932, cloud chambers were discovered, which made a breakthrough discovery in the field of particle physics : the discovery of antimatter. American physicist, Carl Anderson, performed a simple experiment with a cloud chamber in magnetic field and recorded tracks of particles passing through the cloud chamber in a camera. He discovered the positron with this method for which he received the Noble prize in 1936. Cloud chambers and bubble chambers were continued to be used for discovering new particles like the Pion, Omega and Muon.

In the course of time, the method of particle detection improved from optical detection to exclusively electronic detection. This developmental era yielded ever higher resolutions, be it in energy (eV), in time (picoseconds), or in spatial reconstruction (micrometres). The early optical detectors, like cloud chambers and bubble chambers, could only measure particle tracks every once in a minute, while modern detectors, like scintillators, can take measurement in the GHz rates. With GHz rates there are new problems, like demand for fast electronics to process the data.

The history of cosmic ray detection started with the measurement of radiation with electroscopes. In 1910, Wulf observed that the intensity reduces in an electrometer when it is carried to the top of the Eiffel tower. This confirmed the terrestrial origin of the ionizing radiation. Later, in the year 1912, with a similar idea, Hess performed balloon measurements reaching altitudes of close to 5 km. He found that apart from the terrestrial component, there exists an additional source of ionizing radiation, which becomes stronger with increasing altitude. Thus confirming the presence of radiation from space. This marked the discovery of cosmic rays for which the Noble prize in 1936 was awarded to Hess. In 1912, Wilson developed the cloud chamber, which allowed not only the detection but also to visualise the track left by ionizing particles passing through the cloud chamber. The high energy properties of cosmic rays were in the focus of research during the following years, because accelerators capable of producing high energy particles did not yet exist at that time, thus cosmic rays were the only source. In parallel, around 1940, the theory of electromagnetic interactions emerged, followed by the development of the theory of electromagnetic showers. Shower particles were observed in cloud chambers. The particles ionised the medium in cloud chamber and tracks were visible. The thickness of the track depends on the amount of ionization. Another way to precisely measure the amount of ionization is to use nuclear emulsion

stacks. The method was to create layers of photographic emulsions and expose it to cosmic rays. The emulsion could be later developed to view the tracks. In addition to viewing tracks, it became important to count the particles. Geiger-Muller counter was the first in history to be able to count charged particles. The counter gave an electronic pulse when cosmic rays pass through it. Thus development in the detector technology made it possible to discover the nature of cosmic rays. Experimental techniques were modernised. The Geiger counter was only able to count the number of particles but not to measure its energy. These counters were shielded with different amounts of matter around it, to absorb the energy of the particle. The thickness of the shielding determines the threshold energy of the particle to penetrate the shielding and enter the detector.

With the advancement in science of particle accelerators in the 1950s, it was possible to study interactions of particles of known energy and type. This made breakthrough discoveries in particle physics. The charactersitics of hadron interaction became known and this was applied to the cosmic ray shower models. Here it can be seen how the high energy physics experiments helped to advance in the field of cosmic ray physics and astroparticle phyiscs. In 1967 the rise of astroparticle physics began, with the observation of neutrinos originating from the Sun in the Homestake Mine (Davis experiment). The term astroparticle physics refers to the observation of astronomical objects in the 'light' of elementary particles [1]. Thus the field of particle and astroparticle physics were growing continuously and so were the detection techniques.

Accelerators grew in size to achieve higher energy (TeV) and the detectors became large and complex in structure to track as many particles as produced from the collisions. The electronics to readout the data from the detector had to be fast in order to store Terabytes of data each second. With advanced and sophisticated detectors and associated electronics, it was possible to study the interaction of matter at high energies. Every collider experiment has its own physics goals and a specific detector design to achieve that goal. A complex detector system is a collection of many detectors placed in a fashion to accept the particles produced from the collision. The main task of a detector system is to identify the type of particle and measure its momentum. In these collisions, many different particles are produced, which are then categorised as hadrons (such as protons, pions etc.) and leptons (such as electrons, muons etc.). Since these particles are different in nature, they interact differently with matter and hence the detectors need to be designed accordingly for them. This explains why there is the need of a complex detector system, because it is not possible for one detector to detect all types of particles. Section 1.1.1 discusses the three different categories of detectors on the basis of the active medium.

1.1.1 Classification of Detectors

All detectors are based on the fundamental principle of interaction of radiation with matter. Based on the active medium, the detectors are classified in three main categories: (a) gaseous ionization detectors, (b) scintillation detectors and (c) solid state detectors. The detectors depending on the detection of the free charge carriers are classified under the general category of ionization based detectors or gaseous detectors. The detectors that can sense the luminescence photons are called scintillation detectors. The detectors based on the concept of creation of holes and electrons in the active medium, are classified as solid state detectors. Table 1.1 lists the different types of detectors and their uses. In this thesis, only the gaseous detectors and the scintillation detectors and their applications will be discussed in detail.

Table 1.1: Nuclear Radiation Detectors

Name	**Type**	**Year of invention**	**Used in experiment(s)**
Geiger counter	Gaseous	1908	α,β-spectroscopy,
Proportional counter	Gaseous	1928	α,β-spectroscopy, X-ray spectroscopy [2]
Multi-wire proportional chamber	Gaseous	1968	ALICE-TPC [3, 4]
Straw tubes	Gaseous	1984	ATLAS-TRT [5], PANDA [6]
Gas Electron Multiplier (GEM)	Gaseous	1997	COMPASS [7]
Resistive Plate Chambers (RPC)	Gaseous	1981	CMS [8]
Plastic scintillator	Scintillation	1947	DAMPE [9]
In-organic scintillator	Scintillation	1947	Gamma spectroscopy

(a) Gaseous Detectors

Gaseous detectors work because radiation can produce electron-ion pairs in the gas. The ionization chamber, proportional counters, and Geiger counters are the oldest and contemporary gaseous detectors. A gas detector in its basic configuration typically consists of a container, for example a cylinder, fitted with conducting walls (inner side coated with a conductor) and a thin end window, as shown in Figure 1.1. A suitable gas is filled into the cylinder and a thin conducting wire is positioned along its central axis. If a positive voltage is applied to this wire relative to the conductive walls, the central wire works as anode and the cylinder works as a cathode.

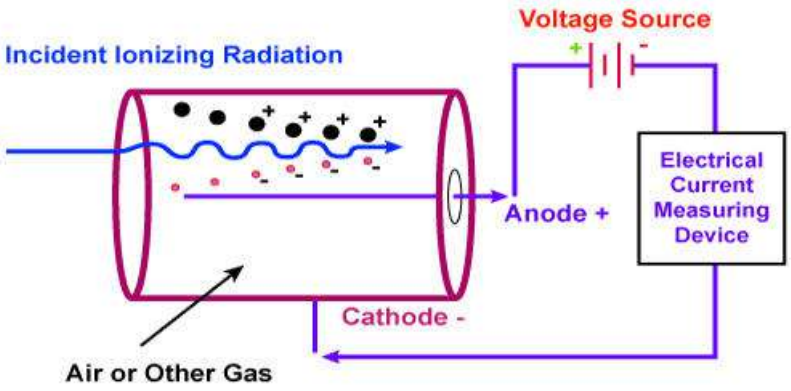

Figure 1.1: Schematic representation of a gaseous detector.

Working principle

To understand the working of a gas detector, assume (as an example) that the detector absorbs the radiation of 1 MeV. The production of an electron-ion pair, that is an electron and a positive ion, takes on average about 30 eV from the incident radiation. The number of primary electron-ion pairs which can be generated by this radiation is given by the the following relation

$$n = 10^6\ eV/30\ eV = 3.3\ \times\ 10^4 \tag{1.1}$$

The average number of generated electron-ion pairs is proportional to the total energy deposited in the detector. The radial electric field inside the cylinder is given by

$$E(r) = \frac{V_0}{r}\frac{1}{ln(\frac{b}{a})} \tag{1.2}$$

where V_0 is the voltage difference between the wire and the cylinder, r is the radial distance from the central wire, b is the inner wall radius and a is the radius of the anode wire. From this equation, one can clearly see that the electric field increases with decreasing distance from the wire as 1/r. If there is no electric field or a very low electric field, the ions recombine with the electrons due to Coulomb attraction. As soon as voltage is applied, positive ions and electrons will move towards respective electrodes and get collected. The electrons are collected by the central wire electrode (which is positive charged) and the positive ions are collected by the outer cylindrical electrode. If the wire voltage is increased, the electron and ion collection efficiency is increased. Those ions and electrons directly created by the incident radiation, the primary ions all are collected above a certain voltage, leading to a measurable pulse. A plot of the pulse height versus the applied voltage is shown in Figure 1.2.

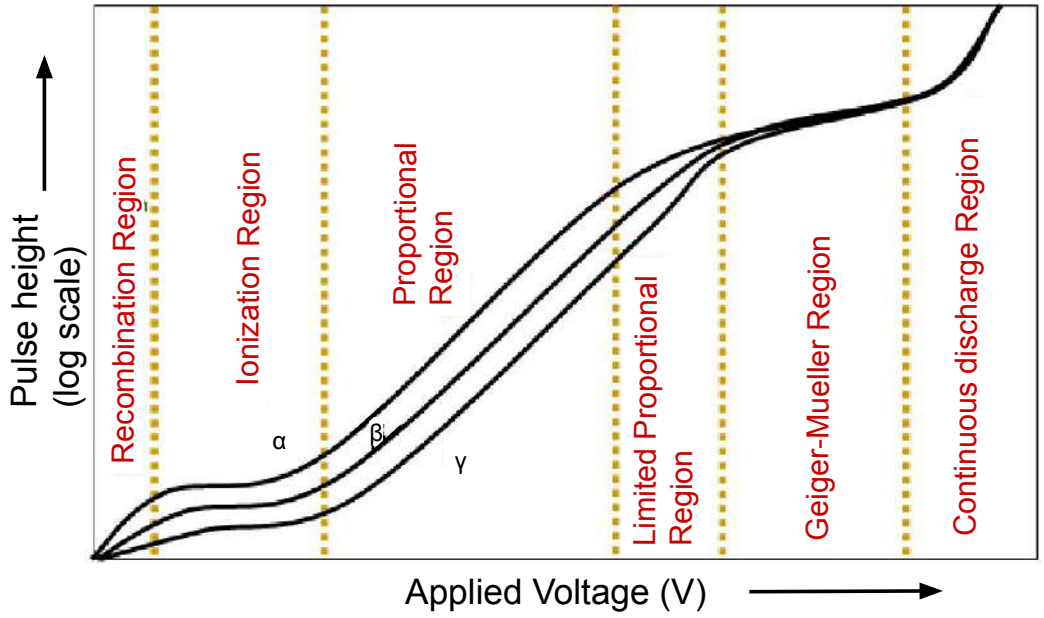

Figure 1.2: Operation regions of a gaseous detector. X-axis is the anode voltage. Y-axis is pulse height, means the detector signal amplitude which is also related to signal current.

In the first region of this figure, the voltage is insufficient to collect all the ions. As the ions may simply recombine, it is therefore called the recombination region. In the second region, all the electron-ion pairs are swept to the respective electrodes by the sufficiently large the electric field, it is called the ionization region. Detectors operating in this region are designated as ionization counters. If the anode voltage is further increased, the resulting current rises again. In this region, free electrons are accelerated by the strong electric field to a kinetic energy where they are then capable of ionizing other gas molecules within the cylinder. These primary electrons will knock-off electrons in the gas atoms, known as secondary electrons. These electrons in turn can also be accelerated to produce even more ionization and so on. Thus an avalanche multiplication of electrons takes place. The applied potential at which multiplication sets in marks the end of the ionization region. At higher potential of a new region called the proportional region sets in. A few examples of detectors operated in proportional region are, Single Wire Proportional Chamber (SWPC), Multi-Wire Proportional Chamber (MWPC), Gas Electron Multiplier (GEM), Straw-Tube detector. For the application in all the recent high energy physics experiments, the detector biasing voltage is scanned to search for this proportional region which is the most desired operating condition of a gaseous detector.

In the region known as Proportional Region, the number of electron-ion pairs in the avalanche relates directly to the number of primary electrons. The interaction

mechanism varies from particle to particle depending on their nature. When α, β and γ particles ionize the gas, they produce different number of primaries and hence they have distinct curves in the proportional region. When the voltage is further increased, the total amount of ionization created through multiplication becomes sufficiently large to distort the electric field around the anode by the created space charge. That region is named the Limited Proportionality Region. Increasing the voltage still higher, the field energy becomes large enough that a discharge occurs in the gas. Photons emitted by de-excited molecules trigger a chain reaction of many avalanches spread out along the entire length of the anode. Under these conditions a full saturation of the output current sets in. This region is known as Geiger Muller Region. In this region, all types of particle will produce the same pulse height and no further differentiation between α, β and γ particles is possible. A Geiger-Muller counter is an example of a very primitive gaseous detector, which works in this operating region. Further increase in high voltage beyond this region the discharge occurs continuously in the gas. This region is known as Continuous Discharge Region [10–12].

(b) Scintillation Detectors

Scintillation detectors are based on the principle of detection of ionizing radiation by means of scintillation light produced in certain materials. Such a kind of detection technique is one of the oldest and most useful on record. The basic properties of an ideal scintillation material is as follows :

- Linear conversion of a part of the kinetic energy of the incident particle into visible photons
- The light yield is proportional to the energy deposited, at least over a wide range
- The scintillator medium must be transparent to its own wavelength of emission
- Must generate fast signal pulses, therefore the decay time of the induced fluorescence must be small
- The refractive index of the material should be same as that of glass so that it can be coupled to photomultiplier tube for electronic signal generation
- Should be able to produce scintillators of any shape and size as per the requirements of the experiment

In 1903 by Sir William Crookes built the first device which used a scintillator and used a ZnS screen. In 1944 scintillators gained additional attention, when Curran and Baker used the newly developed PMT to replace the naked eye measurement. That

marked the birth of modern scintillation detectors and from that point of time the scintillators were able to handle much higher particle rates (>kHz). A scintillation counting system consists of a scintillant or scintillator material, a photo-multiplier tube (PMT), an amplifier-analyzer-scalar system and a power supply.

Working principle

The working principle of a scintillator is simple. Photons are produced, when an ionizing radiation passes through the scintillant by the process of excitation and de-excitation either from special kind of molecular energy levels (observed in organic material) or from activator sites (observed in inorganic crystal). The number of photons produced in the scintillator is proportional to the deposited energy. All sides of the scintillator are covered with a reflector, except for the side connected to the PMT such that the photons produced in the scintillating medium due to the interaction of the radiation have no other way to escape and has to enter the PMT. As its first element the PMT has a photoelectric film (usually coated onto the inner wall of the glass window of the photomultiplier tube). When light falls onto this film, the photo-electric effect releases electrons. The number of photons falling on the photocathode is proportional to the number of electrons produced. The PMT has several dynodes arranged in a fashion to focus electrons and multiplies them at each dynode. Gradually increasing potential to the dynodes is provided by a voltage divider chain which allows to direct the electrons. After 9-10 stages of multiplication, a large number of electrons are collected at the anode that produces a measurable signal [11]. Functioning of the PMT is well explained in Section 3.3.1

Scintillators can be classified into organic and in-organic depending on their type of scintillant material. The working principle of organic scintillators is discussed in Chapter 3, Section 3.3.1 and the working principle of in-organic scintillators is discussed in Chapter 4, Section 4.2.1. In-organic scintillators have very good light output and linearity, but have slow response time. On the other hand organic scintillators are faster but yield less light. The choice of scintillator depends on the intended application. In-organic scintillators are usually alkali halides which have high Z and high density and preferred in gamma spectroscopy, whereas organics are preferred for charged particle spectroscopy. Scintillators are generally used for triggering purposes, since they have fast timing, and for cosmic ray detection, since they can be made in large sizes to suit the experimental requirements very well.

(c) Semiconductor Detectors

Semiconductor detectors are radiation detectors made up of semiconductor material, such as silicon or germanium, to detect the incident particles. The operation of a semiconductor detector is very similar to that of ionization chambers. When a charged particle passes through the semiconductor medium, it creates electron and hole pairs along its trajectory. The energy deposited in the semiconductor material by the incident particle is proportional to the number of created electron hole pairs. The number of holes that are created in the valence band is equal to the number of electrons transferred into the conduction band. If appropriate voltage is supplied across the semiconductor device, the holes and electrons will drift to the respective electrodes, and can produce a measurable signal with the help of a proper electronic circuit [11]. The advantages of semiconductor detector over gaseous detectors is that, the energy required to produce electron-hole pairs is very low (only 3.5 eV) compared to the energy required to produce electron-ion pairs ($\sim$30 eV) in the gaseous detector. Due to this reason, in semiconductor detectors, the number of electron-hole pairs per MeV deposition of radiation increases and the statistical variation of the pulse height decreases, making the energy resolution better than gaseous detectors. Another advantage is that, the electrons travel fast in conduction band than free electrons in gaseous medium, so therefore the time resolution of semiconductor detector is also very good. Also, since the density of semiconductor materail is higher compared to gaseous detectors, the incident particle can loose more energy in smaller distances inside semiconductor than in gaseous detector.

There two types of semiconductor detector on the basis of the material : silicon and germanium semiconductors. Silicon-based semiconductor detectors are generally used for charged particle detection and tracking. It is also used for detection of soft X-rays. Germanium-based semiconductors are widely used for gamma ray spectroscopy.

1.2 Gaseous detectors for high energy physics experiments

In this section, the use of gaseous detectors in high energy physics experiments, particularly the Compressed Baryonic Matter (CBM) experiment, in Darmstadt, Germany is discussed. The section starts with the introduction to the CBM experiment (Section 1.2.1) and its physics goals. This section also includes the current status of other high energy physics experiments having similar physics goals as CBM and discusses their limitations. Section 1.2.2 introduces the Muon Chamber (MuCh) at

CBM which is a complex detector system having gaseous detectors for tracking. This section discusses the challenges to be faced by the detectors of CBM-MuCh, and the general knowledge of these gaseous detectors.

1.2.1 The Compressed Baryonic Matter (CBM) Experiment

Considerable experimental and theoretical efforts are made all over the world to explore the phase diagram of strongly interacting matter. This special branch of physics is called the Quantum Chromodynamics (QCD). QCD is the theory of the strong interactions. It states that quarks and gluons, which are elementary particles, cannot be directly observed at low energies, due to their confinement in bound states (hadrons). An interesting part of the QCD theory is that it is also an asymptotically free theory. It means that quark and gluons are deconfined at high energies, and the Quark-Gluon-Plasma (QGP) phase is formed [13] through a phase transition. The QCD phase diagram in Figure 1.3 represents the transition between the hadronic phase and the QGP phase. The only way to study them in the laboratory is to perform heavy-ion collision experiments at relativistic energies and create the extreme states of strongly interacting matter. At the Large Hadron Collider (LHC) [14] and at top energies of the Relativistic Heavy Ion Collider (RHIC) [15], QCD matter can be investigated at nearly vanishing net-baryon densities and very high temperatures. There is evidence that QGP was created at RHIC and LHC experiments. It is expected that the transition from the QGP back to the hadron gas is a smooth cross over. At larger net-baryon densities and for lower temperatures, the QCD phase diagram has a first order phase transition between hadronic and partonic matter, which terminates in a critical point or exotic phases like quarkyonic matter. These studies are important because these discoveries would be a breakthrough in the understanding of the strong interaction in the nonperturbative regime, structure the core of neutron stars, restoration of chiral symmetry, and the origin of mass for hadrons. It is therefore the primary focus of many high-energy heavy-ion research programs both present and future.
At the future Facility for Anti-proton and Ion Research (FAIR) [16, 17] the CBM experiment [18, 19] is designed to explore the QCD phase diagram in the region of high net-baryon densities. CBM is a fixed target experiment and has a unique design which was made to make it run at unprecedented interaction rates. FAIR will be the only accelerator in the near future, that will be capable of delivering high rate collisions (10 MHz). The importance of high-rate operation is that it promises high-precision measurements and high statistics of rare diagnostic probes and of multi-differential observables which are sensitive to the dense phase of the nuclear fireball, or the compressed matter. CBM will be able to find the relevant degrees of freedom at high-net

baryon densities, study the phase transition from hadronic to quark-gluon matter and phase co-existence.

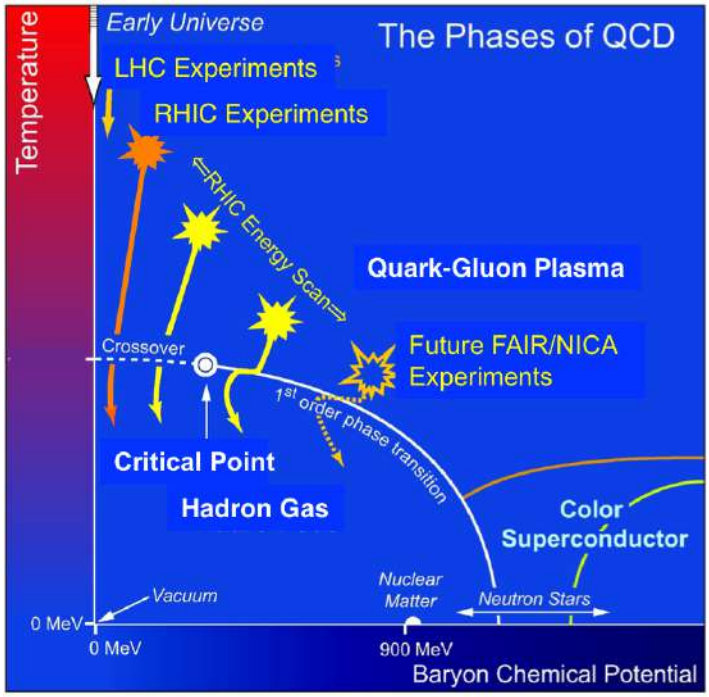

Figure 1.3: A schematic QCD phase diagram in the temperature (T) and baryonic chemical potential (μ_B) plane. The regions probed by different accelerator facilities are indicated. (The Figure is adopted from Ref. [20]).

Status and limitations of other experiments exploring the high-net baryon densities

The study of the QCD phase diagram at high-net baryon densities is the target of many high energy physics experiments [21], apart from CBM, FAIR. The challenge in the study of QGP and dense nuclear matter is that most of the experimental observables like are extremely statistics-demanding.

The STAR experiment [22] at RHIC energies ($\sqrt{s}$ = 130 AGeV, baryonic potential μ_B = 38 MeV to $\sqrt{s}$ = 7.7 GeV, μ_B = 413 MeV), the QCD phase was studied [23]. The experiments had a limitation that it cannot go to energies above $\sqrt{s}$ = 20 AGeV where the reaction rate exceeds 800 Hz because the TPC detector readout cannot handle such high rates. Neither the experiments can study QGP at energies below $\sqrt{s}$ = 7.7 (corresponding to $\mu_B >=$ 413 MeV) due to the decreasing beam luminosity provided by the RHIC accelerator.

The NA61/SHINE experiment [24] at the CERN-SPS is measuring hadrons using

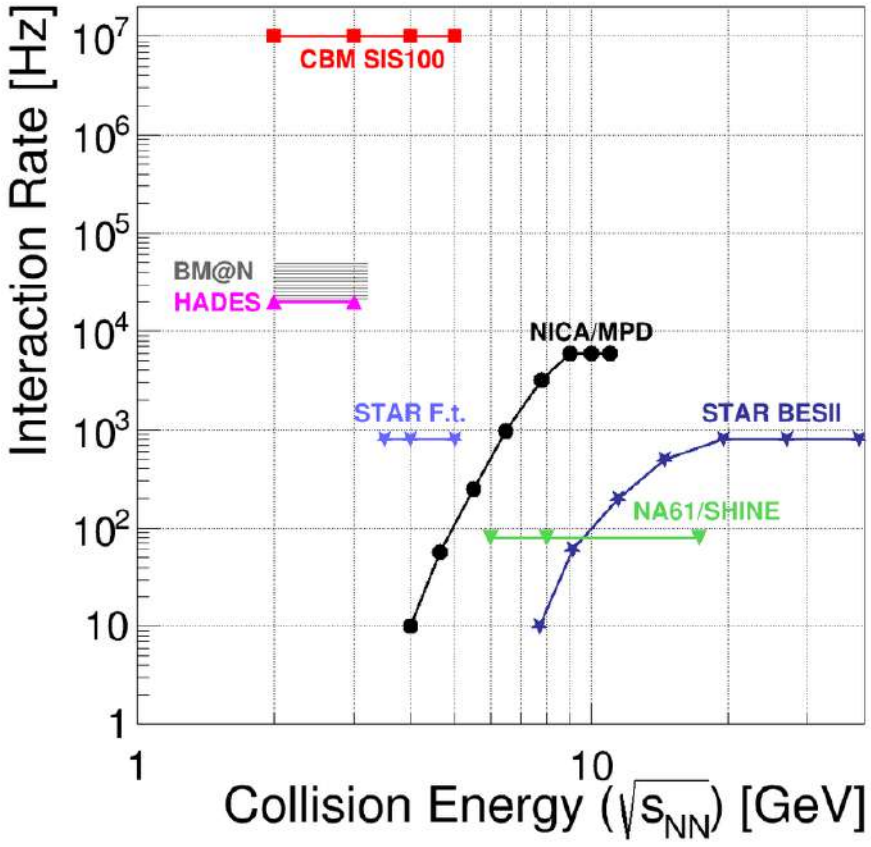

Figure 1.4: Interaction rates achieved by existing and planned heavy-ion experiments as a function of center-of-mass energy. (The Figure is adopted from Ref. [28])

Pb+Pb at energies over a range from $\sqrt{s}$ = 6.7 GeV (μ_B = 472 MeV) to $\sqrt{s}$ = 17.3 GeV(μ_B = 249 MeV) to search for the first-order phase transition. The main problem is that the detector setup is limited to reaction rates of about 80 Hz, which is very low.

The experiments at AGS, Brookhaven, have explored the QCD phase diagram with Au+Au 11.6 AGeV $\sqrt{s}$ = 4.86 AGeV at temperature T = 120 MeV and baryonic potential μ_B = 554 [25]. Due to the accelerator and detector technologies available at that time, these measurements with severely limited statistics were limited to abundantly produced hadrons and di-electrons.

The HADES detector at SIS18 is the only experiment that studies the properties of strongly interacting matter in the energy regime [26] of a few AGeV. It measures hadrons and electron pairs in heavy-ion collision systems at T = 80 MeV and μ_B = 748 MeV with reaction rates up to 20 kHz.

The BM@N fixed target experiment at JINR is designed to study heavy-ion collisions in Au beam at energies of less than 4 AGeV. Also at JINR, the Nuclotron-based Ion

Collider fAcility (NICA) with the Multi-Purpose Detector (MPD) [27] is in preparation. It will study QGP at collision energies between $\sqrt{s} = 8$ GeV to $\sqrt{s} = 11$ GeV at a reaction rate of 6 kHz. Below energy $\sqrt{s} = 5$ GeV, the reaction rate decreases to only 100 Hz because of the decrease in luminosity of the NICA collider. The interaction rates achieved by existing and planned heavy-ion experiments are shown in Figure 1.4 as a function of their center-of-mass energy of collision.
Therefore, the main required characteristic of any experiment which aims to study QGP at high-net baryonic densities is to have an accelerator with high luminosity even at low collision energies and an experiment with high rate capability of detectors and readout. FAIR, currently under construction in Darmstadt, will offer the opportunity to study QGP at low energies and high baryonic chemical potential at extreme interactions rates. The experimental challenge of CBM is to develop a fast detector with large-acceptance and to set up a high-speed read-out system capable to run under conditions with high-luminosity beams delivered by FAIR.

The physics goals of the CBM experiment are to discover fundamental properties of the QCD matter: the structure of the phase diagram of matter at large baryon-chemical potentials ($\mu_B > 500$ MeV) as depicted in Figure 1.3, understand the effects of chiral symmetry, and the equation-of-state at high density baryon matter similar to which is expected to occur in the core of neutron stars [28, 29].

The CBM detector setup

The fixed target experiment CBM will operate at extremely high interaction rates up to 10 MHz [29–31]. The CBM detector is designed to serve as a multipurpose device which will be capable to measure hadrons, electrons and muons in heavy-ion collisions over the full FAIR beam energy range. The CBM detector system has an acceptance for polar emission angles between 2.5 and 25 degrees such that it covers mid-rapidity and the forward rapidity hemisphere for collisions in the FAIR energy range. The duo of high-intensity beams from FAIR accelerator and high-rate handling detection system will provide the unique conditions needed for the study of QCD at the highest net-baryon densities achievable in the laboratory. The CBM experimental setup is shown in Figure 1.5. It consists of the following components:

- A superconducting dipole magnet
- A Micro Vertex Detector (MVD) inside the dipole magnet, having four layers of silicon monolithic active pixel sensors
- A Silicon Tracking System (STS) inside the dipole magnet, consisting of double sided silicon micro-strip sensors forming eight stations to track charged particles

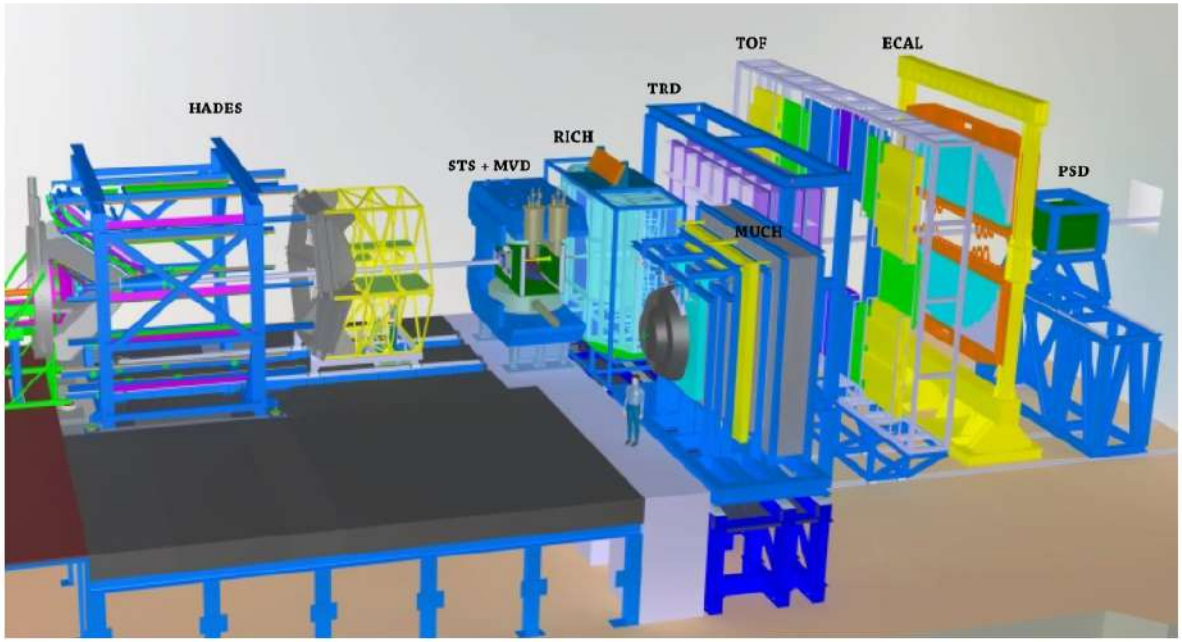

Figure 1.5: The setup of the CBM experiment to the cave with HADES experiment to the left. (The Figure is adopted from Ref. [28])

very close to the interaction point

- A Ring Imaging Cherenkov (RICH) detector for electron identification
- A Muon Chamber (MuCh) system made up of layers of gaseous micropattern chambers sandwiched between hadron absorbers for muon identification
- A Transition Radiation Detector (TRD) for particle tracking and electron identification using specific energy loss
- A Time-of-Flight wall (TOF) based on Multi-Gap Resistive Plate Chambers (MRPC) for particle momentum identification on the basis of their time of flight
- A Projectile Spectator Detector (PSD) for event plane characterization
- A First-Level-Event-Selector (FLES) computer cluster and software system for online event reconstruction and selection

CBM will look at promising obervables of the QCD matter such as collectivity, event-by-event fluctuations, strangeness, charm, and lepton pairs. Di-leptons emitted in heavy ion collisions give way to investigate the microscopic properties of strongly interacting matter. The slope of the di-lepton invariant mass spectra at the energy range 1 to 2.5 GeV is sensitive to both the temperature of the created matter and its

lifetime. Therefore, the di-lepton physics studies are a very important part of the CBM research program. This is the main motive behind construction of the MuCh detector. For the first time the vector mesons which decay into di-leptons in the FAIR energy range will be studied. In the next section, the structure of the MuCh is described.

1.2.2 Detectors for the Muon Chamber of CBM

MuCh : Goals and design

The goal of Muon Chamber (MuCh) is to measure the lepton pairs decaying from vector mesons, that are emitted in heavy-ion collisions. As they are not affected by final-state interactions, they are a sensitive diagnostic probe of the conditions inside the dense fireball. The ρ^0 meson is low-mass vector mesons (mass 775 MeV), having a very short lifetime (4.5×10^{-24} s) and it decays inside the fireball and interacts with the hot and dense medium resulting in the so-called 'in-medium modification'. These could signify chiral symmetry restoration. There is no dilepton data measured in heavy-ion collisions in the FAIR energy range till now. To suppress the huge combinatorial background of lepton pairs is the experimental challenge in dilepton measurements.

The experimental challenge for the MuCh is to identify low-momentum muons in an environment of high particle densities. The idea is to track the collision product particles through a hadron absorber system, and to do a momentum-dependent muon identification. The MuCh has a detector plus hadron absorber sandwich structure, forming several layers of staggered absorber plates and tracking stations. In contrast to muon detectors in other HEP experiments, the uniqueness of the CBM muon detection system is that the hadron absorber is sliced. To allow for momentum dependent track identification the detectors are placed in between these absorber slices. The detection of low momentum muons, which would otherwise have been stopped by a single thick absorber, will be improved by this novel design. Therefore, MuCh will have unique discovery potential.

Structure of the MuCh

The dipole magnet is hosting the target and the Silicon Tracking System (STS), which allows to determine the particle momentum. The MuCh system is located downstream of this dipole magnet. The absorber/detector system needs to be compact in size in order to reduce the number of muons from pion and kaon weak decays, which will add as background to the di-muon spectra. The MuCh has its first absorber made up of carbon of thickness 60 cm and a part of this absorber lies inside the dipole magnet. Downstream to the carbon absorber is the first MuCH station. Each station has 3 layers of detectors for tracking. The thickness and material of the absorbers were

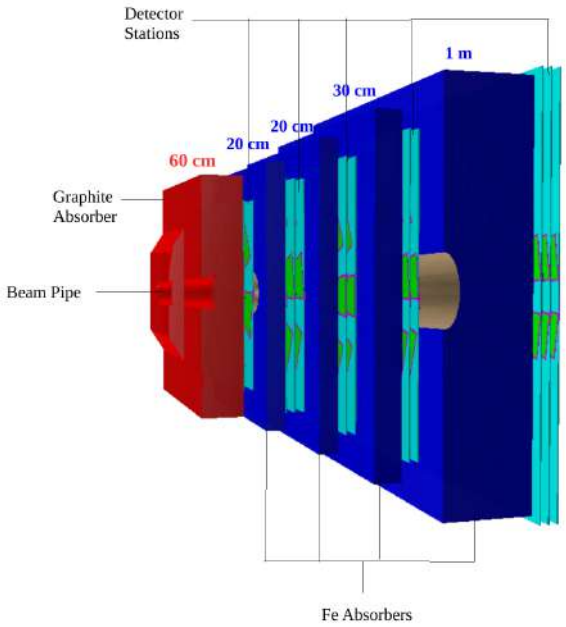

Figure 1.6: The MuCh detector setup for SIS100-B. The red block is graphite absorber (60 cm thick). The blue blocks are iron absorbers of thickness 20 cm, 20 cm, 30 cm and 100 cm. The turquoise colored planes are detector layers. Detector stations no. 1 and 2 will have GEMs, while station no. 3, 4 and 5 will have straw tubes.

optimized by simulating the detector response of the Au+Au collisions in energy range (4 AGeV to 25 AGeV beam energy) by transporting the collision produced particles generated by the UrQMD event generator. The detector performance was simulated and optimized with respect to efficiency, signal-to-background ratio, and phase-space coverage.

The MuCh detector system will have 3 stations in SIS100-A setup which is planned to run at beam energies 4-6 AGev. In SIS100-B setup, MuCh will have an additional fourth station. In SIS100-C there will be another 1 m thick iron absorber and the 5^{th} detector station. Figure 1.6 shows the MuCh geometry for SIS100-C setup as per GEANT4 simulation done with CBMRoot software [32]. The tracking detectors are based on different technologies depending on the hit density and rate. From Fluka simulations, it was found that for minimum bias Au+Au collisions at an energy of 35 AGeV, the particle density is 0.04 hits/cm^2 per event in the first detector station right after the carbon absorber. This converts to 0.4 MHz/cm^2 particle rate in the first station of MuCH at an interaction rate of 10 MHz [33]. To handle such high rates, three layers of Gas Electron Multiplier (GEM) detectors are chosen for the first two stations of MuCh and the third and fourth stations will have straw tube detectors. In Figure 1.6, the SIS100-B setup is the part excluding the 5^{th} absorber and the 5^{th} station. It consists of 4 tracking stations each having 3 layers of chambers. The first

absorber is a carbon block of 60 cm thickness. The second and third absorber is made up of iron of thickness 20 cm each. the fourth absorber is 30 cm thick block of iron. In the next section the charactersitics of the gaseous detector intended to be used in MuCh is discussed.

1^{st} and 2^{nd} MuCh stations : Gas Electron Multiplier

The Gas Electron Multiplier (GEM) was developed first at CERN in 1997 to replace the then existing multi-proportional wire chamber (MWPC). The MWPC was invented in 1968 and that time it was the only gaseous detector that had rate capability better by orders of magnitude compared to contemporary devices [34]. However, with the increase in the interaction rate criteria of most of the modern high energy phyiscs experiments, the demand for detectors outperforming MWPC was raised. MWPC could handle rates upto 10^4 Hz/mm^2, whereas GEMs could handle even above 10^6 Hz/mm^2. Moreover, GEM has better time and position resolution as compared to MWPC. Thus GEM is the best choice of detector that can be used in the first and second stations of MuCh.

GEM is basically a gaseous detector and its advantageous unique feature is its structure made with GEM foil. The GEM foil is a thin polyimide (kapton) foil of thickness 50 μm metalized with 5 μm thick copper on both the surfaces. Each GEM foil is structured with a high density hole pattern (about 50 holes/mm^2). The pitch between holes is 140 μm, while the diameter of each hole is 70 μm. Even when relatively low voltage ($\sim$400V) is applied between the copper surfaces of the foil, a very high (100 kV/cm) electric field is created inside the holes, which avalanche amplifies the electrons produced by ionising particles passing through the gas volume in between drift plane and GEM foil.
Performance studies of the GEM detector for the CBM-MuCh was performed using a prototype GEM detector at SIS18 facility of GSI [35]. The GEMs operated with Ar/CO_2 gas mixture in volume ratio 70:30 have 95% efficiency for muon detection. An important factor of concern for the CBM-MuCh experiment is aging in the detectors under long-term operation, which is a well known problem in gaseous detectors. The effect on performance of GEM under long-term exposure to radiation was studied and the details can be found in Refs. [36–38].

3^{rd} and 4^{th} MuCh stations : Straw Tube Detector

A straw tube detector is a cylindrical drift chamber consisting of a long plastic straw filled with gas and a centrally placed anode wire. Large particle tracking devices can

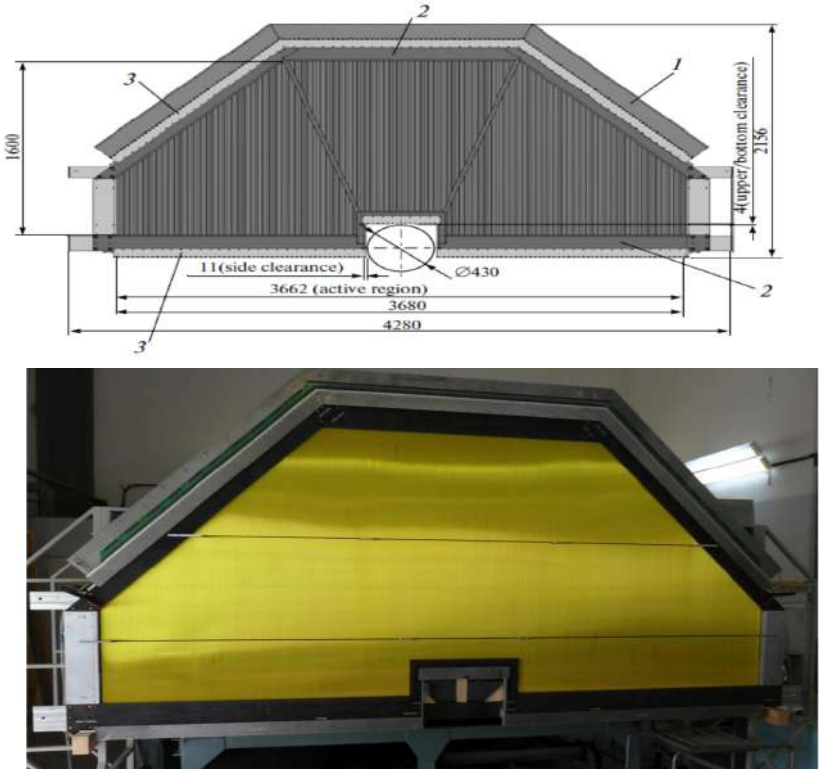

Figure 1.7: (Top) Schematic view of the MUCH straw module. 1-mother boards for the readout and high voltage supply of the straw anodes; 2-carbon plastic elements, and 3-Al elements. (Bottom) Picture of the straw module assembly. (The Figure is adopted from Ref. [39])

be composed of thousands of straw tubes. Prominent features of the straws are low material budget and moderate cost. Gaseous detectors like GEMs were already a very good choice for stations 1 and 2 of MuCh in terms of rate handling capability and aging. Since the GEMs are costly, it will be very expensive to use GEMs in the third and fourth stations of CBM-MuCh which are larger in size than station 1 and 2. The idea is to use a low cost detector to serve the same tracking purpose for MuCh. Ofcourse one has to also take care of the fact that the detector to be chosen as cheaper alternative of GEM should not be made up of high Z material as this would distort the tracks for low momentum muons. Keeping in mind all these requirements, the best option for the third and fourth stations of MuCh is the straw tube detector. Another advantage of the straw tube detector is that each straw cell can be operated independently. This means that if one cell becomes accidently damaged due to wire breakage, the other cells will remain unaffected. This was a major disadvantage of MWPCs that was learned from past experience. Hence, straws tubes fulfill all the requirements for successful functioning at MuCh.

The current MuCh straw subsystem design is based on straw tubes with a diam-

eter of 6 mm. The straw diameter was chosen to be 6 mm which was a reasonable compromise between the detector response speed, number of detecting elements and the occupancy. The parameters of the straw tube was optimised in Monte Carlo simulations for central Au–Au collisions [39]. The straws have a maximum drift time of 60 ns and a pulse duration of 35 ns. The maximum value of the occupancy is $< 7\%$. These parameters are matching well with the requirements in the CBM setup of maximum 10 MHz rate for Au–Au collisions at 25A GeV. For the use of MuCh, an assembly of straw stations containing 12 double layers modules, was developed in JINR, Dubna [39, 40]. Each of these module consists of about 1184 straws. The production technology was similar to the straw tube detector development for the COMPASS experiment at CERN SPS and for the ATLAS TRT at LHC. Each straw station has three identical octagonal chambers measuring X. Two chambers were rotated (by +10, -10 degrees) allowing for the measurement of coordinates of a passing charged particle. Each chamber of MuCh straw station was assembled from two straw layers, where neighboring layers were shifted by half a tube diameter with respect to each other. This design was chosen in order to resolve left-right ambiguities. With this design the single track efficiency for a double layer was found to be 99%. This kind of a double layer arrangement is advantageous in efficiently combining the radial resolution dependences of two layers. The effective average spatial resolution obtained with a chamber made of two layers was estimated to be within a range of 90 μm to 120 μm. From the mechanical point of view, since the chambers are very light weight, they were mounted on a carbon frame. The chambers have an inner hole to accomodate the beam pipe having a diameter of 43 cm. Figure 1.7 shows the schematic layout of the straw module and the straw chamber and the real size straw module. Beam test of a prototype detector was performed [39]. With Ar/CO_2 gas mixture in the ratio 80/20, the efficiency and spatial resolution were found to be 98% and 160 μm respectively in these studies. A lot of thorough R & D was performed with the straws at the laboratory of JINR, Dubna. However, there still remains some questions yet to answer regarding the safe use of straws in CBM-MuCh. These are : what is the rate handling capability and the stability of long term performance of straws? what is the time resolution of the straws? One of the primary focus of this thesis is to address these questions.

1.3 Scintillation detectors for Cosmic Ray Experiments

This section, discusses the application of scintillation detectors in the cosmic ray research programs. Beginning with a general introduction of the experimental cosmic ray research, and the various experiment around the world and their goals are discussed in Section 1.3.1. Section 1.3.2 explains how air shower arrays made of scintillators can explore the high energy cosmic ray spectrum.

1.3.1 Cosmic ray experiments

This section covers the history of cosmic ray research starting from the discovery of cosmic rays, the origin, the interaction properties of cosmic rays, primary cosmic ray spectra and the list of some experiments exploring the cosmic ray spectra.

Cosmic ray discovery

During the early 20^{th} century, when many physicists were studying the nature of radioactivity using electroscopes, a German scientist named Theodor Wulf conducted an experiment to measure the radiation strength as a function of height from the ground. In an electrometer which was taken to the top of the Eiffel tower, he observed a reduced intensity of radiation, thereby confirming that the ionizing radiation is of terrestrial origin. Later in the year 1911, an Austrian-American scientist, Victor Hess planned a similar experiment and targeted to reach an altitude of 5 km with balloons. He found that in addition to the terrestrial component that decreases with altitude, there was another component that becomes stronger with increasing altitude. He concluded the presence of an extra-terrestrial source of radiation, which marks the first evidence of the cosmic rays. Till then all the experiments were done with electroscopes and electrometers. In 1912, Scottish physicist, Charles Thomson Rees Wilson developed a modern equipment called the cloud chamber, which could detect and follow the tracks left by the ionizing particles. As newer detector technologies were developed, more and more properties of the cosmic rays were revealed. In 1926, Hoffmann used new detection techniques and observed the particle multiplication when passed through absorbing layers ('Hoffmann's collisions'). Dutch physicist, named Jacob Clay found out the dependence of the cosmic ray intensity on the geomagnetic latitude in 1927, thereby confirming that primary cosmic rays are charged particles, which get deflected by the magnetic field of Earth. By using coincidence detection techniques in 1929, German physicists Walther Bothe and Werner Kohlhoerster, proved the charged-particle nature of the cosmic rays at sea level. In 1930, Carl Stoermer, a Norwegian astro-

physicist made some calculations to find the trajectories of charged particles passing through the Earth's magnetic field for closer understanding of the geomagnetic effects. In 1927, Johnson and Alvarez & Compton observed the east-west effect, which proved that the primary cosmic rays consist of positively charged particles. Considering the direction of incidence of cosmic-ray particles at the north pole and the direction of the magnetic field, the charged particles follow a spiral trajectory. If the primary is negatively charged then spiral is clockwise, for positively charged primary, it is anti-clockwise. A higher cosmic ray intensity was observed from the west compared to the east, signifying an anticlockwise spiraling and therefore the primaries are positively charged in nature. In 1933, Bruno Rossi, an Italian experimental physicist studied the interaction of secondary cosmic rays in lead and found that cosmic rays at sea level have a soft and a penetrating component. With the development of detection methods, the cosmic ray research advanced and it was established that primary cosmic rays are mostly protons.

Origin of cosmic rays

One of the main unsolved astrophysical problems to date is the origin of cosmic rays. The cosmic rays of highest-energy are associated with the most energetic processes in the universe. The origin of cosmic rays as stated in Ref. [41] is "interrelated with the main processes and the dynamics of star formulation, stellar evolution, supernova explosions and to the state and conditions of the interstellar matter in the Galaxy." As also mentioned in this reference, "The explosion of SN1987a is the only supernova explosion that has been observed by modern science. We use it as an example for all other supernova explosions and the development of supernova remnants, where we believe charged particles become cosmic rays."

Primary cosmic ray spectra

The charged primary cosmic ray are composed of protons (85%), alpha (12%), and other nuclei having $Z > 2$ (3%). The primary cosmic ray spectra is shown in Figure 1.8. The energy spectrum of the primary cosmic ray follows power law with a power index of 2.7 up to energy of 100 TeV. The power index changes to 3.1 at about 4×10^{15} eV and this region is known as the "knee". Up to an energy of 10^{15} eV the cosmic rays are likely to originate from within our galaxy. The so-called 'ankle' appears above the energies around 5×10^{18} eV, and from this region onwards the spectrum flattens again. The change in slope of the spectrum at ankle is often believed as a crossover from a steeper galactic component to an extragalactic component. As mentioned in Ref. [1] "Cosmic rays originate predominantly from within our galaxy. Galactic objects do

not in general have such a combination of size and magnetic field strength to contain particles at very high energies. Particles with energies exceeding 10^{15} eV start to leak from the galaxy. This causes the spectrum to get steeper to higher energies. Since the containment radius depends on the atomic number, the position of the knee should depend on the charge of primary cosmic rays in this scenario, i.e., the knee for iron would be expected at higher energies compared to the proton knee. Another possible reason for the knee in cosmic radiation could be related to the fact that 10^{15} eV is about the maximum energy which can be supplied by supernova explosions. For higher energies a different acceleration mechanism is required which might possibly lead to a steeper energy spectrum."

In general, since with increasing energy the intensity of primary cosmic rays decreases, it becomes difficult to directly observe the high-energy component of cosmic rays. Detection methods like incorporating balloons or satellites at the top of the atmosphere eventually run out of statistics due to limited size of the detectors that can be carried to space. Thus, direct methods of detection cannot be used for the measurements of the charged component of primary cosmic rays at energies above 10^{14} eV and therefore one has to adapt indirect methods of detection.

1.3.2 Air shower arrays made with scintillators

This section covers the development of air shower array experiments around the world, starting with the general introduction to cosmic ray air showers.

Cosmic ray air showers

Cosmic ray air showers are cascades of particles produced by the interaction of cosmic rays in the atmosphere. The first observation of a cosmic ray air shower dates back to the 1920s, when a single charged particle track was split into two. With the participation of many famous physicists in the 1930s, this led to the development of the electromagnetic cascade theory. In 1937, a French physicist called Pierre Auger together with his collaborators observed the extensive air showers.

From the cosmic ray spectra in Figure 1.8, it is evident that at very high energies, the cosmic ray flux is so small, that detecting showers is the only method to observe them. It was the team of Auger, who discovered that the high particle density area of the shower is near the centre of the shower and it is of the order of 10^4 m^2. The observation method for these showers is to place several detectors at some distance from each other and to look for hits in coincidence. The shower array works in a prin-

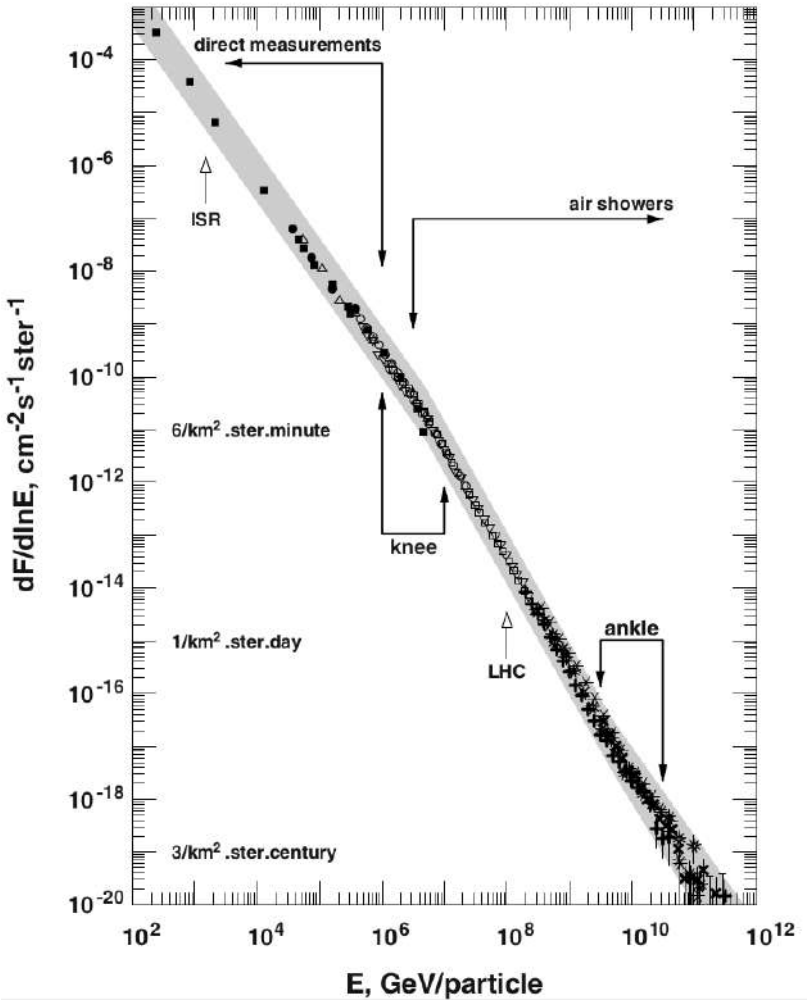

Figure 1.8: Energy spectrum of all cosmic ray nuclei above 100 GeV. Graph taken from Refs. [41].

ciple where all the particles in the shower pass the observation level simultaneously. This does not tell about the energy and type of the primary particle. Therefore, it is important to perform Monte Carlo simulations of the shower development. The observed air shower features can then be compared to the different simulated shower models. Then the particle energy and type could be derived.

The idea of cascade development is well described by Heitler's toy model [41]. This model consists of particles of same type interacting at length λ (interaction length). Two new particle each carrying one half of the energy of the primary, are created in the interaction. Figure 1.9 shows a sketch of the toy model. In every interaction length the number of particles doubles and their energy is halved. At an atmospheric depth $X = N\lambda$ there are 2^N particles in the bunch. This growth goes on until the particles reach a critical energy E_c, below which the interaction cross-section is zero.

The maximum number of particles in the shower is therefore given by the relation : $N_{max} = E_0/ E_c$. The depth maximum is given as : $X_{max} = \lambda \log_2 (E_0/ E_c)$.

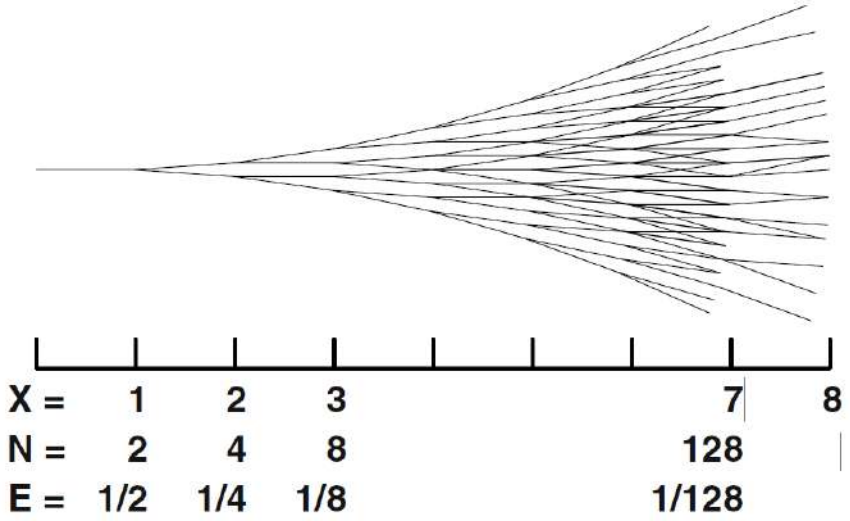

Figure 1.9: Heitler's toy model of cascade development. In this picture, $E_c = E_0/128$. Graph taken from Refs. [41].

Extensive air showers (EAS) are cascades developing in the atmosphere produced by very energetic primary cosmic rays. EAS has mainly three components, an electromagnetic, a muonic and a hadronic. There also exists a fourth component which is the neutrino component. As the air shower develops in the atmosphere, the structure of the shower has a shower nucleus consisting of the energetic hadrons component. This hadron shower nucleus supplies energy to the electromagnetic and the other shower components through hadronic interactions and weak interactions (decays). The neutral pions, which are produced in nuclear interactions, generally decay into photons, which in turn produce electrons and positrons by pair production. Thus the neutral pion contributes to the electron, positron and photon component of the shower. Electrons, positrons and photons undergo processes like pair production and bremsstrahlung, thereby initiating the electromagnetic cascades. The charged pions and kaons decay into muons and neutrinos to produce the muonic cascades and the neutrino components of the shower.

Almost 50% of the energy of the primary particle is inelastically transferred into the production of secondary particles. All the three pions (π^+, π^-, π^0) are produced in equal amounts, so only one third of the inelasticity (from π^0) is invested into the development of the electromagnetic component. Also the hadrons produced undergo multiple interactions through which energy is pumped into the electromagnetic component. The largest fraction of the primary energy is therefore transferred into the

electromagnetic cascade. The electrons and the positrons constitute the main shower component, in terms of the number of particles. The number of particles in the shower increases with shower depth until it reaches a certain atmospheric depth, where for charged particles the absorption or energy loss due to ionization and for photons the Compton scattering and photoelectric effect start to dominate. The shower starts to fade out after this. The atmosphere of the Earth is approximately equivalent to an absorber of 11 interaction lengths and 27 radiation lengths. This means that a primary particle should have a minimum energy of about 10^{14} eV in order to be detected at sea level through air shower measurements. At the height of the shower maximum, about 10% of the total charged particles are muons. But at the sea level, apart from some protons, the charged particle multiplicity shows that muons are the dominant component (approximately 80%). This is because electrons lose energy by radiative processes like bremsstrahlung and this component eventually dies out before reaching the ground level. Whereas muons do not suffer bremsstrahlung energy losses due to their large mass. The cosmic muon flux through a horizontal area at sea-level is roughly one particle per cm^2 per minute [42].

Air shower arrays around the world

Detection of air showers are generally carried out on the surface of the Earth at sea level or at high altitude. For primaries in the energy range 10^{14} eV to 10^{15} eV, the preferred level of observation is at high altitude, close to the maximum of the shower, where its size is big and the fluctuations are small. For energies above 10^{15} eV, the primary could penetrate larger depths in the atmosphere without interacting, and the height from ground of shower maximum could be lower. Therefore, it is better to set the observation level at lower altitudes. Figure 1.10 shows a schematic representation of the shower development and detection. The figure also shows a shower development curve, where at some point it has a peak indicating the shower maximum. It also shows the two different detection techniques. The first technique is direct detection of shower particles by employing counters that are usually made up of liquid or plastic scintillators. The figure shows several types of detectors : squares are counters for electromagnetic component, the small house is for hadron component, and the underground detectors are for muonic component. The figure also shows the second detection technique which is a small symbol of optical detector. The optical detector detects the light (Cherenkov or fluorescence) emitted by the shower particles. The technique most commonly used for the measurement of particles produced in extensive air showers is the sampling of shower particles at sea level, with typically 1 m^2 large water Cherenkov counters or scintillators.

Some of the world-famous air shower experiments are discussed below.

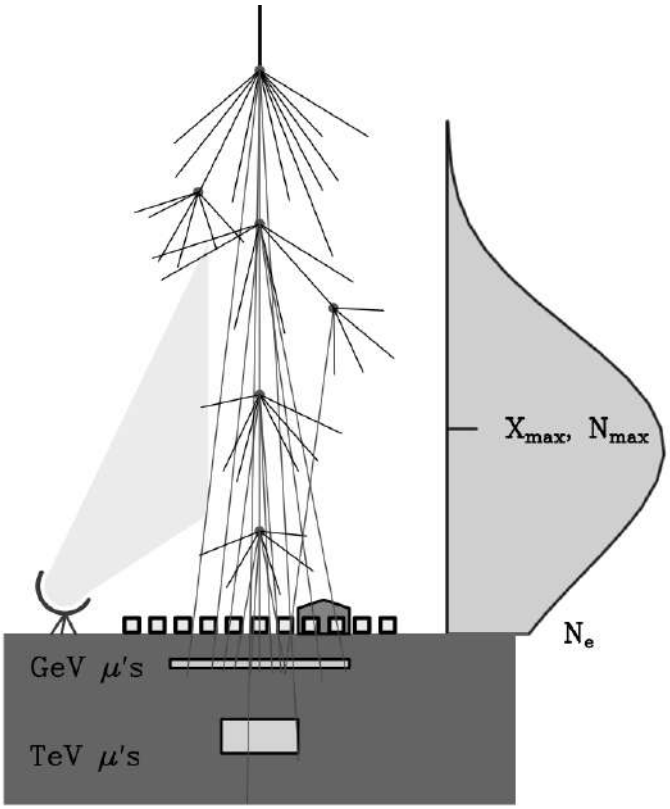

Figure 1.10: Cartoonized picture of the shower development and detection. Picture taken from Refs. [41]. Black squares are counters for detecting the electromagnetic component. Small house is the hadron detector. The box underground is a muon detector. The disk shaped receiver on the left side of the picture is the optical detector for Cherenkov and fluorescence light measurement.

The Auger observatory in Argentina has 3000 counting detectors for the measurement of the components of extensive air showers at sea-level. This experiment can also measure the angle of incidence of the primary particle.
The Karlsruhe Shower Core and Array DEtector (KASCADE) is built 100 m above sea-level and consists of 252 scintillators spread over an area of 600 m^2, for identifying electrons and muons in the shower. It also measures the hadronic component using a 320 m^2 hadronic calorimeter. This experiment can reconstruct the energy and type of the primary nuclei.
The Gamma Ray Astronomy at PeV EnergieS- phase 3 (GRAPES-3) is a high density EAS array designed for a precision study of the cosmic ray energy spectrum and its nuclear composition in the energy below the knee region. It consists of 400 plastic scintillators of dimension 1 m^2 that spreads over an effective area of 25,000 m^2. It can measure electron multiplicity, muon multiplicity and high energy gamma rays in the shower. It is located in Ooty, India at an altitude of 2200 m.

All the above three experiments cannot study the longitudinal development of the showers, because its observation level is one, either ground level or at a specific altitude. On the other hand, optical air shower detectors for example the high resolution Fly's Eye (HiRes) detector, can be used to study the longitudinal development of the air showers. HiRes detects the nitrogen fluorescence produced by very energetic shower (above 10^{17} eV). But one disadvantage is that it can only be observed during clear moonless night (observation probability is less than 10% only).
Ashra (All-sky Survey High Resolution Air-shower detector) is another experiment that aims to observe Cherenkov and fluorescence lights emitted during the lateral and longitudinal developments of very-high energy cosmic rays in the atmosphere. Its optical telescope can process the images of a very wide field of view, that covers 80% of the sky.

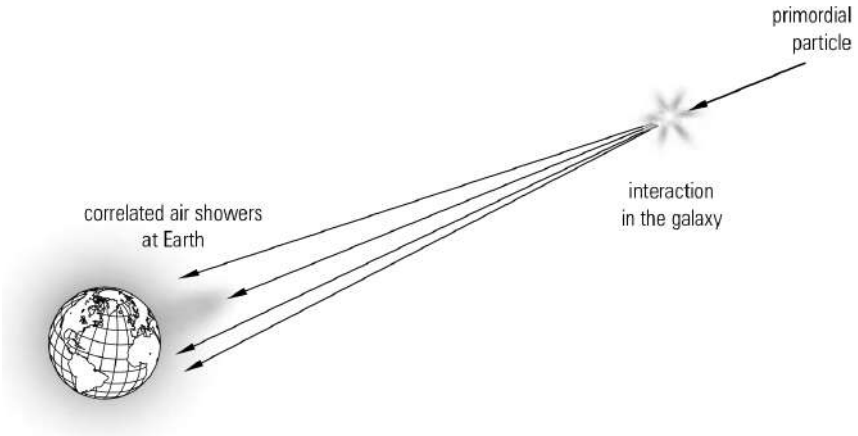

Figure 1.11: Picture depicting a possible explanation for correlations between distant extensive air showers. Picture taken from Refs. [1].

The lateral width of normal extensive air showers, even at the highest energies, is at most 10 km. However, some evidence is indicating that correlations between air showers arriving at the same time but separated by more than 10 km exist. To understand such coincidences, refer to Figure 1.11. Here it is assumed that the energetic primary cosmic particles interacted in space at large distances from Earth. The secondary particles produced in these interactions continue traveling towards Earth and could possibly initiate separate air showers in the Earth's atmosphere. However, this is not studied in great detail because of the lack of availability of two separate air shower stations located thousands of kms away from each other and most importantly that they are synchronized in time. Also both the stations have to be at same altitude in order to catch coincident showers. With a motive to try to fill this gap in the research of correlated air showers, an air shower array made up of plastic scintillators was developed in Darjeeling, India at an altitude to match with that of GRAPES-3

shower array. This is discussed in Chapter 3.

1.3.3 Cosmic Rays and Solar Eclipse

The cosmic ray intensity at sea level depends on various factors such as geophysical parameters, atmospheric weather, space weather, etc. Astrophysical phenomena like solar eclipses have potential influence on the atmospheric conditions, which in turn can affect the cosmic ray intensity. The study of correlation between the solar eclipse phenomena and the change in cosmic ray intensity was done in the past by many researchers and is still an interesting topic. The variation of secondary cosmic gamma ray (SCGR) flux during solar eclipses was studied and reported earlier by several groups. Most of them observed a dip in the SCGR flux during the solar eclipse. There are theories trying to explain such correlations, but non of them is concrete. In this thesis, one of the prime work is to study the correlation between solar eclipse and cosmic rays and try to derive a possible explanation for the observation. This is discussed in Chapter 4.

1.4 Aims and Objectives of the thesis

This thesis belongs to the field of detector development for the study of high energy physics and astrophysics. The thesis has mainly three classified aims :

- to test the feasibility of using the straw tube detectors in the CBM-MuCh detector system
- to develop an air shower array made of plastic scintillation detectors at high altitude for the study of cosmic ray showers
- to study a correlation between solar eclipse and cosmic rays using NaI(Tl) scintillator

The first aim, is based on the designing a detector system for the upcoming CBM experiment. The CBM experimental challenge is to develop a fast, large-acceptance detector and to set up a high-speed read-out system capable to run under these conditions with high-luminosity beams delivered by FAIR. As a consequence of the high luminosity of the SIS100 accelerator, the interaction rate will be very high, higher than any of the existing high energy physics experiments. This means there will be extremely high particle rates at the detector stations, especially the ones which is sitting close to the target. The MuCh detector sits immediate downstream of the STS detector system which is closest to the target, hence will face very high particle rates.

For this reason MuCh will deploy GEMs in the first two stations and straw tubes are proposed for the third and fourth stations. Straw tubes are wire chambers falling in the category of gaseous detectors. Gaseous detectors have rate handling limitations and are also prone to aging effects which degrades the performance of the detector. It is necessary that these properties are studied in great detail especially for the case of straw tubes before its use in CBM-MuCh.

Chapter 2 first introduces the straw tube detector and discusses its basic properties. Then it focuses on the performance studies of the straw tube detector conducted in the laboratory for testing its safe use in the MuCh. It includes the details about the straw tube prototype, the experimental setup and results. Referring to Chapter 2, the objectives are as follows,

Objectives :

- Basic characterization of the straw tube detector:
  This includes development of a detector test system with reduced electronic noise and to study the parameters of the straw tube detector such as gain and energy resolution. It also includes setting the operating region of the prototype detector, find the correlation between gain and the gas parameters like the gas temperature and pressure and gas composition.

- Timing properties of the straw tube detector:
  Objective is to obtain the time spectrum of the straw tube detector with cosmic rays (muons) using a plastic scintillator trigger set-up. This includes studying the variation of the time resolution with detector bias.

- Study of rate handling capability of the straw tube detector:
  One of the primary objective is to study the rate handling capability of straw tube detector filled with Ar/CO_2 gas in order to test the feasibility of using this detector in the high rate CBM environment. This includes measuring the gain and the energy resolution of the detector by varying the X-ray rate from a radioactive source for Ar/CO_2 gas mixtures in different ratios.

- Aging properties of straw tube detector:
  Another primary objective is to study the stability of gain and energy resolution of the straw tube detector under high rate continuous radiation of X-ray, using premixed gas of Argon and CO_2 with conventional NIM electronics. In particular, to find the aging rate of straw tubes and to what extent it can be used in the CBM experiment.

Coming to the second aim of the thesis, it is based on the development of a cosmic ray air shower array made of plastic scintillators, at an altitude similar to that of

GRAPES-3 air shower array.
The question of its origin is something which researchers are trying for more than 50 years to answer, still it is not clearly understood. Cosmic rays of energy more than 10^{14} eV can only be studied through the detection of secondary particles forming extensive air showers (EAS) for which various experimental programs around the world have built large size arrays of detectors [43–46]. **Chapter 3** gives an overview of the recent research going on in the field of cosmic rays. This chapter also introduces the plastic scintillator and its application in cosmic ray experiments. Apart from the basic characterization of plastic scintillators, this chapter discusses the cosmic ray experiments carried out in the detector laboratory of Bose Institute. This chapter also discusses the development of cosmic ray air shower array in Darjeeling, including the array design, fabrication, assembling and finally commissioning. The results are also discussed. Lastly, the simulation of a muon tracker in GEANT4 and the method used to reconstruct the muon momentum is presented. In this regard, the primary objectives can be stated as follows,

Objectives :

- To perform basic characterization of the scintillators, and estimate the energy deposition by muons in the scintillators.
- To set up a cosmic ray muon trigger using plastic scintillators and measure the cosmic muon intensity at sea level.
- The primary aim is to set up a detector array using Plastic Scintillation Detectors (PSD) at the mountains of Darjeeling (27 N, 88 E, and altitude of 2200m above sea level) mainly for the study of the cosmic rays.
- To measure the air shower rate at high altitude and compare the results with GRAPES-3 air shower array (at similar altitude)
- To simulate a cosmic ray muon tracker in GEANT4 using silicon pad detectors and test the feasibility to track cosmic ray muons with it. To also find the momentum resolution of the tracker.

The third aim of the thesis is to draw a correlation between solar eclipse and cosmic rays on the basis of experimental data. There is evidence from the past experiments that cosmic ray gamma flux decreases during solar eclipse but there is no concrete physical explanation for this observation. The cosmic ray flux is dependent on atmospheric parameters. Astrophysical phenomena like solar eclipses produce disturbance in the atmosphere thereby effecting the cosmic ray intensity. The traveling ionospheric

disturbances produced by the solar eclipse travel at great speed and can affect the total electron content (TEC) of the atmosphere. In this thesis, the possibility of any traveling atmospheric disturbance caused due to the Great American solar eclipse on 21 August, 2017 [47] to reach India and whether this could be observed through cosmic rays and TEC or not, was investigated. Some of the geophysical parameters and space weather that has influence on cosmic ray intensity, was taken into account.

Chapter 4 discusses the interplay between solar eclipse and cosmic rays and the application of in-organic scintillators for cosmic ray gamma detection. It also discusses the experimental technique, observation of gamma rays during a solar eclipse, the results and the significance. The objectives in this study can be stated as follows,

Objectives :

- To characterize the NaI(Tl) scintillator and study its temperature dependency.
- To setup an experiment to perform a systematic measurement of cosmic ray gamma flux using inorganic scintillation detector NaI(Tl) in laboratory at India, during the total solar eclipse on 2017 over America. The aim is to continuously record the cosmic ray gamma flux during the eclipse week (18 August 2017 to 24 August 2017).
- To check the space weather report during the eclipse week.
- To measure the cosmic ray charged particle flux during the eclipse week.

Finally, in **Chapter 5** of the thesis, the key findings of the research related to the research objectives is discussed.

Chapter 2

Performance study of the straw tube detector for CBM experiment

2.1 Introduction

The Compressed Baryonic Matter (CBM) experiment [18] in Darmstadt, Germany is designed to understand the Quantum Chromo-Dynamics (QCD) phase diagram in the region of moderate baryon densities. It is designed to be a fixed target experiment with very high interaction rate of 10 MHz (compared to the LHC experiments, having interaction rate in the order of KHz). The Muon Chamber (MUCH) at CBM is designed to search for muon pairs produced in heavy-ion collisions having 4 to 40 AGeV beam energy [19]. In the CBM experimental program, the beam energy will be scanned from 4 to 40 AGeV in order to create different phases of matter. Therefore, the plan is to build the MUCH system in stages so as to accordingly adapt to the avalaible beam energies. The first version of MUCH is the SIS100-A setup and will have 3 tracking stations. The second version of MUCH is the SIS-100B will comprise of 4 stations. The structure of MUCH system is explained in Chapter 1, Section 1.2.2. The MuCh has hadron absorber layers with intermediate gas tracking detectors forming a sandwich-like structure with 4 detector stations in the SIS-100 configuration. The 1^{st} and 2^{nd} station of MuCh will have Gas Electron Multiplier (GEM) detector whereas Straw tubes are possible candidates for the 3^{rd} and 4^{th} station of MuCh. Characterization of the prototype of these detectors were done earlier by other groups when they were used in other experiments [48–52]. Some investigations regarding the performance of straw tubes in high energy physics (HEP) experiments that were done in the past is discussed in section 2.2.3. However, for the case of CBM experiment, the scenario is different from other HEP experiments that were conducted in the past. The high luminosity being a unique feature of FAIR, renders high interaction rate at CBM, thereby giving

a tough challenge to the CBM detectors. This means that the detectors must not only be able to handle the high particle rates, but also deliver stable performance for long-term exposure to radiation at these high rates. The effect on operation of gaseous detectors under long-term exposure to radiation was studied with both GEMs and straw tubes and the details can be found in Refs. [36–38]. This chapter will mainly focus on the performance studies of the straw tube detector to justify its use in the CBM experiment. Section 2.2 introduces the straw tube detector, discusses its background, working principle and its use in high energy physics experiments. The basic characterization of the straw tube detector is mentioned in details in section 2.4. Section 2.5 shows results from the measurement of the time resolution. Section 2.6 discusses the rate handling capability of the straw tubes. Finally, the aging tests of the straw tube detector performed to justify its use in the CBM-MuCh is elaborated in section 2.7.

2.2 The Straw Tube Detector

In the late 20th century, when a reliable chamber was needed for the large detectors at the Stanford Linear Accelerator Center (SLAC) [53], for precise tracking near the interaction point, a tube-like chamber was designed. This was the beginning of the use of sophisticated wire chambers in HEP experiments and this chamber was commonly called as the 'Straw tube detector'.

2.2.1 Invention and background

In 1984, a small, thin and reliable detector was required to replace the contemporary chambers for the High Resolution Spectrometer (HRS) detector to improve tracking near the interaction point of the e^+ e^- collider at SLAC. The HRS chambers were usually inaccessible in its position in the HRS detector. Now if there is a failure in one of the wire of the chamber, this would disable a significant fraction of the chamber and would render it useless for a long period of time. Requirement of a fail-safe device in the HRS, motivated to have a tube-like design of the chambers [54]. Therefore the Straw Tube Detector was invented. The most attractive feature of the design was that all the straws were all isolated from each other. This would prevent any kind of discharge problems such as a broken wire in any one of the straw, will not affect other straws.Another advantage of the tube configuration is that the cathode area is large and cathode associated problems are minimum. Further, it acts like a 'cylindrical transmission line' and minimizes the cross-talk between neighboring cells [55]. Drift chambers made from small thin aluminum tubes were used before in many high energy

physics experiments. Proportional counters were also very popular at that time and were generally used as tracking devices in high energy physics experiments, but due to their high Z material, it was proved to be inefficient for tracking low momentum particles. The most innovative design idea of the 'HRS inner tracking straw tube chamber' was the incorporation of mylar tubes with a thin aluminized inner surface instead of solid aluminum tubes, which were most common at that era. One advantage of the aluminized mylar tubes was that they have smaller atomic number (Z) and therefore less multiple scattering takes place. Another advantage was that, since mylar is tough and resilient, these were not so easy to get damaged.
In 1990, while designing the Transition Radiation Detector (TRD) for use in a Large Hadron Collider (LHC) detector, straw tube chambers were proposed [56]. The straw tubes in the TRD were different from the ones originally invented in the sense that mylar was replaced with Kapton. The straw tubes that are to be used in the CBM-MuCh are made of kapton. Kapton has the following interesting properties: its rigidity and mechanical strength are equivalent to or exceed that of Mylar. It also has exceptional radiation resistance that has been measured to be $\sim$ 15% more transparent to transition radiation compared with Mylar. With these foils, straws of diameter $\sim$ 4mm and wall thickness 30-35 μm could be fabricated easily. Henceforth, this particular design of the straw tube was much widely accepted by many experiments in the following years. The main idea of using straw tube detector for tracking low momentum particles is significant reduction of material budget.

2.2.2 Applications of straw tube detector

Beginning with its first use in the HRS detector at SLAC in 1984, the straw tubes marks its use in several high energy physics experiments over the decades such as ATLAS [5] and NA62 [57] experiments at CERN and GlueX [58] in Hall D at JLab for tracking of charged particles with low material budget. Straw tubes have potential to be used as tracking devices in the future high energy physics experiments like the Compressed Baryonic Matter (CBM) at the Facility for Antiproton and Ion Research [16, 18, 39] involving very high particle density and extremely high interaction rate. Advantages of using straws is that it has good efficiency ($\sim$98% for 4mm diameter straws), and good spatial resolution ($\sim$170μm), which are the two vital criteria for any tracking detector. Unlike proportional or drift chambers, which itself have a rigid and strong structure, straw tubes are thin and delicate and needs good support frames when it comes to its use in large size detectors. The straw tubes must be held straight because they bend easily. Making a good design of the support structure requires good skill. One example is given below which briefly describes the detector geometry that will be

implemented in the future CBM experiment.
The Muon Chamber (MuCh) at CBM will have a detector-absorber sandwich structure, with 4 detector stations in the SIS-100 configuration. The straw tube detector is a possible candidate for the 3^{rd} and 4^{th} station of MuCh. Each straw station will contain three identical octagonal chambers, one will measure the X coordinate and other two are rotated (+10, –10) coordinates of a charged particle track. Each chamber consists of two identical modules with some overlap between them to avoid dead regions. Each module will have two layers of straws which are inserted into a carbon frame. The straws of one layer will be glued together to form a plane. Every plane will have three sections. The central part, being closer to the beam axis, will be exposed to higher rates. This part will have a central half hole for the beam pipe. Each layer will have 592 straws with 6 mm inner diameter. The choice of the straw diameter is done by a compromise between minimizing the number of channels and value of the occupancy [39].

2.2.3 Overview of aging studies for the straw tube detector

The new era of High Energy Physics (HEP) experiments demands the gaseous particle detectors to face high particle rates and high integrated particle fluxes (long term operation). Good and stable performance of these detectors over the lifetime of an experiment in a harsh radiation environment is one of the prime concern to the involved experimenters. This section gives an overview of some of the aging studies with the straw tube detector that were carried out in the past. Straw tubes was most commonly used in the experiments at LHC. The characteristics study of the straws like drift time properties and response simulations for the LHC environment was studied rigorously [51, 59]. Some reports on aging in gaseous detectors like the straw chambers can be found in Refs. [60–64]. Aging studies with 4mm diameter straw tubes at gain 10^4 under radiation of 5 MHz/cm 9 keV X-rays were performed [65]. They observed good tolerance of straw tubes operated with a Xe-CO_2-CF_4 gas mixture to high radiation doses up to collected charges on the anode wire of 0.9 C/cm and 0.5 C/cm for two different gains. In addition, they suggested that neutral, stable but highly electronegative species created in the avalanche plasma during irradiation might be responsible for the so-called transient aging that has been observed at lower gas flows. Similar studies were performed by another group using 4mm diameter straws filled with Xe-CO_2-CF_4 gas mixture and irradiated with 10 kHz/cm X-ray fluxes. This aging study was required specifically for the ATLAS-TRT. Their investigations showed that up to the doses 5 C/cm, no drop in gas gain was observed. Instead at certain experimental conditions, they found that the gas gain of the straw was transient, which

means after the X-ray irradiation was switched off, the value of gas gain returns slowly to the initial gain. The value of the gas gain decrease depends strongly on the dose rate and on the gas flow rate. Owing to the experimental conditions at TRT at the LHC, the investigation results show that the observed transient aging of the straw tubes would be quite negligible [64].
Another report where aging tests with the straws were performed at gas gain of 10^4, moderate gas flow (order of 1 vol/h) and irradiation (order of 10 kHz with 6 keV X-rays), it was found that the straws exhibit no aging for few hundred hours. While very few number of straws were locally affected by a gas gain drop, which can be attributed to wire contamination. They showed that, increasing the gas flow can provoke and accelerate the wire aging (by at least 1-2 orders of magnitude). In some straw tubes aging was seen at X-ray irradiation rates as low as 10 Hz/mm [66].
The main cause of the observed aging was identified as follows. Since, gas mixtures rich in heavy hydrocarbon quenchers were used all the time in order to allow large gains, it initiated a polymerization process caused by the ions produced in the gas under avalanche conditions. These polymers, usually deposited on all electrodes, inducing various kinds of secondary phenomena, ultimately resulting in the detector's performance degradation. Aging tests of wire chambers particularly straw tubes, were carried out rigorously in the past. Straw tubes filled with a $Xe/CF_4/CO_2$ or Ar/C_2H_6 gas mixtures have revealed gain degradation when exposed to X-ray radiation of fluxes 10^4-10^6 X-rays/sec [60,64,65]. As far as CO_2 is concerned, it is believed to be an aging resistant gas unlike other organic gases that are mixed with noble ones to quench secondary photons. Pure Ar/CO_2 gas showed stable operation for gaseous detectors up to $\sim$ 1 C/cm [60–62], while some reports showed unexplained gain reduction in drift chambers and proportional counters filled with this gas [67, 68].

It is clear that the conclusions made by different groups were in contradiction. Some concluded that aging is accelerated on increasing the gas flow rate, whereas some reported that gas gain improves on increasing gas flow rate. This needs further investigation and better knowledge of the aging phenomena that is taking place in straw tube. Performance deterioration due to silicon pollution was observed and investigated by ATLAS experimenters since it concerned the safety operation of the straws at the ATLAS TRT at the LHC [69, 70]. Factors that could lead to a very strong deposition process on the anode wires were the presence of volatile, Si- containing products (such as lubricants, mould- release agents or others). Addition of CF_4 to Xe/CO_2 or Ar/CO_2 gas mixtures was found beneficial since CF_4 partially decomposes into chemically active radicals (F) and H_2O, which together create HF acid vapour. The HF acid destroys the Si-based products, thereby acting as a cleaning agent. Therefore, CF_4-based mixtures were thought to be attractive, in terms of ag-

ing. The competition between the formation of deposits and polymerization and the etching process results in slowing down the aging effects. It appears that the favored process is the etching, because it breaks the chemical bonds in polymers. The products that are produced by etching are eventually removed by the gas flow. Due to this, the use of CF_4-based mixtures would require for yearly cleaning up of gaseous detectors under high radiation to be relaxed. This fact supports the observations made by others [64, 65] because an increase in gas flow depletes the system of ambient oxygen and water and harmful long-lived radicals or ions are flushed out. This may also, at the same time, boost the influx of contaminants from polluted or out-gassing system components and materials. Hence, the acceleration of aging in the TRT straw tubes at large gas flows might be justified.

Another consequence of using CF_4-based mixtures was that, etched silicon-based compounds are effectively removed but distributed ubiquitously, polluting the detector and promoting heavy polymerization. Many nonmetallic components of the gas system and assembly materials can be affected. For instance, the glass wire-joints (containing silicon) inside the long barrel straws can be etched to the point of breakage. These effects depend on the moisture level, gas gain, irradiation conditions, and the fraction of oxygen in the gas mixture. Research showed that the straw cathode material is only slightly affected by active species up to 18 C/cm charge accumulated, and the reaction products do not produce any deposits on the wire [70].

After recollecting all the earlier reports on straw tube aging studies, finally the following conclusions were drawn. First, even at the lowest irradiation rates, aging can occur. Second, one of the conditions favoring aging is large gas flows. While often sufficiently high flow rates are chosen to eliminate remnant nitrogen, oxygen or humidity from the detector, they can introduce simultaneously outgassing contaminants, *e.g.* from glues, lubricants or greases, at a higher rate into the active volume. Third, adding CF_4 to Ar/CO_2 gas mixtures was beneficial as it effectively etched and removed silicon-based compounds, but distributed the same ubiquitously, polluting the detector and promoting heavy polymerization. It is to be noted that, whether or not aging is to be observed in straws, depends on its operating conditions, like gain, gas flow rate, radiation doses, hours of operation. These conditions shall vary from one HEP experiment to the other. Therefore, it is needed to personalize the environment accordingly to study the aging properties of the straws.

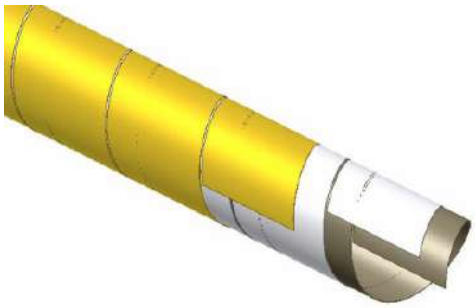

Figure 2.1: The straw tube [taken from TDR CBM MuCh Report] [33]

2.3 Details of the Straw Tube Prototype

2.3.1 The straw

The structure of a straw tube is shown in Figure 2.1 Straw tubes are prepared from two kapton films. One of the kapton was coated with conductive layer of aluminium, and the other was a carbon-loaded kapton film. They are glue to one another [39, 51]. The inner aluminium surface of the straw acts like a cathode. These straws were manufactured by industrial method. The first step was the preparation of the film, second one is the preparation of the film strips with the width of 8±0.1 mm. Two kapton film tapes (4-8 mm wide) were wound in spiral at a temperature around 200 ^{o}C. The wall thickness of such straws is around 60 μm.

2.3.2 Anode wire

The anode wire for the straws is usually made up of tungsten (with 2% of rhenium) plated with gold. The wire has a diameter of 30±0.3 μm. With the help of four small plastic spacers and two end-plugs, the anode wires were held in the center of the straws longitudinally. The wire has an electrical resistance of $\sim$ 60 Ω/m. The wire tension is normally set to 70±10 g, close to the elastic limit which is around 1.2 N. The following are the requirements that the wire should meet.

- Wire ellipticity should correspond to wire diameter variation of ±2%.
- There must not be any defects such as spilts or cracks in the base wire.
- The base wire surface should be carefully treated (light electrolytic cleaning) to eliminate all traces of oxides and other possible pollutants just before gold plating.

- The base wire defects should be removed and the wire should be smoothed by electrically polishing methods.
- The base wire must be plated with pure gold. There should be no nickel additives to the gold, no Ni-flashing of the wire surface before gold plating is done.
- There should not be any mechanical treatment of the wire surface after the gold plating.
- The finally prepared gold plated wire must have a clean surface which is free of any contaminant, e.g. dust, dirt, oil, fibres, chemical residuals etc.

2.3.3 Working principle

A straw tube detector is basically a gas filled single channel proportional counter with a conductive inner layer as cathode and a wire stretched along the cylindrical axis as anode. An electric field is created in the gas filled region, on the application of high voltage between the wire and the tube. The electric field separates electrons and positive ions produced by an incident charged particle along its trajectory through the gas volume. The wire collects the electrons while the ions drift towards the cathode, because the wire is kept at a positive voltage. If the wire is thin, like a few tens of μm is the diameter, then the region near the wire has very high electric field strength leading to an avalanche creation of electrons. Depending on the gas composition and the high voltage of the wire, a gain of about 10^4 - 10^5 can be achieved in such chambers. The specific energy loss (dE/dx) of a charged particle in the straw gas volume can be used to identify the particle species and can be derived from the number of ionization electrons per track length (dx) for the generated straw signal.

2.3.4 Choice of gas fill

The choice of a filling gas for the straw tubes is made by considering several factors like high gain, low working voltage, good proportionality and high rate capability. To meet these conditions, generally a gas mixture is used rather than using a pure gas. Usually, noble gases are chosen, since they require the lowest electric field intensities for avalanche formation at a minimum working voltage. Moreover, the noble gases do not undergo chemical reactions with the material of the detector. Argon is usually preferred because of its higher specific ionization and lower cost. If the filling gas is pure argon, the counter cannot be operated with gains higher than $10^3 - 10^4$ without continuous discharge occurring. This is because of the high excitation energy (11.6 eV) for this element. The excited argon atoms formed in the avalanche de-excite giving

rise to high energy photons. These photons can ionize the cathode element and initiate further avalanches. There is a solution to this problem, by adding a polyatomic gas, such as methane or alcohol, along with the inert gas, the unwanted avalanches can be avoided. Example of such gases are CO_2, BF_3. These gas molecules absorbs the radiated photons (produced by the de-excitation process) and then dissipates the absorbed energy through non-radiative dissociation, thereby acting as quenchers. It has been observed that on adding a small amount of polyatomic gas produces dramatic changes in counter operation and indeed gains of up to 10^6 can be achieved. In the performance study of the straw tubes, the gas used was pre-mixed Ar/CO_2.

2.4 Basic Characterization of the Straw Tube Prototype

It is customary to characterize a particle detector before its use in an experiment, in order to understand its features and set its operating conditions properly. Basic characterization studies were performed for a prototype straw tube detector with premixed $Ar+CO_2$ gas mixtures using conventional NIM electronics [71–74]. In this study, detector count rate, ion current, absolute gain, energy resolution and uniformity of performance were measured systematically. For all the measurements, Fe^{55} X-rays radioactive source of energy 5.9 keV was used. The reason why this radioactive source was chosen is because the X-ray energy is comparable to the energy that is deposited in the detector medium by the particles produced in high energy collisions. In HEP experiments, most of the particles reaching the detector are minimum-ionizing particles (MIP). The mean energy deposited by MIPs in the active detector volume is close to the energy emitted by the X-ray radioactive source used in our experiment. For e.g. 3 GeV muons in the 6 mm drift gap of a Micromegas, filled with Ar/CO_2 80/20 gas mixture will deposit 1.6 keV energy (GEANT4 simulation results) [75].

2.4.1 Experimental setup

The straw tube prototype used in this experiment was built in JINR, Dubna, Russia. The prototype detector is shown in Figure 2.2. It consist of 6 straws of 6 mm diameter and 25 cm length. It was made by two Kapton film strips that were wound together. It was a DUPONT grade aluminized (500 $\mathring{A}$) carbon-loaded Kapton film. The films were covered by a glue layer with a thickness of 7 μm on one side. Kapton film of the NH type were used as inner and outer strips, respectively. A gold-plated tungsten-rhenium wire was used as an anode. The wire diameter was 30 μm and was fixed by the crimp pins inserted in the polycarbonate end-plugs under 70 g tension. The

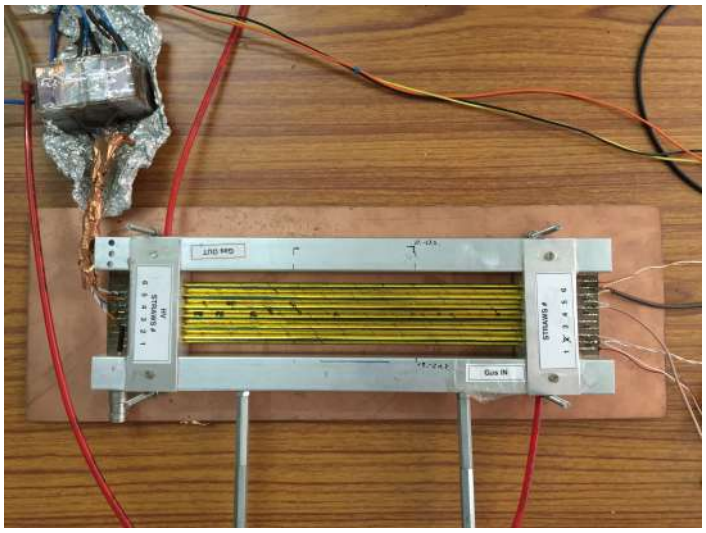

Figure 2.2: Straw tube prototype : 6 straws, each of diameter 6 mm and length 25 cm.

diameter of the end-plugs was 6.0±0.018 mm [39]. The signal from each straw tube was collected through a LEMO connector. A premixed gas composed of Argon and CO_2 in 70/30 volume ratio with purity of 99.9 % was used in flow mode at a rate of 3 l/h and an overpressure of 1 bar. In these straw tubes, overpressure of the working gas mixture of 1 bar was applied. In some of the measurements, Argon and CO_2 in the volume ratio 80/20 and 90/10 was also used. The central anode wire was biased with positive high voltage (HV) using a HV filter box at one end while the signal was collected from the other end after a capacitor. The output signal was fed to a charge sensitive pre-amplifier (VV50-2) having a gain of 2 mV/fC and a shaping time of 300 ns [76]. The output of the pre-amplifier was sent to a linear Fan-in-Fan-Out (FIFO) module. One output of the linear FIFO was put in a timing SCA (Single Channel Analyzer), which was operated in integral mode and the lower level in the SCA was used as the threshold. A NIM based scalar module was used to measure the counting rate of the detector. A typical Fe^{55} signal in the digital storage oscilloscope (DSO) at 1700 V is shown in Figure 3.11 with settings 200 mV/Div, 200 ns/Div. The actual signal generated by the detector was negative, but since the pre-amplifier has a signal inverter, so the final signal looks positive when seen in the DSO.

The current due to ions collected at the cathode was measured from the HV power supply. A Multi Channel Analyser (MCA) was used to obtain the energy spectra with a Fe^{55} X-ray source taking another output from the linear FIFO. A schematic of the setup is shown in Figure 2.4. The straw tube detector count rate was measured using Fe^{55} X-ray source [77]. A plateau in the count rate was observed around 1600V and above.

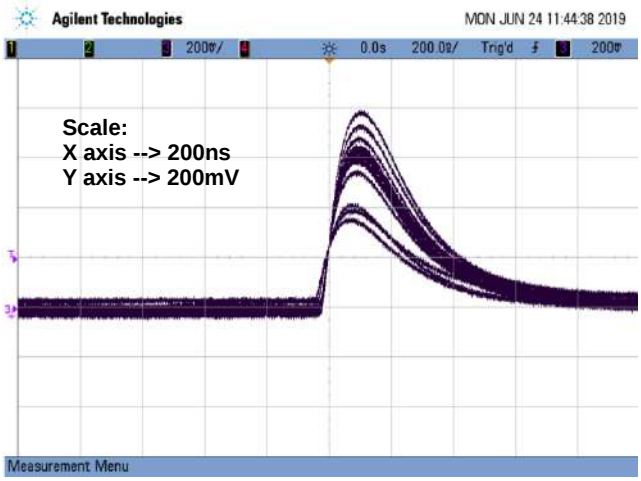

Figure 2.3: A typical straw tube detector signal obtained using Fe^{55} X-ray source, captured with the digital storage oscilloscope at a straw HV of 1700 V. SCA threshold : 200 mV

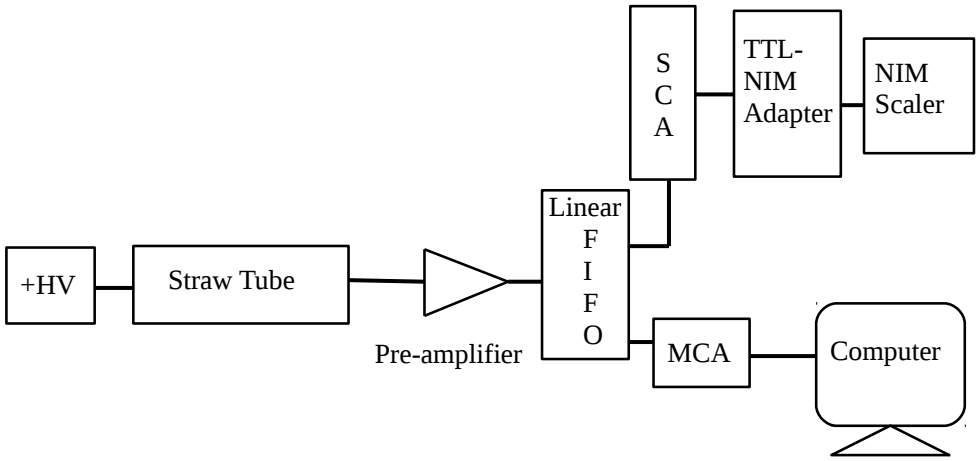

Figure 2.4: Schematic of the setup used for the characterization of the straw tube detector.

The ion current or the relative gain of the straw was also measured from the HV power supply [78]. It was found that the ion current increases exponentially with the voltage.

2.4.2 Gain and energy resolution

The absolute gain and energy resolution of the straw tube were obtained from the energy spectrum of the straw with the Fe^{55} X-rays. Fe^{55} decays to Mn^{55} by electron capture. The excited Mn atom emits photons at basically two different energies:$E_{K\alpha}$= 5.9 keV in 25.4% and $E_{K\beta}$= 6.49 keV in 2.99% of the decays. Since the cross-section

for photo effect dominates at these low energies, almost monoenergetic electrons with $E_e = E_{K\alpha/K\beta}$ - W_e are created. W_e being the electron's binding energy. A third line, the so called K_α escape peak is also visible in the energy spectrum. It corresponds to an energy of $E_{K\alpha,esc} \sim 2.94$ keV. When the incident X-ray photon ionizes an argon atom by displacing an electron from the K shell, the excited argon ion emits a photon with $E_{KL} = 2.96$ keV, resulting from a transition of an L electron to the K shell. If this photon leaves the detector without being detected, only the residual energy of the original K electron is visible, forming the escape peak. Figure 4.12 shows a typical spectrum recorded with a straw tube detector for Fe^{55} source at a biasing voltage of 1650 V with Ar/CO_2 in 70/30 gas mixture. In this spectrum, the main peak (5.9 keV full energy peak) and the escape peak are clearly visible and well separated from the noise peak. The spectra at different straw biasing voltages can be found in Figure 2.6. It can be seen that as the high voltage increases, the spectrum shifts towards the right indicating an increase in the gain of the detector.

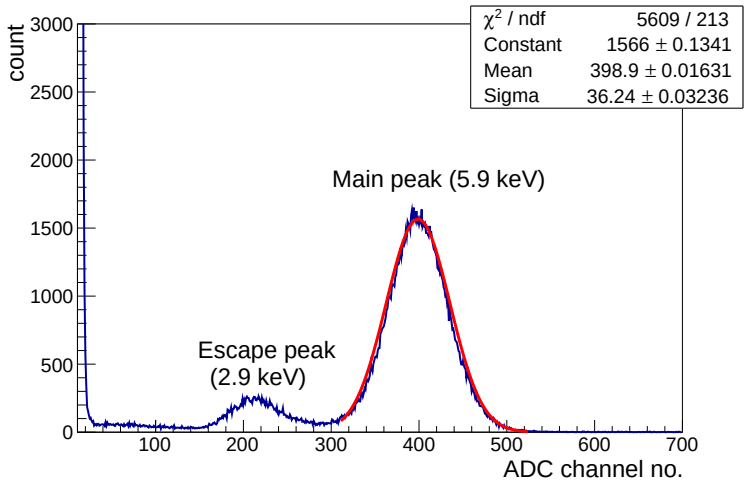

Figure 2.5: Typical energy spectrum for X-ray from Fe^{55} source in Ar/CO_2 gas mixture of 70/30 volume ratio at 1650 V. The main peak was fitted by a gaussian function shown in red line.

To calculate the gain and the energy resolution of the straw tube detector, first the MCA was calibrated in the following way. From a square wave pulse generator, a pulse of known amplitude was passed to the MCA, and the channel number where this pulse appeared was noted. Repeating such measurements for‘ three known pulses, a graph of pulse height vs MCA channel number was plotted as shown in Figure 2.7. The parameters of the straight line fit of the curve was used as calibration factors to convert a given channel number into its corresponding pulse height in mV.

The 5.9 keV energy peak of the Fe^{55} X-ray spectrum was fitted with a Gaussian

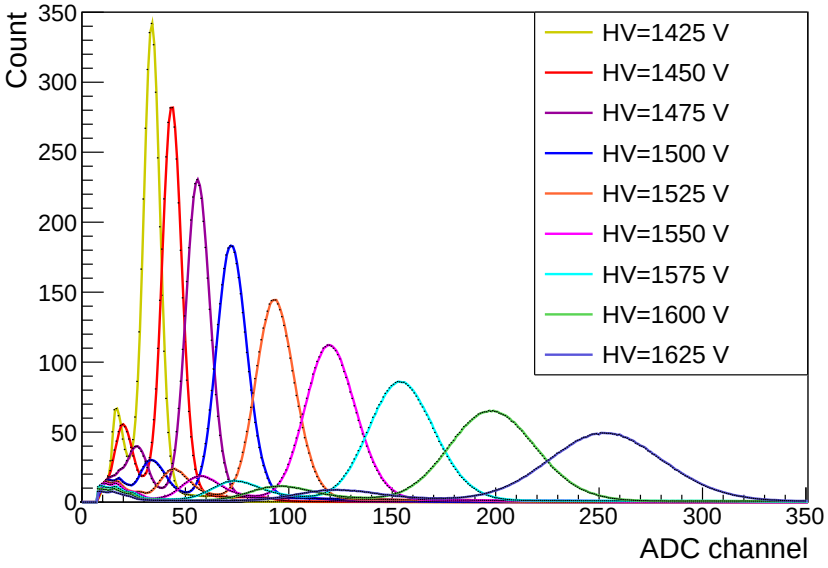

Figure 2.6: Fe^{55} X-ray spectra of the straw tube detector obtained by varying the high voltage.

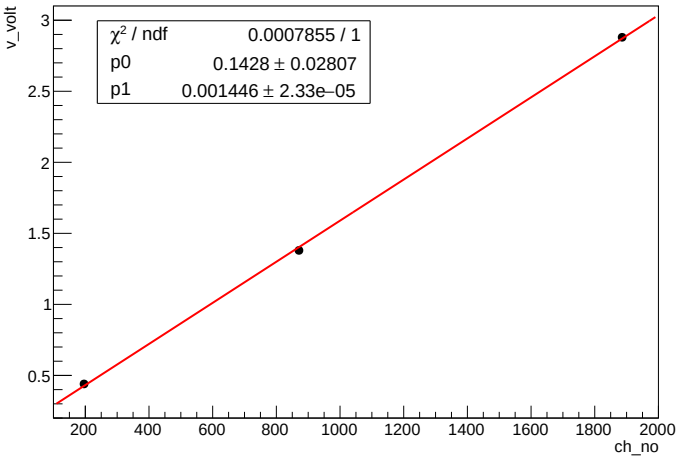

Figure 2.7: Calibration plot of the MCA used in the experiment.

function. From the mean of the fitted peak, the charge after avalanche multiplication (output charge) was calculated using the gain of the pre-amplifier (in mV/fC) and the calibration factor ($C.F.$) of the MCA channel number and pulse height (in mV). The

expression for gain is given by the ratio of output charge and input charge :

$$gain = \frac{output\ charge}{input\ charge} \tag{2.1}$$

$$= \frac{(Mean \times C.F.)/2mV)\ fC}{No.\ of\ primary\ electrons\ \times\ e\ C} \tag{2.2}$$

The average number of primary electrons produced in the gas was taken as 217 for Ar/CO_2 80/20 mixture assuming full energy deposition of 5.9 keV X-ray in the gas volume. The energy resolution of the straw tube detector is defined as :

$$\%\ energy\ resolution = \frac{Sigma\ \times\ 2.355}{Mean} \times 100\,\% \tag{2.3}$$

where 'Sigma' and 'Mean' were obtained from the Gaussian fitting of the 5.9 keV peak of each Fe^{55} X-ray spectrum. The gain and the energy resolution as a function of anode voltage for the straw tube detector is shown in Figure 4.12. From the figure, it can be seen that the gain increases exponentially with voltage, where as the energy resolution decreases with increasing voltage. It is well known that the gain of any gaseous

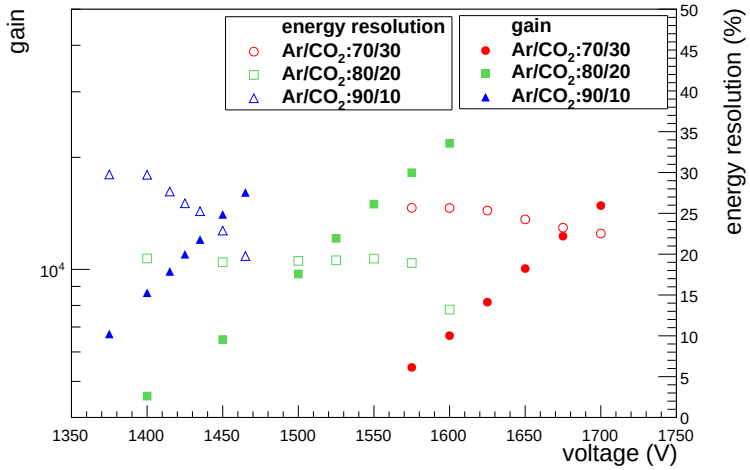

Figure 2.8: Gain and energy resolution as a function of anode voltage for Ar-CO_2 mixtures in the ratio 70/30, 80/20 and 90/10.

detector depends significantly on the ratio of temperature and pressure, (T/p) [63]. The dependence of the gain (G) of a gaseous detector on absolute temperature and pressure is given by the relation,

$$G(T/p) = Ae^{(B\frac{T}{p})} \tag{2.4}$$

where the parameters A and B are to be determined from the correlation plot.

The variation of the gain as a function of temperature and pressure was also studied for the straw tube detector from the energy spectrum obtained using the same Fe^{55} source with Ar/CO_2 gas in 70/30 ratio [78]. The parameters A and B were obtained by fitting the gain vs T/p correlation plot with the function in Eqn. 2.4. The value of the parameters were 854.7 ± 3.305(A) and 0.0079 ± 1.284 × 10^{-5} (B) atm pr/K respectively.

The uniformity of absolute gain and energy resolution of the straw tube detector was also studied [78]. It was found that the gain has 0.8% fluctuation along the length of the wire, while the energy resolution has 1.4% fluctuation, ignoring the values at the edges of the straw tube.

2.5 Study of timing properties

Since straw tubes may be used for tracking in several upcoming high energy physics experiments it is also important to study their timing properties. The time resolution of a gaseous detector depends on the gas mixture and the applied voltage or electric field of the detector. It is actually the measure of the fluctuation in the time required for the electrons to drift along the electric field lines towards the anode wire. For wire chambers, the time resolution is usually of the order of a few *ns*.

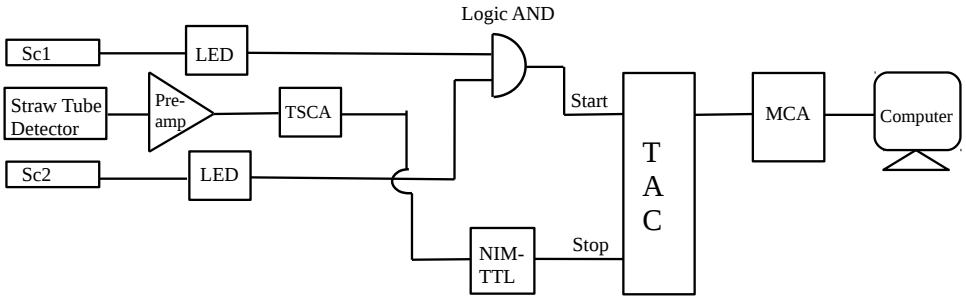

Figure 2.9: Schematic of the electronics setup for time resolution measurement of the straw tube detector.

The time resolution of the straw tube detector was measured with a premixed Ar/CO_2 gas in the 70/30 volume ratio. Two plastic scintillator detectors were used to generate the 2-fold trigger signals with cosmic rays. The photomultipliers coupled to the scintillators were biased with a voltage of + 1550 V. The signals from the scintillators were fed to a Leading Edge Discriminator (LED) with a threshold of -50 mV. The 2-fold coincidence signal was used as the 'start' signal for the Time to Amplitude Convertor (TAC). The TAC was set at 10 μs full scale range. The straw

signal after passing through the pre-amplifier was fed to a Timing Single Channel Analyser (TSCA) which gives a TTL logic output. This TTL signal was converted to NIM signal using TTL-NIM adapter module and the NIM output signal was used as the 'stop' signal for TAC. The time difference between the 'start' and the 'stop'

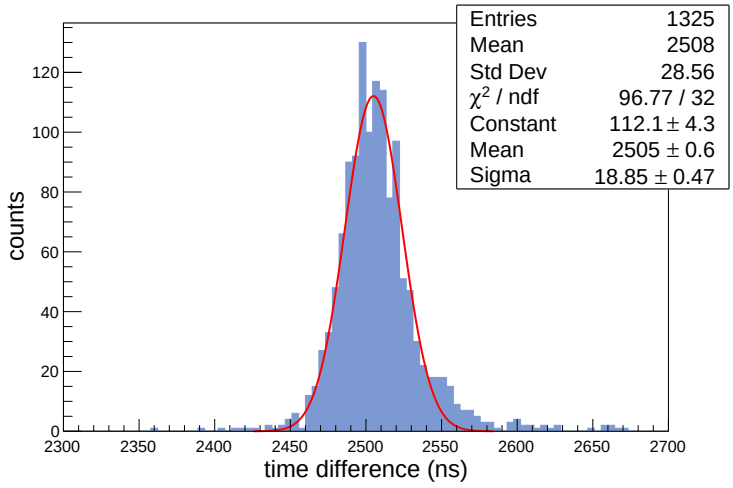

Figure 2.10: Time spectrum of the straw tube detector at 1750 V with Ar/CO_2 70/30 gas mixture.

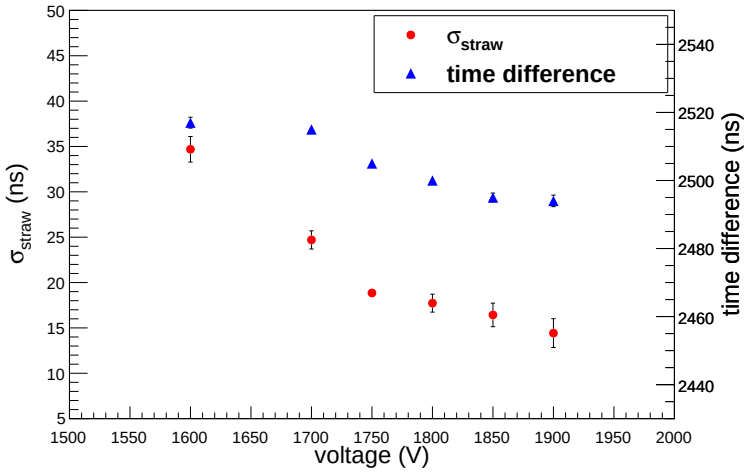

Figure 2.11: Time resolution (σ_{straw}) of the straw tube and mean of difference as a function of voltage.

signal gets converted to amplitude in the TAC and the output was fed to the MCA for obtaining a timing spectrum. The signal from the straw was delayed using long lemo cables connected in between the pre-amplifier output and the TAC 'stop' input. The schematic electronics setup for timing measurement is shown in Figure 4.9. Figure 2.10

shows a typical time spectrum at 1750 V which was fitted with a Gaussian function. The mean of the distribution gives the time difference of the trigger and the straw tube signal. The sigma of this distribution is the effective/combined time resolution of the straw tube and trigger detectors. The time resolution of the straw tube was extracted from the relation:

$$\sigma_{eff}^2 = \sigma_{straw}^2 + \sigma_1^2 + \sigma_2^2 \tag{2.5}$$

where σ_{eff}^2 is the effective time resolution of the combined detector setup, σ_1 and σ_2 are the time resolution of the trigger scintillators Sc1 and Sc2 respectively. The time resolutions of the trigger scintillators were independently measured and the values of σ_1 and σ_2 were found out to be (0.38 $\pm$ 0.01) ns and (0.56 $\pm$ 0.01) ns respectively. The time resolution of the straw tube was measured for different voltage settings. The variation of the time resolution (σ_{straw}) of the straw tube and the time difference between the start and stop signal, as a function of voltage is shown in Figure 2.11. As one can see, the time resolution decreases with the increasing of the voltage. The best achieved time resolution for the straw tube was found to be (14.4 $\pm$ 1.6) ns at 1900 V [80].

2.6 Study of rate handling capability

Most commonly used gaseous detectors in the mid 20^{th} century in HEP experiments were wire chambers. The main factors that limits the use of wire chambers in high energy physics experiments is the rate handling capability and the unavoidable aging effects of these detectors.

There are earlier reports on the rate handling capability of multiwire proportional chambers (MWPCs). The rate handling capabilities of MWPCs having gap of 3mm and wire pitch of 4mm filled with Xe/CO_2 and Ar/CO_2 gas mixtures were measured [81]. It was found that MWPCs can comfortably hold rates above 100 kHz/cm^2. While for straw tubes, the rate handling capability was found to be much better than MWPCs [82]. However, there is not much concrete results that were published in the recent years, to conclude the rate handling capability of straw tubes. There are reports on developing 2-D straws with improved and high rate capability, but the industrial production of such straws are not discussed anywhere, nor maximum rate handling limit is quoted [83]. Overall, there is a lack of knowledge from proper and systematic measurements conducted in laboratory to test the rate handling capability of straw tube detectors. Together with this and the fact that CBM-MuCh will face high particle rates, led to the necessity of testing the rate handling capability of the straws at

rates similar to that in the CBM-MuCh stations. The expected particle rates at the 3^{rd} and 4^{th} station of CBM-MuCh are 15 kHz/cm^2 and 5.6 kHz/cm^2 [84] respectively, for central Au-Au collisions at 10 AGeV with an interaction rate of 1 MHz. To test the performance of the straws at and above these particle rates, the gain and the energy resolution of the straw tube detector was measured varying the rate of incident X-ray photons on the detector using a collimator.

2.6.1 Experimental setup

To measure the rate of incident particle the analog signal from the linear FIFO was put to an amplifier and timing SCA (Single Channel Analyzer). The SCA was operated in integral mode and the lower level in the SCA was used as the threshold to the signal. The threshold was set at 1.3 V to reject all the noise. With 1.3 V thresholds the background count rate and the rate with Fe^{55} source has been found to be 5 Hz and 85 kHz respectively. The discriminated TTL signal was fed to a TTL-NIM adapter and the output was counted using a NIM scalar. The count rate (i.e. counts per second) of the detector was then calculated. To obtain the energy spectrum, one output of the linear FIFO was fed to a Multi Channel Analyzer (MCA).

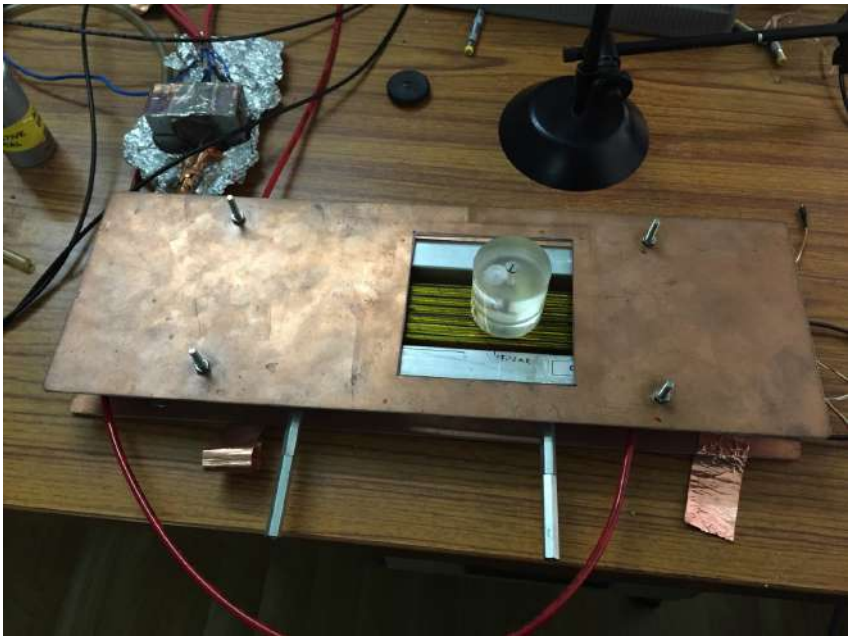

Figure 2.12: The experimental setup for rate handling capability study of the straw tube detector. The transparent cylindrical casing is the perspex collimator holding the Fe^{55} source.

The variation of the gain and the energy resolution of the straw tube detector was measured varying the rate of incident X-ray photons on the detector. A collimator

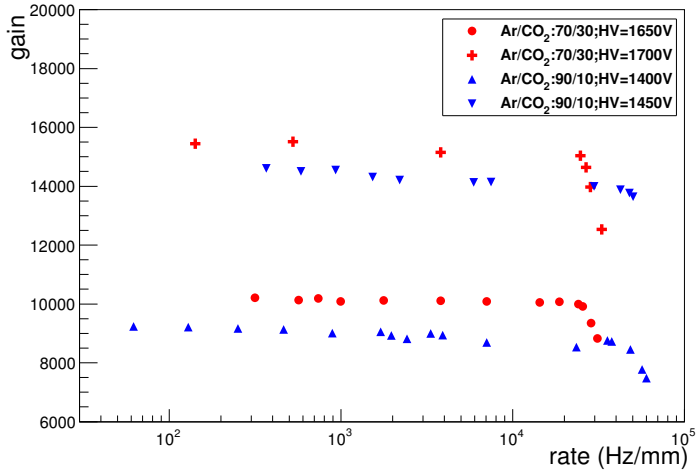

Figure 2.13: Gain as a function of rate for both Ar/CO_2 70/30 and 90/10 mixtures. The error bars are smaller than the symbols.

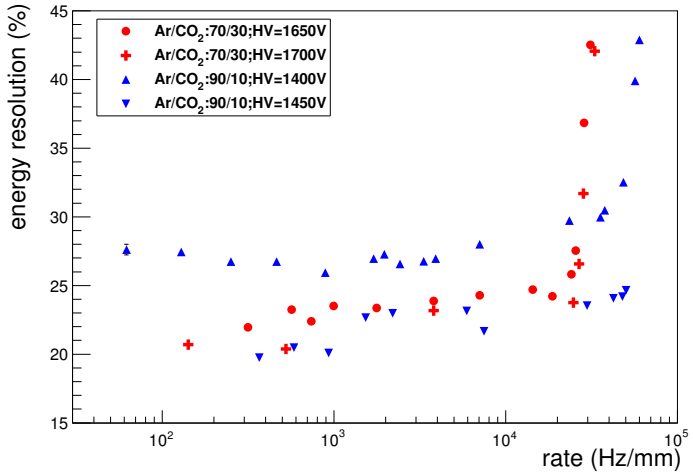

Figure 2.14: Energy resolution as a function of rate for both Ar/CO_2 70/30 and 90/10 mixtures. The error bars are smaller than the symbols.

made with perspex was used for the Fe^{55} source to change the rate of emitted X-ray. The collimator opening was changed to vary the rate of particles incident on the detector. Figure 2.12 shows the experimental setup. The energy spectrum was obtained for each setting of the collimator. These measurements were performed with both Ar/CO_2 70/30 and 90/10 gas mixtures. For Ar/CO_2 70/30 the measurements were performed keeping the HV to the straws at 1650 V and 1700 V whereas for Ar/CO_2 90/10 it was done for HV 1400 V and 1450 V.

2.6.2 Results

For Ar/CO_2 70/30 the gain and energy resolution were measured from a rate of about 200 Hz/mm to about 3×10^4 Hz/mm and that for Ar/CO_2 90/10 were performed for about 100 Hz/mm to about 6×10^4 Hz/mm. Measured gain and energy resolution as a function of X-ray rate per unit length are shown in Figure 2.13 and Figure 2.14 respectively. It was observed that for Ar/CO_2 70/30 the gain and the energy resolution remains constant up to a rate of about 2×10^4 Hz/mm (rate/collimator diameter) or 0.6 MHz/cm^2 [1] (rate/collimator area) then the gain decreases and energy resolution value increases with rate because of space charge effect. Similar effect was observed for Ar/CO_2 90/10 as well, where the gain and energy resolution remains constant up to a rate of about 3.2×10^4 Hz/mm (or 1 MHz/cm^2) [85]. From this it can be concluded that straws are capable of handling the particle rates that are expected at the 3^{rd} and 4^{th} detector station of CBM-MuCh.

For higher rates the gain (G) was fitted with a function [10]

$$G = Pe^{-Q \cdot R} \tag{2.6}$$

where P and Q are the fit parameters and r is the rate.

For higher rates the energy resolution was fitted with a function

$$energy\ resolution = P'e^{Q' \cdot R} \tag{2.7}$$

where P' and Q' are the fit parameters and R is the rate.

The numerical values of P, Q, P' and Q' are tabulated in Table 2.1.

Table 2.1: Values of the fit parameters.

Gas mixture Ar/CO_2	Voltage (Volt)	P	Q	P'	Q'
70/30	1650	1.58×10^4	1.86×10^{-5}	4.72	7.07×10^{-5}
70/30	1700	2.75×10^4	2.38×10^{-5}	4.25	6.98×10^{-5}
90/10	1400	1.08×10^4	5.67×10^{-6}	24.77	6.70×10^{-6}
90/10	1450	1.53×10^4	2.26×10^{-6}	21.41	2.71×10^{-6}

For Ar/CO_2 70/30 gas mixture the detector was operated at relatively higher volt-

[1] Unit conversion from Hz/mm to MHz/cm^2 was done by multiplying a factor of $\frac{d*10^2}{\pi.(d/2)^2.10^6}$

ages and in this case decrease of gain with rate started at relatively lower rate [85].

2.7 Aging tests with Ar/CO_2 gas mixture

Earlier studies on straw tubes filled with a $Xe/CF_4/CO_2$ or Ar/C_2H_6 gas mixtures have revealed gain degradation when exposed to X-ray radiation of fluxes 10^4-10^6 X-rays/sec [51, 60, 64, 65]. As far as CO_2 is concerned, it is believed to be an aging resistant gas unlike other organic gases that are mixed with noble ones to quench secondary photons. Pure Ar/CO_2 gas showed stable operation for gaseous detectors up to ~ 1 C/cm [60–62], while some reports showed unexplained gain reduction in drift chambers and proportional counters filled with this gas [67,68]. Since this observation needed further investigations, so this issue was addressed in this work. The straw tube detector was operated under conditions as close as possible to the real environment of high energy physics experiments in terms of total charge accumulated on the detector over its lifetime. For minimum ionizing particle (MIP) the charge accumulated (Q) [2] along the length in the straws at the 3^{rd} station of MuCh for three months of operation was estimated to be 8.6 mC/cm, which sets the goal for aging studies.

2.7.1 Stability test of straws : Experiment I

The main goal of this experiment was to measure the gain of the straw tube detector continuously at finite intervals in order to study its variation with increasing exposure time of radiation. Since the gain of a gaseous detector has a dependency on ambient temperature and pressure [63], their correlation with gain variation was also checked [86].

Experimental set up

The same schematic setup shown in Figure 2.4 is used for this experiment. A typical energy spectra for Fe^{55} in Ar/CO_2 80/20 mixture at 1550 V is shown in Figure 4.12. The gain of the straw tube was found to be 1.4×10^4 at 1550 V and uniform along the length of the detector. In order to study the effect of a prolonged irradiation of the detector, a collimated X-ray source (activity 3.7 GBq) was placed on top of the detector and a continuous monitoring of the energy spectra was carried out. The collimator was set in such a way that 4 mm length of the straw was irradiated with realistic particle rate in the detector of 40 kHz/mm. The spectra were stored automatically at regular

[2] Q=number of primary × electronic charge × gain × rate × straw diameter × time = 60 e × 10^4 × 15 × 10^3 Hz/cm^2 × 0.6 cm × 10^7 s

intervals of ten minutes. A data logger [79] made in house was used to record ambient temperature and pressure online.

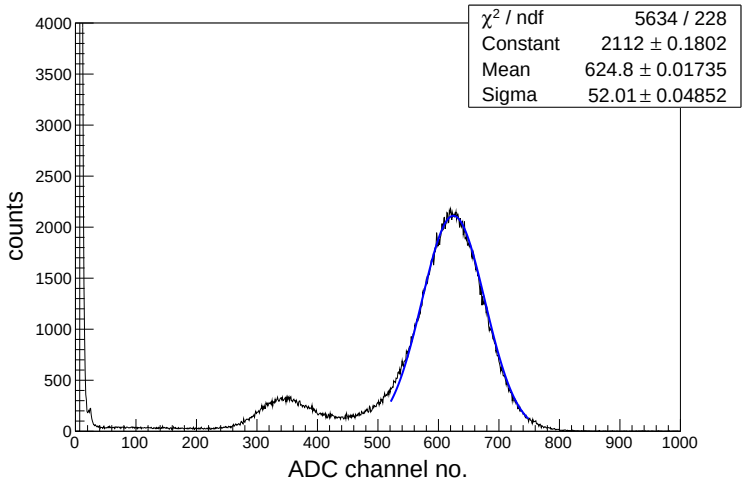

Figure 2.15: Typical energy spectrum for X-rays from Fe^{55} source in Ar/CO_2 gas mixture of 80/20 volume ratio at 1550 V. The main peak is fitted by a gaussian function shown in blue line.

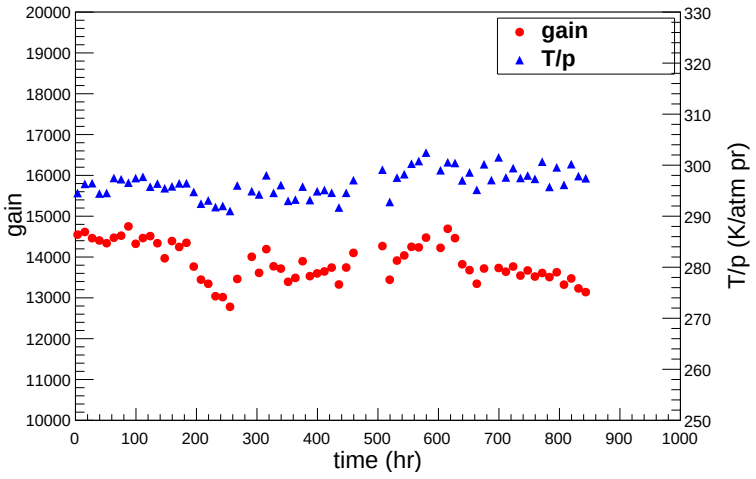

Figure 2.16: Gain and T/p as a function of time. The bias voltage of the straw tube detector is 1550 V. Error bars are smaller than the marker size.

Results

The gain of the straw tube was measured at regular intervals as mentioned earlier. The gain as a function of time is shown in Figure 2.16 along with the variation of the ratio of ambient temperature (T=t+273 K) and pressure (p) with time. The average relative

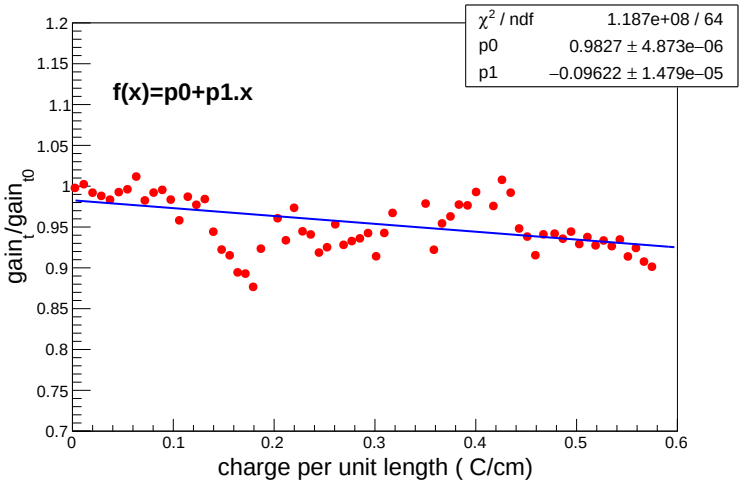

Figure 2.17: Ratio of instantaneous gain and initial gain (normalised gain) as a function of charge accumulated per unit length.

humidity during the measurement was found to be $\sim 55 \pm 5$ %. From Figure 2.16 it can be seen that during a period of more than 800 hrs, the gain decreased from 15000 to 13000. This may be the effect of the prolonged irradiation. Figure 2.18 shows the variation of the energy resolution with time. In this experiment, it was observed that the energy resolution increases from an initial value of 20% to a final value of 21% at the end of the measurement. The rate of aging was parameterized as a normalized gas gain loss:

$$R = -\frac{1}{G_0}\frac{dG}{dQ} \times 100\% \; per \; C/cm \tag{2.8}$$

where G_0 is the initial gas gain, dG is the loss of gas gain after collected charge dQ per unit length. To evaluate the aging rate, the instantaneous gain (gain_t) was normalized by the initial value of the gain (gain_{t0}) and plotted it against charge accumulated per unit length of the straw tube detector as shown in Figure 2.17.

The charge accumulated at a particular time was calculated by

$$\frac{dq}{dL} = \frac{r \times n \times e \times G \times dt}{dL} \tag{2.9}$$

where, r is the measured rate in Hz incident on a particular length of the detector, dt is the time in second, n is the number of primary electrons for a single X-ray photon, e is the electronic charge, G is the gain and dL is the irradiated length. In this case the straw tube was continuously irradiated for more than 800 hrs leading to a charge accumulation of 0.6 C/cm. As shown in Figure 2.17 the normalized gain was fitted by a 1^{st} order polynomial function. The slope p1 of this function corresponds to the

aging rate which resulted to be 9.6 % per C/cm. However, this observation needs a confirmatory test to ensure that this is purely due to the irradiation and not to other external effects. It can be seen from Figure 2.16 that the variation of gain depends on variation in T/p. Although there was not much variation in T/p values throughout the experiment, still a correlation of gain with T/p was drawn and is shown in Figure 2.19. It was seen from Figure 2.19 that the points are scattered and so the χ^2/NDF of the fit was bad. Therefore, it can be said that there are other parameters also in addition to T/p, responsible for the variation of gain.

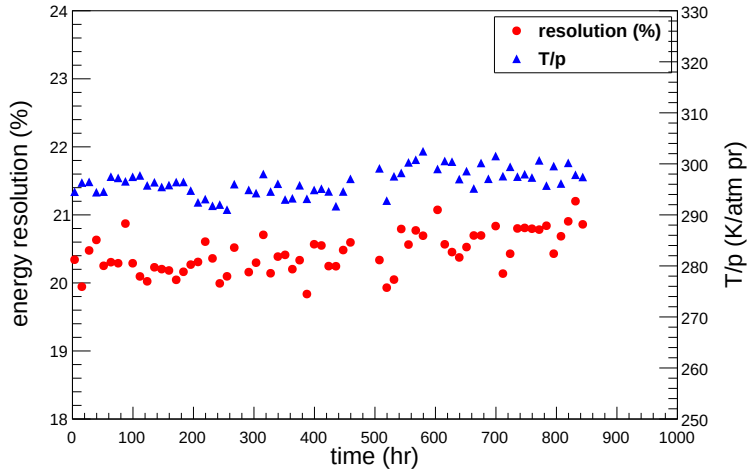

Figure 2.18: Energy resolution and T/p as a function of time. The bias voltage of the straw tube detector was 1550 V.

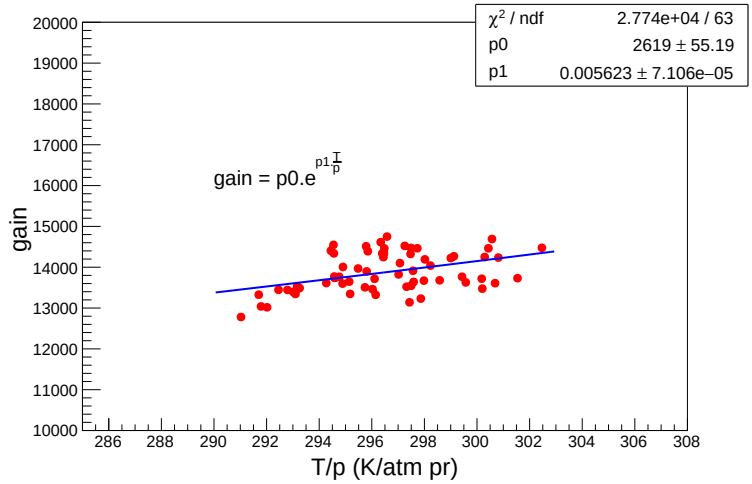

Figure 2.19: Correlation between gain and T/p. Error bars are smaller than the marker size.

It is known that aging of gaseous detectors strongly depend on total accumulated charge [87]. Apart from that, the aging rate is affected by macroscopic parameters such as, high gas gain, radiation intensity and gas flow rate. In that direction, the next experiment was carried out with high radiation intensity and low gas flow rates to observe aging rates for straw tube in a practically lesser amount of time.

Figure 2.18 shows the variation of the energy resolution with time. In this experiment, it was observed that the energy resolution increases from an initial value of 20% to a final value of 21% at the end of the measurement [86].

2.7.2 Stability test of straws : Experiment II

The goal of the second experiment was to verify whether the degradation in the gain of the straw tube detector was purely due to high irradiation or not. To this end, two detectors were positioned adjacent to one another. The idea was to use one straw as a reference detector (marked as R) and the other one (marked as A) for the study of aging effects subjected to a much higher amount of accumulated charge with respect to reference one. To study the performance, gain and energy resolution of both the straws were measured continuously and simultaneously at equal intervals of time [80].

Experimental setup

An identical experimental setup as mentioned in Section 2.7.1 was used to measure the gain and the energy resolution of both the straws. The detectors were connected to the same gas line such that any external factors affecting the performance of the straws cancel out when the ratio of any measured quantity of the two straws such as gain or energy resolution is taken. The same Fe^{55} X-ray source was used to irradiate both the straws. The radiation over straw R was purposely kept at low rates just to use it as a reference detector to monitor the gas gain continuously and compare at fixed time intervals with the gain of straw A. The counting rates in the straw tubes A and R, adjusted by using a perspex collimator, amount to 35 kHz/mm and 0.09 kHz/mm, respectively. The biasing voltages of the detectors A and R were kept at 1550 V and 1450 V respectively. The reference detector R was operated at low gains $\sim$6000 and lower radiation, whereas the straw tube A was operated at high gains $\sim$13000. This was done to achieve a higher amount of accumulated charge on straw A in comparatively lesser amount of time and to minimize the amount of charge accumulation on R. So the expectation was that the ratio of the gains of the two straws normalize all the effects due to external factors such as ambient temperature, pressure, relative humidity and gas flow rate. The energy spectra from both detectors were simultaneously stored at regular intervals of time through two separate MCA modules.

The detector characteristics such as gain and energy resolution were extracted from the Fe^{55} X-ray spectra using the same method as discussed in Section 2.7.1.

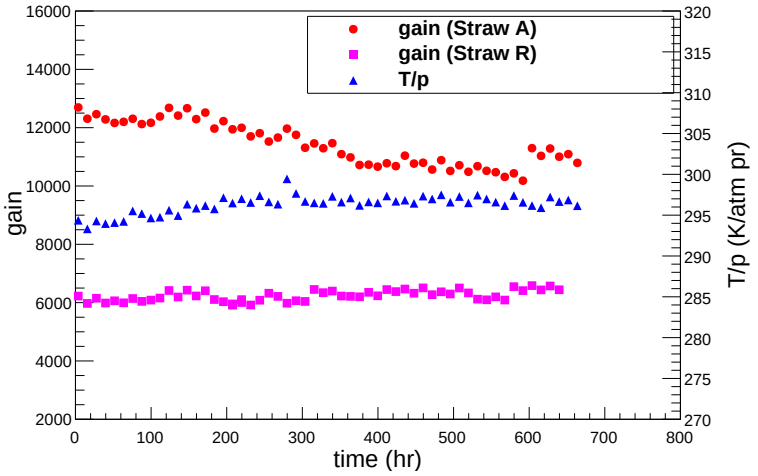

Figure 2.20: Gain and T/p as a function of time of the straws A and R biased at 1550 V and 1450 V respectively.

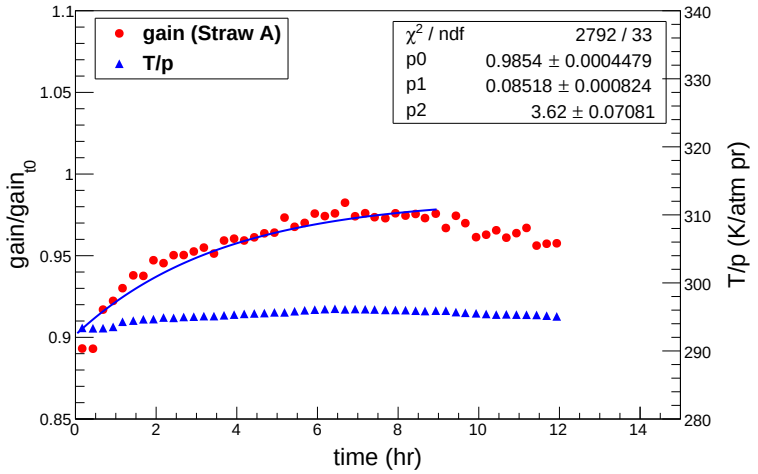

Figure 2.21: Normalised gain and T/p as a function of time (here t=0 hr means t=100 hr of the actual measurement).

Results

The variations over time of the gain and the energy resolution, as well as the ones of T/p, are plotted in Figure 2.20 and Figure 2.23 respectively. As one can see in Figure 2.20, a gradual decrease in the gain of straw A with time was observed with

respect to the straw R. After the first 100 hr of measurement, a decrease of 11 % in the absolute gain was observed at a gas flow rate of 0.02 l/hr. Then the gas flow rate was increased up to $\sim$ 0.13 l/hr in order to check if the gain restores to its original value or not. In Figure 2.21, the normalized gain of straw A, *viz.* the instantaneous gain (gain) over the initial gain (gain_{t0} = 13000) and T/p is plotted as a function of time from the time instant in which the gas flow rate was increased. The time varying normalized gain was fitted by the function:

$$f(t) = p_0(1 - p_1 e^{-\frac{t}{p_2}}) \tag{2.10}$$

where p_0, p_1 are constants, t is the time in hr, and p_2 is the time constant of the function. From this fit one can see that the gain restores to 96 % of its initial value in 3.62 hrs of continuous gas flow at a rate of 0.13 l/hr. T/p was constant through out this time as can be seen from Figure 2.21 so the gain was not needed to be normalized by the T/p effect. After a few hours, the gas flow rate was again reset to a value $\sim$ 0.03 l/hr and the measurement continued. The high voltage was kept ON and the source was not removed from its original position. Observation was that the gain of straw A continuously decreased from 13000 to 10000 *viz.* 77% of the initial value. Again the gas flow rate was increased to a value of 0.8 l/hr after $\sim$ 600 hr of operation, and an increase in the normalized gain was observed as shown in Figure 2.22. The normalized gain was fitted with the same function as in eqn. 2.10. From the fit it was found that the gain increases from about 80% to 87% of its initial value in a time duration of 3.15 hrs, but the gain did not restore to its original value (gain_{t0}) even after flowing the gas at a high rate for more than 10 hrs. The effect of changing the gas flow rate was also observed for straw R, but this effect was more prominent for the straw A. There was an overall slight increase in the gain of straw R which was due to the increase in T/p with time. For the same reason, there was a decrease in the energy resolution value of straw R from 25 % to 23 % as shown in Figure 2.23. However, it can be seen from Figure 2.23 that the energy resolution of straw A increases from 29 % to 34 % (which is 17 % increment). It should also be noted here that the energy resolution of straw A does not improve with the increasing of the gas flow rate. This may indicate the performance degradation of the straw at high radiation environment.

To understand the effect of the prolonged irradiation on the degradation of the gain of the straw tube detector, the ratio of the gains of the straws was taken and it was normalized by the ratio of the initial gains. As changes in temperature, pressure, relative humidity and gas flow rate will effect both the straws similarly, therefore, the ratio of the two gains can properly express the long term effect of the radiation only on the test straw.

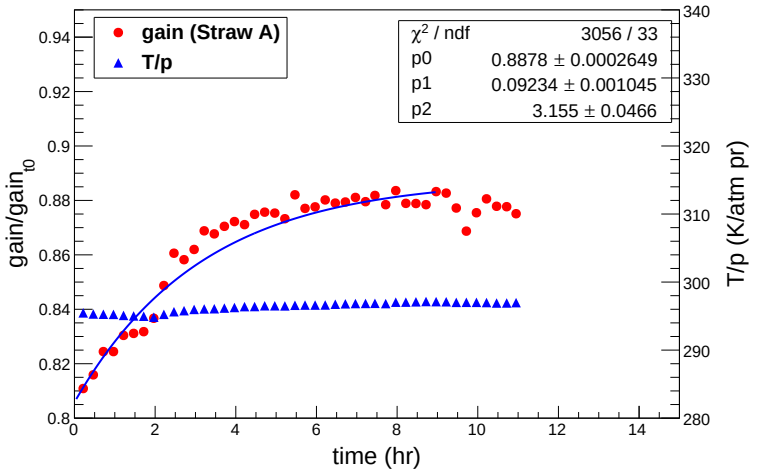

Figure 2.22: Normalised gain and T/p as a function of time (here t=0 hr means t=600 hr of the actual measurement).

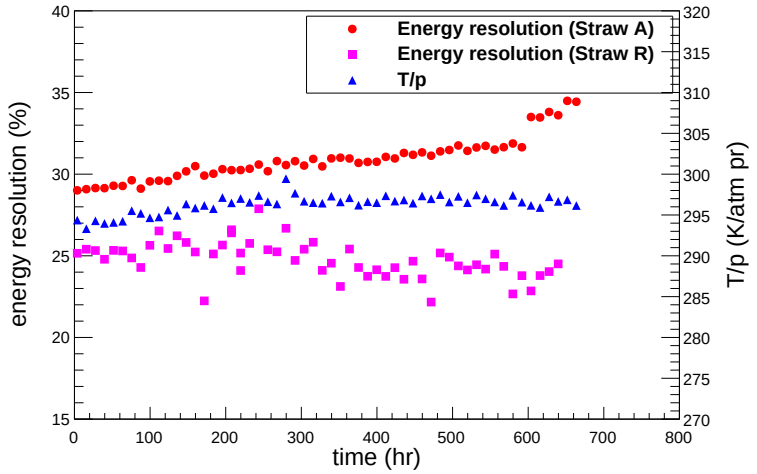

Figure 2.23: Energy resolution and T/p as a function of time for both the straws. The bias voltage of straw A and R were 1550 V and 1450 V respectively.

The normalized ratio was calculated as

$$ratio_{normalised} = \frac{\frac{gain_{strawA}(t)}{gain_{strawR}(t)}}{\frac{gain_{strawA}(0)}{gain_{strawR}(0)}} \tag{2.11}$$

where $gain_{strawA}(0)$ and $gain_{strawR}(0)$ are the initial gains in straw A and straw R respectively. The normalized ratio was fitted by a 1^{st} order polynomial function as shown in Figure 2.24. Here also a negative slope of -1.15 clearly may indicate a degradation of the gain in straw A because of the high rate of radiation and large

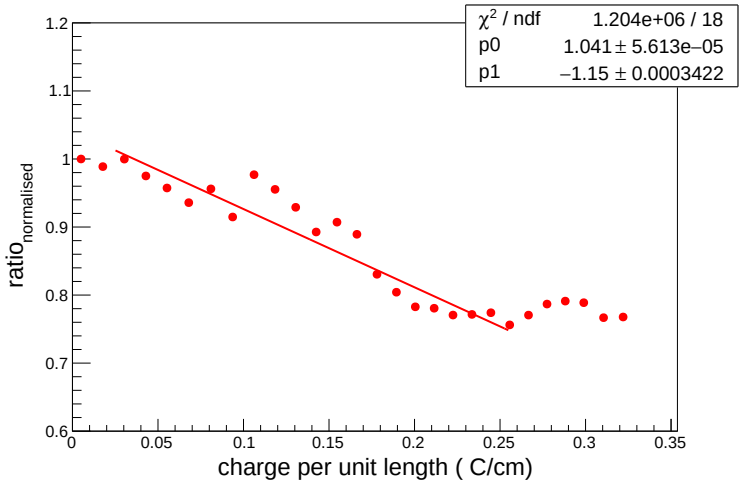

Figure 2.24: Normalised ratio of gains of straw A and straw R as a function of charge accumulated per unit length of straw A.

charge accumulation.

2.7.3 Conclusion of the aging tests

From the first experiment, it can be concluded that the gain reduction by 9.6% per C/cm after a total charge accumulation of 0.6 C/cm wire on the straw might be due to continuous and high radiation intensity. The observed aging rate was small but not negligible. In the second experiment, it was confirmed that the occurred aging was due to the large charge collection and also drawn a conclusion on the dependence of this aging rate on the gas flow rate. It takes about 3 hrs time for the gain of a continuously irradiated straw to partially restore after increasing the gas flow rate. The transient nature of the aging was proven by the fact that the gain tends to restore as one increases the gas flow rate. After a very long term exposure to radiation, one can observe that the gain degrades continuously and it did not restore. The gain did not restore to its initial value even after flowing the gas at a very high rate for a long time. This means that there was some aging due to long term operation of the straw tube detectors which was not observed in case of accelerated aging measurements reported in references [64, 65]. Therefore, this needs further detailed investigation. For Ar/CO_2 gas mixture operated at high rates over long time periods, a gradual decomposition of CO_2 can occur and the resulting pure carbon deposition at the cathode [88]. An important observation in both the experiments were that the gain degradation of the straw tube detector starts immediately from the time of operation under high intensity radiation. The degradation was slow and gradual. The difference between the first and the second experiment was that, the latter was conducted at relatively lower gas flow

rates. Another conclusion that can be drawn from our experiment is that the straw tubes can be safely operated at low radiation intensities ($\sim$ 0.1 kHz/mm) and at low gas flow rates ($\sim$ 0.02 l/h) (as no aging observed in straw R of experiment 2) and at high radiation intensities ($\sim$ 40 kHz/mm) at high gas flow rates (>3 l/h) (since slight gain reduction observed even after 800 hr of operation of the straws in experiment 1). On the other hand it is well known that the Ar/CO_2 mixtures is very robust and do not produce deposits on the wire. So an alternative reason of gain degradation in both experiments might be the use of a gas mixture of low purity (99.9%) and of a polyurethane(PU) tube. There might be diffusion of water vapour through the walls of PU tube. Water vapour does affect the gain, since it modifies slightly the Townsend coefficients, but this effect, if due to leakage, should plateau at some point, and in addition it should not affect the energy resolution. Since, a residual, true degradation was observed, which can only be due to contaminants in the gas, e.g. from material outgassing. To check this in near future the measurements will be repeated with gas having higher purity and using stainless tube for the gas distribution. A systematic study of the aging rates at different radiation intensities, gas gains and gas flow rates will also be carried out in the future to fix the operating conditions of the straws in the real experiment.

Chapter 3

Detector development for the study of cosmic rays

3.1 Introduction

Cosmic rays are high energy particles (mostly protons) that continuously bombard the upper atmosphere resulting in the production of air showers containing various secondary particles such as the charged kaons, pions etc. which decay into muons and neutrinos. Cosmic rays can be classified into two types: (i) galactic cosmic rays (GCR) and extragalactic cosmic rays, i.e., high-energy particles originating outside the solar system, and (ii) solar energetic particles, high-energy particles (predominantly protons) emitted by the sun, primarily in solar eruptions.
Detection and study of cosmic rays is a very active and interesting field of physics since many years. There are numerous experiments located in space and ground to detect these cosmic rays and study their origin and energy spectrum. The detection methods can be classified into two. First, the direct detection of the primary cosmic rays at high altitude by balloon-borne instruments or in space. Second, the indirect detection through the measurements of secondary particles, i.e., extensive air showers at higher energies. There are several experiments for space and balloon-borne detection of air showers. However, the flux of cosmic rays decreases with energy, which limits the scope for space or balloon-borne experiments for the energy range above 1 PeV. Therefore, there are more ground based experiments that have been developed lately for the detection of high-energy cosmic rays.

Cosmic rays of energy more than 10^{14} eV can only be studied through the detection of secondary particles forming extensive air showers (EAS). Section 3.2 discusses the recent research topics in the field of cosmic ray physics and connects to the motivation of our study in this chapter. This chapter focuses mainly on the development of an

air shower array for the study of EAS. EAS are studied by developing large size arrays of detectors spreading over kilometers. For such large scale experiments, the most commonly used detector is scintillators. Since scintillators are easy to fabricate and can be made of any shape and size according to the experiment's requirement, it has become very popular since a very long time. A study of cosmic muons using plastic scintillators at the laboratory of Bose Institute, Kolkata is reported in Section 3.3.
To study the origin, composition and direction of primary cosmic rays, a cosmic ray air shower array was set up at the Darjeeling campus of Bose Institute. Because of the reduced air mass along the line of sight and lower galactic cosmic ray background at Indian mountain altitude station, it is very favourable for the studies for cosmic ray air shower and high energy solar neutron events. In that spirit, a detector array using Plastic Scintillation Detectors (PSD) was built and summoned at the mountains of Darjeeling (27 N, 88 E, and altitude of 2200m above sea level). Air shower arrays are important for the study of the cosmic ray primary spectrum near the "knee", the composition of primaries as a function of energy and the physics of the primary interactions. For the study of cosmic ray air showers, several plastic scintillator modules were fabricated, tested and characterized. Experiment details and observations are included in Section 3.4. This experiment was designed to measure the air shower rate at high altitude and compare the results with air shower stations at similar altitude, but no information on the energy of the cosmic ray muons can be gained. In order to advance in the knowledge of cosmic muon spectrum and measure the cosmic ray muon energy, another experimental setup has to be made. A feasibility study to track and measure the energy of cosmic ray muon was performed using GEANT4 and the simulation results are presented in Section 3.5.

3.2 Overview of recent research in Cosmic Rays

Cosmic rays were discovered in 1912 by Victor Hess, who conducted an experiment in a balloon at an altitude of 5 km. His observation that ionization of air strongly increases with altitude, led to a conclusion "a radiation of very high penetrating power enters the atmosphere from above". Afterwards several other scientists tried to repeat this experiment with improved detection technology to understand the origin and find out the energy spectra of cosmic rays. During the following several decades, cosmic ray research concentrated on the 'highly energetic cosmic rays' because it was not known what processes in the cosmic world could produce it. Before the accelerators were invented, many new particles were discovered in experiments detecting cosmic rays by studying the interaction of cosmic rays with matter.

Even after 100 years of the discovery of cosmic rays, there is no solid theory of its origin. A large number of experimental programs all over the world [89–93] are studying the characteristics of cosmic rays to answer the questions about the origin, composition and structures in the energy spectrum of primary cosmic rays. One of the most important topic of research in the recent times is the measurement of the cosmic ray composition in the "knee" region [94–97]. The cosmic ray spectrum is a power law spectrum with a power index of 2.7 up to energy of 100 TeV. It features two transition regions where the slope changes. The power index changes to 3.1 at about 4×10^{15} eV. The interesting thing to observe in the primary cosmic ray spectrum is that, the primary cosmic ray flux at 100 GeV is 16 orders of magnitude higher than the flux at 10^{11} GeV. The region in the spectrum between 10^6 to 10^7 GeV where the cosmic ray spectrum becomes steeper, is called the 'knee' region. Below the knee region, the flux decreases by a factor of 50 when the energy is increased by a factor of 10. At higher energy the spectrum becomes flatter and this region is called the 'ankle'. It is believed that the cosmic rays below the knee region are accelerated at supernova remnants [41], the particles of energy between the knee and the ankle is from some other galactic sources, and the highest energy cosmic rays are of extragalactic origin. The only possible way to detect these particles above the knee region is with the help of cosmic ray air shower arrays [43–46].
The second important topic is the end of cosmic ray spectrum. This is the region where there is only 3 particles per square km per steradian per century. To detect such particles, there are some experiments (Pierre Auger Observatory) [46, 98] having effective detection area of several thousands of square kilometers for good statistics. One interesting idea could be to set up cosmic ray shower detector stations at similar altitude located far from each other (few thousand kms apart) and look for coincident shower events. This idea is followed up in Section 3.4, where the development of air shower array in Darjeeling is discussed in detail. The main goal of this work was to measure the air shower rate at high altitude and compare the results with GRAPES [44] (at similar altitude).

3.3 Detection of Cosmic Ray Muons with Plastic Scintillators

This section is devoted to the cosmic ray experiments performed at the cosmic ray laboratories at Bose Institute, Kolkata. At the detector laboratory of Bose Institute, Kolkata, fabrication and characterization of Plastic Scintillation Detector (PSD) was

done for the study of cosmic ray muons. These studies include time variation and energy deposition of cosmic ray muons in PSD. The section begins with a brief introduction and working principle of scintillators (Section 3.3.1). The characterization of the PSDs is included in Section 3.3.2. The calculation of energy deposition by cosmic muons in PSD can be found in Section 3.3.3. The time variation and angular variation of cosmic ray muons at sea level is given in Section 3.3.4.

When a cosmic ray primary particle such as proton impacts atomic nuclei in the upper atmosphere, pions are created. These pions decay within a relatively short distance (few meters) into muons, and muon neutrinos. The muons from these high-energy cosmic rays travel at a speed very close to that of the speed of light, in the same direction as the original proton. Because of the time dilation effect of special relativity, the cosmic ray secondary muons (from the viewpoint of the Earth) does not decay before reaching the Earth's surface, since in the Earth frame the muons have a longer half-life due to their velocity. Otherwise, their lifetime without relativistic effects would allow a half-survival distance of only about 456 meters (2.197 μs $\times$ ln(2) $\times$ 0.9997 $\times$ c) at most (as seen from the Earth). Muons, being leptons can easily penetrate matter (hadrons) without much interaction, which makes them detectable on the Earth's surface and also deep underground and therefore they form a major part of the natural background ionizing radiation. For the detection of muons, plastic scintillators are most commonly used. Scintillators are materials that are able to convert the energy deposited by high energy particles into photons of near visible region. Scintillators can be of gaseous, liquid or solid form and could be either organic or inorganic. So, the scintillating material converts the collision energy into photons, which is accepted, converted into electrons and multiplied by the photomultiplier tube (PMT) for measuring the signal. The requirements that a scintillator detector should have are:
1) Transparency to its fluorescent radiation.
2) High efficiency for conversion of exciting energy to fluorescent radiation.
3) Emission in a spectral range consistent with the spectral response of existing photomultipliers.
4) Short decay constant.

3.3.1 Plastic Scintillation Detector

Plastic scintillator is a device consisting of a scintillating material coupled with a photomultiplier to convert scintillation light into electrical signal that can be recorded and counted. Plastic scintillators have vast application in high-energy physics and cosmic ray experiments because of several reasons. First, it offers an extremely fast signal, which makes it perfect for triggering purposes. Second, they are flexible, which means

that they can be made of small (finger size) to large (meters) in dimension as per the experiment design. Third, they are reliable, robust, and convenient to use.

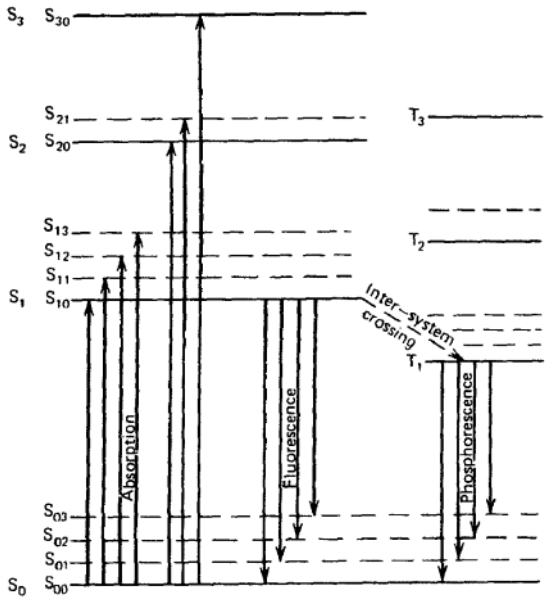

Figure 3.1: Energy levels of an organic molecule with π-electron structure. Picture is taken from Refs. [99]

The mechanism of scintillation can be explained as follows. A charged particle traversing these plastic material leaves behind some excited molecules. Certain types of molecules, however, will release a small fraction (about 3%) of this energy as optical photons. This scintillation process, is especially marked in those organic substances which contain aromatic rings, such as polystyrene (PS) and polyvinyltoluene (PVT). The organic scintillators have a organic molecules possessing certain symmetry properties which gives rise to special electronic energy structure called the π-structure. A schematic of the π-electron structure is shown in Figure 3.1. The electron residing in the ground state (energy level S_0) can absorb energy and jump to any of the excited states. There are a series of Singlet states S_0, S_1, S_2,... and Triplet states T_1, T_2, T_3,... The spacing between S_0 and S_1 is around 3 or 4 eV, but the spacing between higher energy levels are much lower. There are also some finer vibrational energy levels with energy gap of 0.15 eV. When the electron jumps to any of the higher energy states S_2, S_3 or higher, it quickly de-excites to the state S_1 through radiation-less internal conversion. The electron can also suffer vibrational energy losses. Therefore, the overall effect of the excitation process in case of organic scintillators is that there will be a sudden population increase in the S_{10} state, and when all the electrons de-excite to S_0 levels, prompt fluorescence (or scintillation light) is emitted. There can be an inter-system crossing from singlet to triplet state, which further results in a delayed

light emission called the Phosphorescence.

A scintillator detector has three main components:

1) Scintillator material

2) Light guide

3) Photomultiplier tube (shown in Figure 3.2)

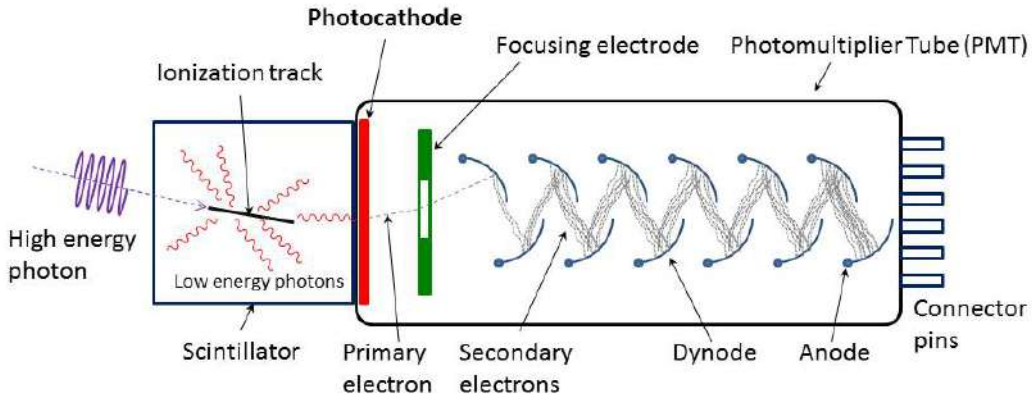

Figure 3.2: Schematic diagram of a scintillator and photomultiplier tube

Photomultiplier Tube

Photomultiplier tubes (PMTs) are devices which convert light into a measurable electric current. They are extremely sensitive. Figure 3.2 shows a schematic diagram of a typical photomultiplier. It consists of a photosensitive material made cathode followed by an electron collection system, an electron multiplier section (or dynode string) and finally an anode from which the electronic signal can be collected. All the parts are usually housed in an evacuated glass tube. When high voltage is applied to the cathode, dynodes and anode, a potential "ladder" is set up along the length of the cathode - dynode - anode structure. When a photon (produced in the scintillator material) enters through the glass window and falls on the photocathode, it emits an electron via the photoelectric effect. The presence of the applied voltage, causes the electron to accelerate and directly move towards the first dynode, where upon striking, it transfers

some of its energy to the electrons in the dynode. This causes secondary electrons to be emitted from the dynode surface, which are accelerated towards the next dynode where more electrons are released and further accelerated. Thus, an electron cascade down the dynode string is created. On collection of the cascade of electrons at the anode, a current is generated which can be measured by suitable electronics.

3.3.2 Characterization of plastic scintillators

The material for the plastic scintillators used in our study is an organic substance which contains aromatic rings, such as polystyrene (PS) and polyvinyl-toluene (PVT) as its base and contains 65% anthracene. The light output of this material is 65%. Light guides were used for guiding light from scintillator to the PMT. The material of the light guide was chosen to be plastic having similar refractive index of BC400 so that the transmitted light absorption is minimum. The details of the plastic scintillator and fabrication process is explained in the Refs. [78].

One BC400 type scintillator plate of dimension 40 cm $\times$ 40 cm and thickness 1 cm was procured and was cut into several small pieces to build scintillator detectors. 3 plastic scintillator paddle detectors having dimensions 20 cm $\times$ 20 cm (Sc-01), 20 cm $\times$ 19 cm (Sc-04) and 10 cm $\times$ 10 cm (Sc-03) was build and characterized for the study of cosmic ray muons. A finger scintillator detector of size 10 cm $\times$ 2 cm (Sc-02) was also build for triggering a small area.

Experimental Setup

The experimental setup is shown in Figure 3.3. Conventional NIM electronics were used in this experiment. The PMT of the scintillator was biased with positive voltage from a High Voltage (HV) NIM module. The signal from the PMT was transferred to the Leading Edge Discriminator (LED) for rejection of noise signals. The signals that passed the discriminator was fed to a Scalar Counter for counting the number of signals in a predefined time window of the counter.

Results

Basic characterization of these scintillators are reported in Refs. [78]. The voltage scan of the scintillators were performed using three different radioactive sources e.g. Cs^{137}, Na^{22}, Co^{60} emitting low energy gamma rays [78]. It was observed that for each sources the count rate increases with voltage and reaches a plateau. The plateau voltage for Sc-01, Sc-03 and Sc-04 is $\sim$ 1600 V, while for Sc-02 it was $\sim$ 1500 V. To reject the low amplitude noise in the PMTs, the threshold of the LED was optimized using the same radioactive sources [78]. A threshold of -50 mV was sufficient to cut off the noise. The

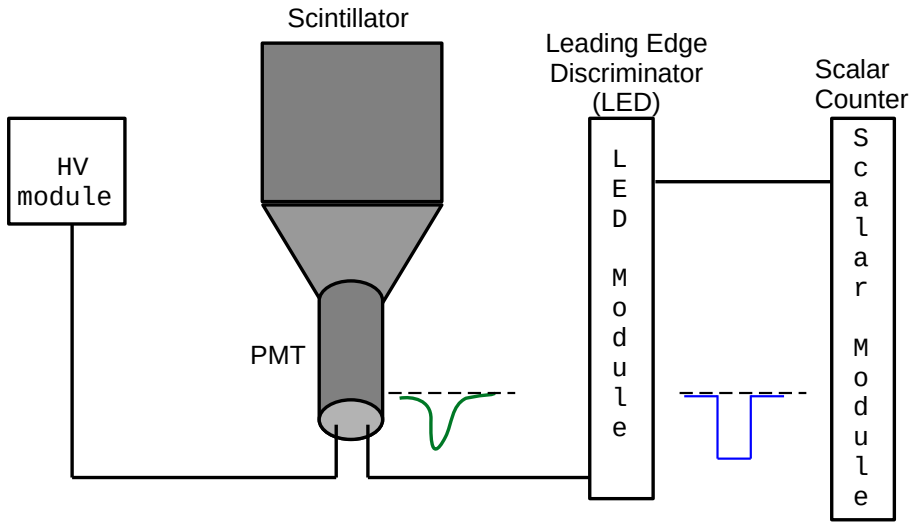

Figure 3.3: Schematic showing the experimental setup for the characterization of a scintillation detector.

noise rate in these detectors was nearly ∼0.12 kHz at a PMT biasing voltage of 1650 V and threshold of -50 mV. The light yield of the scintillators, which was tested using Fe^{55} X-ray source, was uniform in the central region, with a variation of 12 % over the entire surface [101]. The efficiency of the cosmic ray muon trigger setup was found to be 72 % at 1650 V. These scintillators have excellent time resolution ∼ 0.4 ns which was measured using cosmic rays.

3.3.3 Calculation of energy deposition by cosmic ray muons

Typical cosmic ray muons have energy of the order of GeV range. While passing through matter it deposits small amount of energy in it due to interaction. The deposited energy can be expressed the by Bethe-Bloch formula.

$$-\frac{dE}{dx} = 2\pi N_a r_e^2 m_e c^2 \rho \frac{Z}{A}\frac{z^2}{\beta^2}\left[\left(\ln\frac{2m_e\gamma^2\nu^2 W_{max}}{I^2}\right) - 2\beta^2 - \delta - 2\frac{C}{Z}\right] \quad (3.1)$$

According to the Bethe-Bloch formula, the deposited energy is a function of initial energy of the charged particle, which is muons in this case, as shown in Eqn. 3.1. Since the plastic scintillator is a thin media ∼1 cm thickness, the energy loss distribution by a large number of charged particles passing through it will follow a Landau distribution. According to Landau formula the energy loss distribution in a thin media

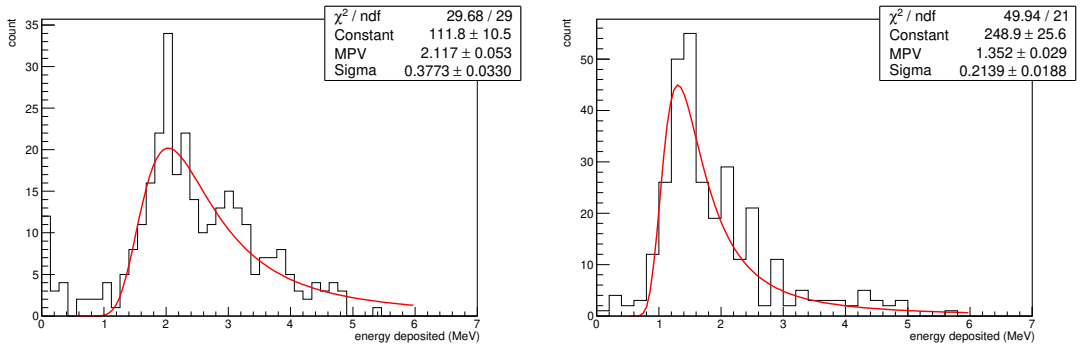

Figure 3.4: Energy deposition distribution of cosmic ray muons in plastic scintillator. Left panel:(a) Scintillator Sc-03 (10 cm × 10 cm). Right panel:(b) Scintillator Sc-04 (20 cm × 19 cm). The distribution was fitted with a Landau function (red curve).

is written as,

$$f(\lambda) = \frac{1}{\sqrt{2\pi}} e^{-\frac{1}{2}\left(\lambda + e^{-\lambda}\right)} \tag{3.2}$$

were λ is an energy variable and represent the normalized deviation from the most probable energy loss $(\Delta E)_{mp}$:

$$\lambda = \frac{\Delta E - (\Delta E)_{mp}}{\xi} \tag{3.3}$$

ΔE is actual loss and ξ be the average energy loss, it is given by first term in Bethe-Bloch equation (Eqn. 3.1).

To obtain an energy loss spectrum of the cosmic rays, the signals from the PMT was sent to the Digital Storage Oscilloscope (DSO). In the quick measure mode, the pulse height can be directly read out from the DSO. Pulse heights from all three scintillators were recorded from the DSO which was triggered by the 3 fold coincidence signal. The trigger was used to confirm a real signal from a cosmic ray particle. The pulse height, fall-time and rise-time of each pulse was used to calculate the energy deposited by muons for a corresponding pulse on DSO. It can be well realised that the energy deposited by muons in the plastic scintillator is directly proportional to the pulse height of the detector signal. A formula was derived specific to the plastic scintillator material BC 400 for obtaining the energy deposition in MeV by cosmic ray muons. The detailed derivation of the formula is included in Appendix I.

From Figure 3.4(a) and 3.4(b), the most probable value (MPV) of the energy deposited by cosmic ray muons in 1 cm thick plastic scintillator was found to be 2.117 ± 0.053 and 1.352 ± 0.029 for detectors Sc-03 and Sc-04 respectively. The MPV is smaller for the case of Sc-04. This does not mean that cosmic ray muons loose lesser energy in Sc-04 than in Sc-03. The scintillation light produced passes through the light

guide before entering the PMT. While passing through the light guide, small fraction of the light can get absorbed because of the properties of the light guide material used in the fabrication process. This absorption will increase with the size of the light guide. Since, Sc-04 is larger in size than Sc-03, and the size of light guide for Sc-04 is also bigger than that of Sc-03, so there are additional energy losses when the scintillation light passes through the light guide.

3.3.4 Measurement of cosmic ray muon at sea level

The cosmic ray muons at sea level come from the decay of pions that are produced in the interaction of primary cosmic rays with the atmosphere. Pions are typically produced at altitudes of 15 km and decay relatively fast to produce gamma or muons depending on whether the pion is neutral or charged. Figure 3.5 shows the cosmic muon intensity as a function of atmospheric depth. At sea level, the muon intensity is $\sim 10^{-2}$ cm^{-2} s^{-1} sr^{-1} which is much higher than the intensity of secondary protons and electrons. For muons in the vertical direction, this value is 1 cm^{-2} min^{-1}.

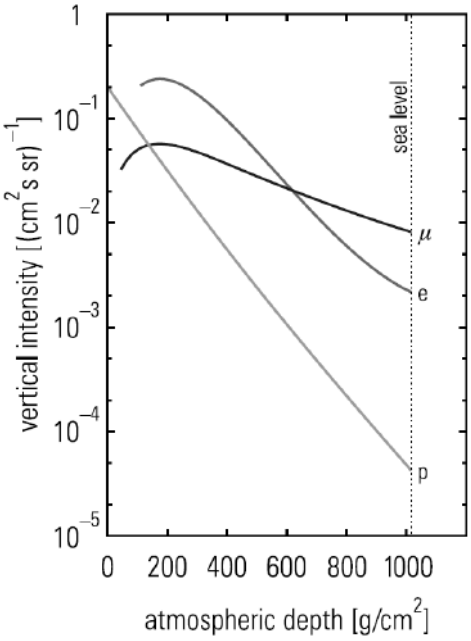

Figure 3.5: Particle composition in the atmosphere as a function of atmospheric depth. Plot taken from Ref. [1]

In the detector laboratory of Bose Institute, Kolkata (altitude = 9 m) the cosmic muon flux was measured using three PSDs. The experimental setup is shown in Figure 3.6. Three PSDs named Sc-01, Sc-03 and Sc-04 were used as the trigger detectors. The PMT voltage was set at +1650 V and threshold at -50 mV of all three scintillators.

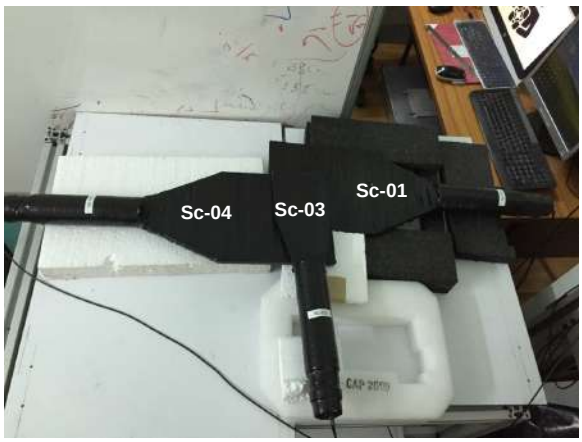

Figure 3.6: Experimental setup for the cosmic muon flux measurement. Three scintillators, Sc-01, Sc-03 and Sc-04 form the trigger system for cosmic ray muons.

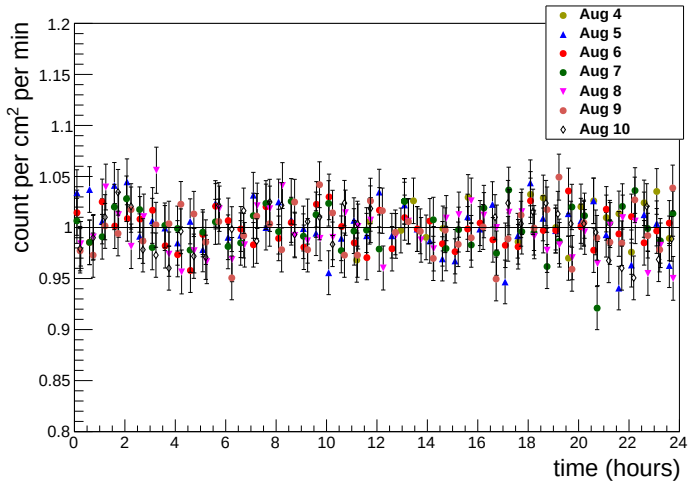

Figure 3.7: Cosmic ray muons count per cm^2 per min as recorded by the trigger system. The plot shows the daily variation of the cosmic muon flux throughtout a week from August 4, 2017 to August 10, 2017.

The three-fold coincidence trigger window was set at 50 ns. The output of the logic AND (three-fold coincidence) was fed to a NIM-TTL converter and the produced TTL signal had a specific amplitude. This TTL signal was fed to a Multi channel analyser (MCA) which was programmable to take continuous data at regular intervals. This method was used to continuously record the cosmic ray muon trigger counts every 15 mins for a duration of one week. Figure 3.7 shows the daily variation of the cosmic muon flux over a week. The count was normalised with the efficiency of the trigger ($\sim$72%). The distribution of muon counts is shown in Figure 3.8. It was found that there is a fluctuation of 0.02 (σ) about the mean value of 1.014 per cm^2 per minute at Kolkata.

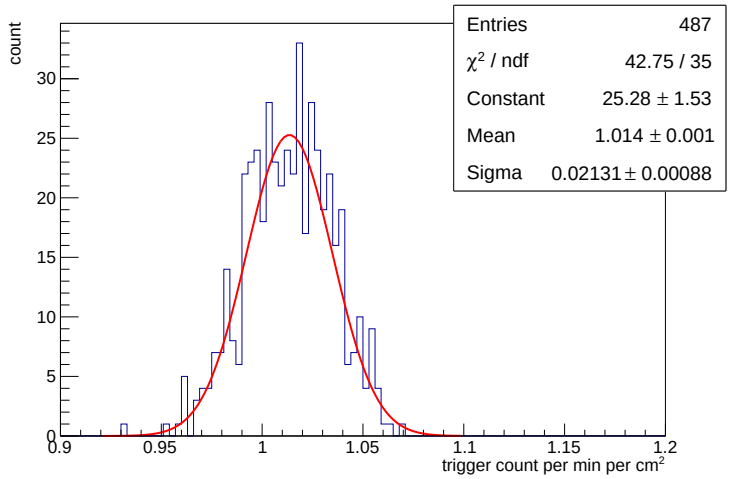

Figure 3.8: Distribution of the cosmic ray muons count per min per cm^2 as recorded by the trigger system for one week.

The vertical cosmic ray muon flux (zenith angle=0°) was found to be $7\times\ 10^{-3}$ s^{-1} cm^{-2} sr^{-1}, which matches with earlier results [42, 102, 103]. The cosmic ray muons arriving at the surface of the Earth has a $\cos^2\theta$ angular dependency on the zenith angle θ [42, 102]. We conducted an experiment to measure the angular variation of cosmic ray flux [101]. This of cosmic ray flux value decreases from $7\times\ 10^{-3}$ s^{-1} cm^{-2} sr^{-1} to $3\times\ 10^{-3}$ s^{-1} cm^{-2} sr^{-1} corresponding to a change in the zenith angle from 0° to 70°.

3.4 Development of cosmic ray air shower array

A large number of experimental programs are trying to answer the questions about the origin and composition of the primary cosmic rays and structures in the energy spectrum of them. Our goal was the study of cosmic rays using ground based measurements at high altitude. In that spirit, an hexagonal array of seven PSDs each of active area 1 m^2 and thickness of 1 cm, was built at Darjeeling (27^o 3' N 88^o 16' E, 2200m above sea level) to study the cosmic ray air showers in the Eastern Himalayas. The objective was to measure the shower rate at Darjeeling which has the same altitude as of Ooty (experimental site for GRAPES [44]) within few meters, so that any observation at Ooty could be compared with that in Darjeeling. Another motivation for this experiment was that, there was no air shower measurement between AGASA [104] in Japan and GRAPES in Southern India. So another measurement in Darjeeling would strengthen the baseline for any observation. Moreover, two air shower arrays at a distance but at almost similar altitude would be useful in search of correlated air showers.

Figure 3.9: Construction of PSD modules: (Top left) WLS fiber insertion, (Top right) Voltage divider network, (Bottom left) HV cable connected in proper position, (Bottom right) Closing the box.

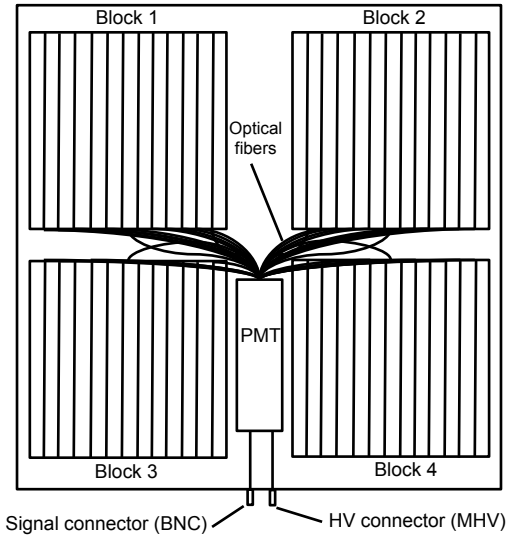

Figure 3.10: Block diagram of a detector module.

Figure 3.11: Typical muon signal at -1500 V (100 mV/Div, 50 ns/Div, 50Ω load).

3.4.1 Characteristics of the detectors

The Darjeeling air shower array has seven elements. Each of the elements of this array is a 1 m × 1 m plastic scintillator coupled with wavelength shifting (WLS) fibers and photomultiplier tube (PMT). The scintillators were indigenously fabricated in the Cosmic Ray Laboratory (CRL), Tata Institute of Fundamental Research (TIFR), Ooty, India [105, 106].

All 1 m × 1 m scintillators are made of four 0.5 m × 0.5 m blocks of thickness 1 cm. The scintillators are of same type as used in Ref [106]. Circular WLS optical fibers (Kuraray scintillating fiber) were used to connect all the four scintillator blocks to a single PMT. 12 parallel grooves are made in a 0.5 m × 0.5 m block to place the

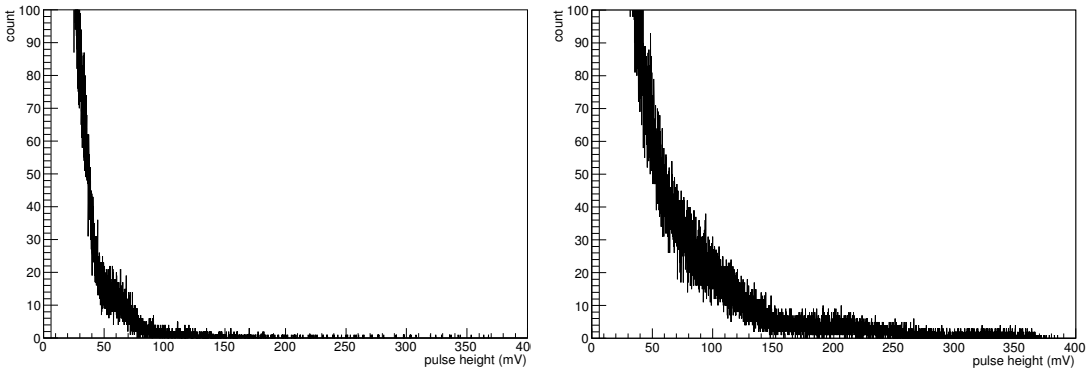

Figure 3.12: Typical pulse height distribution of a scintillator detector at applied voltages of -1500 V and -1725 V.

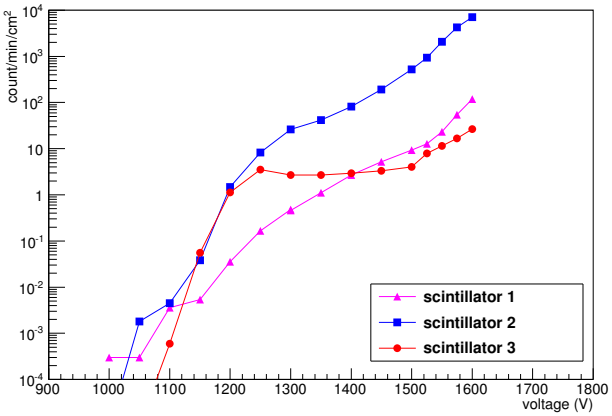

Figure 3.13: Voltage scan of scintillator 1, scintillator 2 and scintillator 3.

WLS fibers. Total 48 fibers from all 4 blocks are collectively coupled optically to a PMT model ETL9807B of diameter 5 cm. A few steps of fabrication of the detector are shown in Figure 3.9. Four scintillator blocks covered by black polyethelene sheets along with the WLS optical fiber and PMT is shown in Figure 3.9. Each block of scintillator was wrapped first with white tyvek sheet and then black polyethelene sheets. The four individual scintillator blocks are optically isolated from each other. The whole system was kept in an aluminum box. The PMT was mechanically fixed and connected to the base circuit. The PMTs was applied a negative high voltage (HV) using MHV cable and a BNC cable was used to collect the signal. The schematic diagram of a detector module is shown in Figure 3.10.

One typical signal from one scintillator detector taken from the oscilloscope is shown in Figure 3.11. The typical signal amplitude was -200 mV and rise time 5 ns at -1500 V as shown in Figure 3.11. Initially the calibration was done for all the PMTs

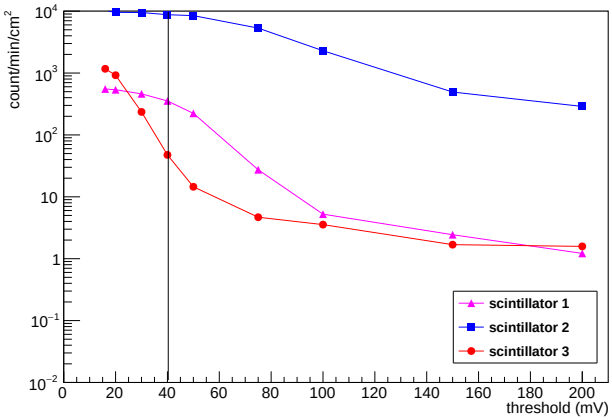

Figure 3.14: Threshold scan of scintillator 1, scintillator 2 and scintillator 3. The X axis label shows the modulus of the threshold.

and their individual efficiencies are measured using other scintillator blocks of same kind. The efficiency study can be found in the next section.

The pulse height distribution of one scintillator detector at applied voltages of -1500 V and -1725 V are shown in Figure 3.12. It is clear from the pulse height distribution that larger pulse height was obtained at higher voltage. The voltage scan plot is shown in Figure 3.13. It was found that the count rate reaches a plateau at a voltage of -1300 V. Keeping the applied voltage constant at -1725 V for all three scintillator detectors singles count rates were measured varying the threshold voltage. The threshold scan plot is shown in Figure 3.14. It was found that -40 mV is enough to cut all the noise. With -40 mV threshold settings the three-fold coincidence of any three such detectors give a cosmic ray muon flux of about 1.2 per min per cm^2.

3.4.2 Experimental set-up

At first, only three detectors were used to detect the cosmic ray shower. The efficiency of these three scintillators were studied with cosmic rays in the following method. To detect the coincidence signal of cosmic ray muon, the scintillators were kept in a vertical stack. The muon detection efficiency of a particular detector from the stack, was measured using trigger from other three modules. The trigger was taken from the three fold coincidence of three scintillators. The trigger width was fixed at 400 ns. The efficiency is defined as the (four fold coincidence)/(three fold coincidence). The results are discussed in Section 3.4.3.

Three scintillator detectors were placed on a horizontal plane (as a preliminary test) to detect the cosmic ray shower. Horizontal stack of three scintillator detectors to measure cosmic ray shower is shown in Figure 3.15. The centres of the scintillator

detector made a triangle of sides 1.9 m, 3 m and 3.5 m respectively. The biasing voltage that was applied to all three PMTs was -1725 V and threshold to the leading edge discriminator module was set to -40 mV. The width of the discriminated NIM signal was fixed at 150 ns for each detector. Measurement of the three-fold coincidence from this horizontal stack of three detectors, which mimics a cosmic ray shower, was carried out for about a period of 1 month. Each reading was taken for one hour duration. The result from long term measurements are discussed in Section 3.4.3.

Figure 3.15: Horizontal stack of three scintillator detectors to measure cosmic ray shower.

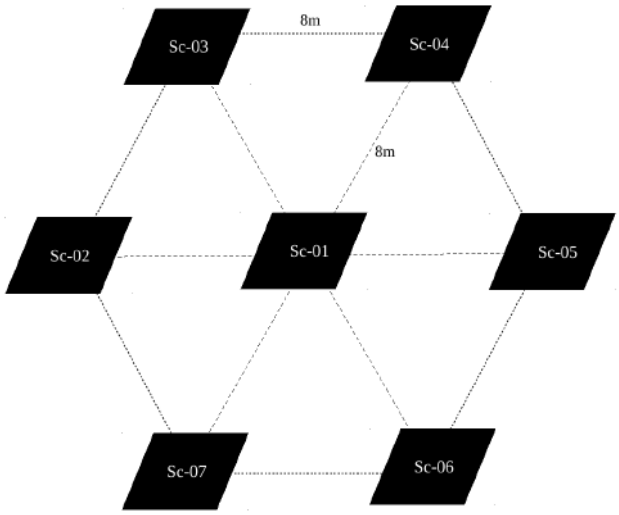

Figure 3.16: Schematic of the air shower array of seven PSDs in Darjeeling.

Figure 3.17: Cosmic ray air shower detector array at Darjeeling.

Shower detection set-up

Six detector modules were placed at the vertices of the hexagon as shown in the Figure 3.16 and one at the center to build a cosmic ray air shower array. The arms of the hexagon were 8 m and the array covers an area of 168 m^2 with an effective detector area of 7 m^2. The configuration of the cosmic ray air shower detector array at Darjeeling is shown in Figure 3.17. All detectors were biased with -1740 V from a single high voltage (HV) power supply using an external HV distribution network. The signals from the detectors were passed through a leading edge discriminator (LED) with a common threshold of -20 mV for all signals to eliminate the noise.
A shower trigger was defined as coincidence signal in the central detector and any two detectors. A custom-built logic module with seven inputs was used to generate a multi-fold trigger. Seven individual signals from the discriminator were fed to the trigger module and the shower trigger was generated when the central detector and any two detectors give signal simultaneously. The large shower was defined as the seven fold coincidence and was also recorded using the customized module. Figure 3.22 shows the schematic representation of the shower logic and seven fold logic. The NIM output from the trigger module was counted using a NIM scalar module. The trigger output was counted for 60 min to get each data point. The data were acquired so far manually. It was observed that in 60 minutes a significant number of counts are accumulated.

3.4.3 Results and discussion

Preliminary air shower array

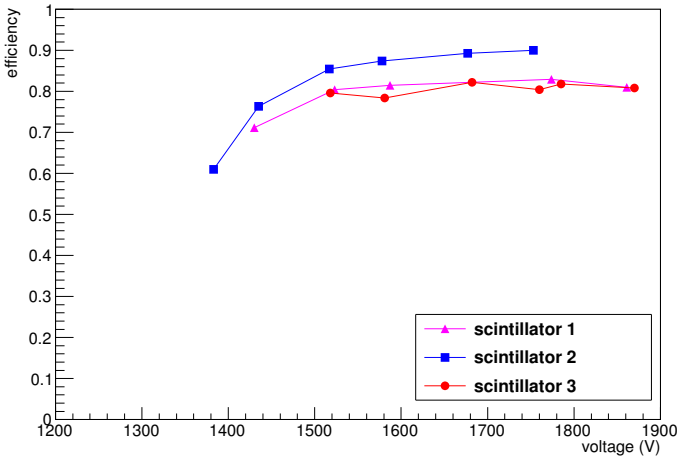

Figure 3.18: Efficiency as a function of applied voltage.

As described in Section 3.4.2 the efficiency of the three scintillator detectors as a function of applied HV was measured and is shown in Figure 3.18. It can be seen from Figure 3.18 that for all three detectors the efficiency reaches a plateau at a value greater than 80% and the voltage regions are nearly same for all modules. The applied voltage was increased till -1850 V to see the efficiency plateau. The value of efficiency is a little different for different modules. This is because of different area coverage of trigger detectors as explained next.

Consider Figure 3.19 showing the experimental setup of the efficiency measurement when the test scintillator was placed above the other scintillators (scintillator 1, 2 and 3). The detectors were placed in a vertical stack for these measurements. Trigger was taken by the coincidence signal of the three detectors (scintillator 1, 2 and 3). In Figure 3.20, the test scintillator was in the middle of the stack of trigger scintillators. In such a case the efficiency measured for the detector, which was placed in the middle of the trigger set-up will give the best result, because as shown in Figure 3.20, the particle that was detected by the trigger scintillators must pass through the test scintillator (in the middle). For other cases, as shown in Figure 3.19, the triggering particle (in this case cosmic muons) passing through all the three scintillators (either placed on top or bottom of the scintillator under test) may leave the system without passing through the test detector, resulting a decrease in efficiency.

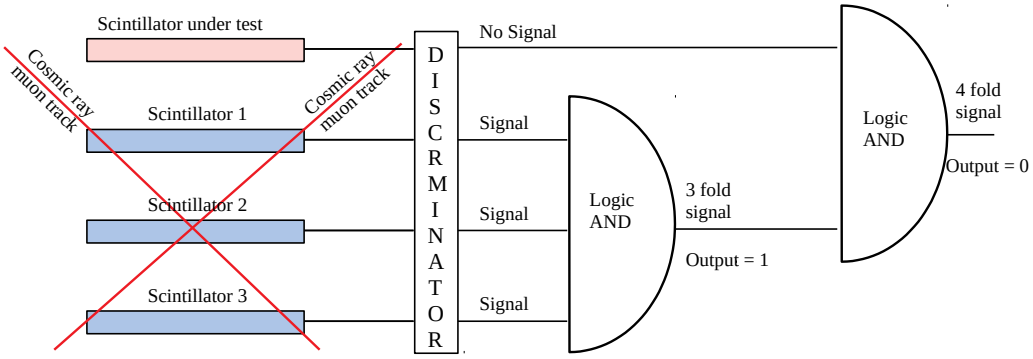

Figure 3.19: Schematic of the efficiency measurement setup of the scintillators. Here the scintillator under test was placed on the top of the trigger scintilators stack (Scintillator 1, Scintillator 2 and Scintillator 3). Figure shows that cosmic muons may pass through the trigger scintillators without passing through the scintillator under test.

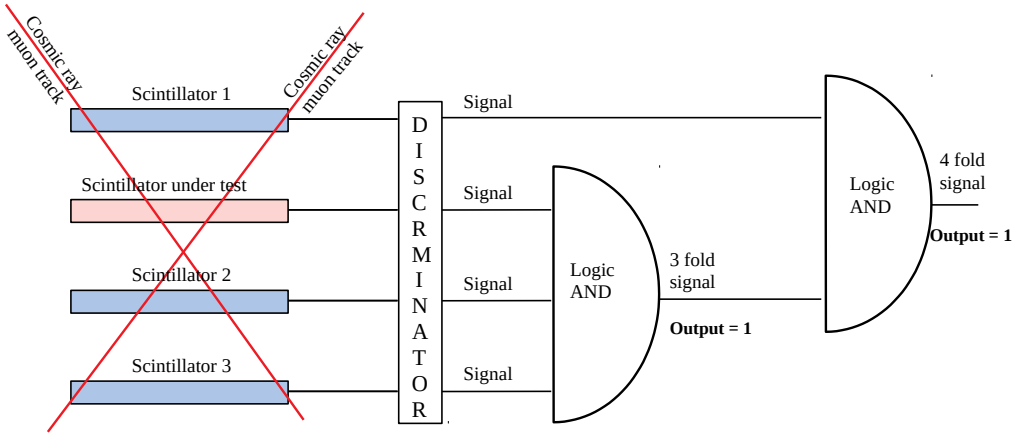

Figure 3.20: Schematic of the efficiency measurement setup of the scintillators. Here the scintillator under test was placed in the middle of the trigger scintilators stack (Scintillator 1, Scintillator 2 and Scintillator 3). Figure shows that cosmic muons passes through the trigger scintillators and the scintillator under test.

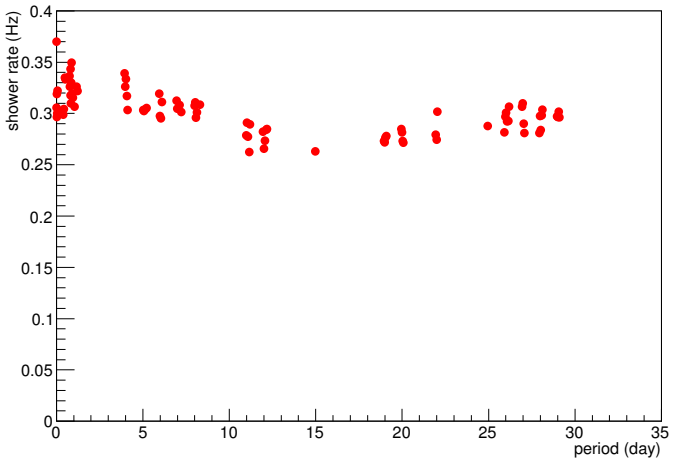

Figure 3.21: Shower rate vs. time during mid November - mid December, 2016.

To determine the preliminary cosmic ray air shower rate, the three-fold coincidence of three scintillators placed horizontally was demanded as stated in Section 3.4.2. PMT voltage of -1725 V was applied to all three detectors and the cosmic ray shower signals were counted for a period of one month during the middle of November to middle of December, 2016. The result is shown in Figure 3.21. It was observed that the shower rate varies with time within the range 0.25-0.35 Hz in this period.

The final air shower array

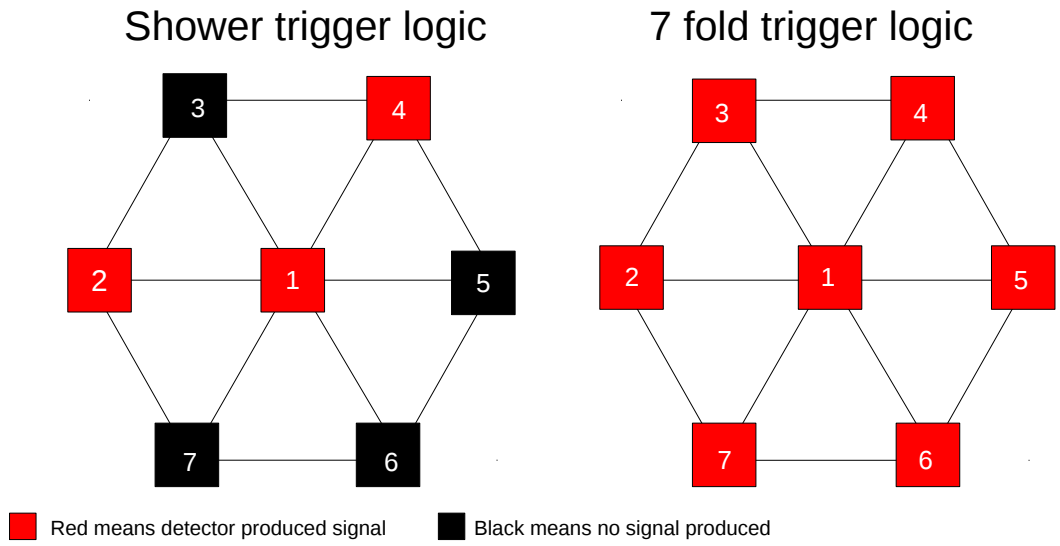

Figure 3.22: Diagram explaining the shower logic and seven fold logic of the air shower array in Darjeeling.

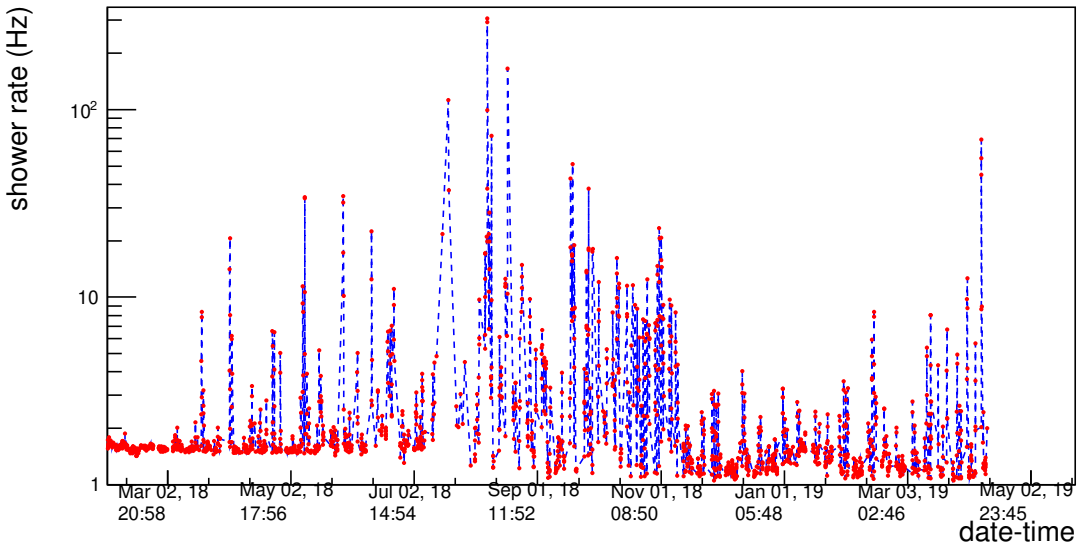

Figure 3.23: Cosmic ray air shower rate as a function of date and time. Error bars are obscured by the marker symbols.

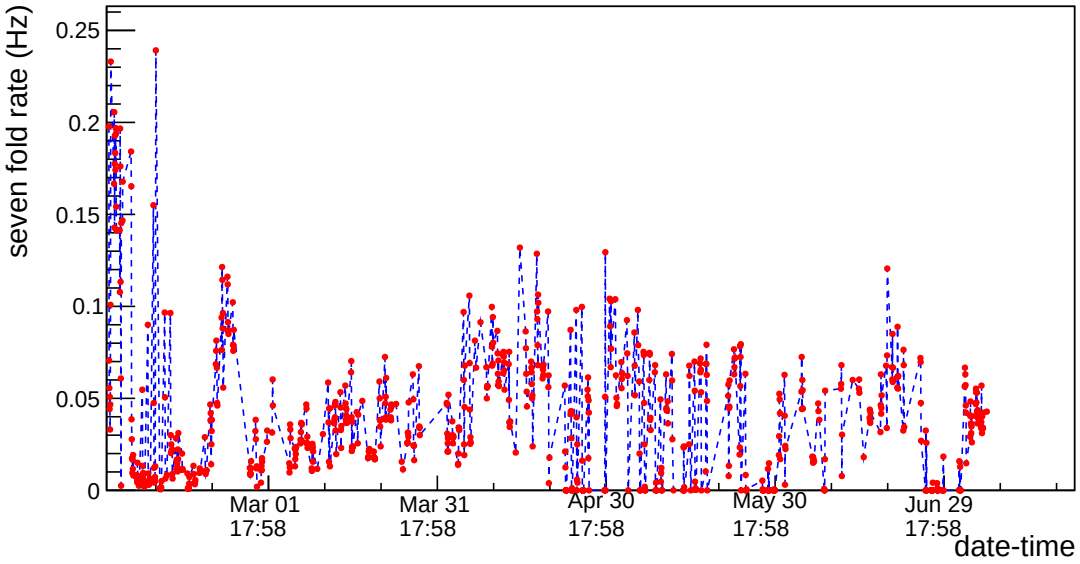

Figure 3.24: Large cosmic ray air shower (seven fold) rate as a function of date and time. Error bars are obscured by the marker symbols.

The final air shower array was set up and made operational in 2018. The data of the detector array during the period January 2018 to April 2019 recorded at day time only (Morning 7 a.m. – Evening 6 p.m. Indian Standard Time (IST)) was analyzed. Each data set consists of the number of showers triggered and the number of coincident counts in all the seven PSDs recorded within a duration of 60 minutes. The shower rate

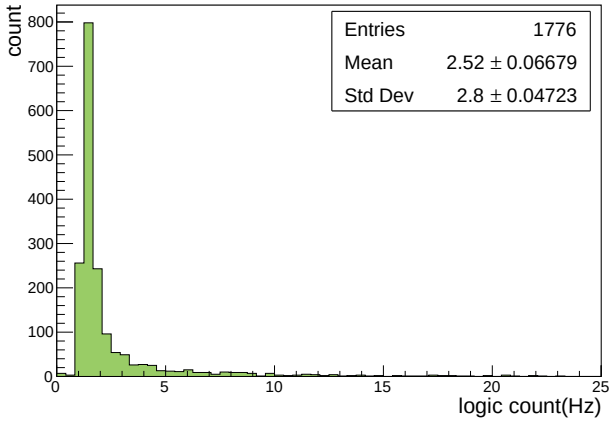

Figure 3.25: Cosmic ray air shower rate distribution in Darjeeling.

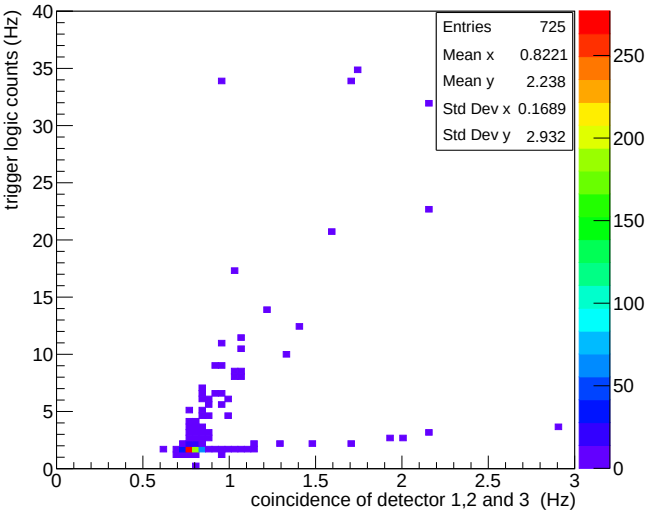

Figure 3.26: Correlation between cosmic ray air shower rate and three-fold coincidence rate.

as a function of date and time is shown in Figure 3.23. The distribution of the shower rate is shown in Figure 3.25 and the mean shower rate was found to be (2.52 ± 0.06) Hz having a standard deviation of 2.8 Hz.

It was found that the most probable value of the air shower rate is (1.3 ± 0.01) Hz with a variation of 10% over the total duration of measurement [107]. The large shower rate (seven fold) as a function of date and time is shown in Figure 3.24. The average large shower rate is (0.044 ± 0.0009) Hz is much lower than the shower rate. The three-fold coincidence of scintillator 1, scintillator 2, and scintillator 3 was also measured simultaneously with the shower triggers. A correlation of the three-fold

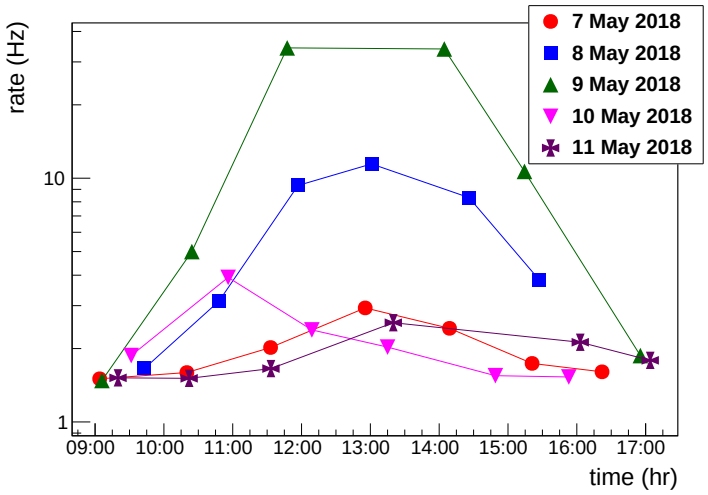

Figure 3.27: Daily shower rate variation for a few days in May, 2018

coincidence and the shower trigger is shown in Figure 3.26. This plot tells that the shower trigger is well correlated with the three-fold coincidence. Which means that number of showers triggered was truly due to cosmic ray air shower and not because of some chance coincidence that could be produced by a noisy detector in the array. The chance coincidence of getting three-fold coincidence was also calculated and was found to be $\sim 10^{-5}$ which is almost negligible.

In the shower rate plot (Figure 3.23) it can be observed that on some days the shower rate was significantly high. It was found that there was either some solar flares or proton fluence, electron fluence, increase of K_p index on these particular days [108–110]. Most of the jumps are observed during 12:00-15:00 hours as shown in Figure 3.27.

Comparison of the results with GRAPES-3 experiment

In our experiment, the shower trigger rate per unit effective area of detection was calculated to be 0.18 Hz/m^2. This value was compared with that obtained from GRAPES-3 experiment [44]. The GRAPES-3 air shower array is much larger with large active area of detection. The array at GRAPES-3 consists of 400 plastic scintillation detector modules covering an area of 25,000 m^2 and effective area of 400 m^2. Details of this array are well decsribed in this Refs. [111–113]. The shower trigger rate at GRAPES-3 was 42 Hz measured from 2014 data. The shower trigger rate per unit effective area was 0.105 Hz/m^2. The observed difference in the shower rate may be attributed to the difference in the trigger logic used in two experiments. The GRAPES-3 experiment uses a two level trigger system in which a three line coincidence and an additional condition of hits in at least 10 out of all the trigger participating detectors

is demanded.

3.5 Simulation of a cosmic muon tracker

The measurement of muon flux and momentum at sea level is an important study and was carried out by several groups since a very long time. Although the general features of the muon spectrum is well understood nowadays, but there are still some differences upto 25% in the modern calculations [41]. The muons come from the pion decays. Therefore, the muon spectrum at sea level directly follows consequence of the pion source spectrum [1]. The muon abundance is due to the fact that pions are produced in large numbers in hadron cascades due to their light mass. Since pions are typically produced at an altitudes of 15 km and decay relatively fast (for $\gamma = 10$ the decay length is only $\gamma\ \tau_\pi\ c = 78$ m). The growth curve of the muons is important to understand and it has to be matched with the theoretical model. For this reason, the energy of the muon has to be measured at different altitudes. A muon of 1 GeV with a Lorentz factor of $\gamma = E/m_\mu\ c^2 = 9.4$ has a mean decay length of $\gamma\ \tau_\mu\ c = 6.2$ km. The decay muons might not reach sea level, but rather decay themselves or get absorbed in the atmosphere.

These muons could be detected at high altitude cosmic ray stations.
In order to know the energy of the cosmic muons at high altitude, one of the way is to use a tracker and magnetic field. In the presence of magnetic field, charged particles like muon would bend and from the curvature of the track one could reconstruct the momentum of the particle. Our aim was to test the feasibility of building a low energy cosmic ray muon tracker using silicon detectors. For this purpose, a tracker was designed using Silicon pad detectors in layers [114] and simulated using GEANT4 [115]. The details of the tracker is given in Section 3.5.1.

3.5.1 Tracker Simulation

Simulation of a tracker consisting of silicon pad detectors was performed to track cosmic muons and to determine its energy in the low momentum regime. The cosmic muon tracker was simulated using GEANT4. The physical dimension of the tracker was 50 cm $\times$ 50 cm $\times$ 50 cm. The tracker has 10 layers and the gap between each layer was 5 cm. Each layer consists of an array of 35 $\times$ 35 silicon pad detectors. The silicon pads were 300 μm thick and 1 cm $\times$ 1 cm in size. Keeping in mind the large size of the tracker, the chosen realistic value of the uniform magnetic field was $\sim$0.5 Tesla, perpendicular to the direction of motion of the muons (cosmic muons were assumed to be vertically incident on the detector set up, although practically there will be muons

from all directions). In a particular case, if the cosmic muons are incident vertically (along -Z axis) on our setup, then the magnetic field will be applied along X axis. The incident muon hits the silicon pad of the tracker layers. The hit points (x, y, z) and pad numbers on different detector layers are recorded and used for track reconstruction. Figure 3.28 shows the trajectory of an incident muon of energy 1 GeV passing through the silicon tracker placed in 0.5 Tesla magnetic field.

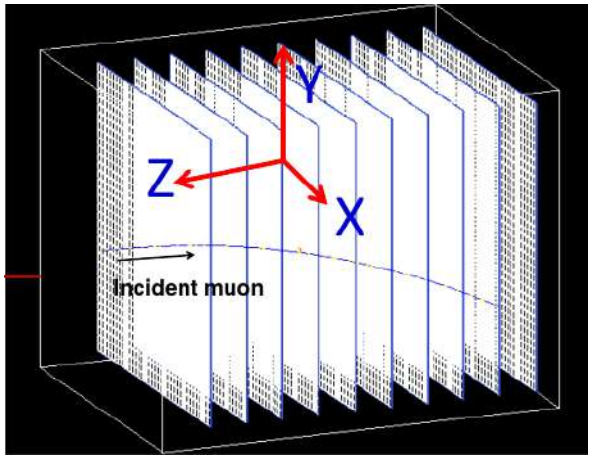

Figure 3.28: Muon tracker simulated in GEANT4. There are 10 layers of silicon pad detectors. Figure shows the muon track through the simulated tracker. The magnetic field was set to 0.5 Tesla.

3.5.2 Muon Reconstruction

The tracks of the incident muons were reconstructed using the recorded hit points information of the muons on different detector layers. The radius of the track curvature was estimated by fitting the reconstructed tracks by a circle function in ROOT. Figure 3.29 shows an example of the circle fit to the trajectory of a 100 MeV muon passing through the tracker with a magnetic field value of 0.5 Tesla. To reconstruct the momentum of the muon passing through the tracker, the following relation was used. The equation was developed as shown below. Starting with the Lorentz force.

$$\mathbf{F} = q.\mathbf{v} \times \mathbf{B} \tag{3.4}$$

where B is the magnetic field, q is the electric charge of the particle, and v is the velocity of the incident particle If v $\perp$ B, then the particle moves in a circle. For circular motion,

$$F = \frac{mv^2}{r} \tag{3.5}$$

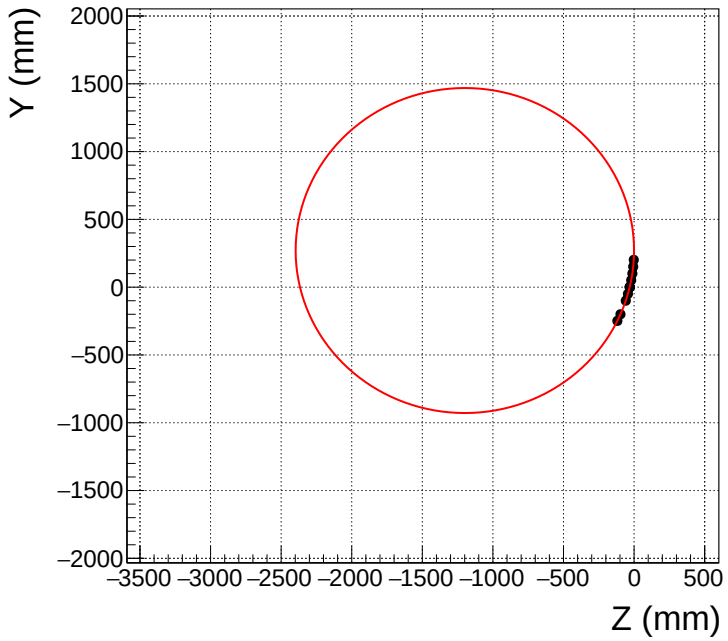

Figure 3.29: Fitting the points where the muon has produced a hit in the Si tracker. The circle fitting was done using the ROOT software.

where r is the radius of the circular path Substituting Eqn. 3.5 in Eqn. 3.4 we get,

$$\frac{mv^2}{r} = qvB \tag{3.6}$$

$$mv = p = qBr \tag{3.7}$$

$$p_{reconstructed} = 0.3 \times qBr \tag{3.8}$$

in units of MeV/c kilogauss cm
Using this relation and putting q = 1e, B = 0.5 Tesla and the value of r from fitting the muon tracks, the momentum of the incident muon was calculated.

3.5.3 Results and discussion

The lower and the upper bound of the incident muon energy which can be detected using this set up were studied. The table below shows the lower and upper energy cut off for cosmic muons that can be measured using this muon tracker operating at different magnetic field values. It was observed that below 15 MeV, the track was distorted due to multiple scattering. At high energies the track was nearly a straight line and the upper cut off was determined by finding out the energy for which the bending of the track was smaller than the granularity of the detector. One of

the important parameters for a tracking detector is the resolution of the momentum reconstruction because this would limit its use to a particular momentum range of the incoming particle. The momentum resolution was calculated using the following formula

$$\frac{\Delta p}{p}\% = \frac{p_{reconstructed} \sim p_{incident}}{p_{incident}} \times 100\% \tag{3.9}$$

Figure 3.30 shows the momentum resolution of the muon tracker. It was found that the tracker has a good momentum resolution ($< 3\%$) in the energy range 200-1000 MeV/c. It is feasible to use this tracker in this particular energy range for cosmic muons. However, it is still possible to reconstruct the muon momentum upto 4000 MeV/c at 1 Tesla magnetic field. Results show that it is feasible to develop a cosmic ray muon tracker of the above mentioned dimensions to find momentum of low energy muons (<5 GeV) at high altitude

Table 3.1: Lower cut and upper cut of cosmic ray muon momentum that can be reconstructed with good resolution at different magnetic field values.

Magnetic Field (Tesla)	**Lower cut** (MeV)	**Upper cut** (MeV)
0.1	15	250
0.25	15	750
0.5	15	1850
0.75	15	2600
1	15	4000

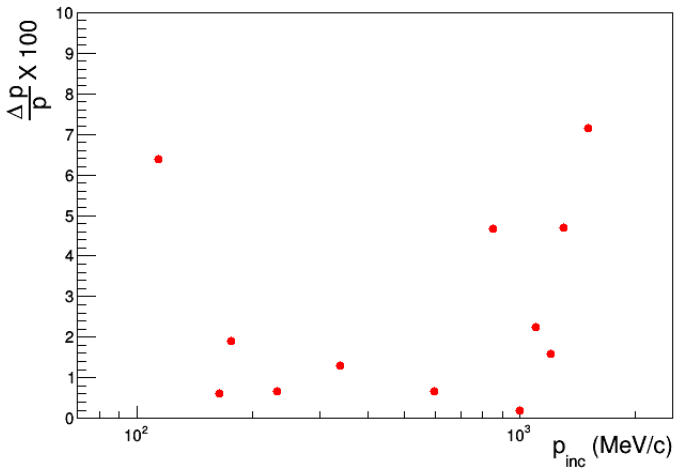

Figure 3.30: Momentum resolution of the tracker

Chapter 4

Study of cosmic rays during solar eclipse

Solar eclipse occurs when the Moon comes in between the Sun and the Earth, and the Sun rays get blocked by the Moon resulting in a shadow on the Earth. This happens when the Sun, the Moon and the Earth are aligned. There are earlier reports conveying that a solar eclipse can affect the Earth's upper atmosphere by significantly reducing the ionospheric electron density, conductance, and thermospheric temperature. All this happens because of the rapid reduction in the solar radiation caused by the obscuration during the eclipse. However, one may relate these effects to be similar to day-night variations because at night there is no Sun rays and this leads to thermal changes in the atmosphere. But, in fact the day-night variation is slow and gradual, but the solar eclipse causes sudden change in atmospheric parameters, the science of which is interesting to learn. Although it is well-known that solar eclipses can significantly impact the ionosphere and thermosphere, its influences on the magnetosphere-ionosphere system is a recent research topic [116]. Moreover, there are evidences that solar eclipse can induce fluctuations in the cosmic ray intensity on Earth. In the last few decades, many scientists have studied the cosmic ray intensity especially gamma rays during total solar eclipse and found significant reduction in soft cosmic ray flux. A total solar eclipse is a nice opportunity to study the fraction of cosmic rays directly coming from the Sun to Earth that is blocked by the Moon. Several groups have come up with their own explanations for the reduction in cosmic ray flux during the eclipse. However, there is no concrete theory and so this calls in for further investigation on this topic. This chapter is devoted to the interplay between solar eclipse and cosmic rays. It discusses the findings of earlier groups and their theories to explain the phenomena (Section 4.1), the detection techniques, (Section 4.3.1) and results (Section 4.3.3). The main goal was to find out if solar eclipse could globally effect the cosmic ray intensity or not. Section 4.3.5 discusses the results of this exper-

iment and tries to find a connection between the ionospheric electron density and the cosmic ray intensity. In Section 4.4, the influence of solar eclipse on the cosmic ray muon flux is also discussed.

4.1 Solar eclipse and cosmic rays

Solar eclipse is a very important astronomical event that provides the opportunity to study the disturbance in the atmosphere it produces and its influence on cosmic ray intensity. It was observed in the past during the eclipse that when the solar irradiation undergoes rapid reduction, it causes many secondary effects on the Earth's atmosphere [117]. The variation of secondary cosmic gamma ray (SCGR) flux during solar eclipses was studied and reported earlier by several groups of researchers. Most of them observed a dip in SCGR flux during the solar eclipse [118]. The experiment carried out by Chintalapudi *et al.* during total solar eclipse of October 24, 1995 at Diamond Harbour, showed that there is 11% dip in γ-rays (600 keV - 1350 keV) and on the average 9-10 % decrement in high energy photon counts [119]. In another experiment performed by Bhattacharyya *et al.* during the same solar eclipse, observation of a maximum drop of 25% in the secondary γ-ray flux in the energy interval 2.4 MeV - 2.7 MeV was reported [120]. Nayak *et al.* reported an observation of 9% dip just prior to the total solar eclipse and 4% steady decrement during the eclipse of August 1, 2008 in the energy range 50 keV - 4600 keV [121]. According to observations by Bhaskar *et al.* during solar eclipse of January 15, 2010, there was a 21 % drop in SCR flux in 1 MeV - 1.5 MeV energy range during annularity [122]. The explanation given by some groups is that a quasi-periodic pressure wave is set up in the ionosphere by the shadow band in the ozone layer which may, considerably, affect the production of SCR [123]. Another explanation is that π - μ component production layer of the atmosphere is lowered due to atmospheric cooling during eclipse which shortens the path (or the time available) for decay of π^0 meson to γ-rays and μ meson to $e^{\pm}$ and induces the changes in relative cosmic ray counts [120]. However, the drop in SCR intensity cannot be explained by atmospheric cooling alone because geophysical disturbances are present at all levels of the atmosphere. The interaction of the cosmic rays in the atmosphere is affected by the weather parameters and solar activities. A few percent of cosmic gamma rays are influenced by atmospheric pressure. So one needs to take all these parameters into account while explaining the drop in SCR during solar eclipse.

4.2 NaI(Tl) scintillation detector

4.2.1 Invention and properties

In 1948, it was first observed by Robert Hofstadter, that crystalline NaI, shows enhanced scintillation light output compared to organic scintillators, when traces of thallium iodide was added to it. The reason for this is explained next. The scintillation mechanism in inorganic crystals depends on the energy states of the lattice. Absorption of energy causes the electron in the valence band to jump to the conduction band leaving a hole in the valence band. The typical gap widths are so large that the emitted photon does not lie in the visible energy range. However, if small amounts of impurities, called activators are added to the crystal, then the energy band structure gets modified and there are special sites created in the lattice. When a charged particle passes through the lattice, it creates electron-hole pair. The hole drifts to a position of the activator site and ionizes it. The free electron can also fall into an activator site, creating a neutral configuration having its own set of energy levels. Now, these electrons or holes sitting at the activator sites jump from excited state to ground state to emit a visible photon. This photon is guided to a photomultiplier tube (PMT) for producing a measurable electronic signal.
NaI(Tl) scintillators are the most used devices for gamma spectroscopy since its discovery. Even though many new crystals having scintillation properties tried to win the position in the market, NaI(Tl) remained the preferred choice for many experiments for several reasons. First, NaI(Tl) scintillators have very good light yield. Second, they can be made of many shapes and sizes easily. And third, they have short decay time for scintillation pulse ($\sim$ 230 ns). Generally, the wavelength of light emission is 415 nm and the crystal has a refractive index of 1.85. One of the disadvantages of NaI(Tl) scintillator is that, NaI is hygroscopic in nature and therefore it has to be canned inside a air-tight container to prevent it from absorbing moisture from air. Also the crystal being fragile, it needs to be protected from thermal or mechanical shock.

4.2.2 Temperature dependence

The properties of NaI(Tl) scintillator mentioned in the previous section holds true for room temperature operation. However, if the temperature changes too much from the room temperature, then the crystal shows different behavior. The fact that NaI(Tl) scintillator has a temperature dependent light yield is well known and was studied intensively in the 1960s [99]. This temperature dependence is in fact due to the complexity of the scintillation process and could be explained by theoretical models.

According to these models, temperature dependence is a consequence of non-radiative transitions between activator levels. Such models are well described in Refs. [124–126] along with experimental data to verify the models. These properties are also important to study with currently manufactured NaI detectors to check consistency of results and ensure its safe application.

Experimental setup

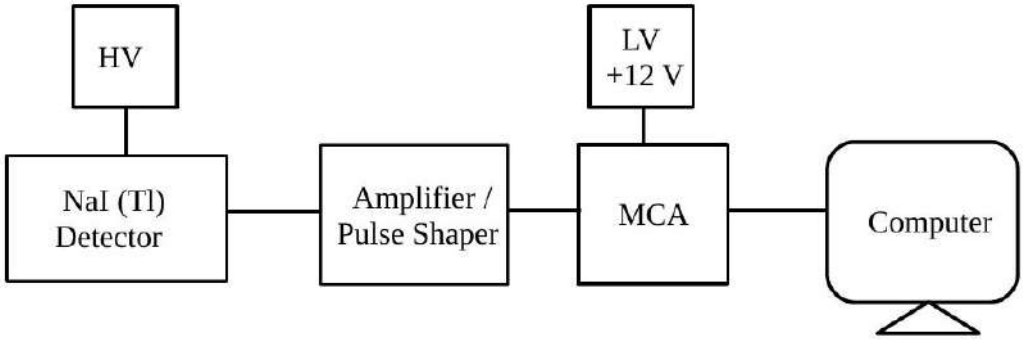

Figure 4.1: Block diagram of the experimental arrangement

The temperature dependence of the gain of a NaI(Tl) scintillator was studied. The goal was to study how the diurnal variation of the ambient temperature affects the detector gain and count rate. The gain of the NaI scintillator and gamma ray count rate was measured at regular intervals for several days and monitored the ambient temperature for drawing a correlation between the two. For this experiment, a NaI(Tl) scintillator of crystal size 4 in $\times$ 4 in $\times$ 16 in was used. The crystal was hermetically sealed inside a thin aluminium casing with a 1 mm thick white reflecting material placed between the crystal and the casing. The scintillation crystal was optically coupled to photomultiplier tube (PMT), inside the hermetically sealed case. A schematic of the signal processing electronics is shown in Figure 4.1. The signal from the dynodes was fed to a fixed gain charge sensitive pre-amplifier, integrated with the base of the PMT. The pre-amplifier signal was further shaped and amplified using a Spectroscopy Amplifier. The amplifier output was digitized using multi-channel analyzer (MCA). Finally, the data were stored in a personal computer (PC). For each case the energy spectra were stored in PC. The detector was kept outside under the sky without lead shielding. Temperature, pressure and humidity were continuously recorded at 1 min interval. The detector calibration was done by terrestrial radioactive sources for e.g. ^{40}K and ^{208}Tl whose energies were known. The radioactive peaks of ^{40}K and ^{208}Tl were fitted with a gaussian function. The gaussian mean is the ADC channel corresponding to the characteristic energy of the respective terrestrial radioactive source.

The calibration plot is shown in Figure 4.2.

During the study, the threshold of the detector was set to 125 keV. The γ-ray spectra was saved at an interval of 4 minutes. In a typical background gamma ray spectrum of the detector, it was found that the detector measures gamma rays in the energy range 125 keV to 15 MeV, with about 90% of the counts within 125 keV to 4 MeV. Eliminating the detector noise that generally comes in the first few ADC channels of the MCA, the counts in the detector was considered only above 150 keV (i.e. the energy range 150 keV to 4 MeV). A typical background γ-ray spectra for NaI(Tl) scintillator is shown in Figure 4.3. The total counts in the detector was evaluated by integrating the gamma-ray spectrum from 150 keV to 4 MeV energy.

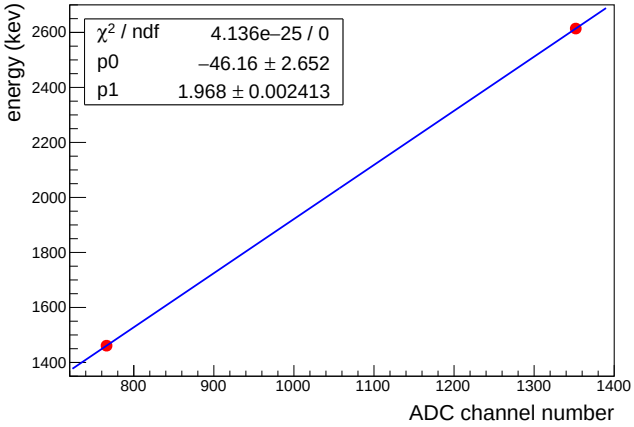

Figure 4.2: The energy calibration plot for NaI(Tl) scintillator

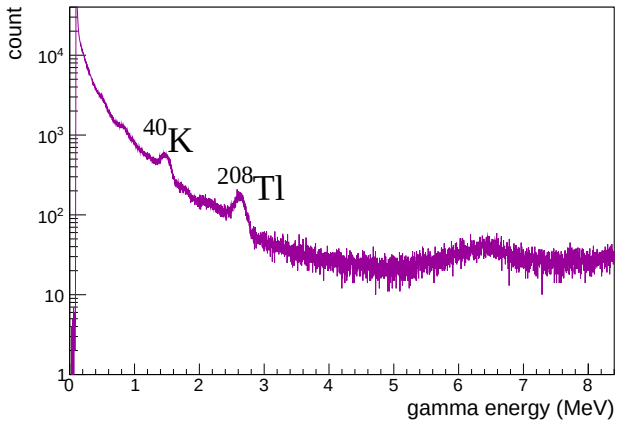

Figure 4.3: The background γ-ray spectra for NaI(Tl) scintillator

Results and discussions

Data were collected during the period 23 December to 29 December, 2019. The gamma ray flux measured by our NaI(Tl) scintillator is shown in Figure 4.4. The figure also shows the variation of temperature and the detector gain. The detector gain was realized by the peak position of the terrestrial radioactive source ^{208}Tl (Figure 4.3). The peak was fitted with a gaussian function for each data set and the mean of the function is the relative gain of the detector.

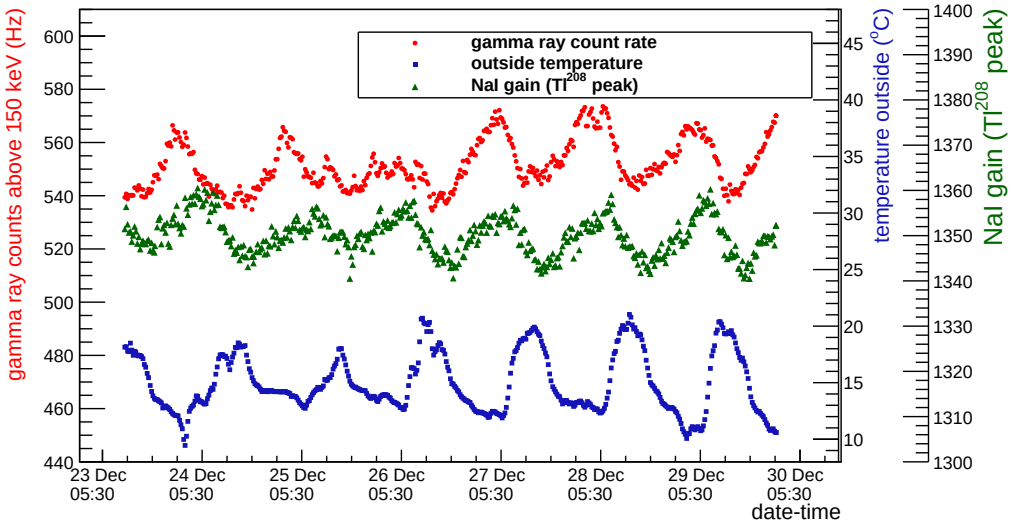

Figure 4.4: γ-ray count rate in the energy range 150 keV to 4 MeV (upper curve), NaI detector gain or ^{208}Tl peak position (middle curve) and ambient temperature (lower curve) as a function of time

From the figure, it can be seen that the γ-ray count rate has an inverse correlation with ambient (outside) temperature, which could be attributed to the temperature dependent gain of NaI(Tl) detector crystal. To find out the correlation between γ-ray count rate and temperature, the γ-ray count rate falling in a unit temperature bin (1 degree) was collected for all days (23 December to 29 December, 2019). The average γ-ray count rate in each temperature bin was plotted as a function of temperature as shown in Figure 4.5. The error bars are the standard deviation in the γ-ray count rate distribution for the associated temperature bin. The correlation points are fitted by a second order polynomial function, p0+p1.T+p2.T^2 as shown in Figure 4.5, where p0, p1, p2 are the fit parameters and T is the temperature. The values of the fit parameters are p0 = 730, p1 = -21.3, and p2 = 0.6. These values are used to normalize the γ-ray flux temporal variation, so that the temperature effect of the crystal is eliminated.

The normalized γ-ray count was calculated as,

$$Normalised\ gamma\ ray\ count\ rate = A \times \frac{measured\ gamma\ count\ rate}{(p0 + p1.T + p2.T^2)} \tag{4.1}$$

where A is a normalisation constant. Figure. 4.6 shows the temperature normalized γ-ray count rate during the period 23 December to 29 December, 2019.

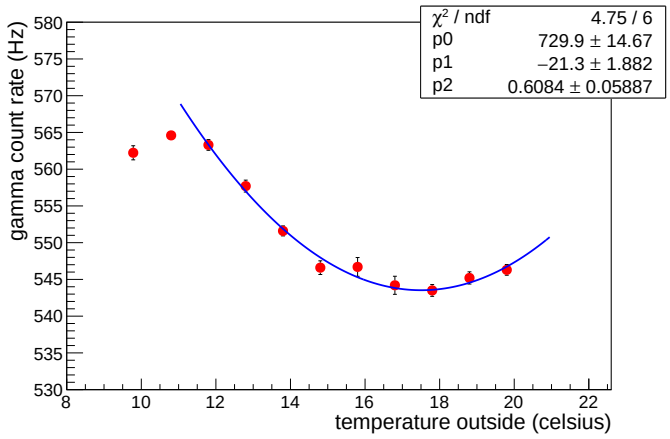

Figure 4.5: Correlation between γ-ray count rate and ambient (outside) temperature

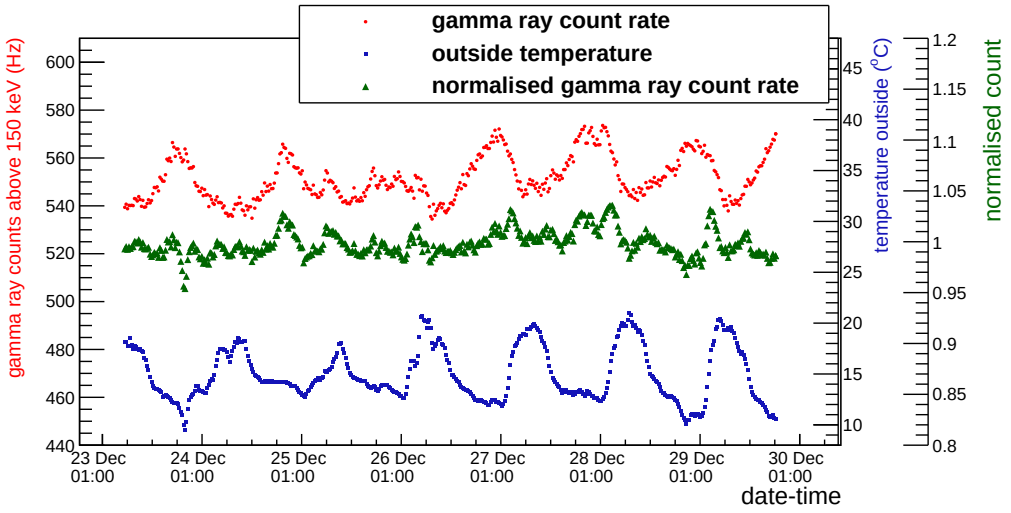

Figure 4.6: γ-ray count rate in the energy range 150 keV to 4 MeV (upper curve), normalized γ-ray count (middle curve) and ambient temperature (lower curve) as a function of time

The correlation plot of the NaI(Tl) detector gain with the temperature was done in a similar method. The average of the detector gain in a unit temperature bin was obtained by taking all the data and was plotted against temperature. The error bars

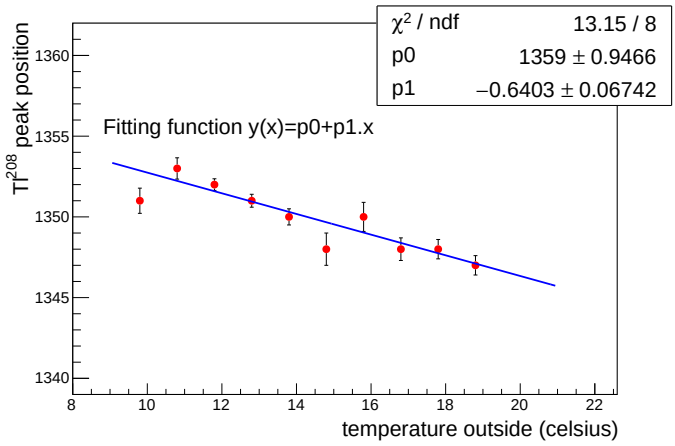

Figure 4.7: Correlation between NaI(Tl) detector gain and ambient (outside) temperature

are the standard deviation in the gain distribution for the associated temperature bin. The correlation points are fitted by a straight line, p0+p1.T, where p0, p1 are the fit parameters. The values of the fit parameters are p0 = 1359 and p1 = -0.6. From the correlation plots, it can be concluded that the NaI(Tl) scintillator performance (gain, count rate) has an inverse temperature dependence. The γ-ray count rate clearly shows a second order polynomial dependence on temperature, which is in agreement with the results in Refs. [125]. However, the gain shows first order dependence on temperature. This discrepancy can be attributed to the methodology of analysis. The gain was calculated by fitting the peak of ^{208}Tl in each of the 4 min γ-ray spectrum. Due to statistical fluctuations in the mean position of the ^{208}Tl peak, the fit parameters corresponding to different data sets, have large enough fluctuations to hide the true behavior of the detector gain with respect to temperature changes. Also, the temperature range available in this study is small (10 to 20 degrees celsius) for observing a property of the NaI(Tl) that is expected to show constant temperature coefficient over the range of room temperatures [99].

4.3 Cosmic gamma ray measurement during solar eclipse

All the cosmic ray experiments during solar eclipse done so far by previous groups were performed at the location of the eclipse occurrence. Their results and explanations hold locally. However, any study of cosmic rays in places falling on the other side of the Earth where eclipse is not occurring was not carried out previously. Recently, there was a study on the effect of solar eclipse on the Magnetosphere-Ionosphere System [116].

They mentioned that the geospace response to a polar-region solar eclipse was not limited just to the eclipse region but has global implications. There was no information on the effects on cosmic ray intensity globally. The Great American eclipse gave us a good opportunity to study the atmospheric response to the total solar eclipse observed through cosmic rays in Kolkata, India [127].

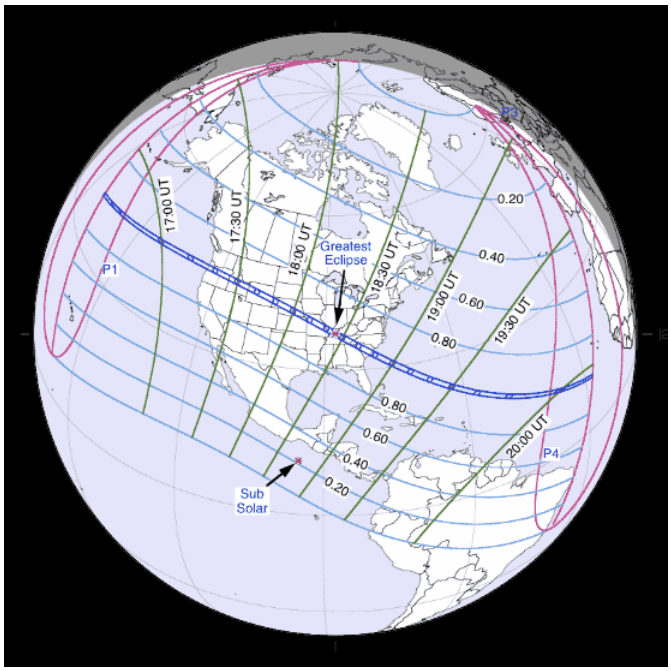

Figure 4.8: Path of the total solar eclipse on 21 August 2017 shown by the blue line

The solar eclipse of August 21, 2017, also known as "The Great American Eclipse" was a total solar eclipse visible within a band across the entire continental United States, passing from the Pacific to the Atlantic coasts. The partial eclipse started on August 21 at 15:46:50 UTC and ended on August 21 at 21:04:21 UTC. Our goal was to measure the secondary cosmic ray gamma flux variation in Kolkata, due to the effect of atmospheric disturbances propagating towards India from the path of the solar eclipse in America. Detection of gamma rays was rather simple. It was more crucial to monitor the parameters that can influence the gamma ray flux and finding out the dependencies or correlation. The secondary cosmic ray (SCR) flux depends on atmospheric weather parameters and interplanetary solar and geomagnetic parameters. It is also affected by tidal or gravitational waves created by the motion of the moon. Some of these important parameters were studied and is mentioned in Section 4.3.4. It is known that, on the surface of the Earth, there is a substantial flux of sub-MeV to MeV cosmic gamma rays. Of the total observed gamma radiation, only a few percent consists of the cosmic ray induced component, the rest is a component due to terrestrial radioactivity from sources like ^{40}K, ^{222}Rn, ^{232}Th, ^{238}U. The terrestrial gamma

ray (TGR) background level normally does not change over time interval of an hour, except due to presence of Radon in the atmosphere which may be transported to the ground during rainfall [128]. During clear weather, there is no significant variation in the TGR component to be expected within a short interval of time. Therefore any observed sudden variation in the measured gamma ray flux will be purely of extraterrestrial origin.

Some of the important parameters that could effect cosmic ray gamma intensity in India were checked. The overall atmospheric weather and solar activity report during the eclipse week (19 August to 23 August, 2017) is discussed in Section 4.3.5. For shielding the NaI(Tl) detector from TGR as much as possible, a lead box with 1 cm thick walls was used. Measurements were started a few days prior to the day of the solar eclipse, and continued the same for the next few days for good statistics of the background counts and estimation of fluctuations. In order to estimate the amount of terrestrial component of radiation, measurements were performed with different shielding configurations. An observed significant variation in gamma ray flux correlated with astrophysical phenomena like the solar eclipse, can only be claimed provided the TGR background is measured and properly subtracted.

4.3.1 Experimental setup

The NaI(Tl) detector used in the present experiment, has a crystal of size 5.1 cm $\times$ 5.1 cm. The crystal is hermetically sealed inside an aluminium casing of 0.8 mm thickness with a 1 mm thick white reflecting material placed between the crystal and the casing. The scintillation crystal is optically coupled to photomultiplier tube (PMT) of diameter 5.1 cm, inside the hermetically sealed case. The PMT was biased with a voltage of +600 V from an adjustable power supply ORTEC-556. A schematic of the signal processing electronics is shown in Figure 4.9. The signal from the dynodes is fed to a fixed gain charge sensitive pre-amplifier, integrated with the base of the PMT. The pre-amplifier signal is further shaped and amplified using ORTEC-671 Spectroscopy Amplifier with coarse gain of 500 and shaping time of 0.5 μs. The amplifier output is digitized using multi-channel analyzer (MCA). Finally, the data were stored in a personal computer (PC). A picture of the setup in laboratory is shown in Figure 4.10.

The detector was calibrated using standard gamma ray sources ^{137}Cs (662 keV), ^{60}Co (1173 and 1332 keV) and ^{22}Na (511 keV and 1275 keV) of known energies. For each case the energy spectra are stored in PC and then analyzed offline for finding the calibration parameters. The gamma peaks were identified in the spectra obtained using NaI(Tl) detector, with each of the sources one by one. The peak is the ADC

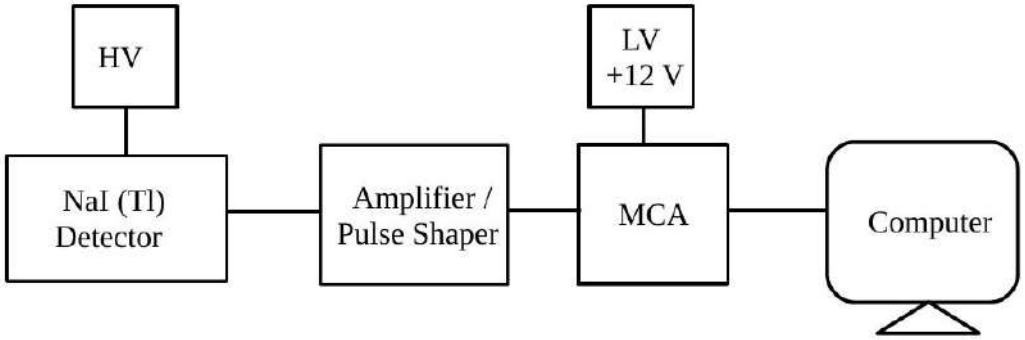

Figure 4.9: Block diagram of the experimental arrangement

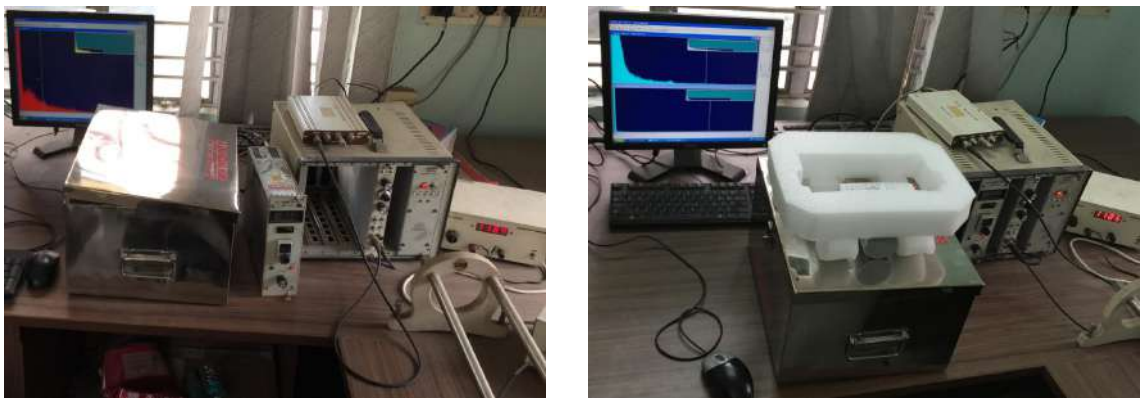

Figure 4.10: Setup of the experiment with NaI inside the Pb box (left panel) and on top of the box (right panel)

channel number corresponding to the characteristic energy of the gamma ray source. The calibration curve is shown in Figure 4.11.

4.3.2 Background gamma ray spectrum with NaI(Tl)

After the energy calibration, the background study with different configurations of lead shielding was performed. As mentioned earlier, the estimation of the contribution from the terrestrial radioactivity is extremely important for our experiment to be able to give precise results. Four different configurations were used (i) The detector was kept on top of a wooden table without any lead shielding, such that γ-rays can reach the detector from all directions. (ii) The detector was kept on top of a lead box such that the γ-rays can reach the detector's active medium from all sides except the bottom. (iii) The detector was kept inside the lead box with the top lid of the box kept open, such that γ-rays can be incident on the detector from top only. (iv) The detector was placed inside a closed lead box. Figure 4.12 shows spectra of the cosmic background radiation obtained for all four cases. The peaks due to terrestrial

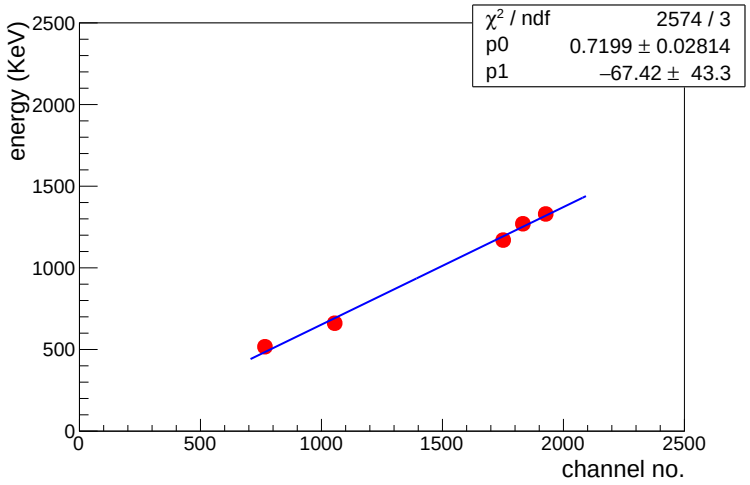

Figure 4.11: The NaI(Tl) detector calibration curve. Five points are for the five different gamma peaks that were observed with three independent radioactive sources.

radioactive sources are clearly visible. Continuous measurements were carried out from 16^{th} August, 2017 to 23^{rd} September, 2017. The DAQ framework enables automatic feeding of the spectrum data to a buffer in every two minutes which is saved to an ASCII file in the computer before the MCA starts acquiring the next spectrum.

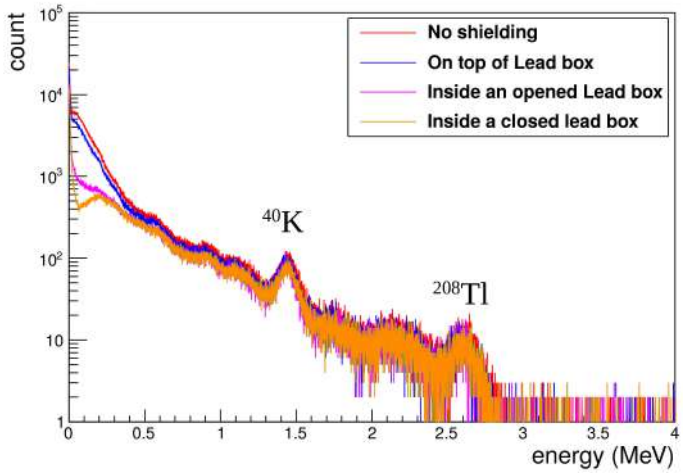

Figure 4.12: Gamma spectrum with different configurations

4.3.3 Results

All the further measurements were made keeping the detector on top of the lead box such that it is exposed to background radiations from all three directions. No

radioactive sources apart from terrestrial radioactivity were present nearby. Ambient temperature and relative humidity were kept constant at an average value around 28 °C and 50 % respectively during the entire duration of measurements using air conditioning system. Figure 4.13 shows the temperature, atmospheric pressure and humidity measured inside the laboratory during the night of 21 August. The outside temperature was around 28 °C and the outside relative humidity was within 80 % to 90 %. The weather data of Kolkata can also be obtained from the site [136]. The γ-ray spectra are stored for 2 minutes and the number of detector signals per second was calculated by summing up the counts in all the ADC channels, thereby integrating the entire spectrum and then dividing by the time taken for accumulation of each of the spectrum. Figure 4.14 shows the total γ-ray counts per second over the detector area measured during 19^{th} to 23^{rd} August, 2017.

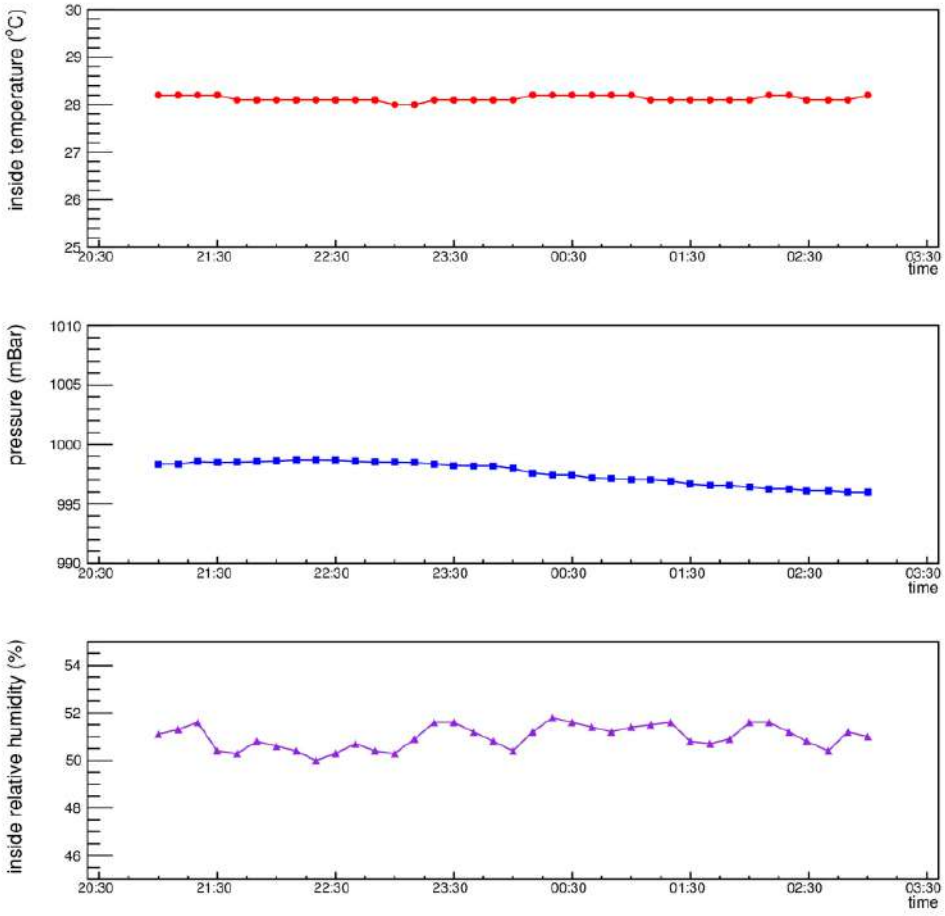

Figure 4.13: Inside temperature, pressure and relative humidity during the night of 21 August 2017.

The decrease in γ-ray counts is clearly visible in the plot. In order to know the nature of fluctuations and its energy dependence, the data for the detector counts was

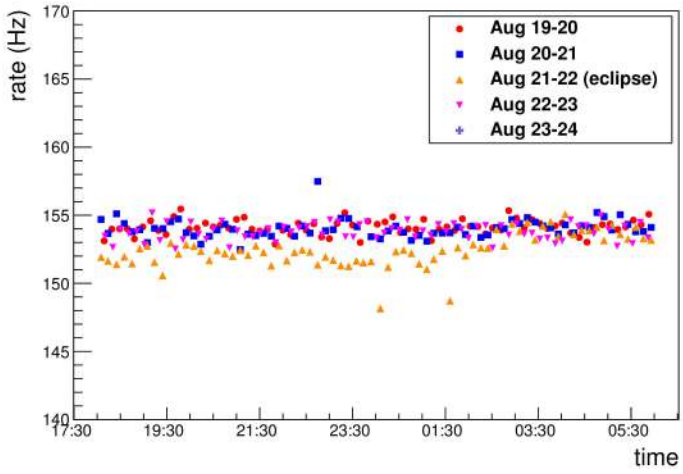

Figure 4.14: Total count rate from NaI due to cosmic and terrestrial radiation

analysed in low and high energy ranges separately. The integration over energy was done by selecting energy ranges as, Region 1: low energy (25 - 100 keV), Region 2: moderate energy (100 - 500 keV), Region 3: 500 - 1000 keV, Region 4: 1000 - 1500 keV and Region 5: above 1500 keV respectively. The data of each day (5 days of eclipse week) was analyzed and for these days only the specific hours during which the eclipse took place in America, i.e. from first contact to last contact, was considered. This corresponded to 15:46(UTC) + 05:30 hour to 21:04 + 05:30 hour in IST which is a duration of 5 hours and 18 mins (21:16 August 21 to 02:34 August 22). Assuming, the bulk of the cosmic rays are in the vertically downwards direction and most probably it is to be affected by the eclipse effects, so only this contribution was extracted from the total measured gamma ray flux. Since the TGR background coming from the bottom was already shielded by the lead box, the TGRs coming from the sides was estimated by methods discussed in the earlier section as

$$count_{sides} = count_{sides+top} - count_{top} \tag{4.2}$$

where $count_{sides+top}$ is the gamma count rate measured with detector placed on top of the lead box (only bottom shielded) and $count_{top}$ is the gamma count rate measured with detector placed inside the lead box with the top lid open. The value of $count_{sides}$ was estimated for different energy bins and it was subtracted from each data point in the corresponding energy regions. Table 4.3.3 shows the estimated count rates of gamma rays coming from different directions, mainly the $\text{count}_{sides+top}$, count_{top} and count_{sides} for a sample data collected over a period of one hour in a normal day.

The day to day variation for two different energy regions - Region 1 to Region 5, is shown in Figure 4.15, Figure 4.16, Figure 4.17, Figure 4.18 and Figure 4.19

Table 4.1: Estimated gamma ray counts (terrestrial and cosmic) coming from different directions

Energy range (keV)	**count**$_{sides+top}$ **(Hz)**	**count**$_{top}$ **(Hz)**	**count**$_{sides}$ **(Hz)**
25-100	49.35	13.89	35.46
100-500	69.17	37.43	31.74
500-1000	15.04	13.47	1.57
1000-1500	6.04	5.51	0.53
above 1500	2.90	2.58	0.32

respectively. The most significant variation during the eclispe was observed in Region 1 and Region 5.

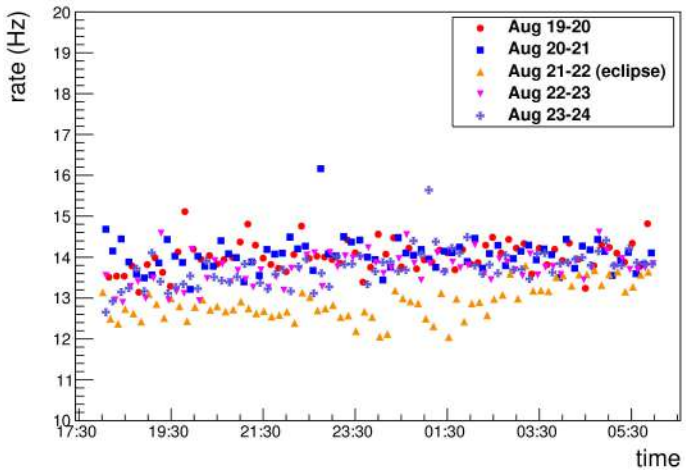

Figure 4.15: Total counts of secondary cosmic gamma ray per second in the energy range 25-100 keV

To get an idea of the change in secondary γ-ray flux during these hours and to compare with the same on normal days during those specific hours, a histogram of gamma counts per second in all the energy regions for normal days was plotted and also the same during the eclipse as shown in Figure 4.20. The mean of the gaussian count rate distribution in Region 1 for normal days is 13.89 Hz with a precision of 0.03 Hz, while for the eclipse day the mean is 12.62 Hz with a precision of 0.05 Hz. The difference in means during the eclipse and during normal days was calculated using the relation

$$\delta m = \frac{mean_{eclipse} - mean_{normal}}{mean_{normal}} \times 100\% \tag{4.3}$$

and the error in δm is given by the relation

$${\sigma_m}^2 = (\frac{\sigma_E}{N})^2 + (\frac{1}{N} + \frac{(E-N)}{N^2})^2 \sigma_N^2 \tag{4.4}$$

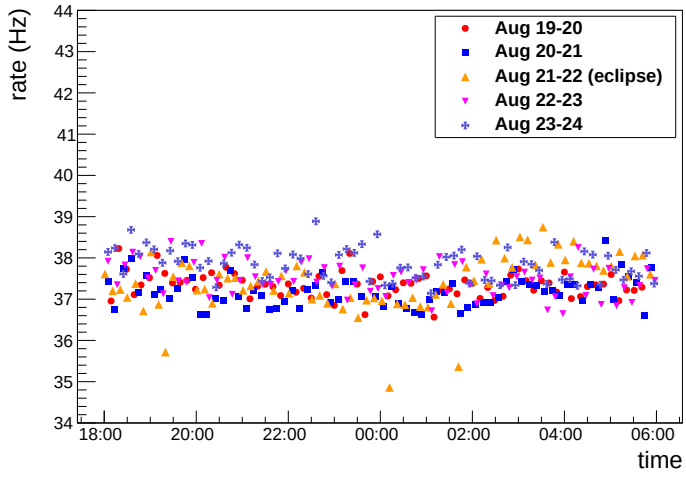

Figure 4.16: Total counts of secondary cosmic gamma ray per second in the energy range 100-500 keV

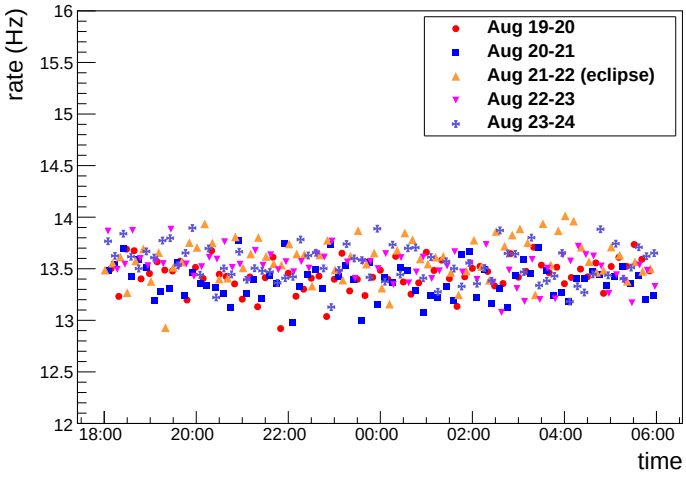

Figure 4.17: Total counts of secondary cosmic gamma ray per second in the energy range 500-1000 keV

where E and N are the mean counts during eclipse and normal day and σ_E and σ_N are the errors in eclipse and normal day counts respectively. The value of δm for Region 1 is found out to be (-9.1 $\pm$ 0.4) % which means that there is a significant decrement in the SCGR flux in this particular energy range. The SCGR flux distribution for normal days from 21:16 hr to 02:34 hr was compared with SCGR flux distribution during the eclipse. Both the distributions were fitted with a gaussian function (red line) in the Figure 4.20. Similar analyses were done for all the energy regions and the values of δm are quoted in Table 4.3.3. A peculiar trait in the SCR flux distribution was observed in Region 5. An unexpected high value of the mean of the gaussian count

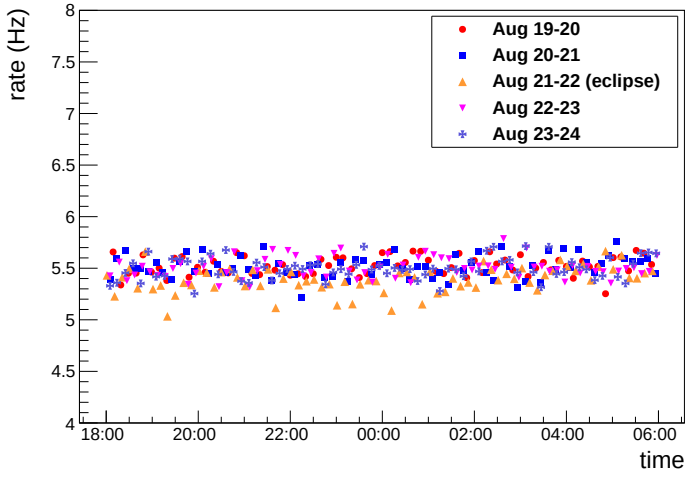

Figure 4.18: Total counts of secondary cosmic gamma ray per second in the energy range 1000-1500 keV

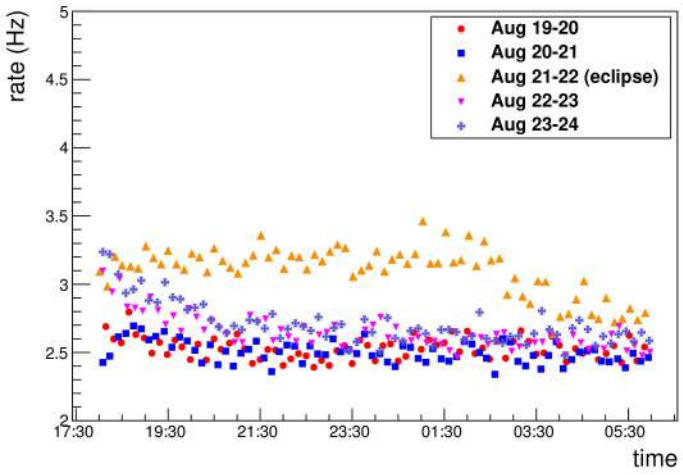

Figure 4.19: Total counts of secondary cosmic gamma ray per second in the energy range above 1500 keV

rate distribution for eclipse day was observed and the value is 3.211 Hz, while for the normal days the mean is 2.579 Hz. The value of δm is (24.5 ± 0.6) %. This increment was observed through out the duration of eclipse and after this the count rate falls back to normal value gradually as seen in Figure 4.19.

4.3.4 Space weather condition

Space weather is a very important factor that can largely affect the atmosphere of Earth and thereby, the cosmic ray flux. The space weather report mainly refers to the geophysical parameters such as Earth's magnetic field, Kp index, electron fluence,

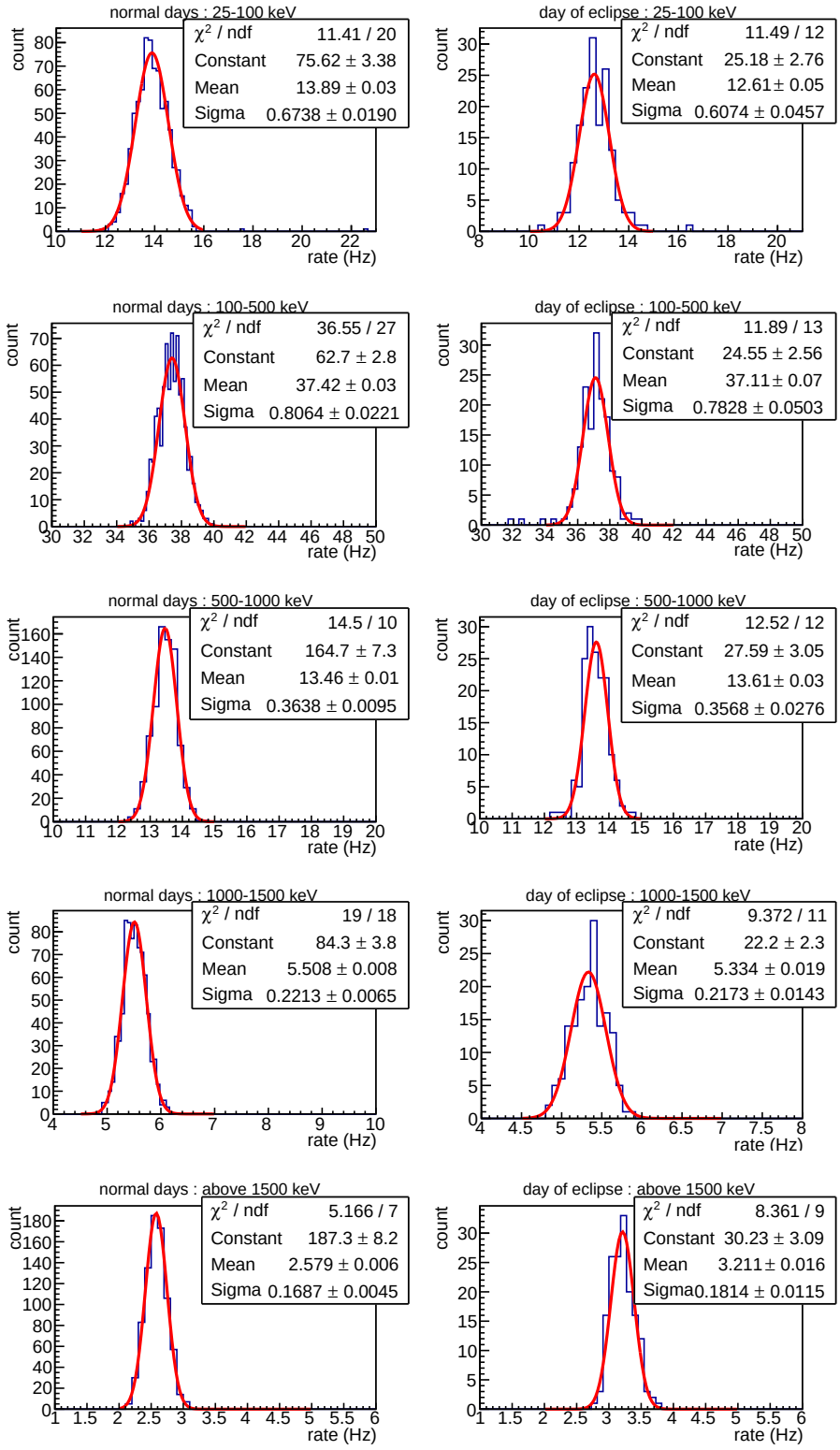

Figure 4.20: Frequency distribution of total counts of secondary cosmic gamma ray per second in different energy regions for normal days (left) and day of eclipse (right) during only those particular hours when the eclipse occurred

Table 4.2: Count rates during normal days and eclipse day and % variation for different energy ranges

Energy range (keV)	**Count rate during normal days (Hz)**	**Count rate during the eclipse (Hz)**	δm (%)
25-100	13.89 ± 0.03	12.62 ± 0.05	-9.1 ± 0.4
100-500	37.42 ± 0.03	37.11 ± 0.07	-0.8 ± 0.2
500-1000	13.46 ± 0.01	13.61 ± 0.03	+1.1 ± 0.2
1000-1500	5.508 ± 0.008	5.334 ± 0.019	-3.1 ± 0.3
above 1500	2.579 ± 0.006	3.211 ± 0.016	+24.5 ± 0.6

proton fluence, etc. It also includes the disturbances caused by the Sun, like the solar wind. The National Oceanic and Atmospheric Administration (NOAA) [134] has a Geostationary Operational Environmental Satellites (GOES). Two GOES operational satellites are there, one is located over the east coast of the U.S. (GOES East) and the other located over the Pacific (GOES West). GOES Magnetometer monitors the geomagnetic field and its variations. It provides information on the geomagnetic activity level and also detects magnetic storms. Figure 4.21 shows the GOES magnetometer data plotted for days August 19, 2017 to August 23, 2017. The location of the satellites when this data was recorded was 75 degrees West longitude and 135 degrees West longitude respectively. From the plot, it is evident that during the eclipse hours (August 21 15:46:50 UTC to 21:04:21 UTC) there was no abnormal behavior in the geomagnetic field value.

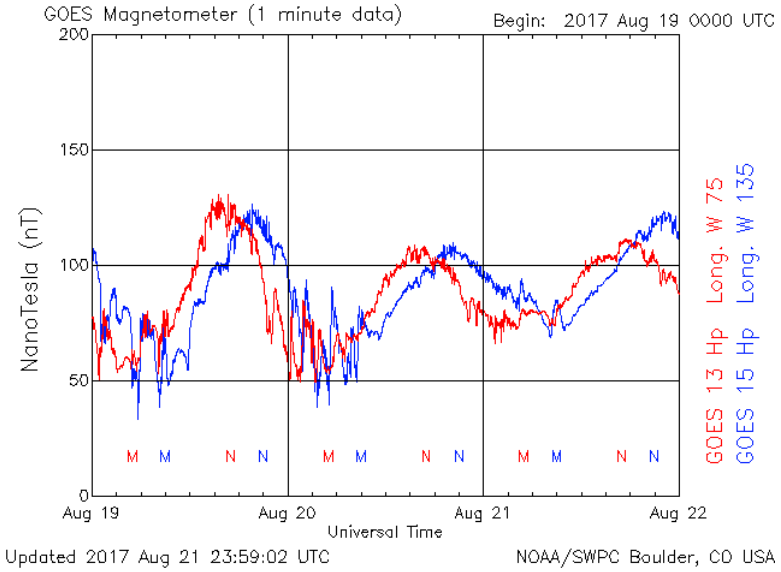

Figure 4.21: The 1-minute averaged parallel component of the magnetic field in nanoTeslas (nT), measured at GOES-13 (75 degrees west geographic longitude) and GOES-15 (135 degrees west geographic longitude). Noon and midnight local time at the satellite are plotted as N and M.

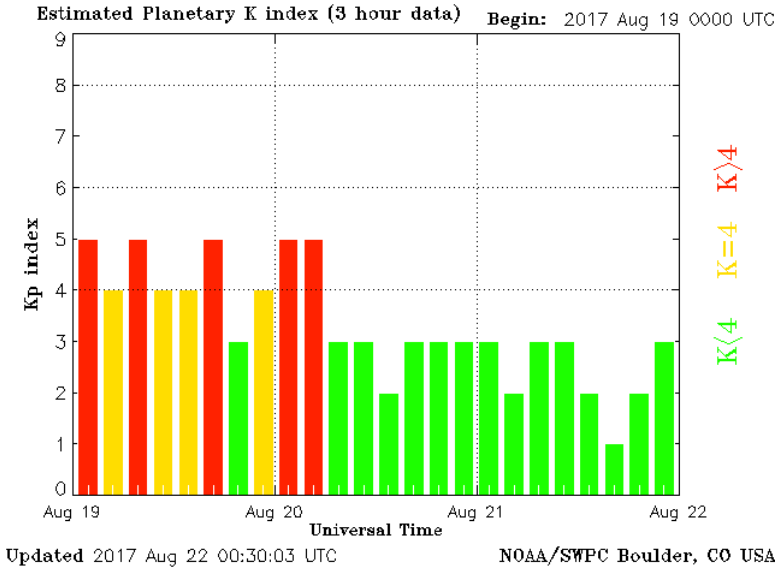

Figure 4.22: The Planetary K-index for the period August 19, 2017 to August 23, 2017.

The Planetary K-index, were used to characterize the magnitude of geomagnetic storms. The K-index quantifies with an integer in the range 0-9, the disturbances in the horizontal component of Earth's magnetic field. Calm weather has K-index 1 and a geomagnetic storm has K-index 5 or more. The magnetometer measures the maximum fluctuations of horizontal components during a three-hour interval. The planetary 3-hour-range index Kp is "the mean standardized K-index from 13 geomagnetic observatories between 44 degrees and 60 degrees northern or southern geomagnetic latitude" as quoted in the website [134]. Figure 4.22 shows that the K-index was around 3, which means calm situations during August 21 and August 22, 2017.

Acoording to Ref. [134], "The electron flux measured by the GOES satellites indicates the intensity of the outer electron radiation belt at geostationary orbit. Measurements were made in two integral flux channels, one channel measuring all electrons with energies greater than 0.8 million electron Volts (MeV) and one channel measuring all electrons with energies greater than 2 MeV.

Electron Event Alerts are issued when the >2 MeV electron flux exceeds 1000 particles/(cm^2 s sr). Abrupt increases and decreases in flux can occur due to reconfigurations in the magnetospheric magnetic field, as well as due to various particle acceleration and loss mechanisms. The electron fluxes at geostationary orbit typically have their highest values near local noon and their lowest values near local midnight. This spatial feature is due to the structure of the magnetospheric magnetic field, strong at noon and weak at midnight, caused by the pressure of the solar wind on the day

side of the magnetosphere". Figure 4.23 shows the electron fluence during August 19 and August 23, 2017. During the solar eclipse hours, there is a slight increasing trend visible in the plot, but this might be due to the nature of the diurnal variation. There was no special signature or Electron Event Alerts reported that could be referred to having an impact due to the solar eclipse.

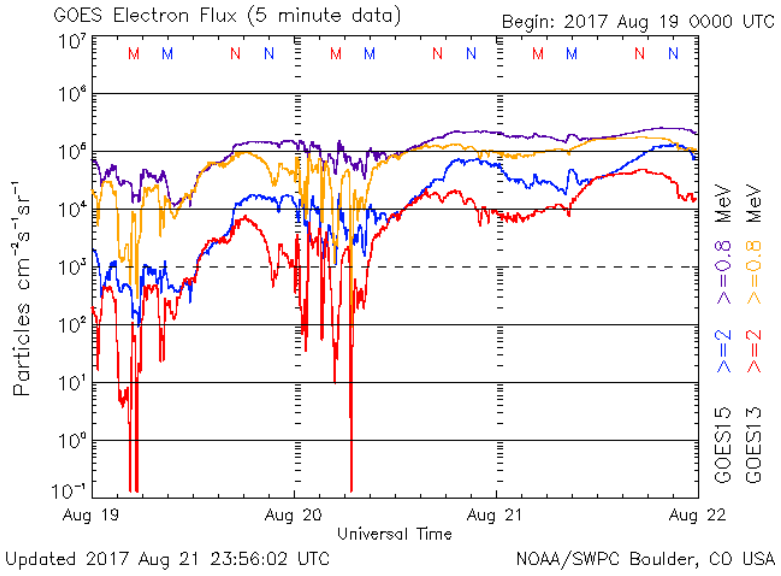

Figure 4.23: GOES electron fluence for the period August 19, 2017 to August 23, 2017.

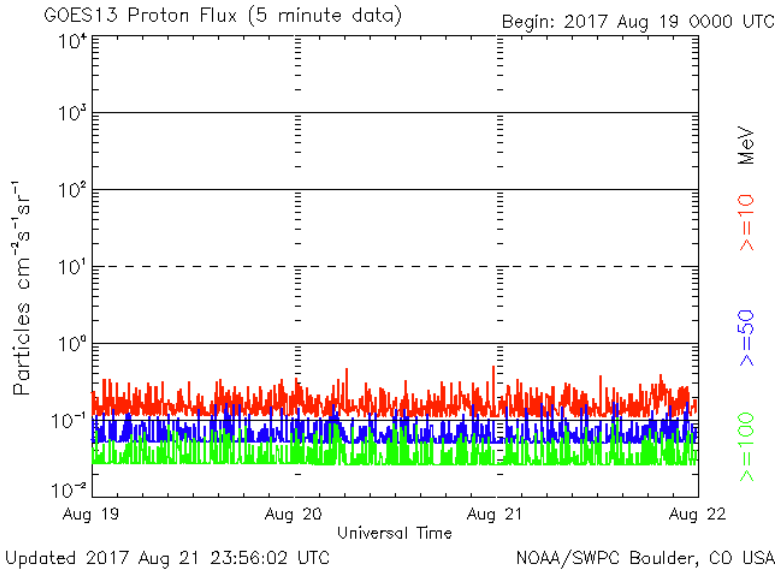

Figure 4.24: GOES proton fluence for the period August 19, 2017 to August 23, 2017.

There are high-energy proton detectors on the GOES geostationary and NOAA polar-orbiting satellites. Proton Event Alerts are issued upon confirmation of >10

MeV or >100 MeV Integral Flux exceeding certain thresholds like 10 pfu and 1 pfu, respectively. Figure 4.24 shows the proton fluence during August 19 and August 23, 2017. The plot clearly shows that there was no sudden changes in the proton fluence during the eclipse. It was more or less stable through out the 4 days.

4.3.5 Discussion

All earlier reports of flux variations are based on observations from measurements performed at places lying on the path of the solar eclipse i.e. the shadow region. Our experiment is unique in the sense that the measurements were done at a place lying on the other side of the globe. Therefore, all the explanations and interpretations of results obtained by earlier groups of researchers might not hold in our case. SCGR flux decrement of 9.1% in the energy range 25 - 100 keV, 0.8% decrement in the energy range 100 - 500 keV, 1.1% increment in the energy range 500 - 1000 keV, 3.1% decrement in the energy range 1000 - 1500 keV and 24.5% increment for energies above 1500 keV were observed. One more interesting thing is that the increment or decrement that was observed sustained throughout the solar eclipse duration that is from the time of the first contact to the time of the last contact. The count rates are consistent with each other before and after this duration. A tentative explanation of the observations is as follows. During a solar eclipse, the Moon's shadow constitutes a cooling region in the Earth's atmosphere that travels at supersonic speed which may generate a bow wave. This was first pointed out by Chimonas and Hines in 1970 [129] and later investigated by other groups [130, 131]. They predicted pressure perturbation that trails the umbra (in the form of a bow wave), and propagates sideways and upwards at a speed of about 250 m/sec to soon reach the ionospheric layers at around 200 km altitude. In reference [132] a strong signature of ionospheric bow waves was identified as disturbance in the Total Electron Content (TEC) over central/eastern United States during the Great American Eclipse 2017. Interestingly they not only found the eclipse bow wave in the ionosphere, they discovered strong TEC perturbations that move along meridional direction and zonal direction at supersonic speeds that are too fast to be associated with known large-scale traveling ionospheric disturbance (LSTID) processes or gravity wave . As mentioned in their paper, atmospheric and ionospheric disturbances can be excited by many different sources. In order to observe the bow waves, the atmospheric disturbances due to other sources should be minimal. This is a very important point that unless the environmental parameters during the eclipse are known, one cannot claim to observe an effect that is not very large. According to the data from NOAA's GOES there were no space weather turbulences on 21 August. The space weather is already summarized in Section 4.3.4. The planetary K index (K_p) had

a low value (<4) during the eclipse. The solar wind speed and geomagnetic parameters were also normal during the day of solar eclipse [133–135]. The overall conclusion that can be made from the NOAA's data is that there were no disturbances in the space weather conditions during the day of the solar eclipse event. Other atmospheric parameters like atmospheric pressure at Kolkata, showed no abnormal traits and no rainfall occurred throughout the days from 19 August to 23 August, 2017 during the experiment [136].

Connection between solar eclipse and total electron content

It is well-known that a solar eclipse can affect the Earth's upper atmosphere by significantly decreasing the ionospheric electron density. The idea was to draw a connection between the solar eclipse phenomena and the TEC of the atmosphere and from this try to explain the decrement in cosmic gamma ray intensity.
As discussed in Section 4.3.4, there were no disturbance in the space weather that could have caused significant decrement in cosmic gamma ray intensity. This means, the perfect clear weather on August 21, 2017 caused the effects of environmental parameters on the measured gamma ray fluxes to be negligible, thereby increasing the chances to observe the effects of the solar eclipse. This was an advantage for the bow waves which propagated to larger distances effectively. The implication of all these may be that it was observed in India, through gamma ray counts, some effects of the Travelling Ionospheric Disturbances (TIDs) during the solar eclipse in America. TIDs are propagating perturbations in the ionospheric electron density.

A possible connection between the TIDs and the secondary cosmic gamma-ray flux can be drawn as follows. The TIDs have the potential to increase or decrease the TEC in the region of the atmosphere they are traveling through. When the electron concentration increases in the ionospheric layers, the primary cosmic rays tend to lose more energy by bremsstrahlung while passing through it. In this process, mostly low energy gamma rays (X-rays) having energy in the range of few keV to few hundred keV are produced. If the TEC decreases, it will cause the low energy secondary gamma-ray flux to decrease. The speculation over here is that the TIDs reaching India due to the solar eclipse in America might have influenced the TEC in such a way that the low energy secondary gamma-ray flux decreased at the expected time of arrival of the TIDs.

The feasibility of this newly proposed mechanism was checked using ionospheric TEC data from Indian Institute of Geomagnetism (IIG). IIG operates GPS receivers to measure the ionospheric TEC across India. The data from two GPS stations nearby Kolkata were studied. Figure 4.25 shows the TEC variations measured during the period 19 August 2017 to 24 August 2017 by the GPS station at Shillong, India. From

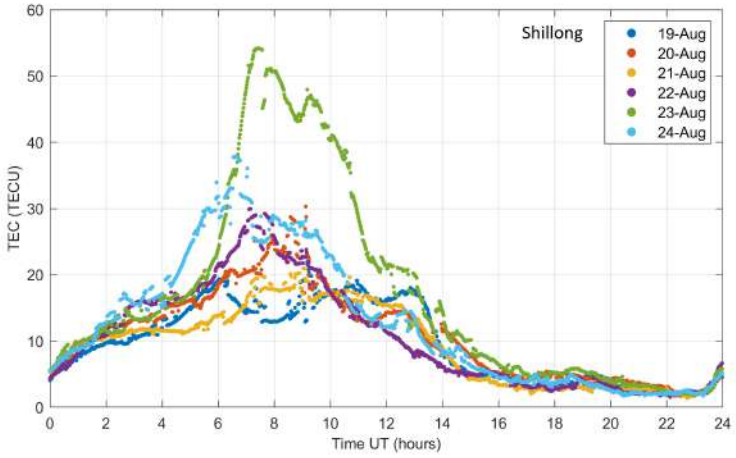

Figure 4.25: Total Electron Content (TEC) for the period 19 August to 24 August 2017, measured by GPS station at Shillong, India

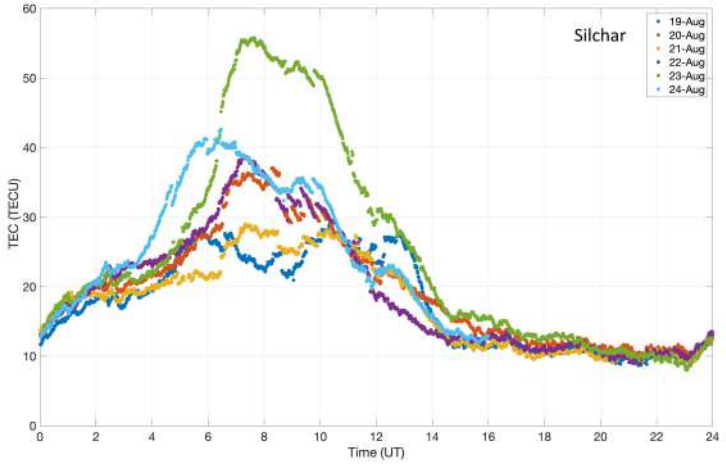

Figure 4.26: Total Electron Content (TEC) for the period 19 August to 24 August 2017, measured by GPS station at Silchar, India

the figure, it can be observed that the TEC value during the day of eclipse (August 21) denoted by the yellow marker, is lower than other days of the week. The eclipse started at 15:46 UTC and ended at 21:04 UTC on 21 August. Since the time at which the TIDs would arrive in India was unknown, so the TEC data was considered only

during the night time i.e. 16:00 UTC to 23:59 UTC, when large fluctuations due to solar radiation is absent. The average TEC value during the night of August 21 was compared with the average TEC value during the night of other days of the week. A reduction of 48 % in the average TEC on August 21 is found. TEC data from another station situated at Silchar is presented in Figure 4.26 and here also a similar trait in TEC was observed. Similar analysis was done with data from this station and a reduction of 20 % in the average TEC on August 21 is found. The observed reduction in the TEC during the night of August 21 along with the fact that weather was clear in India, is enough to conclude that the eclipse induced TIDs have possibilities to reach India.

The decrement in SCGR rate observed in 25 - 100 keV energy was not observed in any other day of the week. This may have occurred because the TEC disturbances had propagated all the way to Kolkata (approximately 13000 km from East-Central USA) and had an impact on the secondary gamma ray production in the atmosphere. The results obtained from this experiment using NaI(Tl) detector are statistically significant enough to conclude that there is some effect of the eclipse on the SCR fluxes even at places on the globe which do not fall within the path of the eclipse. According to calculations mentioned in Appendix II, it is found that the TEC zonal disturbance would have taken a minimum of 4 hr 36 min to travel from Oregon to Kolkata and reach here at 1:52 am IST 22 August. The meridional wave could have taken 2 hr 4 min to travel from St. Louis to Kolkata and arrive at around 00:51 am IST 22 August. But the time of propagation of the meridional disturbance could in fact be larger because the velocity of the wave used in the calculation is the maximum velocity; the actual velocity could be lower. Thus the zonal and meridional disturbances could have reached Kolkata almost at the same time causing the observed decrement in the gamma ray flux. However, this is just a speculation, not an assertion, it is really not known how fast a disturbance in TEC propagates and in which direction for a certain height of the layer. The decrement and increment observed in gamma ray counts in energy regions 100 - 500 keV and 500 - 1000 keV respectively are considered insignificant. The decrement of 3.1 % observed in the energy range 1 - 1.5 MeV, is in agreement with earlier report [122], where they observed 21 % drop in this energy range. There is no suitable explanation for the 24.5 % increment in gamma counts above energy 1.5 MeV. There was a report in the past by Jafferey *et al.* during the total solar eclipse on 24th October, 1995 [137] that showed enhancement in the radiations around 1.2 MeV. Recently, there was another report by A. Pandya who observed sizeable enhancement at the characteristic energy 1460 keV during a solar eclipse [138]. Both these groups explained this enhancement to be the phenomena of secondary radiations occurring near the limb of the Moon. This could be one of the

reason for the enhancement above energy 1.5 MeV. However, the actual reasoning for this observation cannot be given based only on the present measurements and needs to be confirmed in future eclipses. A detailed investigation must be carried out in the future for a deep understanding of the phenomenon and its consequences. It is hoped that this work will motivate others to study the propagation of atmospheric disturbances produced by the solar eclipse to places located far away from the path of the eclipse.

4.4 Cosmic muon measurement during solar eclipse

The cosmic muon was also measured in the period of August 18, 2017 to August 24, 2017. This measurement was done because, there is no existing strong reports on the cosmic muon flux measurement during solar eclipse. Results from earlier studies only refer the decrement in gamma flux. In our case, the measurement was conducted at a place which is half of the perimeter of the Earth away from the eclipse path. There could be chances that solar eclipse affects the interplanetary magnetic field, which governs the path of cosmic muons travelling towards Earth (suppose towards India). Then a slight change could be observed in the cosmic muon flux during the night time in India.

Experimental Setup

The experimental setup is shown in Figure 4.27. Conventional NIM electronics were used in this experiment. The PMT of the scintillator was biased with positive voltage from a High Voltage (HV) NIM module. The signal from the PMT was transferred to the Leading Edge Discriminator (LED) for rejection of noise signals.

To measure the cosmic muon flux, three plastic scintillator paddles were used. They stacked like one on top of the other on an aluminium rack as shown in Figure 4.27. The area of overlap or the effective area of the muon trigger was 100 cm^2. The HV to the PMT of all three scintillators was 1650 V and the LED threshold was set at -50 mV. Signals from the LED was fed to an AND logic unit (NIM standard) to generate the three-fold coincidence of the scintillators. Continuous data was taken throughout this period at an interval of 15 mins. The output of the logic AND (three-fold coincidence) was fed to a NIM-TTL converter and the produced TTL signal had a specific amplitude. This TTL signal was fed to a Multi channel analyser (MCA) which was programmable to take continuous data at regular intervals. MCA was used to save the data that was accumulated every 15 mins automatically.

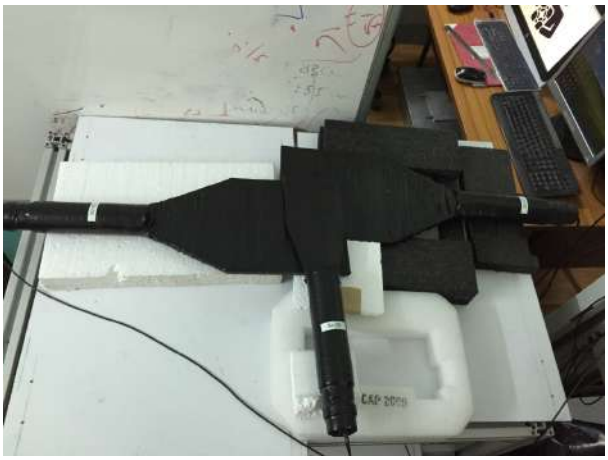

Figure 4.27: Experimental setup for the cosmic muon flux measurement. Three scintillators, Sc-01, Sc-03 and Sc-04 form the trigger system for cosmic ray muons.

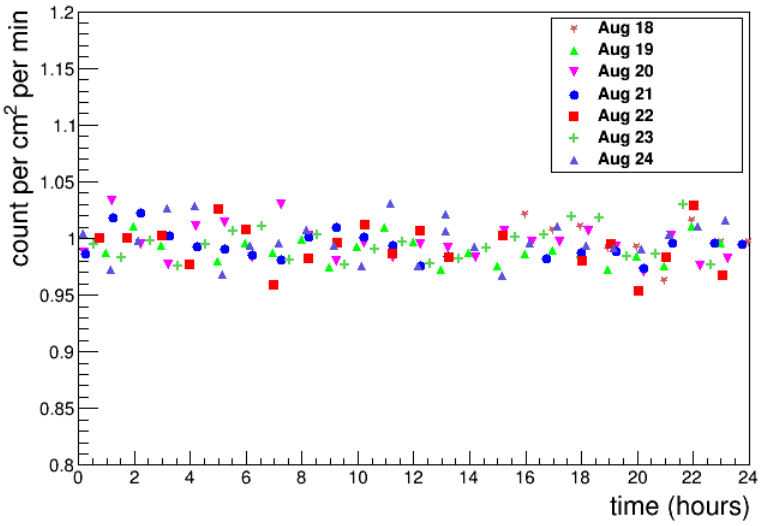

Figure 4.28: Cosmic muon count for the period 18 August to 24 August 2017, measured by trigger scintillators in Kolkata, India. Error bars are smaller than the marker size.

Results

Figure 4.28 shows the count of muon recorded on an average in one hour by the trigger detector setup for all the 7 days. A day-night variation in the cosmic muon flux was observed for all the days of the week. The average muon flux during the solar eclipse was similar to that during the normal days. Figure 4.29 shows the variation of muon flux during the night time, to get a closer view of the muon flux fluctuations during the eclipse and other days. Overall, it can be concluded that in our experiment no significant change in the muon flux was observed during the solar eclipse.

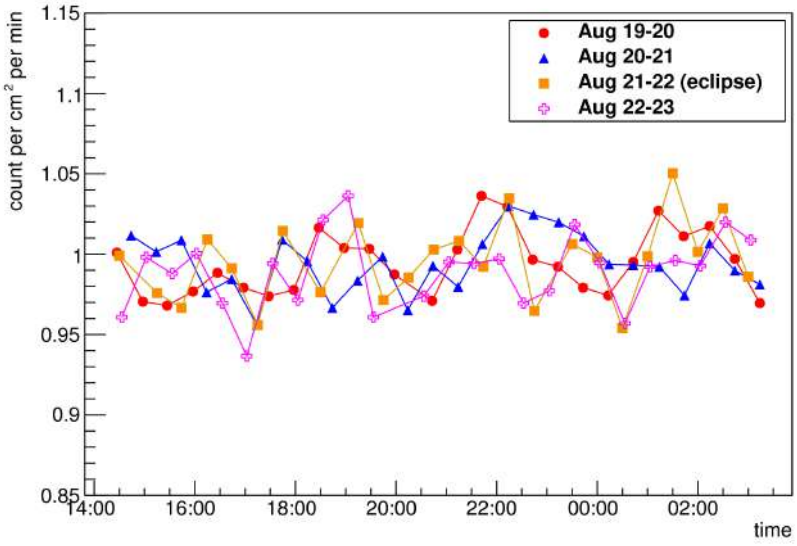

Figure 4.29: Cosmic muon count during the night (including the solar eclipse hours) for the period 19 August to 23 August 2017, measured by trigger scintillators in Kolkata, India. Error bars are smaller than the marker size.

Chapter 5

Summary

This chapter summarizes the key findings of the research in relation to the research questions, as well the importance and primary contribution thereof. It also reviews the limitations of the study and proposes future research opportunities. The thesis is based on characterization and application of detectors in two important experimental research fields, high energy physics and cosmic rays. This chapter will address the three classified aims of the thesis separately and discuss the outcome of the studies individually.

The first aim of the study was to investigate the feasibility of using the classical Straw Tube detectors for the CBM-MuCh detector system. The results from our experiments indicate that straw tubes can withstand the particle rates expected at the 3^{rd} and 4^{th} station of CBM-MuCh. Further findings were that, the straw tubes show long-term stable operation when subjected to low radiation rates, but show a transient aging when subjected to high radiation rates, which can be controlled by changing the gas flow rate. This effect is insignificant in the scenario of CBM experiment, and overall conclusion was that straw tubes can be safely used in the 3^{rd} and 4^{th} station CBM-MuCh.

The second aim of the thesis was to develop an air shower array made of plastic scintillation detectors at high altitude for the study of cosmic ray showers. For this purpose, large size detectors were fabricated and an array of detectors was commissioned at high altitude. Successful operation of the array resulted in collection data of cosmic ray air showers for one year. The air shower rate was compared to that measured by GRAPES-3 experiment which has a very large air shower array at similar altitude.

The third aim was to study a correlation between solar eclipse and cosmic rays using inorganic scintillation detector. An experiment was setup to measure the cosmic ray gamma flux using NaI(Tl) scintillator during the total solar eclipse on 21 August 2017 taking place in North America. Results show that there is decrement in cosmic ray gamma flux during the eclipse when measured at Kolkata, India. Further, it indicates

a possibility for eclipse-induced atmospheric disturbances to travel large distances and affect the total electron content of the atmosphere globally, thereby impacting on the cosmic ray intensity.

Straw Tube Detector for the CBM experiment

In the CBM experiment, the challenge is to develop a large-acceptance fast detector and set up a high-speed data read-out system capable to run under conditions with high-luminosity beams delivered by FAIR. The di-lepton physics study is a very important part of the CBM research program. This is the main motive behind the construction of the MuCh detector. The MuCh detector system will have 4 stations in the SIS100-B setup. The first two stations of MuCh will consist of triple Gas Electron Multiplier (GEM) detectors, because the particle rate will be of the order of MHz and conventional wire chambers cannot handle that high rate. The third and fourth stations will have straw tube detectors instead of GEMs to cover larger active detection area at low cost. The aim of the study was to test the performance of straws at close to CBM-MuCh environment. The MuCh detector performance evaluation with straw tubes using the Monte Carlo simulation is already done by other groups. We have performed characterization of straw tubes with a prototype detector in our laboratory. The time resolution of the prototype detectors in our experiment using cosmic rays as the trigger was found to be (14.4 $\pm$ 1.6) ns at 1900 V. This value could be lower if the same measurement is done with particle beams and not cosmic rays. The reason is that, with collimated beams, the drift time of the charge carriers inside the gaseous medium suffers less fluctuations due to irradiation over a small and concise region of the straw tube. Whereas, cosmic rays can pass through the straw tube at any distance from the anode wire, causing greater fluctuations in the drift time, therefore the time resolution measured with cosmic rays will be higher than that with collimated beams. The rate handling capability of the straws was studied in order to justify its use in the 3^{rd} and 4^{th} stations of MuCh. For central Au-Au collisions at 10 AGeV (interaction rate-1 MHz) the expected particle rates at the 3^{rd} and 4^{th} stations of MuCh are 15 kHz/cm^2 and 5.6 kHz/cm^2, respectively. Our experiment shows that for the gas mixture Ar/CO_2 70/30, the straws can handle particle rates upto 0.6 MHz/cm^2 and for Ar/CO_2 90/10 upto rates of about 1 MHz/cm^2, which concludes that straws can be safely used in the MuCh subsystem. Beyond these rates, the gain decreases and energy resolution value increases with rate because of the space charge effect which is common in gaseous detectors.

Aging in gaseous detectors is a strong challenge when it comes to its use in HEP

experiments that is designed to run for several years alike CBM experiment. For minimum ionizing particle (MIP) the charge accumulated along the length in the straws at the 3^{rd} station of CBM-MuCh for three months of operation is estimated to be 8.6 mC/cm. In this regard, two separate experiments were performed to test the aging in straw tube detectors with Ar/CO_2 gas mixture. In experiment I, only one straw tube was operated and we observed slight gain reduction of about 9.6% per C/cm after a total charge accumulation of 600 mC/cm wire on the straw. The reason for the gain degradation was not understood, and therefore in experiment II, we used two straws, one as test detector (straw A) and the other as reference detector (straw R). On purpose, the straw A was operated at higher gains ($\sim 10^4$) and higher in radiation rates (35 kHz/mm) compared to straw R (gain $\sim 6 \times 10^3$, rate = 0.9 kHz/mm). The gas flow rate was lower than in experiment I. Both the straws were connected to the same gas line such that any external factors affecting the performance of the straws cancel out on taking the ratio of any measured quantity such as the gain or the energy resolution. In experiment II, a gain reduction was observed thereby verifying the observation of experiment I. From this experiment, we confirmed that the occurred aging in straws was due to the high intensity of irradiation. Further, it was found that the aging rate has a dependency on the gas flow rate. Important findings were that straw tubes showed 'transient aging', which could be controlled by increasing the gas flow rate.

Regarding the use of straw tubes in CBM-MuCh, the following conclusions can be made on the basis of our experiment. From the aging tests of the straws with Ar/CO_2 80/20, the overall conclusion is that the straw tubes can be safely operated continuously at low radiation intensities ($\sim$ 0.1 kHz/mm or 1.6 kHz/cm^2) and at low gas flow rates ($\sim$ 0.02 l/h) (as no aging observed in straw R of experiment II) and at high radiation intensities ($\sim$ 40 kHz/mm or 0.7 MHz/cm^2) at high gas flow rates (>3 l/h) (which means that, at CBM-MuCh 3^{rd} station, straw gain will decrease by 0.08% in 3 months operation). However, if straws are operated at high radiation intensities and low gas flow rates, transient aging is observed, for e.g. at CBM-MuCh 3^{rd} station, straw gain will decrease by 1% in 3 months operation, which can be controlled by increasing the gas flow rate. It takes about 3 hrs time for the gain of a continuously irradiated straw to partially restore after increasing the gas flow rate.

One of the limitations of our research was that, all the results were obtained using radioactive source of X-ray in our lab and not using any accelerator facility. The X-ray energy was greater than the mean energy deposited by the MIPs in the active detector volume.

Detector development for the study of Cosmic Rays

For the detection and study of cosmic rays, we have built an experimental set-up in the laboratory of Bose Institute, Kolkata to measure the cosmic ray flux.
We have also built an air shower array of seven PSDs covering an area of 168 m^2 and commissioned it at an altitude of 2200 meters above sea level in the Eastern Himalayas (Darjeeling) for the study of cosmic rays at high altitude. It was found that the most probable value of the air shower rate is 1.3 ± 0.01 Hz with a year round 10% variation. This value was compared and justified with that obtained at GRAPES-3. We also measured the large shower rate (seven fold coincidence) and the value was found to be (0.044 ± 0.0009) Hz. The future plan is to extend this to an array of 64 such detectors and build a muon tracker-detector system to identify the muons in the air shower.
A GEANT4 simulation was done to check the feasibility of tracking cosmic ray muons with silicon pad sensors (a type of semiconductor detector). The first design of the tracker was proposed and it has 10 layers of detector planes, each having 10×10 silicon pads of area 1 cm $\times$ 1 cm. Simulation results show that the tracker has a good momentum resolution ($< 3\%$) in the energy range 200-1000 MeV/c when magnetic field is set at 0.5 Tesla. However, it is still possible to reconstruct the muon momentum upto 4000 MeV/c at 1 Tesla magnetic field. Results show that it is feasible to develop a cosmic ray muon tracker of the above mentioned dimensions to find momentum of low energy muons (<5 GeV) at high altitude with a suitable and practical value of magnetic field.

Interplay between Solar Eclipse and Cosmic Rays

Solar eclipses have potential to produce disturbances in the Earth's atmosphere that can travel large distances and effect the cosmic ray intensity. To experimentally verify this statement, we have systematically measured the Secondary Cosmic Gamma Ray (SCGR) flux using a NaI(Tl) scintillator in India, during a total solar eclipse on August 21, 2017 that took place over America. We observed maximum decrement of gamma ray flux of about 9.1% in the energy range 25-100 keV with a good statistics of data. A decrement of 0.8% in the energy range 100 - 500 keV and 1.1% increment in the energy range 500 - 1000 keV was considered insignificant. One interesting thing is that the increment or decrement that we observed were sustained throughout the duration of the solar eclipse that is from the time of the first contact till the time of the last contact. The count rates are consistent with each other before and after this duration. To explain the decrement in the low energy gamma rays, a correlation of the SCGR

with the Total Electron Content (TEC) of the atmosphere was drawn. We have also checked the space weather during the entire period of measurement and found that there were no unusual events, apart from the solar eclipse itself, that could affect the atmospheric parameters.

Solar eclipse induced disturbances (like Travelling Ionospheric Disturbances (TID)s) can travel large distances (from North America to India) and influence the TEC in Indian atmosphere. The SCGR and TEC correlation was checked using ionospheric TEC data from two stations of Indian Institute of Geomagnetism (IIG). Data shows that there is good correlation between the two and that during solar eclipse there was a TEC decrement of 48% and 20% in the two stations respectively. Calculations show that TIDs could have taken approximately 4 hours to travel from Oregon to Kolkata (see Appendix 3). The TEC disturbance could reach Kolkata at 1:52 am IST 22 August, which is the time when we observed a sudden drop of 11% in the measured SCGR flux. However, it is difficult to explain this observation cannot be given based only on the present measurements and needs to be confirmed in future eclipses. In the energy range 1 - 1.5 MeV, we observed decrement of 3.1 %, which is in agreement with earlier report, where they observed 21 % drop in this energy range. We have not found any suitable explanation for the 24.5 % increment in gamma counts above energy 1.5 MeV. There was a report in the past by Jafferey *et al.* during the total solar eclipse on 24^{th} October 1995, that showed enhancement in the radiations around 1.2 MeV. Recently, there was another report by A. Pandya who observed sizeable enhancement at the characteristic energy 1460 keV during a solar eclipse. Both these groups explained this enhancement to be the phenomena of secondary radiations occurring near the limb of the Moon. This could be one of the reason why we observed enhancement above energy 1.5 MeV. The novelty of this work is an effort to study the geophysical effect due to solar eclipse through cosmic rays.

Bibliography

[1] C. Grupen, *Astroparticle Physics*, ISBN -10 3-540-25312-2 (2005)

[2] Korff, S.A. (1958). Geiger Counters. In: Creutz, E. (eds) Nuclear Instrumentation II / Instrumentelle Hilfsmittel der Kernphysik II. Encyclopedia of Physics / Handbuch der Physik, vol 8 / 45. Springer, Berlin, Heidelberg.

[3] https://home.cern/science/experiments/alice

[4] https://alice-tpc.web.cern.ch/

[5] https://atlas.cern/Discover/Detector

[6] https://panda.gsi.de/

[7] https://home.cern/science/experiments/compass

[8] https://home.cern/science/experiments/cms

[9] http://dpnc.unige.ch/dampe/

[10] F. Sauli, *Principles of operation of multiwire proportional and drift chambers*, Lecture Notes CERN **77-09** 1997

[11] Glenn F. Knoll, *Radiation Detection and Measurement*, Third Edition, John Wiley and Sons, Inc.

[12] William R. Leo, *Techniques for Nuclear and Particle Physics Experiments,A How-to Approach,* (Second Revised Edition, Springer-Verlag Berlin Heidelberg GmbH)

[13] K. Fukushima and T. Hatsuda, *The phase diagram of dense QCD*, Rept. Prog. Phys. **74** 014001 (2011)

[14] https://home.cern/science/accelerators/large-hadron-collider

[15] https://www.bnl.gov/rhic/

[16] https://fair-center.eu/

[17] I. Selyuzhenkov, *Status of the FAIR facility in Darmstadt*, Journal of Physics: Conference Series. **1685** 012020 (2020)

[18] http://www.fair-center.eu/for-users/experiments/cbm.html

[19] Compressed Baryonic Matter Experiment Technical Status Report (2005)

[20] https://cds.cern.ch/record/2729160/plots

[21] J. Cleymans, H. Oeschler, K. Redlich, and S. Wheaton, *Comparison of chemical freeze-out criteria in heavy-ion collisions*, Phys. Rev. C **73**, 034905 (2006)

[22] https://www.bnl.gov/rhic/star.php

[23] P. Braun-Munzinger *et al.*, *Hadron production in Au-Au collisions at RHIC*, Phys. Lett. B518, **41** (2002)

[24] https://shine.web.cern.ch/

[25] F. Becattini, *et al.*, *Chemical equilibrium study in nucleus-nucleus collisions at relativistic energies*, Phys. Rev. C **69**, 024905 (2004)

[26] P. Salabura [HADES], *Hades experiment probing baryonic matter at SIS18 overview of results*, EPJ Web Conf. **137** (2017), 09008

[27] S. Alexander, *Status of the NICA Project* **042** 10.22323/1.217.0042 (2015)

[28] T. Ablyazimov, *et al.*, *Challenges in QCD matter physics –The scientific programme of the Compressed Baryonic Matter experiment at FAIR*, Eur. Phys. J. A **53**, 60 (2017)

[29] B. Friman *et al.* (Eds.), The CBM Physics Book, Lect. Notes Phys. **814**, Springer (2011)

[30] Heuser, *et al.*, *Status of the CBM experiment*, The European Physical Journal Conferences **95** 01006 (2015)

[31] P. Senger, *Status of the Compressed Baryonic Matter experiment at FAIR*, International Journal of Modern Physics E **29**, No. 02, 2030001 (2020)

[32] https://git.cbm.gsi.de/computing/cbmroot

[33] Technical Design Report for the CBM : Muon Chambers (MuCh), http://repository.gsi.de/record/161297

[34] G. Charpak, *et al.*, *The use of multiwire proportional counters to select and localize charged particles*, Nucl. Instrm. and Meth. A, Vol **62** (1968) 262

[35] A. Kumar, *et al.*, *Testing of triple gem prototypes for the CBM Muon Chamber system in the mCBM experiment at the SIS18 facility of GSI*, JINST **15** 10 (2020)

[36] R. P. Adak, *et al.*, *Long-term stability test of a triple GEM detector*, JINST **11** T10001 (2016)

[37] S. Roy, *et al.*, *Stability study of gain and energy resolution for GEM detector*, Nucl. Instrm. Meth. A, Vol **936** (2019)

[38] S. Chatterjee, *et al.*, *Study of uniformity of characteristics over the surface for triple GEM detector*, Nucl. Instrm. Meth. A, Vol **936** (2019)

[39] V. Peshekhonov, *et al.*, *Straw Tube Subsystem of the CBM Muon Detector*, Physics of Particles and Nuclei Letters Vol. **9**, No.2, (2012)

[40] V. Peshekhonov *et al.*, *Straw tube subsystem of the CBM muon detector*, CBM Progress Report (2008) 35

[41] Todor Stanev, *High Energy Cosmic Rays*, Second Edition, Springer ISBN 978-3-540-85 47-9

[42] Peter K. F. Grieder, *Cosmic Rays At Earth*, ISBN: 0 444 50710 8 (2001)

[43] https://$www.icrr.u-tokyo.ac.jp/en/research\_projects/$

[44] https://grapes-3.tifr.res.in/

[45] https://web.ikp.kit.edu/KASCADE/

[46] https://www.auger.org/

[47] https://en.wikipedia.org/wiki/Solar_eclipse_of_August_21,_2017

[48] R. N. Patra, *et al.*, *Measurement of basic characteristics and gain uniformity of a triple GEM detector*, Nucl. Instrm. Meth. A **862** (2017)

[49] R. N. Patra, *et al.*, *Characterisations of GEM detector prototype*, Nucl. Instr. Methods A **824** (2016)

[50] T. Åkesson, *et al.*, *Straw tube drift-time properties and electronics parameters for the ATLAS TRT detector*, Nucl. Instrm. Meth. A, **449** (2000)

[51] T. Åkesson, *et al.*, *Study of straw proportional tubes for a transition radiation detector/tracker at LHC*, Nucl. Instr. and Meth. in Phys. A **361** (1995)

[52] C. Adorisio, *et al.*, *A non-invasive technique to replace the anode wires into the drift tube chambers of the muon spectrometer of the ATLAS experiment at the LHC proton-proton collider*, Nucl. Instrm. Meth. A, **575** (2007)

[53] https://www6.slac.stanford.edu/about/slac-overview

[54] D. R. Rust, *Recent developments in high precesion vertex chambers at SLAC*, SLAC-PUB 3311, IUHEP-54, April 1984

[55] W. W. Ash, *et al.*, *Design, construction, prototype tests and performance of a vertex chamber for the MAC detector*, Nucl. Instr. and Meth. in Phys. A **261** (1987)

[56] V.A. Polychronakos, *Integrated high-rate transition radiation detector and tracking chamber for the LHC*, CERN/DRDC/90-38 (1990)

[57] https://home.cern/news/news/experiments/new-straw-trackers-na62

[58] Y. Van Haarlem, *et al.*, *The GlueX central drift chamber: Design and performance*, Nucl. Instr. and Meth. in Phys. A **622** (2019)

[59] T. Åkesson, *et al.*, *Straw tube drift-time properties and electronics parameters for the ATLAS TRT detector*, Nucl. Instr. and Meth. in Phys. A **449** (2000)

[60] J. A. Kadyk, *et al.*, *Use of straw tubes in high-radiation environments*, Nucl. Instr. and Meth. in Phys. A **300** (1991)

[61] J. Va'vra, *Review of wire chamber aging*, Nucl. Instr. Meth. in Phys. A **252** (1986)

[62] M. Titov *et al.*, *Summary and Outlook of the International Workshop on Aging Phenomena in Gaseous Detectors (DESY, Hamburg, October 2001)*, https://cds.cern.ch/record/546220/files/cer-002303542.pdf (downloaded on 13.06.2022)

[63] M. C. Altunbas, *et al.*, *Aging measurements with the gas electron multiplier (GEM)*, Nucl. Instrum. Meth. A **515** (2003)

[64] V. G. Bondarenko, *et al.*, *Studies of radiation aging of the straw proportional tubes with Xe-CO2-CF4 gas mixture*, Nucl. Phys. B - Proceedings Supplements **44** (1995) 577.

[65] M. Capeans, *et al.*, *Ageing properties of straw proportional tubes with Xe/CF_4 $/CO_2$ gas mixture*, CERN-PPE/93-136 (1993)

[66] P. Cwetanski, *STRAW PERFORMANCE STUDIES AND QUALITY ASSURANCE FOR THE ATLAS TRANSITION RADIATION TRACKER*, Dissertaion published in Report series in Physics, ISBN 952-10-2121-7 (2006)

[67] V. Blinov, *Influence of materials and sense wire surface quality on aging with DME and other gases*, Proceedings of the International Workshop on Aging Phenomena, DESY, Hamburg, Oct. 2-5, (2001)

[68] T. Kowalski, *A study of aging effect in gas monitoring proportional counters of the BAC calorimeter of the ZEUS experiment*, Proceedings of the International Workshop on Aging Phenomena, DESY, Hamburg, Oct. 2-5, 2001

[69] M. Capeans, *et al.*, *Recent Aging Studies for the ATLAS Transition Radiation Tracker*, IEEE TRANSACTIONS ON NUCLEAR SCIENCE, VOL. **51**, NO. 3, JUNE (2004)

[70] T. Åkesson, *et al.*, *Aging studies for the ATLAS Transition Radiation Tracker (TRT)*, Nucl. Instr. and Meth. in Phys. A **515** (2003)

[71] R. P. Adak *et al.*, *R&D on Straw Tube detector for CBM Muon Chamber*, Proceedings of the DAE-BRNS Symposium on Nuclear Physics Vol. **61** (2016)

[72] N. Nandi *et al.*, *Characterization of Straw tube detector*, Proceedings of the DAE Symp. on Nucl. Phys. Vol. **62** (2017)

[73] S. Roy *et al.*, *Variation of gain and energy resolution with temperature and pressure of straw tube detector*, Proceedings of the DAE Symp. on Nucl. Phys. Vol. **63** (2018)

[74] S. Roy *et al.*, *R&D of Straw Tube detector for High Energy Physics experiments*, Proceedings of the DAE Symp. on Nucl. Phys. Vol. **64** (2019)

[75] J. Bortfeldt, *Development of Micro - Pattern Gaseous Detectors – Micromegas*, Thesis submitted at Ludwig-Maximilians-Universitat Munchen (2010)

[76] CDT CASCADE Detector Technologies GmbH, Hans-Bunte-Str. 8-10, 69123 Heidelberg, Germany, www.n-cdt.com.

[77] R. P. Adak, *et al.*, *Study of characteristics of Straw Tube detector for CBM Muon Chamber*, CBM Progress Report (2016)

[78] Shreya Roy, Master's Thesis, *https : //indico.gsi.de/event/6440/contributions/29549/attachmer* (downloaded on 20 May 2022)

[79] S. Sahu, *et al.*, *Design and fabrication of data logger to measure the ambient parameters in gas detector R&D*, JINST **12** C05006 (2017)

[80] S. Roy, *et al.*, *Stability study and time resolution measurement of Straw Tube detectors*, Pramana – J. Phys. **95:50** (2021)

[81] A. Andronic, *et al.*, *A comprehensive study of rate capability in Multi-Wire Proportional Chambers*, JINST **4**, 10 (2009)

[82] V. Peshekhonov, *TRD Straw Tracker*, Talk given on the CBM Collaboration Meeting in Strasbourg, 2006.

[83] N. A. Kuchinskiy, *et al.*, *2-D straw detectors with high rate capability*, arXiv 1502.05363 (2017)

[84] E. Nandy *et al.*, *Feasibility Study of Using RPCs in CBM Muon Chamber*, Proceedings of the DAE-BRNS Symp. on Nucl. Phys. **61** (2016)

[85] S. Roy *et al.*, *Study of performances of a straw tube detector with high rate*, Nucl. Instrm. Meth. A Vol **936** (2019)

[86] S. Roy *et al.*, *Aging studies of Straw tube detector*, CBM Progress Report 2018, ISBN 978-3-9815227-6-1, DOI:10.15120/GSI-2019-01018

[87] J. A. Kadyk, *Wire chamber aging*, Nucl. Instr. Meth. in Phys. A **300** (1991)

[88] V. Pashhoff, *Studies on ageing and reanimation of drift tubes for the ATLAS muon spectrometer*, Dissertation, University Freiburg, CERN-THESIS-99-083 (1999)

[89] M. Aglietta, *et al.*, *The EAS-TOP array at Gran Sasso: results of the electromagnetic detector*, Nucl. Phys B **16** 493 (1990)

[90] M. Aglietta, *et al.*, *Detection of the UHE Burst from the Crab Nebula on February 23, 1989, from the EAS-TOP Array*, Europhysics Letters 1 **15** 81 (1991)

[91] S. K. Gupta, *et al.*, *The current status of the GRAPES-3 extensive air shower experiment*, Nuclear Physics B - Proceedings Supplements, **196** 153M (2009)

[92] KASCADE Collaboration, *Electron, muon, and hadron lateral distributions measured in air showers by the KASCADE experiment*, Astroparticle Physics **14** 245 (2001)

[93] W. D. Apel, *et al.*, *The KASCADE-Grande experiment*, Nucl. Instrm. Meth. A **620** 202 (2010)

[94] H. Zhang, *et al.*, *Measurement of muon contents in cosmic ray shower with LHAASO-KM2A around knee region*, emphPoS (ICRC2021) **352** (2021)

[95] S. K. Gupta, *et al.*, *GRAPES-3 A high-density air shower array for studies on the structure in the cosmic-ray energy spectrum near the knee*, Nucl. Instrm. and Meth. in Phys. A **540** 311 (2005)

[96] A. Aab (Pierre Auger Collaboration), *Muons in Air Showers at the Pierre Auger Observatory: Mean Number in Highly Inclined Events*, *Phys. Rev. D* **91** 3, 032003 (2015)

[97] T. K. Gaisser, *Spectrum of cosmic-ray nucleons, kaon production, and the atmospheric muon charge ratio*, Astroparticle Physics **35** 801-806 (2012)

[98] P. Abreu (Pierre Auger Collaboration), *The energy spectrum of cosmic rays beyond the turn-down around 10^{17} eV as measured with the surface detector of the Pierre Auger Observatory*, Eur. Phys. J. C **81** 966 (2021)

[99] J. B. Birks, *The Theory and Practice of Scintillation Counting*, Pergamon Press Ltd. (1964)

[100] S. Shaw, *et al.*, *Study of cosmic ray with plastic scintillator detector*, Proceedings of the DAE Symp. on Nucl. Phys. Vol. **62** (2017)

[101] S. Roy, *et al.*, *Measurement of angular variation of cosmic ray flux with plastic scintillator*, Proceedings of ADNHEAP, Springer Book Series $doi.org/10.1007/978-981-10-7665-720$

[102] M.P. De Pascale, *et al.*, *Absolute spectrum and charge ratio of cosmic ray muons in the energy region from 0.2 GeV to 100 GeV at 600 m above sea level*, J. Geophys. Res. **98** 3501 (1993)

[103] K. Nakamura, *et al.*, *Cosmic Rays* (PDG), JP G37, 075021 (2010)

[104] http://www-akeno.icrr.u-tokyo.ac.jp/AGASA/

[105] P. K. Mohanty, S. R. Dugad, S. K. Gupta, *Monte Carlo code G3sim for simulation of plastic scintillator detectors with wavelength shifter fiber readout*, Review of Scientific Instruments **83** 043301 (2012)

[106] P.K. Mohanty, *et al.*, *Measurement of some EAS properties using new scintillator detectors developed for the GRAPES-3 experiment*, Astroparticle Physics **31** 24 (2009)

[107] S. Roy, *et al.*, *Development of an Extended Air Shower array at Darjeeling : an update*, Springer Proceedings in Physics **261** (2021)

[108] https://www.spaceweatherlive.com/en/solar-activity/top-50-solar-flares/year/2018.

[109] ftp://ftp.swpc.noaa.gov/pub/forecasts/SGAS/

[110] $http://tesis.lebedev.ru/en/forecast\_activity.html?m=3\&d=19\&y=2018$.

[111] S. Biswas, *et al.*, *Development of scintillator detector for detection of cosmic ray shower*, JINST **12** (2017) C06026

[112] S. Roy, *et al.*, *Plastic scintillator detector array for detection of cosmic ray air shower*, Nucl. Instrm. Meth. A Vol **936** (2019)

[113] M. Zuberi, *et al.*, *Dependence of the GRAPES-3 EAS particle density and trigger rate on atmospheric pressure and temperature*, PoS (ICRC2017) 302

[114] S. Muhuri, *et al.*, *Test and characterization of a prototype silicon-tungsten electromagnetic calorimeter*, arXiv:1407.5724v1

[115] S. Agostinelli, *et al.*, *GEANT4—A Simulation Toolkit*, Nucl. Instrm. Meth. A Vol **506** (2003)

[116] X. Chen, *et al.*, *Global Effects of a Polar Solar Eclipse on the Coupled Magnetosphere-Ionosphere System*, Geophysical Research Letters, Vol. **48**, Issue 23 (2021)

[117] S. D. Eckermann, *et al.*, *Atmospheric effects of the total solar eclipse of 4 December 2002 simulated with a high-altitude global model*, J. Geophys. Res, Vol. **112**, D14105 (2007)

[118] A. Bhattacharya, *et al.*, *Transient Variation of Cosmic Ray Intensity*, Current Science **98**, 1609-1614 (2010)

[119] Chintalapudi, *et al.*, *γ and X ray measurements during the total solar eclipse on October 24, 1995 at Diamond Harbour*, Kodaikanal Obs. Bull 13 (1997) http://hdl.handle.net/2248/6022

[120] A. Bhattacharyya, *et al.*, *Variation of γ-ray and particle fluxes at the sea level during the total solar eclipse of 24 October, 1995*, Astrophysics and Space Science **250**: 313 (1997)

[121] P. K. Nayak, *et al.*, *A study of the γ-ray flux during the total solar eclipse of 1 August 2008 at Novosibirsk, Russia*, Astroparticle Physics Vol. **32**, Issue 6 (2010)

[122] A. Bhaskar, *et al.*, *A study of secondary cosmic ray flux variation during the annular eclipse of 15 January 2010 at Rameswaram, India*, Astroparticle Physics Vol. **35**, Issue 5 (2011)

[123] V. P. Antonova, *et al.*, *Effect of Solar Eclipses on Neutron Flux Variations at the Earth's Surface*, Bull. Russ. Acad. Sci. Phys. **71**: 1054 (2007)

[124] W. Van Sciver and R. Hofstadter, *Scintillations and Luminescence in Unactivated NaI* Phys. Rev. **97** 1181 (1955)

[125] K. D. Ianakiev, *et al.*, *Temperature behavior of NaI(Tl) scintillation detectors*, Nucl. Instrm. Meth. A Vol **607** (2006)

[126] H. B. Dietrich, A. E. Purdue, R. B. Murray, and R.T. Williams, *Branching transport model of NaI (Tl) alkali-halide scintillator*, Phys. Rev. B, Vol. **8**, p. 5894 (1973)

[127] S. Roy, *et al.*, *A study of the secondary cosmic γ-ray flux in India during the Great American solar eclipse on 21st August 2017*, Astrophysics and Space Science **365** 172 (2020)

[128] P. K. Nayak, *et al.*, *Study of terrestrial γ-ray background in presence of variable radioactivity from rain water*, Astroparticle Physics **72** (2016)

[129] G. Chimonas, *Atmospheric gravity waves induced by a solar eclipse*, Journal of Geophysical Research, Space Physics Vol. **75** No. 28 (1970)

[130] M. J. Davis, *et al.*, *Magnetic observations in Canada during the solar eclipse of March 7, 1970*, Nature, **226** (5251), 1123–1123 (1970)

[131] T. Beer, *et al.*, *Atmospheric gravity waves to be expected from the solar eclipse of June 30, 1973*, Nature **240** (5375), 30–32 (1972)

[132] S. Zhang, *et al.*, *Ionospheric Bow Waves and Perturbations Induced by the 21 August 2017 Solar Eclipse*, Geophys. Res. Lett., Vol. **44**, 12,067–12,073 (2017)

[133] https://www.swpc.noaa.gov/

[134] https://www.gfz-potsdam.de/en/kp-index/

[135] https://www.swpc.noaa.gov/products/solar-and-geo physical-activity-summary

[136] https://www.timeanddate.com/weather/india/kolkata/ historic?month=8&year=2017

[137] S. N. A. Jafferey, *el al.*, *High energy photon detection using scintillation counter during total solar eclipse of October 24, 1995 Kodaikanal Obs. Bull.*, Vol. **13** (1997)

[138] A. Pandya, *et al.*, *Variation in cosmic ray flux during Solar Eclipse on 21 June, 2020 at Jaipur, India*, *Astroparticle Physics*, Vol. **136** 102659 (2022)

Appendix I

Calculation of Energy Deposition by Cosmic Muons in 1 cm Plastic Scintillator(BC400)

In order to calculate the energy deposited by cosmic ray muons in a 1 cm thick plastic scintillator, the signal from the PMT was analyzed. The signal amplitude, rise time and fall time of the signal were measured from the oscilloscope using BenchVue software. The total number of electrons collected at the anode of PMT produces the signal whose shape can be approximated to be a triangle with dimensions as follows :

$$\begin{aligned} Base\ of\ the\ triangle &= \frac{(Rise\ Time + Fall\ Time)}{0.8} \\ Height\ of\ the\ triangle &= Amplitude\ of\ the\ signal \\ Area &= \frac{1}{2} \times Base \times Height \end{aligned} \tag{5.1}$$

$$\tag{5.2}$$

Since, Rise time or Fall time is only 80% of the total time development of the signal. The total charge collected at the anode of PMT and hence the total number of electrons can be expressed as:

$$q = \frac{area}{Impedance(\ 50\Omega)} \tag{5.3}$$

$$No.\ of\ electrons\ (N) = \frac{q}{1.6 \times 10^{-19}} \tag{5.4}$$

From the specification of PMT, it is known that the gain of PMT is of the order of 10^6, so the primary number of electrons is :

$$N_p = \frac{N}{10^6} \tag{5.5}$$

Thus knowing the primary electrons and from the definition of the quantum efficiency (QE) of the photocathode of the PMT, i.e

$$QE = \frac{Number\ of\ Photoelectrons}{Number\ of\ Photons} \tag{5.6}$$

$$We\ can\ write, \tag{5.7}$$

$$Number\ of\ Photons\ (N_{ph}) = \frac{N_p}{QE}, where\ QE = 0.3 \tag{5.8}$$

Now, there are various factors that introduce light losses. One of them is Light Trapping, which is internal reflection of photons at the surface of the scintillator. If μ is the refractive index of the scintillator, then the Critical angle for total internal reflection is C=sin^{-}1$(1/\mu)$.
Thus, only light incident on the surface within a cone of semi-angle C is able to escape from the scintillator surface. The fraction of light that is permanently entrapped in the crystal is f = (3 cos C - 2) [99]. For BC400 μ=1.58 and the calculated value of f$\sim$0.3.

$$Actual\ number\ of\ Photons\ (N'_{ph}) = \frac{N_p}{QE \times f} \tag{5.9}$$

$$Thus, \tag{5.10}$$

$$Amount\ of\ energy\ deposition = \frac{100eV \times N'_{ph}}{10^6} \tag{5.11}$$

where 100 eV is the energy required to produce 1 scintillation photon in plastic scintillators [11].
With (Rise time + Fall Time) $\sim$ 20-30 ns, and amplitude $\sim$500 mV, the energy deposited per unit cm is approximately 2.028 MeV.

Appendix II

Calculation of the time which could have been taken by the zonal and meridional disturbances due to the solar eclipse to reach Kolkata

Refer to the paper by Zhang *et al.*, (on the TSE of 21^{st} August 2017) [132].

1. Angular distance between Kolkata and East St. Louis (near Memphis) along 88° ∼ 268° meridian (from 38° N-lat. to 22° N-lat. across the north pole) = (90° - 38°) + (90° - 22°) = 120°

Radius of the Earth = 6400 km (approx.) [polar radius = 6356 km; equatorial radius = 6378 km]

Linear distance ($L_{meridional}$) = $120 \times \frac{180}{\Pi} \times 6400$ km = 13403 km

Speed of propagation of meridional disturbance ($v_{meridional}$) = 1800 m/sec = 6480 km/hr

Assuming that the meridional disturbance propagates at this speed a very long way along a meridian (amplitude certainly decreases with distance), time for disturbance to reach Kolkata from East St. Louis:

$T_{meridional} = \frac{L_{meridional}}{v_{meridional}} = \frac{13403}{6480}$ = 2.06 hr = 2 hr 4 min

Totality time at St. Louis = 1:17 pm CDT ∼ 1:17 + 10.5 hrs IST = 11:47 pm IST.

Expected time of arrival of meridional TEC perturbation in Kolkata:

11:47 + 2:04 hrs IST = 00:51 am IST, 22 August

(A smaller value of speed of propagation, say 1500 m/sec, would push this time towards 01:30 am)

2. Angular distance b/w Kolkata (88° E lon.) and 1st pt. of contact with CONUS at 125° W-lon. (Oregon) along 45° N-latitude = 147°

Linear distance (L_{zonal}) = $147 \times \frac{180}{\Pi} \times 6400 \times \cos 45° = 11610$ km

Speed of propagation of zonal TEC perturbation (v_{zonal}) = 700 m/sec = 2520 km/hr.

Assuming that the zonal disturbance propagates at this speed (but with diminishing amplitude) a very long way along a line of constant latitude, travel time of zonal perturbation from 1st pt. of contact to Kolkata:

$T_{zonal} = \frac{L_{zonal}}{v_{zonal}} = \frac{11610}{2520}$ = 4.6 hr = 4 hr 36 min

Expected time of arrival of zonal TEC perturbation in Kolkata:

21:16 + 4:36 hrs IST = 01:52 am IST, 22 August, 2017

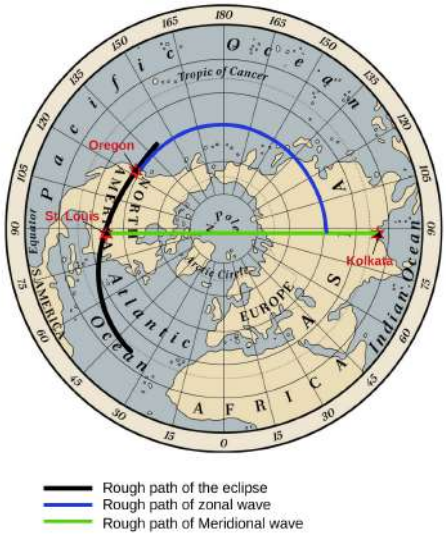

Figure 5.1: Schematic showing the path of zonal and meridional disturbances (Picture downloaded from VectorStack.com/8141533)

Reprints

Pramana – J. Phys. (2021) 95:50
https://doi.org/10.1007/s12043-021-02094-0

Stability study and time resolution measurement of straw tube detectors

S ROY[1], S JAISWAL[1], S. CHATTERJEE[1], A SEN[1], S DAS[1], S K GHOSH[1], S RAHA[1], V M LYSAN[2], G D KEKELIDZE[2], V V MYALKOVSKY[2] and S BISWAS[1,*]

[1]Department of Physics, Bose Institute, EN-80, Sector V, Kolkata 700 091, India
[2]LHEP-JINR, Dubna, Russian Federation
*Corresponding author. E-mail: saikat@jcbose.ac.in, saikat.ino@gmail.com

MS received 29 September 2020; revised 9 December 2020; accepted 14 December 2020

Abstract. Straw tube detectors are single wire proportional counters that are widely used as tracking devices. We have carried out R&D activity with a straw tube detector prototype. The aim of this work is to study the stability of the performance in terms of gain and energy resolution of these types of detectors under high rate of radiation. The gain and energy resolution of the detector are studied along with its variation with ambient temperature and pressure. X-rays from a radioactive source are used to irradiate the detector and to monitor the energy spectra simultaneously for calculating the gain. The method followed here is unique as the ageing measurements have been performed without using an accelerated particle beam or any radiation generator. The performance of a straw tube detector has been studied in a laboratory for more than 800 h at a stretch using a single sealed radioactive X-ray source with high intensity. Variation of gain and energy resolution of the straw tube detector under X-ray irradiation in Ar/CO_2 gas mixture (volume ratio 80/20) is discussed in this article. The gain of an aged straw depends on gas flow rate. We have estimated the time required for the gain of a straw tube detector under ageing tests to recover on increasing the gas flow rate. We have also estimated the time resolution of the straw tube detectors by using cosmic rays as the trigger for the Ar/CO_2 gas mixture in 70/30 volume ratio (different gas mixture was used for the measurement of the time resolution). This type of ageing and time resolution measurements in Ar/CO_2 gas mixture has not been reported earlier. The details of the measurement process and the experimental results are presented in this article.

Keywords. Straw tube detector; gain; energy resolution; radiation effect; time resolution.

PACS No. 29.40.Cs

1. Introduction

Straw tube detectors such as ATLAS [1] and NA62 [2] experiments at CERN and GlueX [3] in Hall D at JLab are single-wire cylindrical proportional chambers that have been used in many high-energy physics experiments over the decades for tracking charged particles with low material budget. Straw proportional tubes have the potential to be used as tracking devices in future high-energy physics experiments [4–6] involving very high particle density and extremely high interaction rate. Therefore, it is crucial to test their rate handling capability [8] and the effect of prolonged irradiation of these detectors. Earlier studies on straw tubes filled with a $Xe/CF_4/CO_2$ gas mixture have revealed gain degradation [9–12]. This transient ageing phenomenon observed in strongly irradiated straw tubes is because of the change in gas composition due to the production of long-lived and highly electronegative radicals during the avalanche process. This causes a temporary reduction in gain which can be restored by appropriately increasing the gas flow rate. There are more reports on radiation hardness and ageing effects of straw tube detectors [13,14] performed with Xe-based gas mixtures. However, Ar/CO_2 is by far a much more widely used mixture in gaseous particle detectors. As far as CO_2 is concerned, it is believed to be an ageing-resistant gas unlike other organic gases that are mixed with noble ones to quench secondary photons. Pure Ar/CO_2 gas showed stable operation up to ~ 1 C/cm [14–17], while some reports showed unexplained gain reduction with this gas [18,19]. Our goal was to operate the straw tube detector under conditions as close as possible to the real environment of high-energy physics experiments in

Published online: 25 March 2021

terms of total charge accumulated on the detector over its lifetime. We wanted to study the effect of long-term exposure to radiation of straw tube detectors and to verify if gas ageing phenomena take place or not without imposing accelerated ageing. In this regard, two separate experiments were performed. In the first one, stability tests for the absolute gain and energy resolution of one straw tube under irradiation with X-rays were carried out. The experimental set-up and results are discussed in §2.1 and §2.2 respectively. The influence of temperature and pressure on the gas gain is also investigated. Reduction in gain after continuous operation for a very long time is observed in this experiment. To confirm that this gain reduction is due to ageing phenomena, another experiment using two straw tubes, one as a reference and the other as a test detector, was carried out. The reference straw was under the influence of a low rate of X-ray radiation whereas the other one was under a higher rate of X-ray radiation. A comparison of the gain of both the straws was done at certain time intervals during continuous radiation exposure. A detailed description of the experimental set-up and discussion of the results are included in §3.1 and §3.2 respectively. Time resolution of the detector is another important factor of concern in any tracking system. We have used cosmic rays as the radiation source and measured the time resolution of the straw tube detector. The experimental set-up and results are discussed in §4.

2. Stability test of straws: Experiment I

The main goal of this experiment was to measure the gain of the straw tube detector continuously at finite intervals in order to study its variation with increasing exposure. As the gain of a gaseous detector depend on ambient temperature and pressure [20], we also tried to check their correlation with gain variations.

2.1 *Experimental set-up*

The straw tube prototype used in this experiment was built in JINR, Dubna, Russia. It consists of 6 straws of 6 mm diameter and 25 cm length which are wound by two Kapton film strips. Carbon-loaded Kapton film of the 160 XC 370 type from DUPONT and aluminised (500 Å) Kapton film of the NH type are used as inner and outer strips, respectively. Both films are covered by a glue layer with a thickness of 7 μm on one side. A gold-plated tungsten-rhenium wire of 30 μm diameter (type 861, Luma) is used as the anode. The wire under 70 g tension is fixed by the crimp pins inserted in the polycarbonate end-plugs. The diameter of the end-plug is 6.0 ± 0.018 mm [6]. The signals from each straw tube are collected

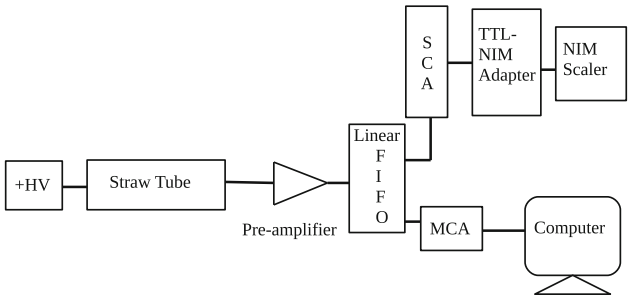

Figure 1. Schematic of the set-up used for the stability tests of the straw tube detector.

using LEMO connectors. A premixed gas composed of argon and CO_2 in 80/20 volume ratio is used in flow mode at a rate of 3 l/h and an overpressure of 1 bar. In these straw tubes, overpressure of the working gas mixture of 1 bar is applied. The gas purity is 99.9% and a polyurethane (PU) tube is used for the gas distribution.

The central anode wires are biased with positive high voltage (HV) using a HV filter box at one end while the signal is collected from the other end after a capacitor. The output signal is fed to a charge-sensitive pre-amplifier (VV50-2 pre-amplifier manufactured by CDT, Heidelberg, Germany) having a gain of 2 mV/fC and a shaping time of 300 ns [7]. The output of the pre-amplifier is sent to a linear fan-in-fan-out (FIFO) module. One output of the linear FIFO is put in a timing single channel analyser (SCA), which is operated in integral mode and the lower level in the SCA is used as the threshold. A NIM-based scalar module is used to measure the counting rate of the detector. A multichannel analyser (MCA) is used to obtain the energy spectra with a ^{55}Fe X-ray source taking another output from the linear FIFO. A schematic of the set-up is shown in figure 1. A typical energy spectrum for ^{55}Fe in Ar/CO_2 80/20 mixture at 1550 V is shown in figure 2.

The gain of the straw tube detector is calculated in the following way. The 5.9 keV peak of the ^{55}Fe X-ray spectrum is fitted with a Gaussian function and from the mean of the fitted peak, the charge after avalanche multiplication (collected charge) is calculated using the gain of the pre-amplifier (PA gain in mV/fC) and the calibration factor (CF in mV/ch) of the MCA to convert the channel number in pulse height (in mV). The small effect of stray capacitances (due to cables, connectors, and so on) on the amplitude of the signal is neglected in the calculation. The expression for gain is given by the ratio of the collected charge and primary charge:

$$\text{Gain} = \frac{\text{Collected charge}}{\text{Primary charge}} = \frac{[(\text{Mean} \times \text{CF})/\text{PA gain}]}{[\text{No. of primary electrons} \times e]}, \quad (1)$$

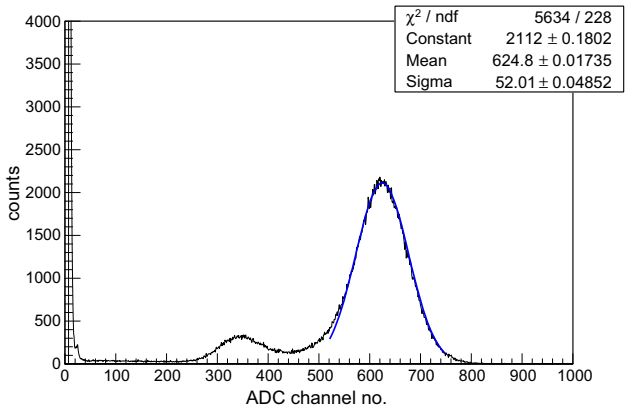

Figure 2. Typical energy spectrum for X-rays from ^{55}Fe source in Ar/CO_2 gas mixture in the 80/20 volume ratio at 1550 V. The main peak is fitted by a Gaussian function shown in blue line.

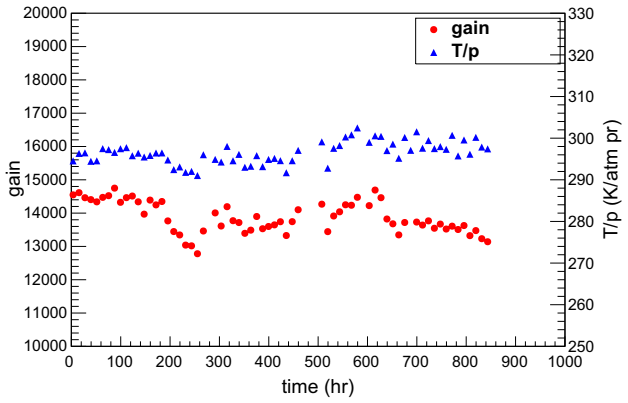

Figure 3. Gain and T/p as a function of time. The bias voltage of the straw tube detector is 1550 V. Error bars are smaller than the marker size.

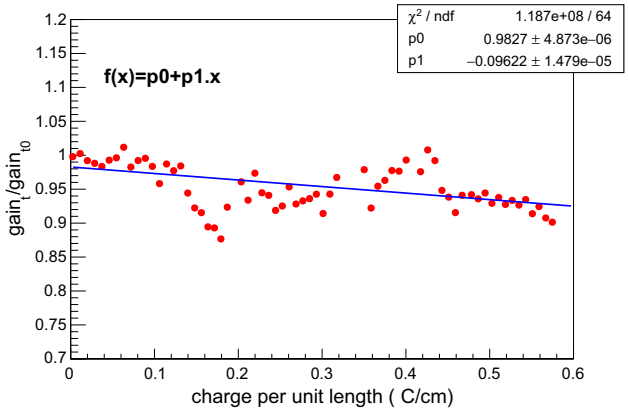

Figure 4. Ratio of instantaneous gain and initial gain (normalised gain) as a function of charge accumulated per unit length.

where e is the electronic charge in Coulomb. The average number of primary electrons produced in the gas is taken as 217 for Ar/CO_2 mixture in the 80/20 volumn ratio assuming full energy deposition of 5.9 keV X-ray in the gas volume and using the average energy required to produce an electron–ion pair. For X-rays in a Ar/CO_2 gas mixture, the primary number of electrons n is calculated using the formula:

$$n = E_X \left(\frac{\%\text{ of Ar}}{W_{Ar}} + \frac{\%\text{ of } CO_2}{W_{CO_2}} \right), \quad (2)$$

where E_X is the energy of the X-ray (for ^{55}Fe $E_X = 5.9$ keV), W_{Ar} and W_{CO_2} are the average energies required to produce an electron–ion pair in Ar and CO_2 gas respectively. W_{Ar} and W_{CO_2} are 26 eV and 33.2 eV respectively. For 80% Ar and 20% CO_2 gas

$$n = 5.9 \times 10^3 \left(\frac{0.8}{26} + \frac{0.2}{33.2} \right) \approx 217. \quad (3)$$

The energy resolution of the straw tube detector is defined as

$$\%\text{energy resolution} = \frac{\text{Sigma} \times 2.355}{\text{Mean}} \times 100\%, \quad (4)$$

where sigma and mean are obtained from the Gaussian fitting of the 5.9 keV peak of each ^{55}Fe X-ray spectrum. The gain of the straw tube is found to be 1.4×10^4 at 1550 V and uniform along the length of the detector.

In order to study the effect of prolonged irradiation of the detector, a collimated X-ray source (activity 3.7 GBq) is placed on top of the detector and a continuous monitoring of the energy spectra is carried out. The collimator is set in such a way that 4 mm length of the straw is irradiated with realistic particle rate in the detector of 40 kHz/mm. The spectra are stored automatically at regular intervals of 10 min. A data logger [21] made in-house is used to record ambient temperature and pressure online.

2.2 *Results*

The gain of the straw tube is measured at regular intervals as mentioned earlier. The gain as a function of time is shown in figure 3 along with the variation of the ratio of ambient temperature ($T = t + 273$ K) and pressure (p) with time. The average relative humidity during the measurement is found to be $\sim 55 \pm 5\%$. From figure 3 it can be seen that during a period of more than 800 h, the gain decreases from 15000 to 13000. This may be the effect of prolonged irradiation. The ageing rate is parametrised as a normalised gas gain loss:

$$R = -\frac{1}{G_0}\frac{dG}{dQ} \times 100\% \text{ per C/cm}, \quad (5)$$

where G_0 is the initial gas gain, dG is the loss of gas gain after collected charge dQ per unit length. To evaluate

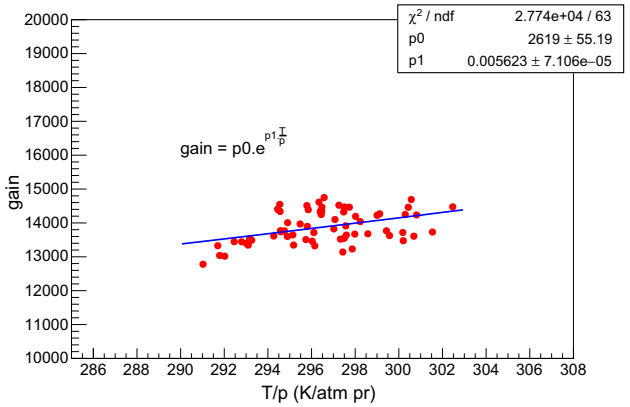

Figure 5. Correlation between gain and T/p. Error bars are smaller than the marker size.

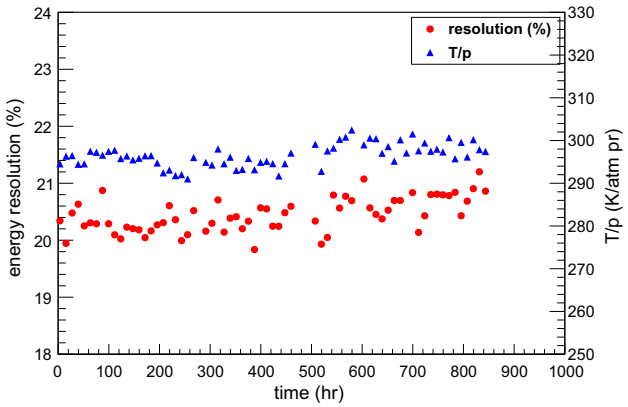

Figure 6. Energy resolution and T/p as a function of time. The bias voltage of the straw tube detector is 1550 V.

the ageing rate, we normalised the instantaneous gain (gain_t) by the initial value of the gain (gain_{t0}) and plotted it against charge accumulated per unit length of the straw tube detector as shown in figure 4. The accumulated charge over the straw tube is calculated using the relation

$$\frac{\mathrm{d}Q}{\mathrm{d}l} = \frac{r \times n \times e \times G \times \mathrm{d}t}{\mathrm{d}l}, \tag{6}$$

where r is the measured rate (in Hz) in a particular area of the detector, n is the number of primary electrons for a single X-ray photon, e is the electronic charge, G is the gain of the detector, $\mathrm{d}t$ is the time in second and $\mathrm{d}l$ is the irradiated length of the straw. In this case, the straw tube is continuously irradiated for more than 800 h leading to a charge accumulation of 0.6 C/cm. As shown in figure 4, the normalised gain is fitted by a first-order polynomial function. The slope $p1$ of this function corresponds to the ageing rate which is 9.6% per C/cm. However, this observation needs a confirmatory test to ensure that this is purely due to the irradiation and not due to other external effects. It can be seen from figure 3 that the variation of gain depends on variation in T/p. Although there is not much variation in T/p throughout the experiment, we still tried to find a correlation of gain with T/p which is shown in figure 5. It is seen from figure 5 that the points are scattered and so the χ^2/NDF of the fit is bad. Therefore, it can be said that in addition to T/p, other parameters also are responsible for the variation of gain.

It is known that ageing of gaseous detectors strongly depend on total accumulated charge [22]. Apart from that, the ageing rate is affected by macroscopic parameters such as high gas gain, radiation intensity and gas flow rate. In that direction, the next experiment is carried out with high radiation intensity and low gas flow rates to observe ageing rates for the straw tube in a practically lesser time.

Figure 6 shows the variation of energy resolution with time. In this experiment, it is observed that the energy resolution increases from an initial value of 20% to a final value of 21% at the end of the measurement.

3. Stability test of straws: Experiment II

The goal of the second experiment was to verify whether the degradation in the gain of the straw tube detector is purely due to high irradiation or not. To this end, gain and energy resolution measurements with two straws are carried out. The detectors are positioned adjacent to one another. The idea is to use one straw as a reference detector (marked as R) and the other one (marked as A) for the study of ageing effects due to a much higher amount of accumulated charge with respect to the reference detector. To study the performance, gain and energy resolution of both the straws are measured continuously and simultaneously at equal intervals of time.

3.1 *Experimental set-up*

An identical experimental set-up as mentioned in §2.1 is used to measure the gain and the energy resolution of both the straws. The detectors are connected to the same gas line such that any external factors affecting the performance of the straws cancel out when we take the ratio of any measured quantity of the two straws such as gain or energy resolution. The same ^{55}Fe X-ray source is used to irradiate both the straws. The radiation over straw R is purposely kept at low rates just to use it as a reference detector to monitor the gas gain continuously and compare at fixed time intervals with the gain of straw A. The counting rates in the straw tubes A and R, adjusted by using a perspex collimator, amount to 35 kHz/mm and 0.09 kHz/mm, respectively. The biasing voltages of the

detectors A and R are kept at 1550 V and 1450 V respectively. The reference detector R is operated at low gains ∼6000 and lower radiation, whereas the straw tube A is operated at high gains ∼13000. This is done to achieve a higher amount of accumulated charge on straw A in comparatively lesser amount of time and to minimise the amount of charge accumulation on R. So the expectation is that the ratio of the gains of the two straws normalises all the effects due to external factors such as ambient temperature, pressure, relative humidity and gas flow rate. The energy spectra from both detectors are simultaneously stored at regular intervals of time through two separate MCA modules. The detector characteristics such as gain and energy resolution are extracted from the ^{55}Fe X-ray spectra using the same method as discussed in §2.1.

3.2 *Results*

The variations over time of the gain and the energy resolution, as well as the ones of T/p, are plotted in figures 7 and 10 respectively. As one can see in figure 7, a gradual decrease in the gain of straw A with time is observed with respect to the straw R. After the first 100 h of measurement, a decrease of 11% in absolute gain is observed at a gas flow rate of 0.02 l/h. Then the gas flow rate is increased up to ∼0.13 l/h to check if the gain restores to its original value or not. In figure 8, the normalised gain of straw A, viz. the instantaneous gain (gain) over the initial gain (gain_{t0} = 13000) and T/p are plotted as a function of time from the time instant in which the gas flow rate is increased. The time-varying normalised gain is fitted by the function

$$f(t) = p_0(1 - p_1 e^{-t/p_2}), \tag{7}$$

where p_0, p_1 are constants, t is the time in h and p_2 is the time constant of the function. From this fit, one can see that the gain restores to 96% of its initial value in 3.62 h of continuous gas flow at a rate of 0.13 l/h. T/p was constant throughout this time as can be seen from figure 8 and so the gain was not needed to be normalised by the T/p effect. After a few hours, the gas flow rate is again reset to ∼0.03 l/h and the measurement is continued. The high voltage is kept ON and the source is not removed from its original position. We can see that the gain of straw A continuously decreases from 13000 to 10000, viz. 77% of the initial value. If we again increase the gas flow rate to a value of 0.8 l/h after ∼600 h, we can see an increase in the normalised gain as shown in figure 9. The normalised gain is fitted with the same function as in eq. (7). From the fit it is found that the gain increases from about 80% to 87% of its initial value in a time duration of 3.15 h, but the gain did not restore to its original value even after flowing the gas at

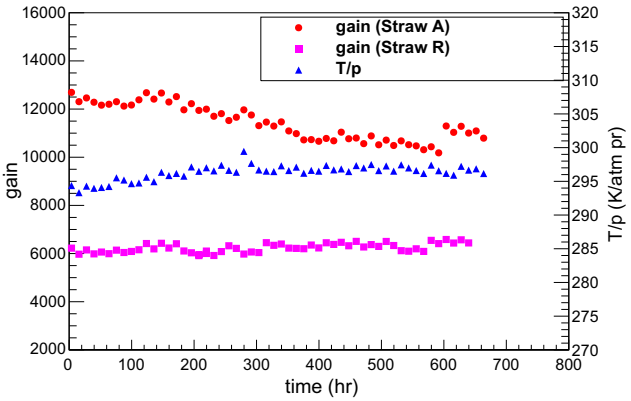

Figure 7. Gain and T/p as a function of time of the straws A and R biased at 1550 V and 1450 V respectively.

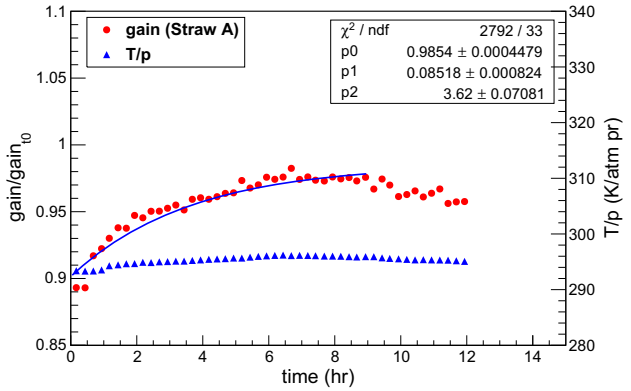

Figure 8. Normalised gain and T/p as a function of time (here $t = 0$ h means $t = 100$ h of the actual measurement).

a high rate for more than 10 h. The effect of changing the gas flow rate is also observed for straw R, but this effect is more prominent for straw A. There is an overall slight increase in the gain of straw R which is due to the increase in T/p with time. For the same reason, there is a decrease in the energy resolution value of straw R from 25% to 23% as shown in figure 10. However, it can be seen from figure 10 that the energy resolution of straw A increases from 29% to 34% (which is 17% increment). It should also be noted here that the energy resolution of straw A does not improve by increasing the gas flow rate. This may indicate the performance degradation of the straw at high radiation environment.

To understand the effect of prolonged irradiation on the degradation of the gain of the straw tube detector, the ratio of the gains of the straws is taken and normalised by the ratio of the initial gains. As changes in temperature, pressure, relative humidity and gas flow rate will affect both the straws similarly, the ratio of the two gains can properly express the long term effect of the radiation only on the straw under ageing study.

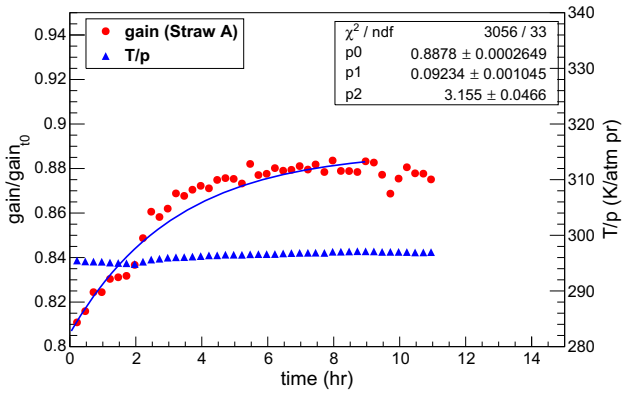

Figure 9. Normalised gain and T/p as a function of time (here $t = 0$ h means $t = 600$ h of the actual measurement).

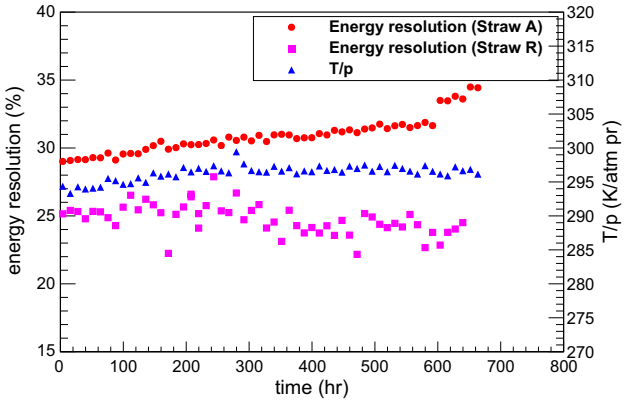

Figure 10. Energy resolution and T/p as a function of time for both the straws. The bias voltage of straws A and R are 1550 V and 1450 V respectively.

The normalised ratio is calculated as

$$\text{Ratio}_{\text{normalised}} = \frac{\frac{\text{Gain}_{\text{straw A}}(t)}{\text{Gain}_{\text{straw R}}(t)}}{\frac{\text{Gain}_{\text{straw A}}(0)}{\text{Gain}_{\text{straw R}}(0)}}, \tag{8}$$

where $\text{Gain}_{\text{straw A}}(0)$ and $\text{Gain}_{\text{straw R}}(0)$ are the initial gains in straw A and straw R respectively. The normalised ratio is fitted by a first-order polynomial function as shown in figure 11. Here also a negative slope of -1.15 clearly may indicate a degradation of the gain in straw A because of the high rate of radiation.

4. Measurement of time resolution

Since straw tubes may be used for tracking in several upcoming high-energy physics experiments, it is also important to study their timing properties. The time resolution of a gaseous detector depends on the gas mixture and the applied voltage or electric field of the detector. It is actually the measure of the fluctuation in the time

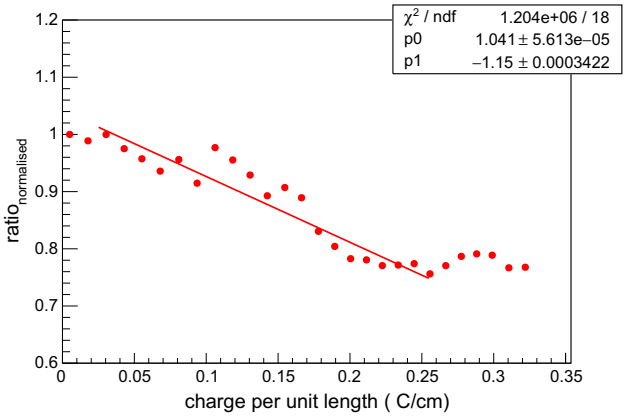

Figure 11. Normalised ratio of gains of straws A and R as a function of charge accumulated per unit length of straw A.

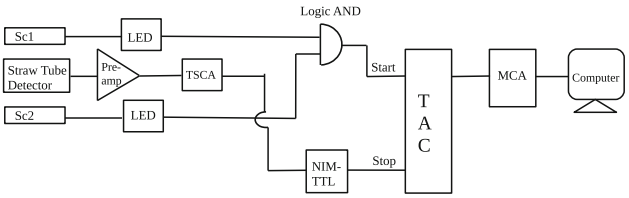

Figure 12. Schematic of the electronics set-up for time resolution measurement of the straw tube detector.

required for the electrons to drift along the electric field lines towards the anode wire. For wire chambers, the time resolution is usually of the order of a few ns.

The time resolution of the straw tube detector is measured with a premixed Ar/CO_2 gas in the 70/30 volume ratio. Two plastic scintillator detectors are used to generate 2-fold trigger signals with cosmic rays. The photomultipliers coupled to the scintillators are biased with a voltage of +1550 V. The signals from the scintillators are fed to a leading edge discriminator (LED) with a threshold of −50 mV. The 2-fold coincidence signal is used as the 'start' signal for the time to amplitude convertor (TAC). The TAC is set at 10 μs full scale range. The straw signal after passing through the pre-amplifier is fed to a timing single channel analyser (TSCA) which gives a TTL logic output. This TTL signal is converted to NIM signal using TTL-NIM adapter module and the NIM output signal is used as the 'stop' signal for TAC.

The time difference between the 'start' and the 'stop' signal gets converted to amplitude in the TAC and the output is fed to the MCA for obtaining a timing spectrum. The schematic electronics set-up for timing measurement is shown in figure 12. Figure 13 shows a typical time spectrum at 1750 V which is fitted with a Gaussian function. The mean of the distribution gives the time difference of the trigger and the straw tube signal. The sigma of this distribution is the effective/combined time resolution of the straw tube

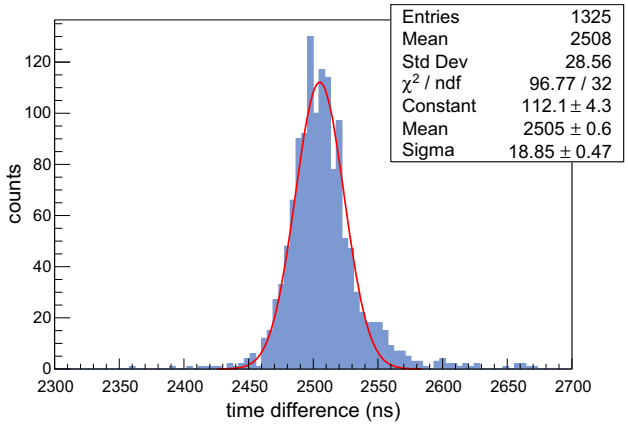

Figure 13. Time spectrum of the straw tube detector at 1750 V with Ar/CO_2 in the 70/30 volume ratio.

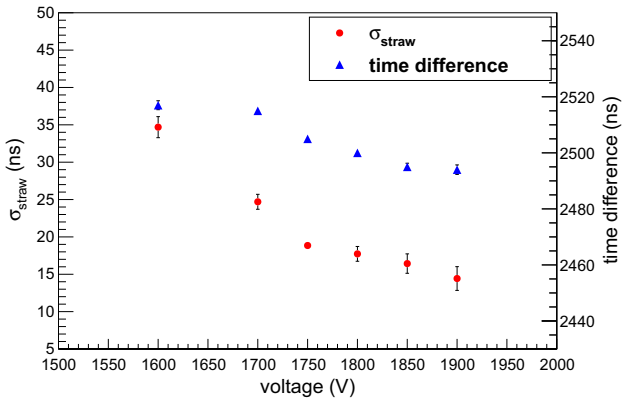

Figure 14. Time resolution (σ_{straw}) of the straw tube and time difference as a function of voltage.

and trigger detectors. The time resolution of the straw tube is extracted from the relation:

$$\sigma_{eff}^2 = \sigma_{straw}^2 + \sigma_1^2 + \sigma_2^2, \quad (9)$$

where σ_{eff}^2 is the effective time resolution of the combined detector set-up, σ_1 and σ_2 are the time resolution of the trigger scintillators Sc1 and Sc2 respectively. The time resolutions of the trigger scintillators are independently measured and the values of σ_1 and σ_2 are found out to be (0.38 ± 0.01) ns and (0.56 ± 0.01) ns respectively. The time resolution of the straw tube is measured for different voltage settings. The variation of the time resolution (σ_{straw}) of the straw tube and the time difference between the start and stop signal, as a function of voltage is shown in figure 14. As one can see, the time resolution decreases with the increase in voltage. The best achieved time resolution for the straw tube is found to be (14.4 ± 1.6) ns at 1900 V.

5. Summary and outlooks

From the first experiment, we concluded that the gain reduction by 9.6% per C/cm after a total charge accumulation of 0.6 C/cm wire on the straw might be due to continuous and high radiation. The observed ageing rate is small but not negligible. In the second experiment, we confirmed that the occurred ageing was due to the high radiation intensity and also have drawn a conclusion on the dependence of this ageing rate on the gas flow rate. It takes about 3 h for the gain of a continuously irradiated straw to partially restore after increasing the gas flow rate. The transient nature of ageing is proven by the fact that the gain tends to restore as one increases the gas flow rate. After a very long exposure to radiation, one can observe that the gain degrades continuously and it did not restore. The gain did not restore to its initial value even after we allow the gas to flow at a very high rate for a long time. This means that there is some ageing due to long term operation of the straw tube detectors which is not observed in the case of accelerated ageing measurements reported in refs [9,10]. Therefore, this needs further detailed investigation. For Ar/CO_2 gas mixture operated at high rates over long time periods, a gradual decomposition of CO_2 can occur and the resulting pure carbon can be deposited at the cathode [23]. An important observation in both the experiments is that the gain degradation of the straw tube detector starts immediately from the time of operation under high intensity radiation. The degradation is slow and gradual. The difference between the first and the second experiments was that, the latter was conducted at relatively lower gas flow rates. Another conclusion that can be drawn from our experiment is that the straw tubes can be safely operated at low radiation intensities (∼0.1 kHz/mm) and at low gas flow rates (∼0.02 l/h) (as no ageing is observed in straw R of experiment 2) and at high radiation intensities (∼40 kHz/mm) at high gas flow rates (>3 l/h) (as slight gain reduction is observed even after 800 h of operation of the straws in experiment 1).

On the other hand, it is well known that the Ar/CO_2 mixture is very robust and does not produce deposits on the wire. So an alternative reason of gain degradation in both experiments might be the use of a gas mixture of low purity (99.9%) and of a polyurethane tube. There might be diffusion of water vapour through the walls of PU tube. Water vapour does affect the gain, as it modifies the Townsend coefficients slightly, but this effect, if due to leakage, should plateau at some point, and in addition it should not affect the energy resolution. A residual, true degradation is observed, which can only be due to contaminants in the gas, e.g. from material outgassing. To check this in the near future, the measurements will be

repeated with gas having higher purity and using stainless tube for the gas distribution. A systematic study of the ageing rates at different radiation intensities, gas gains and gas flow rates will also be carried out in future to fix the operating conditions of the straws in the real experiment.

The time resolution of the straw tube detector is also measured with cosmic rays. The best achieved time resolution is found to be 14.4±1.6 ns at a biasing voltage of 1900 V.

Acknowledgements

The authors would like to thank Late Prof. Vladimir Peshekhonov of JINR, Dubna and Dr Christian J Schmidt of GSI Detector Laboratory for providing the straw tube prototype. They also would like to thank Dr S Chattopadhyay and Mr J Saini of VECC, Prof Rajarshi Ray, Prof Somshubhro Bandyopadhyay and Dr Sidharth K Prasad of Bose Institute for valuable discussions and suggestions during the course of the study. This work is partially supported by the research grant SR/MF/PS-01/2014-BI from DST, Govt. of India and the research grant of CBM-MuCh project from BI-IFCC, DST, Govt. of India. S Raha would like to acknowledge the support received under the Raja Ramanna Fellowship scheme of the Department of Atomic Energy, Government of India. S Biswas acknowledges the support of Intramural Research Grant provided by Bose Institute and DST-SERB Ramanujan Fellowship.

References

[1] https://atlas.cern/discover/detector/inner-detector
[2] https://home.cern/news/news/experiments/new-straw-trackers-na62
[3] Y Van Haarlem *et al.*, *The GlueX central drift chamber: Design and performance*, *Nucl. Instr. and Meth. in Phys. A* **622** (2019) 142.
[4] http://www.fair-center.eu/for-users/experiments/cbm.html
[5] http://www.fair-center.eu/
[6] V Peshekhonov *et al*, *Phys. Particles Nucl. Lett.* **9**(**2**), 172 (2012)
[7] CDT CASCADE Detector Technologies GmbH, Hans-Bunte-Str. 8-10, 69123 Heidelberg, Germany. www.n-cdt.com
[8] S Roy, N Nandi, R P Adak, S Biswas, S Das, S K Ghosh, S K Prasad and S Raha, *Nucl. Instrum. Methods Phys. Res. A* **936**, 488 (2019)
[9] V G Bondarenko, B A Dolgoshein, V A Grigoriev, A A Kruglov and I S Markina, *Nucl. Phys. B* **44**, 577 (1995)
[10] M Capeans, C Garabatos, R Heuer, R Mackenzie, T Meyer, F Sauli and K Silander, *Ageing properties of straw proportional tubes with* $Xe/CF_4/CO_2$ *gas mixture*, CERN-PPE/93- 136 (1993)
[11] M Capeans, *IEEE Trans. Nucl. Sci*. **51**(**3**), 994 (2004)
[12] E Abat *et al*, *JINST* **3**, P02013 (2008)
[13] T Akesson *et al*, *Nucl. Instrum. Methods Phys. Res. A* **361**, 440 (1995)
[14] J A Kadyk, J Va'vra and J Wise, *Nucl. Instrum. Methods Phys. Res. A* **300**, 511 (1991)
[15] J Va'vra, *Nucl. Instrum. Methods Phys. Res. A* **252**, 547 (1986)
[16] A Dwurazny, Z Hajduk and M Turala, Ageing effects in gaseous detectors and search for remedies, *Proceedings of the Workshop on Radiation Damage to Wire Chambers* **LBL-21170** (1986) p. 113
[17] E Conti and F Gasparini, *Nucl. Instrum. Methods Phys. Res. A* **465**, 472 (2001)
[18] V Blinov, Influence of materials and sense wire surface quality on aging with DME and other gases, *Proceedings of the International Workshop on Aging Phenomena* (DESY, Hamburg, Oct. 2–5, 2001)
[19] T Kowalski, A study of aging effect in gas monitoring proportional counters of the BAC calorimeter of the ZEUS experiment, *Proceedings of the International Workshop on Aging Phenomena* (DESY, Hamburg, Oct. 2–5, 2001)
[20] M C Altunbas, K Dehmelt, S Kappler, B Ketzer, L Ropelewski, F Sauli and F Simon, *Nucl. Instrum. Methods Phys. Res. A* **515**, 249 (2003)
[21] S Sahu, D Nag, S Rudra, S Swain, S Biswas, S Das and P K Sahu, *JINST* **12**, C05006 (2017)
[22] J A Kadyk, *Nucl. Instrum. Methods in Phys. Res. A* **300**, 436 (1991)
[23] V Pashhoff, *Studies on ageing and reanimation of drift tubes for the ATLAS muon spectrometer*, Dissertation (University Freiburg, 1999) CERN-THESIS-99-083

Astrophys Space Sci (2020) 365:172
https://doi.org/10.1007/s10509-020-03886-3

ORIGINAL ARTICLE

A study of the secondary cosmic γ-ray flux in India during the Great American solar eclipse on 21st August 2017

S. Roy[1] · S. Biswas[1] · S. Das[1] · S.K. Ghosh[1] · S. Raha[1]

Received: 25 June 2020 / Accepted: 21 October 2020 / Published online: 26 October 2020

Abstract We present the results from the measurement of secondary cosmic gamma-ray flux using a NaI(Tl) scintillator detector during a total solar eclipse. The unique feature of this experiment is that it was carried out at a place where the solar eclipse was not observable. The total solar eclipse of August 21, 2017, was visible in most of the regions of North America during the day, whereas India, falling on the other half of the globe missed this particular eclipse. Our aim was to measure and examine if there are any variations in the secondary cosmic ray (SCR) flux at Kolkata, India due to the occurrence of the eclipse in America. Detailed experimental techniques used for this experiment are mentioned in this article. Method of data analysis and results are presented. We observe unexpected decrement and increment in SCR flux in certain energy regions.

Keywords Solar eclipse · SCGR · NaI scintillator · Bow wave

1 Introduction

The solar eclipse of August 21, 2017, also known as "The Great American Eclipse" was a total solar eclipse visible within a band across the entire continental United States, passing from the Pacific to the Atlantic coasts. The partial eclipse started on August 21 at 15:46:50 UTC and ended on August 21 at 21:04:21 UTC. Solar eclipse is a very important astronomical event that provides the opportunity for studying the disturbance produced in the atmosphere and its effect on cosmic ray intensity. It has been observed in the past that the rapid reduction in solar irradiation during the eclipse causes many secondary effects on the Earth's atmosphere (Eckermann et al. 2007). However, any study of cosmic rays in places falling on the other side of the Earth where eclipse is not occurring has not been carried out previously. The Great American eclipse was a good opportunity to study its effect on the atmosphere just above Kolkata, India.

Cosmic rays are high energy particles (mostly protons) that continuously bombard the upper atmosphere resulting in the production of various secondary particles such as the charged pions, kaons, etc. which decay into muons and neutrinos. The neutral pions decay to produce pairs of gamma rays and they contribute to the electromagnetic component of the shower. Muons are produced in the interactions of primary cosmic rays with the nuclei present in the atmosphere and those being more massive compared to the lighter leptons, lose less energy through radiative processes. On the surface of the Earth, a substantial flux of sub-MeV to MeV gamma rays and GeV muons is detected. Besides the secondary cosmic ray (SCR) flux, terrestrial radioactive nuclei namely ^{40}K, ^{222}Rn, ^{232}Th, ^{238}U, also make additional contributions to the sub-MeV to MeV gamma rays. Of the total observed gamma radiation, only a few percent consists of the cosmic ray induced component, the rest is a component due to terrestrial radioactivity. The terrestrial gamma ray (TGR) background level normally does not change over time interval of an hour, except due to presence of Radon in the atmosphere which may be transported to the ground during rainfall (Nayak et al. 2016). During clear weather, there is no significant variation in the TGR component to be expected within a short interval of time. Therefore any observed sudden variation in the mea-

S. Roy
shreyaroy2509@gmail.com

[1] Department of Physics and Centre for Astroparticle Physics and Space Science, Bose Institute, EN-80, Sector V, Kolkata 700091, India

sured gamma ray flux will be purely of extraterrestrial origin.

The variation of secondary cosmic gamma ray (SCGR) flux during solar eclipses have been studied and reported earlier by several groups of researchers. Most of them observed a dip in SCGR flux during the solar eclipse (Bhattacharya et al. 2010). The experiment carried out by Chintalapudi et al. during total solar eclipse of October 24, 1995 at Diamond Harbour, showed that there is 11% dip in γ-rays (600 keV–1350 keV) and on the average 9–10% decrement in high energy photon counts (Chintalapudi et al. 1997). In another experiment performed by Bhattacharya et al. during the same solar eclipse, observation of a maximum drop of 25% in the secondary γ-ray flux in the energy interval 2.4 MeV–2.7 MeV was reported (Bhattacharyya et al. 1997). Nayak et al. reported an observation of 9% dip just prior to the total solar eclipse and 4% steady decrement during the eclipse of August 1, 2008 in the energy range 50 keV–4600 keV (Nayak et al. 2010). According to observations by Bhaskar et al. during solar eclipse of January 15, 2010, there was a 21% drop in SCR flux in 1 MeV–1.5 MeV energy range during annularity (Bhaskar et al. 2011). The explanation given by some groups is that a quasi-periodic pressure wave is set up in the ionosphere by the shadow band in the ozone layer which may, considerably, affect the production of SCR (Antonova et al. 2007). Another explanation is that π–μ component production layer of the atmosphere is lowered due to atmospheric cooling during eclipse which shortens the path (or the time available) for decay of π^0 meson to γ-rays and μ meson to $e^{\pm}$ and induces the changes in relative cosmic ray counts (Bhattacharyya et al. 1997). The drop of SCR intensity cannot be explained by atmospheric cooling alone because geophysical disturbances are present at all levels of the atmosphere. The interaction of the cosmic rays in the atmosphere is affected by the weather parameters and solar activities. A few percent of cosmic gamma rays are influenced by atmospheric pressure.

The overall atmospheric weather and solar activity report during the eclipse week (19 August to 23 August, 2017) is discussed in section 4. We have used a NaI(Tl) detector to detect the gamma rays. For shielding the detector from TGR as much as possible, we have used a lead box with 1 cm thick walls. We started our measurements a few days prior to the day of the solar eclipse, and continued the same for the next few days for good statistics of the background counts and estimation of fluctuations. In order to estimate the amount of terrestrial component of radiation, we performed measurements with different shielding configurations. An observed significant variation in gamma ray flux correlated with astrophysical phenomena like the solar eclipse, can only be claimed provided the TGR background is properly subtracted.

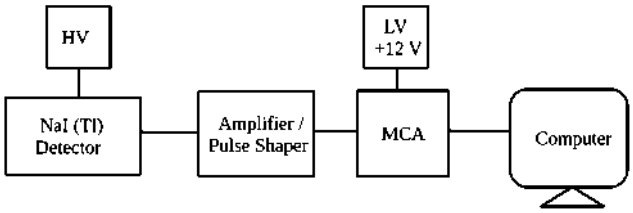

Fig. 1 Block diagram of the experimental arrangement

2 Experimental setup

The NaI(Tl) detector used in the present experiment, has a crystal of size 5.1 cm × 5.1 cm. The crystal is hermetically sealed inside an aluminium casing of 0.8 mm thickness with a 1 mm thick white reflecting material placed between the crystal and the casing. The scintillation crystal is optically coupled to photomultiplier tube (PMT) of diameter 5.1 cm, inside the hermetically sealed case. The PMT was biased with a voltage of +600 V from an adjustable power supply ORTEC-556.

A schematic of the signal processing electronics is shown in Fig. 1. The signal from the dynodes is fed to a fixed gain charge sensitive pre-amplifier, integrated with the base of the PMT. The pre-amplifier signal is further shaped and amplified using ORTEC-671 Spectroscopy Amplifier with coarse gain of 500 and shaping time of 0.5 μs. The amplifier output is digitized using multi-channel analyzer (MCA). Finally, the data were stored in a personal computer (PC). A picture of the setup in laboratory is shown in Fig. 2. The detector was calibrated using standard gamma ray sources ^{137}Cs (662 keV), ^{60}Co (1173 and 1332 keV) and ^{22}Na (511 keV) of known energies. For each case the energy spectra are stored in PC. After the energy calibration, we performed the background study with different configurations of lead shielding. As mentioned earlier, the estimation of the contribution from the terrestrial radioactivity is extremely important for our experiment to be able to give precise results. Four different configurations were used (i) The detector was kept on top of a wooden table without any lead shielding, such that γ-rays can reach the detector from all directions. (ii) The detector was kept on top of a lead box such that the γ-rays can reach the detector's active medium from all sides except the bottom. (iii) The detector was kept inside the lead box with the top lid of the box kept open, such that γ-rays can be incident on the detector from top only. (iv) The detector was placed inside a closed lead box. Fig. 3 shows spectra of the cosmic background radiation obtained for all four cases. The peaks due to terrestrial radioactive sources are clearly visible. Continuous measurements were carried out from 16th August, 2017 to 23rd September, 2017. The DAQ framework enables automatic feeding of the spectrum data to a buffer in every two minutes which is saved to an ASCII file in the computer before the MCA starts acquiring

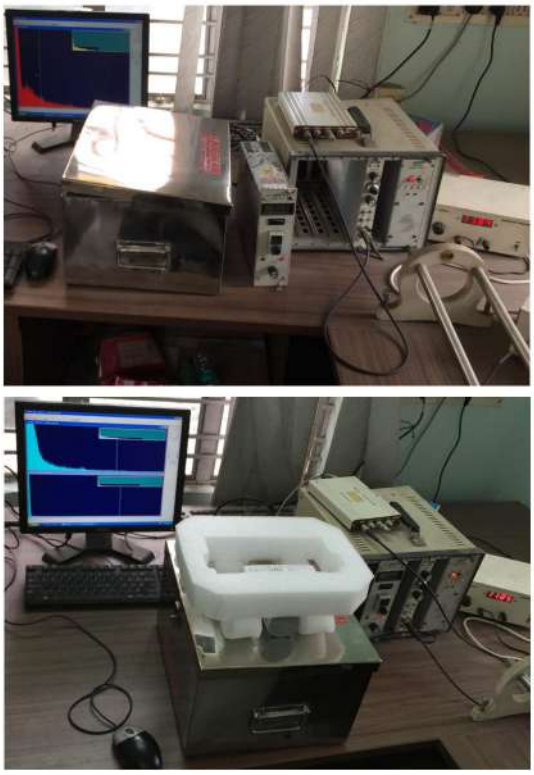

Fig. 2 Setup of the experiment with NaI inside the Pb box (top) and on top of the box (bottom)

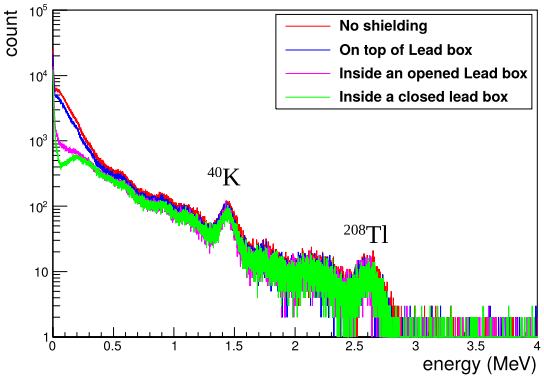

Fig. 3 Gamma spectrum with different configurations

the next spectrum. This ASCII file is analyzed offline and the spectrum is plotted using the ROOT analysis software package (Brun and Rademakers 1997).

3 Results

All the further measurements were made keeping the detector on top of the lead box such that it is exposed to background radiations from all three directions. No radioactive sources apart from terrestrial radioactivity were present nearby. Ambient temperature and humidity were

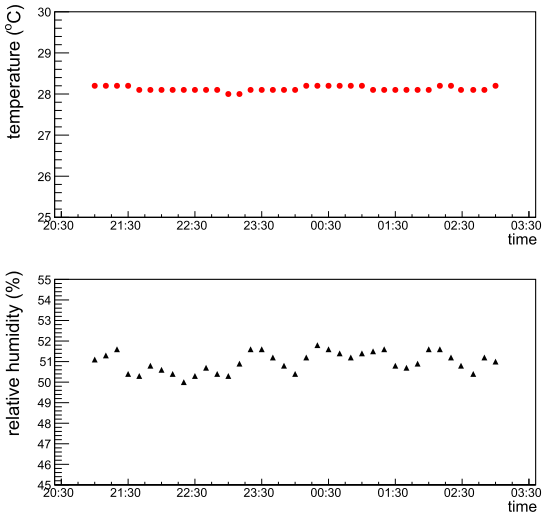

Fig. 4 Inside temperature and relative humidity during the night of 21 August 2017

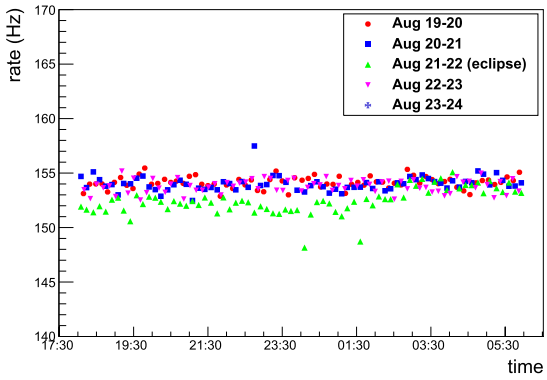

Fig. 5 Total count rate from NaI due to cosmic and terrestrial radiation

kept constant at an average value around 28°C and 50% respectively during the entire duration of measurements using air conditioning system. Fig. 4 shows the temperature and humidity measured inside the laboratory during the night of 21 August. The outside temperature was around 28°C and the outside humidity was within 80% to 90%. The weather data of Kolkata can be obtained from the site https://www.timeanddate.com/weather/india/kolkata/historic?month=8&year=2017. The γ-ray spectra are stored for 2 minutes and the number of detector signals per seconds was calculated by summing up the counts in all the ADC channels, thereby integrating the entire spectrum and then dividing by the time taken for accumulation of each of the spectrum. Fig. 5 shows the total γ-ray counts per second over the detector area measured during 19th to 23rd August, 2017.

The decrease in γ-ray counts is clearly visible in the plot. In order to know the nature of fluctuations and its energy dependence, the data for the detector counts was analysed in low and high energy ranges separately. The inte-

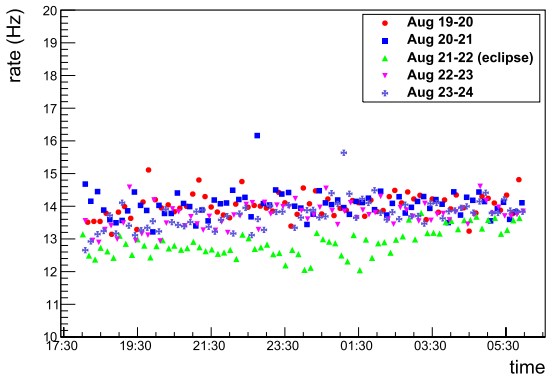

Fig. 6 Total counts of secondary cosmic gamma ray per second in the energy range 25–100 keV

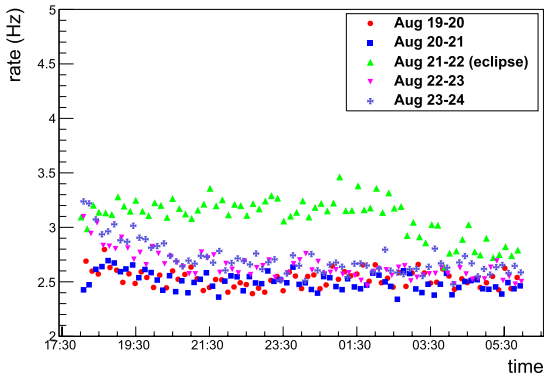

Fig. 7 Total counts of secondary cosmic gamma ray per second in the energy range above 1500 keV

gration over energy was done by selecting energy ranges as, Region 1: low energy (25–100 keV), Region 2: moderate energy (100–500 keV), Region 3: 500–1000 keV, Region 4: 1000–1500 keV and Region 5: above 1500 keV respectively. The data of each day (5 days of eclipse week) was analysed and for these days only the specific hours during which the eclipse took place in America, i.e. from first contact to last contact was considered. This corresponded to 15:46(UTC) + 05:30 hour to 21:04 + 05:30 hour in IST which is a duration of 5 hours and 18 mins (21:16 August 21 to 02:34 August 22). Assuming, the bulk of the cosmic rays are in the vertically downwards direction and most probably it is to be affected by the eclipse effects, we attempted to extract only this contribution from the total measured gamma ray flux. Since the TGR background coming from the bottom was already shielded by the lead box, the TGRs coming from the sides was estimated by methods discussed in the earlier section as

$$count_{sides} = count_{sides+top} - count_{top} \tag{1}$$

where $count_{sides+top}$ is the gamma count rate measured with detector placed on top of the lead box (only bottom shielded) and $count_{top}$ is the gamma count rate measured with detector placed inside the lead box with the top lid open. The value of $count_{sides}$ was estimated for the different energy bins and it was subtracted from each data point in the corresponding energy regions. The day to day variation for two different energy regions – Region 1 and Region 5, is shown in Fig. 6 and Fig. 7, since the most significant variation during the eclipse was observed in these energy ranges.

To get an idea of the change in secondary γ-ray flux during these hours and to compare with the same on normal days during those specific hours, we have plotted a histogram of gamma counts per second in all the energy regions for normal days and also plotted the same during the eclipse as shown in Fig. 8. The mean of the Gaussian count rate distribution in Region 1 for normal days is 13.89 Hz with a precision of 0.03 Hz, while for the eclipse day the mean is 12.62 Hz with a precision of 0.05 Hz. The difference in means during the eclipse and during normal days was calculated using the relation

$$\delta m = \frac{mean_{eclipse} - mean_{normal}}{mean_{normal}} \times 100\% \tag{2}$$

and the error in δm is given by the relation

$$\sigma_m{}^2 = (\frac{\sigma_E}{N})^2 + (\frac{1}{N} + \frac{(E-N)}{N^2})^2 \sigma_N^2 \tag{3}$$

where E and N are the mean counts during eclipse and normal day and σ_E and σ_N are the errors in eclipse and normal day counts respectively. The value of δm for Region 1 is found out to be $(-9.1 \pm 0.4)\%$ which means that there is a significant decrement in the SCGR flux in this particular energy range. The SCGR flux distribution for normal days from 21:16 hr to 02:34 hr was compared with SCGR flux distribution during the eclipse. Both the distributions were fitted with a Gaussian function (red line) in the Fig. 8. Similar analyses were done for all the energy regions and the values of δm are quoted in Table 1. A peculiar trait in the SCR flux distribution was observed in Region 5. An unexpected high value of the mean of the Gaussian count rate distribution for eclipse day was observed and the value is 3.211 Hz, while for the normal days the mean is 2.579 Hz. The value of δm is $(24.5 \pm 0.6)\%$. This increment was observed through out the duration of eclipse and after this the count rate falls back to normal value gradually as seen in Fig. 7.

4 Discussions

All earlier reports of flux variations are based on observations from measurements performed at places lying on the path of the solar eclipse i.e. the shadow region. Our experiment is unique in the sense that the measurements are done

Table 1 Increment or decrement in secondary cosmic gamma ray count rate for different energy regions during the eclipse

Energy range (keV)	Count rate during normal days (Hz)	Count rate during the eclipse (Hz)	δm (%)
25–100	13.89 ± 0.03	12.62 ± 0.05	-9.1 ± 0.4
100–500	37.42 ± 0.03	37.11 ± 0.07	-0.8 ± 0.2
500–1000	13.46 ± 0.01	13.61 ± 0.03	$+1.1 \pm 0.2$
1000–1500	5.508 ± 0.008	5.334 ± 0.019	-3.1 ± 0.3
above 1500	2.579 ± 0.006	3.211 ± 0.016	$+24.5 \pm 0.6$

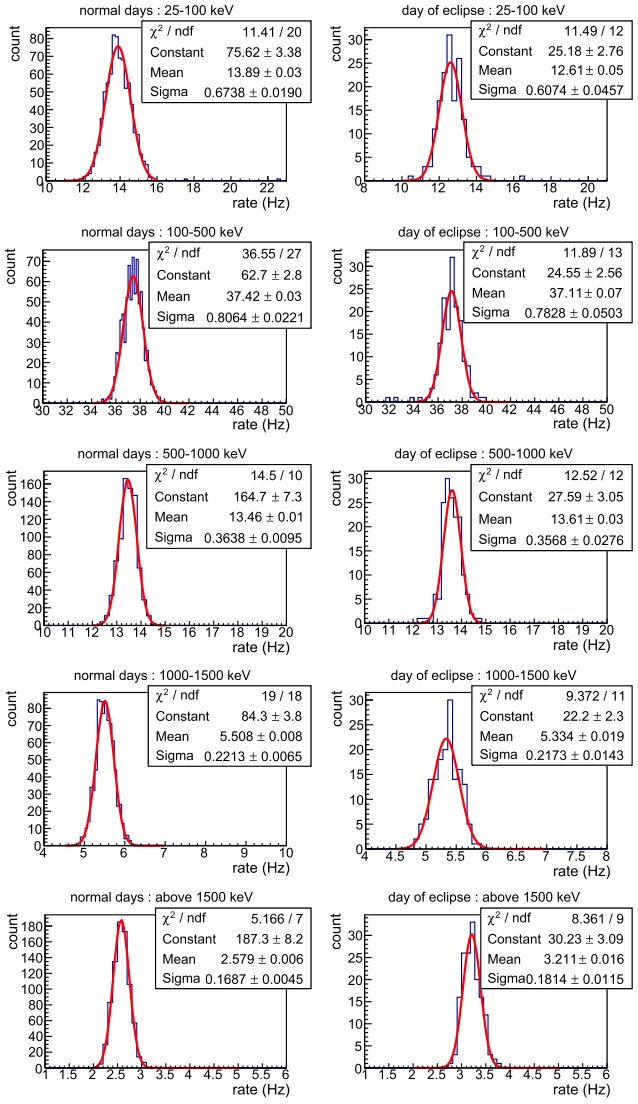

Fig. 8 Frequency distribution of total counts of secondary cosmic gamma ray per second in different energy regions for normal days (left) and day of eclipse (right) during only those particular hours when the eclipse occurred

at a place lying on the other side of the globe. Therefore, all the explanations and interpretations of results obtained by earlier groups of researchers might not hold in our case. We observed SCGR flux decrement of 9.1% in the energy range 25–100 keV, 0.8% decrement in the energy range 100–500 keV, 1.1% increment in the energy range 500–1000 keV, 3.1% decrement in the energy range 1000–1500 keV and 24.5% increment for energies above 1500 keV. One more interesting thing is that the increment or decrement that we observed were sustained throughout the solar eclipse duration that is from the time of the first contact to the time of the last contact. The count rates are consistent with each other before and after this duration. We shall now attempt to give a tentative explanation of our observations. During a solar eclipse, the Moon's shadow constitutes a cooling region in the Earth's atmosphere that travels at supersonic speed which may generate a bow wave. This was first pointed out by Chimonas and Hines in 1970 (Chimonas 1970) and later investigated by other groups (Davis et al. 1970; Beer et al. 1972). They predicted pressure perturbation that trails the umbra (in the form of a bow wave), and propagates sideways and upwards at a speed of about 250 m/sec to soon reach the ionospheric layers at around 200 km altitude. In reference (Zhang et al. 2017) a strong signature of ionospheric bow waves was identified as total electron content (TEC) disturbances over central/eastern United States during the Great American Eclipse 2017. Interestingly they not only found the eclipse bow wave in the ionosphere, they discovered strong TEC perturbations that move along meridional direction and zonal direction at supersonic speeds that are too fast to be associated with known gravity wave or large-scale travelling ionospheric disturbance (LSTID) processes. As mentioned in their paper, atmospheric and ionospheric disturbances can be excited by many different sources. In order to observe the bow waves, the atmospheric disturbances due to other sources should be minimal. This is a very important point that unless we know the environmental parameters during the eclipse, we cannot claim to observe an effect that is not very large. According to the data from NOAA's Geostationary Operational Environmental Satellites (GOES)[1] there were no space weather turbulences on 21 August. The planetary K index (K_p) had a low value (<4) during the eclipse.[2] The solar wind speed and geomagnetic parameters were also

[1] https://www.swpc.noaa.gov/.

[2] https://www.gfz-potsdam.de/en/kp-index/.

normal during the day of solar eclipse.[3] The overall conclusion that can be made from the NOAA's data is that there were no disturbances in the space weather conditions during the day of the solar eclipse event. Other atmospheric parameters like atmospheric pressure at Kolkata, showed no abnormal traits and no rainfall occurred throughout the days from 19 August to 23 August, 2017 when we carried out the experiment.[4] A perfect clear weather caused the effects of environmental parameters on the measured gamma ray fluxes to be negligible, thereby increasing the chances to observe the effects of the solar eclipse. This might have been an advantage for the bow waves to have propagated to larger distances effectively. The implication of all these may be that we might have observed in India, through gamma ray counts, some effects of the Travelling Ionospheric Disturbances (TIDs) during the solar eclipse in America. TIDs are propagating perturbations in the ionospheric electron density.

A possible connection between the TIDs and the secondary cosmic gamma-ray flux can be drawn as follows. The TIDs have the potential to increase or decrease the TEC in the region of the atmosphere they are travelling through. When the electron concentration increases in the ionospheric layers, the primary cosmic rays tend to lose more energy by bremsstrahlung while passing through it. In this process, mostly low energy gamma rays (X-rays) having energy in the range of few keV to few hundred keV are produced. If the TEC decreases, it will cause the low energy secondary gamma-ray flux to decrease. The speculation over here is that the TIDs reaching India due to the solar eclipse in America might have influenced the TEC in such a way that the low energy secondary gamma-ray flux decreased at the expected time of arrival of the TIDs.

We tried to check the feasibility of this newly proposed mechanism using ionospheric TEC data from Indian Institute of Geomagnetism (IIG). IIG operates GPS receivers to measure the ionospheric TEC across India. We studied the data from two GPS stations nearby Kolkata. Fig. 9 shows the TEC variations measured during the period 19 August 2017 to 24 August 2017 by the GPS station at Shillong, India. From the figure, it can be observed that the TEC value during the day of eclipse (August 21) denoted by the yellow marker, is lower than other days of the week. The eclipse started at 15:46 UTC and ended at 21:04 UTC on 21 August. Since we do not know exactly at which time the TIDs would arrive in India, so we focused on the TEC data during the entire night time i.e. 16:00 UTC to 23:59 UTC, when large fluctuations due to solar radiation is absent. The average TEC value during the night of August 21 was compared with the average TEC value during the night of other days of the week. A reduction of 48% in the average TEC on August 21 is found. TEC data from another station situated at Silchar is presented in Fig. 10 and here also we observed similar traits in TEC. Similar analysis was done with data from this station and a reduction of 20% in the average TEC on August 21 is found. The observed reduction in the TEC during the night of August 21 along with the fact that weather was clear in India, is enough to conclude that the eclipse induced TIDs have possibilities to reach India.

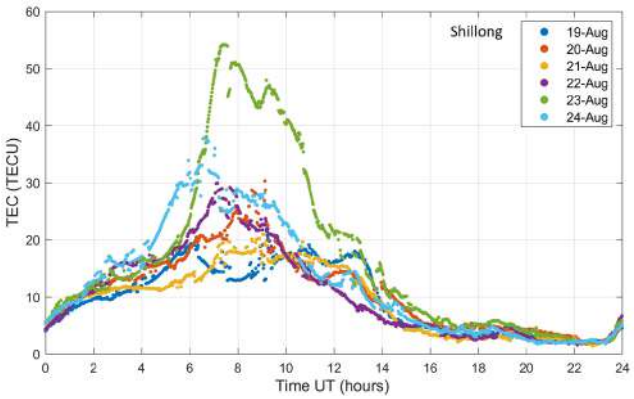

Fig. 9 Total Electron Content (TEC) for the period 19 August to 24 August 2017, measured by GPS station at Shillong, India

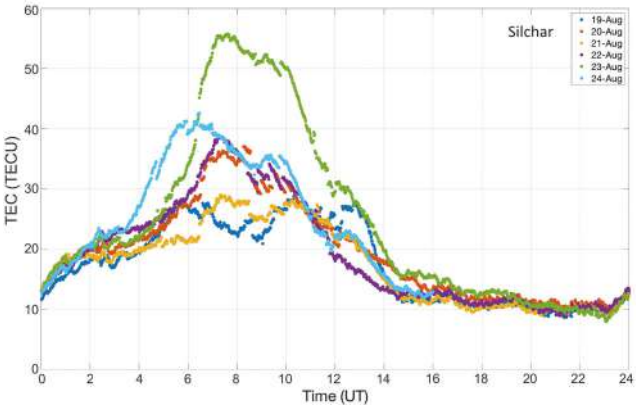

Fig. 10 Total Electron Content (TEC) for the period 19 August to 24 August 2017, measured by GPS station at Silchar, India

The decrement in SCGR rate observed in 25–100 keV energy has not been observed in any other day of the week. This may have occurred because the TEC disturbances had propagated all the way to Kolkata (approximately 13000 km from East-Central USA) and had an impact on the secondary gamma ray production in the atmosphere. The results we obtained from our experiment using NaI(Tl) detector are statistically significant enough to conclude that there is some effect of the eclipse on the SCR fluxes even at places on the globe which do not fall within the path of the eclipse. According to calculations mentioned in Appendix, it is found

[3] https://www.swpc.noaa.gov/products/solar-and-geophysical-activity-summary.

[4] https://www.timeanddate.com/weather/india/kolkata/historic?month=8&year=2017.

that the TEC zonal disturbance would have taken a minimum of 4 hr 36 min to travel from Oregon to Kolkata and reach here at 1:52 am IST 22 August. The meridional wave could have taken 2 hr 4 min to travel from St. Louis to Kolkata and arrive at around 00:51 am IST 22 August. But the time of propagation of the meridional disturbance could in fact be larger because the velocity of the wave used in the calculation is the maximum velocity; the actual velocity might have been lower. Thus the zonal and meridional disturbances could have reached Kolkata almost at the same time causing the observed decrement in the gamma ray flux. However, this is just a speculation, not an assertion, we do not really know how fast a disturbance in TEC propagates and in which direction for a certain height of the layer. The decrement and increment observed in gamma ray counts in energy regions 100–500 keV and 500–1000 keV respectively are considered insignificant. We observed decrement of 3.1% in the energy range 1–1.5 MeV, which is in agreement with earlier report (Bhaskar et al. 2011), where they observed 21% drop in this energy range. We have not found any suitable explanation for the 24.5% increment in gamma counts above energy 1.5 MeV. This observation needs explanation which cannot be given based only on the present measurements and needs to be confirmed in future eclipses. A detailed investigation must be carried out in the future for a deep understanding of the phenomenon and its consequences. We hope that this work will motivate others to study the propagation of atmospheric disturbances produced by the solar eclipse to places located far away from the path of the eclipse.

Acknowledgements We would like to thank Prof. Roger Barlow, University of Huddersfield, UK, for his help and guidance in analysing the data, especially the importance of the statistics. We are most grateful to the colleagues of the Indian Institute of Geomagnetism, Navi Mumbai, especially its Director, Dr. D. S. Ramesh, and Dr. S. Tulasi Ram and his team, for providing us the ionospheric data from their stations in Eastern India. We thank Mr. Shibnath Shaw, Dr. Rama Prasad Adak, Mr. Rathijit Biswas and Mr. Sayak Chatterjee for their help during the experiments. We are most grateful to Prof. Manashi Roy and Dr. Debapriyo Syam for their invaluable advices and discussions on various aspects of this work. S. Raha would like to acknowledge the support received under the Raja Ramanna Fellowship scheme of the Department of Atomic Energy, Government of India. S. Biswas acknowledges the support of DST- SERB Ramanujan Fellowship. This work was supported in part by the Department of Science & Technology, Government of India, under the IRHPA scheme (IR/S2/PF-01/2011, dated 26/6/2012).

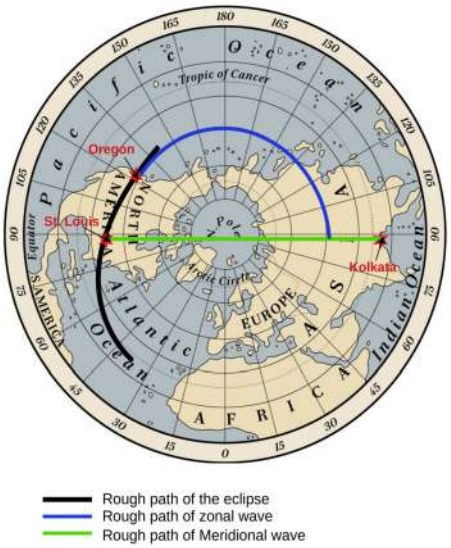

Fig. 11 Schematic showing the path of zonal and meridional disturbances (Picture downloaded from VectorStack.com/8141533)

Appendix. Calculation of the time which could have been taken by the zonal and meridional disturbances due to the solar eclipse to reach Kolkata

Refer to the paper by Zhang et. al., (on the TSE of 21st August 2017) (Zhang et al. 2017).

1. Angular distance between Kolkata and East St. Louis (near Memphis) along 88° ~ 268° meridian (from 38° N-lat. to 22° N-lat. across the north pole) = (90° − 38°) + (90° − 22°) = 120°.

Radius of the Earth = 6400 km (approx.) [polar radius = 6356 km; equatorial radius = 6378 km].

Linear distance ($L_{meridional}$) = $120 \times \frac{180}{\Pi} \times 6400$ km = 13403 km.

Speed of propagation of meridional disturbance ($v_{meridional}$) = 1800 m/sec = 6480 km/hr.

Assuming that the meridional disturbance propagates (a schematic of the path of zonal and meridional disturbances is shown in Fig. 11) at this speed a very long way along a meridian (amplitude certainly decreases with distance), time for disturbance to reach Kolkata from East St. Louis:

$$T_{meridional} = \frac{L_{meridional}}{v_{meridional}} = \frac{13403}{6480} = 2.06 \text{ hr} = 2 \text{ hr } 4 \text{ min}$$

Totality time at St. Louis = 1:17 pm CDT ~ 1:17 + 10.5 hrs IST = 11:47 pm IST.

Expected time of arrival of meridional TEC perturbation in Kolkata:

11:47 + 2:04 hrs IST = 00:51 am IST, 22 August

(A smaller value of speed of propagation, say 1500 m/sec, would push this time towards 01:30 am).

2. Angular distance b/w Kolkata (88° E lon.) and 1st pt. of contact with CONUS at 125° W-lon. (Oregon) along 45° N-latitude = 147°.
Linear distance (L_{zonal}) = $147 \times \frac{180}{\Pi} \times 6400 \times \cos 45° =$ 11610 km.
Speed of propagation of zonal TEC perturbation (v_{zonal}) = 700 m/sec = 2520 km/hr.
Assuming that the zonal disturbance propagates at this speed (but with diminishing amplitude) a very long way along a line of constant latitude, travel time of zonal perturbation from 1st pt. of contact to Kolkata:

$$T_{zonal} = \frac{L_{zonal}}{v_{zonal}} = \frac{11610}{2520} = 4.6 \text{ hr} = 4 \text{ hr } 36 \text{ min}$$

Expected time of arrival of zonal TEC perturbation in Kolkata:

21:16 + 4:36 hrs IST = 01:52 am IST, 22 August, 2017

References

Antonova, V.P., et al.: Bull. Russ. Acad. Sci., Phys. **71**, 1054 (2007)
Beer, T., et al.: Nature **240**(5375), 30–32 (1972)
Bhaskar, A., et al.: Astropart. Phys. **35**(5), 223–229 (2011)
Bhattacharya, R., et al.: Curr. Sci. **98**, 1609–1614 (2010)
Bhattacharyya, A., et al.: Astrophys. Space Sci. **250**, 313 (1997)
Brun, R., Rademakers, F.: ROOT - An Object Oriented Data Analysis Framework. Proceedings AIHENP'96 Workshop, Lausanne, Sep. 1996 Nucl. Instrum. Methods Phys. Res. **389**, 81–86 (1997). See also http://root.cern.ch/
Chimonas, G.: J. Geophys. Res. Space Phys. **75**(28), 5545–5551 (1970)
Chintalapudi, S.N., et al.: (1997). http://hdl.handle.net/2248/6022
Davis, M.J., et al.: Nature **226**(5251), 1123 (1970)
Eckermann, S.D., et al.: J. Geophys. Res. **112**, D14105 (2007)
Nayak, P.K., et al.: Astropart. Phys. **32**(6), 286–293 (2010)
Nayak, P.K., et al.: Astropart. Phys. **72**, 55–60 (2016)
Zhang, S., et al.: Geophys. Res. Lett. **44**, 12,067–12,073 (2017)